Doctoral dissertation

Mineralogical and geochemical study on magnesium silicate hydrates

マグネシウムシリケートハイドレートに関する鉱物学的・地球化学的研究

Nishiki Yuto

西 木　悠 人

Division of Sustainable Resource Engineering,

Graduate School of Engineering, Hokkaido University

国立大学法人北海道大学 大学院工学院環境循環システム専攻

March 2023

北海道大学
HOKKAIDO UNIVERSITY

概要

マグネシウムシリケートハイドレート（M-S-H）はマグネシウム，シリカ，水から構成される低結晶性の物質である。セメント工学において，カルシウムシリケートハイドレート（C-S-H）に関しては古くから多くの知見が得られてきたが，M-S-H に関してはここ十年で研究が始められてきたばかりである。M-S-H は地球科学的にも重要であり粘土鉱物（すなわち 2:1 型や 1:1 型の層状ケイ酸塩鉱物）に類似する構造を有することが知られているものの，具体的にどのような条件下でどのような構造を形成するのかに関しては理解が不十分である。そこで本研究の目的は，複数の室内実験および地質調査という様々なアプローチから，M-S-H の構造，生成条件，特性に関して明らかにすることである。特に本研究では，M-S-H がセメント工学に限らず，様々な地球工学的フィールドにおいて生成されることを想定し，その地球工学的課題に対処するために，M-S-H に関して鉱物学的・地球化学的観点から基本的に調査した。本研究は，以下に示す全 9 章で構成されている。

第 1 章は序論であり，地球科学分野や地球工学分野にとっての M-S-H の重要性を示した。またセメント工学で理解が進んでいる C-S-H の基本特性にも注目しながら，これまで M-S-H が学術的にどのような位置づけで研究されてきたのかを記述し，本研究としての目的を示した。

第 2 章では M-S-H に関する先行研究をレビューした。これまで，M-S-H の基本特性を明らかにするために実施されてきた実験を説明するとともに，地球表層環境で実際に生成された M-S-H の観察事例も示した。

第 3 章では，閉鎖系において酸化マグネシウム（MgO）とシリカフューム（SiO_2）と超純水を 1 年間反応させて M-S-H を合成し，様々な分析手法を駆使してその構造に関するキャラクタリゼーションを行った。MgO/SiO_2 モル比を 0.8, 1.3 とし，温度は 25°C, 50°C, 90°C とした。合成 M-S-H 試料は，MgO/SiO_2 0.8 で 25°C の条件では 2:1 リボン型のセピオライト様の構造を，MgO/SiO_2 0.8 で 50°C および 90°C の条件では含水された 2:1 層の積み重なりからなるスチブンサイトまたは

ケロライト様の構造を有していた。MgO/SiO_2 1.3 で 25°C および 50°C の条件では 2:1 層と 1:1 層の両方の特徴が見られ，MgO/SiO_2 1.3 で 90°C の条件では 1:1 層で管状のクリソタイル様の構造を有した。第 3 章では，MgO/SiO_2 や温度に応じて異なるタイプの層状ケイ酸塩構造が形成されることが示された。

第 4 章では，塩化マグネシウム（$MgCl_2$）水溶液とオルトケイ酸テトラエチル（TEOS）水溶液を混合したのちに水酸化ナトリウム水溶液を添加することで pH を 7, 10, 12 に固定し，M-S-H, 非晶質シリカ，水酸化マグネシウム（$Mg(OH)_2$）の沈殿条件および形成される M-S-H の構造に関して調査した。大気中の二酸化炭素による pH の変動を防ぐために，本実験は窒素雰囲気のチャンバー内にて実施した。$MgCl_2$ と TEOS のモル比率（Mg/Si）を 0.4, 0.7, 1.0, 1.3, 1.5 とし，室温条件下で実験した。pH 7 における沈殿物は，どの Mg/Si 比においても非晶質シリカのみであった。pH 10 では Mg/Si 0.7, 1.0, 1.3, 1.5 において M-S-H，Mg/Si 0.4 においては M-S-H と非晶質シリカの混合物が確認された。pH 12 では Mg/Si 0.4, 0.7, 1.0, 1.3 において M-S-H，Mg/Si 1.5 において M-S-H と $Mg(OH)_2$ が確認された。また，第 4 章で形成された M-S-H は含水 2:1 型の層状ケイ酸塩（スチブンサイトまたはケロライト）であることが示唆された。第 4 章において Mg/Si が高い（Mg/Si ≥ 1.3）条件であっても M-S-H が 2:1 型構造であることは，第 3 章において 1:1 層が確認されていた事実とは異なるが，それは合成実験における液固比や共存する陽イオン（Na^+イオン）が要因となっている可能性が考えられる。

第 5 章においては，フロースルー実験を実施し，地下水のように水の流入・流出がある系（開放系）において M-S-H の生成を確認するとともに，速度論的観点から出発物質の溶解や M-S-H の生成を評価した。MgO を出発物質とし，それに溶存 Si（Na_2SiO_3）を含む pH 10 の水溶液を定流量（~0.06 mL min^{-1}）で供給した。溶存 Si の濃度は 0 mM（ブランク実験）, 0.15 mM, 1.5 mM である。結果として，溶存 Si 濃度が小さい条件（0.15 mM）では Mg/Si の大きい（= 1.59）M-S-H が形成され，溶存 Si 濃度が大きい条件（1.5 mM）では Mg/Si の小さい（= 1.00）M-S-H が形成された。両方の実験においてアウトプット溶液は M-S-H に対して過飽和であるが，1.5 mM での実験の方が 0.15 mM での実験よりも飽和指数が大きかった。アウトプット溶液の Si 濃度から生成速度を評

価すると，1.5 mM での実験の方が 0.15 mM での実験よりも生成速度が大きくなることが確かめられた。一方で，ブランク実験を含め全実験で $Mg(OH)_2$ に対しては不飽和であり，ブランク実験，0.15 mM の実験，1.5 mM の実験の順に飽和指数が小さくなっていった。このことから，M-S-H が生成されることで溶液中から Mg^{2+}イオンが消費されていくため，MgO の溶解が促進されることが示唆された。

第 6 章では M-S-H に関する地質調査を行った。北海道神居古潭帯の赤岩青巌峡付近の蛇紋岩体にて湧水（pH＞10）とそれに伴う沈殿物が確認された。沈殿物は，蛇紋岩を構成する蛇紋石粒子を固結しており，低結晶性のマグネシウムシリケートであることから M-S-H（低結晶性のクリソタイル）であると同定された。水の分析結果より，これは，pH の高い湧水と溶存 Si を多く含む地表水が混合して，M-S-H の形成が誘発されたものと考察した。湧水には溶存炭酸種も含まれているが，溶存 Mg^{2+}はマグネシウム炭酸塩鉱物としては消費されていなかった。代わりに，溶存 Mg^{2+}に加え溶存 Ca^{2+}も多く含んでいる湧水の周辺からは M-S-H とカルシウム炭酸塩鉱物（霰石）の共生を観察した。

地球表層の岩石（特に超苦鉄質岩や苦鉄質岩）と水の相互作用においては，Mg^{2+}は Fe^{2+}と共存する場合も十分に想定される。したがって第 7 章では，Fe(II)–Si–H_2O 系や Mg–Fe(II)–Si–H_2O 系において合成実験を実施し，沈殿物のキャラクタリゼーションを行った。Fe(II)–Si–H_2O 系の実験は第 4 章と同様に，窒素雰囲気にて塩化第一鉄（$FeCl_2$）水溶液と TEOS 水溶液を混合し，水酸化ナトリウム水溶液の添加で pH 7, 10, 12 に固定した。$FeCl_2$ と TEOS のモル比率（Fe/Si）を 0.4, 0.7, 1.0, 1.3, 1.5 とし，室温条件下で実験した。全条件において二価鉄のシリケートハイドレートの生成が確認され，本研究ではこれを F(II)-S-H と定めた。F(II)-S-H と共生する相として，pH 7 のすべての条件と pH 10 かつ Fe/Si 0.4 の条件では非晶質シリカ，pH 10 および pH 12 の Fe/Si が高い条件では水酸化鉄（II）も確認された。また，pH 12 で Mg/Fe 1 かつ (Mg + Fe)/Si 1 の条件で $MgCl_2$ 水溶液, $FeCl_2$ 水溶液, TEOS 水溶液を混合した際の，沈殿物の調査も行った。生成物粒子内は，Mg, Fe, Si が均質に分布しており，Mg と Fe(II)が固溶したシリケートハイドレートが確認され，これ

を本研究では M-F(II)-S-H と定めた。XRD パターンや Si–O 伸縮振動の IR バンドにおいて，M-F(II)-S-H は M-S-H と F(II)-S-H の中間的な特徴を有していた。

第 8 章では地球工学的フィールドを想定した M-S-H に関する地球化学反応モデリングを行った。地熱発電所の熱水配管内での M-S-H スケールの生成を推測し，その阻害のための適切な pH 条件を提案した。また，かんらん石の風化を利用した大気中の二酸化炭素の鉱物化に関するモデリングも行った。近年注目されている岩石風化促進（ERW）では，かんらん石が雨水などと反応して，含水炭酸マグネシウム鉱物が形成されることが期待されているが，かんらん石より溶脱される Mg^{2+}は含水炭酸マグネシウムではなく，主として M-S-H の生成に使われることが想定され，M-S-H の生成を考慮することで CO_2 固定量の試算に大きな影響を与えることを示した。

第 9 章は本研究全体の結論であり，それぞれの章で得られた知見をまとめるとともに，本研究が地球科学分野や地球工学分野において示唆することを述べた。

Abstract

Magnesium silicate hydrate (M-S-H) is a poorly crystalline phase composed of magnesium, silica, and water. In cement engineering, M-S-H has been studied only in the last decade, whereas calcium silicate hydrate (C-S-H) has been studied extensively for almost a century. The author mainly focused on the significance of M-S-H phases in geology as their structures are based on tetrahedral-octahedral-tetrahedral (TOT) or tetrahedral-octahedral (TO) units of clay minerals. Studies of M-S-H are still in their infancy, and further study needs to elucidate the structures and formation conditions of M-S-H phases. In this context, the author conducted various experiments and geologic surveys and sought to understand the structures, formation conditions, and chemical properties of M-S-H phases. This study was carried out especially from mineralogical and geochemical points of view to contribute to some geoengineering issues (e.g., geothermal power generation, CO_2 mineralization, and radioactive waste disposal). This dissertation consists of the following nine chapters.

Chapter 1 refers to the introduction of this study and the significance of the M-S-H study for geosciences and geoengineering. This chapter also explains the history of M-S-H study, referring to C-S-H, a well-known material in cement engineering. The objectives of this study are to (i) characterize mineralogical structures of M-S-H, (ii) clarify the formation conditions of M-S-H, (iii) clarify the geochemical behaviors of M-S-H, and (iv) to predict the formation of M-S-H in engineering geology applications.

Chapter 2 reviews the literatures of M-S-H. An important point is how M-S-H has been synthesized and characterized in previous studies. Besides the experimental studies, this chapter also refers to natural M-S-H precipitates on the Earth surface.

Chapter 3 characterizes the M-S-H samples synthesized from MgO and silica fume (MgO/SiO_2 = 0.8 and 1.3) in solution (water/solid ratio = 45) at 25°C, 50°C, and 90°C. From MgO/SiO_2 0.8, M-S-H phases were identified to be phyllosilicate with TOT ribbons (a sepiolite-like phase) at 25°C and the one

with hydrous TOT layers (a stevensite- or kerolite-like phase) at 50°C and 90°C. From MgO/SiO_2 1.3, M-S-H phases are identified to be phyllosilicate having both TOT and TO units at 25°C and 50°C and TO phyllosilicate (chrysotile) at 90°C. This chapter, therefore, demonstrates types of phyllosilicate in the M-S-H structures depend on MgO/SiO_2 ratio and temperature.

Chapter 4 characterizes the products formed by mixing aqueous Mg solution and aqueous Si solution (Mg/Si = 0.4, 0.7, 1.0, 1.3, and 1.5) at pH 7, 10, and 12 and discusses the formation conditions of M-S-H, amorphous silica, and Mg hydroxide ($Mg(OH)_2$) and structure of the M-S-H. Amorphous silica formed at pH 7 from all Mg/Si ratios. The precipitates at pH 10 were identified as M-S-H from Mg/Si 0.7, 1.0, 1.3, and 1.5 and as a mixture of M-S-H and amorphous silica from Mg/Si 0.4. M-S-H was also precipitated at pH 12. Besides M-S-H, the precipitate from Mg/Si 1.5 also contained $Mg(OH)_2$. All the M-S-H samples were identified as TOT phyllosilicate in the experiments, indicating that pH and Mg/Si ratio did not affect phyllosilicate types. This contradicts the results in Chapter 3. Factors such as the water/solid ratio and the presence of alkali ions (e.g., Na^+) may also determine the phyllosilicate types.

Chapter 5 demonstrates M-S-H formation in open-flow systems and discusses the primary material (MgO) dissolution and the M-S-H formation from a kinetic point of view. The pH 10 solutions ([Si] = 1.5, 0.15, and 0 mM) at pH 10 were injected into the reactors. The M-S-H phases with low Mg/Si (= 1.00) and high Mg/Si (= 1.59) precipitated when input Si concentrations were high (1.5 mM) and low (0.15 mM), respectively. Output solutions in both Si-solution experiments were undersaturated with respect to $Mg(OH)_2$ and supersaturated to M-S-H. The high Si experiment showed a lower saturation index with respect to $Mg(OH)_2$ and a higher saturation index with respect to M-S-H, suggesting that an increase in aqueous silica enhances the primary material dissolution and M-S-H precipitation.

Chapter 6 describes geologic surveys for natural M-S-H samples at alkaline seepages (pH > 10) on an ultramafic body in the Kamuikotan tectonic belt, Hokkaido, Japan. The sediments contained solid phases precipitated interstitially around the detrital serpentine particles. This chapter identifies the phases as M-S-H that may be mineralogically considered as poorly crystalline chrysotile with nano-

tubular morphology. Thermodynamic calculations for the collected liquid samples suggest that a mixed solution of seepage and surface water having high Si activity can induce the formation of M-S-H. In addition to the precipitation of M-S-H in Mg–Si–H_2O systems, it was also observed that M-S-H precipitated even under conditions including Ca and CO_2 species (i.e., Mg–Ca–Si–CO_2–H_2O systems), with simultaneous precipitation of aragonite.

Mg^{2+} is often dissolved with Fe^{2+} in geological settings (especially mafic or ultramafic rocks). Chapter 7, therefore, investigates the effect of Fe(II) during M-S-H formation by characterizing the precipitates in Fe(II)–Si–H_2O and Mg–Fe(II)–Si–H_2O systems. The experiments in the Fe(II)–Si–H_2O systems were similar to those in the Mg–Si–H_2O systems (Chapter 4). Aqueous Fe(II) solution and aqueous Si solution (Fe/Si = 0.4, 0.7, 1.0, 1.3, and 1.5) were mixed at pH 7, 10, and 12. Under all the conditions, poorly crystalline Fe(II) silicate phases were formed. These were identified to be "Fe(II) silicate hydrate" (F(II)-S-H) in this study. The experiment in an Mg–Fe(II)–Si–H_2O system was also conducted by mixing the Mg solution, the Fe(II) solution, and the Si solution (Mg/Fe = 1 and (Mg + Fe)/Si = 1) at pH 12, showing the formation of a solid solution of M-S-H and F(II)-S-H (i.e., M-F(II)-S-H) with intermediate characteristics of M-S-H and F(II)-S-H.

Chapter 8 focuses on geochemical reaction modeling of M-S-H formation in geoengineering applications. The formation of M-S-H scale in a geothermal power plant is predicted, and an appropriate pH condition for its inhibition is suggested in this modeling. This chapter also estimates the M-S-H formation with CO_2 mineralization in enhanced rock weathering. In most situations, Mg carbonate minerals are expected to form as Mg-bearing minerals (e.g., olivine) react with rainwater. However, most aqueous Mg^{2+} derived from olivine dissolution will be consumed by precipitation of M-S-H, rather than the Mg carbonate phases. The M-S-H formation significantly impacts the estimation of the amount of fixed CO_2.

Chapter 9 concludes the results obtained in Chapters 3–8 and describes the implications for geosciences and geoengineering.

Acknowledgements

I would like to extend my sincerest and deepest gratitude to my supervisors: Professor Dr. **Tsutomu Sato**, Professor Dr. **Tsubasa Otake**, Assistant Professor Dr. **Ryosuke Kikuchi**, and Assistant Professor Dr. **Yoko Ohtomo** (Division of Sustainable Resource Engineering, Faculty of Engineering, Hokkaido University). It has been an honor to be a student under the supervision of Dr. Sato, one of the world-famous researchers for applied mineralogy for environmental and resource engineering. Thanks to him, I made presentations at various conferences, visited other institutes many times, and performed variable studies with originality and innovativeness. Dr. Otake gave me critical comments from mineralogical and geochemical points of view. He also taught me how to plan studies, present the results, and write scientific papers. Dr. Kikuchi gave me knowledge regarding clay mineralogy and electron microscopy. Dr. Ohtomo helped with my sample preparation for microscopy and commented on my presentations. In addition, Ms. **Yoshie Hoshi**, Ms. **Yuka Ishioka**, and Ms. **Junko Hasegawa,** secretaries in the laboratory, helped me purchase laboratory instruments and organize my business trips and field works. I had valuable discussions with Ms. **Kanako Toda**, Ms. **Misato Shimbashi**, Mr. **Ryohei Kawakita,** and Mr. **Yuki Sakuma**, who were students in the laboratory.

Besides the people in the laboratory, I would like to extend my appreciation to the staff at Hokkaido University. The petrographic sections were made by Mr. **Kosuke Nakamura** (Faculty of Science), and nuclear magnetic resonance spectroscopy was conducted by Mr. **Naoya Nakagawa** (Faculty of Engineering). I received instruction in transmission electron microscopy (TEM; JEM-2010) from Dr. **Yongming Wang** (Faculty of Engineering). Mr. **Ryo Ota** (Faculty of Engineering) helped me with scanning transmission electron microscopy (STEM; Titan3 G2 60-300) in High-Voltage Electron Microscope Laboratory.

My sincere thanks also go to some off-campus people. Dr. **Takayuki Katoh** (Earth Science Co., Ltd.) introduced the study sites and gave me petrological and mineralogical knowledge related to the

study. Dr. **Jordi Cama** and Mr. **Jordi Bellés** (Spanish National Research Council: CSIC) helped me to design the flow-through experiments. Dr. **Paul Clarence Magdael Francisco** (Japan Atomic Energy Agency) helped me with infrared spectroscopy (Nicolet 6700). Mr. **Takei Toshiaki** and Mr. **Minghui Song** (National Institute for Materials Science: NIMS) helped with transmission electron microscopy (JEM-2100F). I received instruction in thermal analysis from Dr. **Ya Xu** and Dr. **Yoshihiko Takeda** (NIMS) during *NIMS Internship Program*. I had a valuable discussion of carbon mineralization with Dr. **Masao Sorai** (National Institute of Advanced Industrial Science and Technology).

This research has been financially supported by SPRING (No. JPMJSP2119) from the Japan Science and Technology Agency (JST) to the author and Grants-in-Aid for Scientific Research A (No. 19H00878) from the Japan Society for the Promotion of Science (JSPS) to the supervisors (Tsutomu Sato and Tsubasa Otake). The author is a *Hokkaido University DX Doctoral Fellowship* member and indebted to Office for Advancement of Graduate Education Reform, Hokkaido University. The TEM and STEM studies were supported by the Nanotechnology Platform of the Ministry of Education, Culture, Sports, Science and Technology (MEXT), Japan.

Table of contents

List of Tables

Chapter 6

Chapter 7

Chapter 8

List of Figures

Chapter 1

Chapter 2

Chapter 3

Chapter 7

Chapter 8

Chapter 9

List of Abbreviations

ATR: Attenuated total reflection

BET: Brunauer–Emmett–Teller

CEC: Cation exchange capacity

CGS: CO_2 geological storage

C-S-H: Calcium silicate hydrate

CP: Cross polarization

DD: Dipolar decoupling

DO: Dissolved oxygen

DTA: Differential thermal analysis

DTG: Differential thermogravimetry

EDS: Energy dispersive X-ray spectroscopy

ERW: Enhanced rock weathering

F(II)-S-H: Ferrous silicate hydrate

FE: Field emission

FT: Fourier transform

HT–**XRD**: High temperature X-ray diffraction

HWHM: Half width at half maximum

IC: Ion chromatography

ICP–**AES**: Inductively coupled plasma atomic emission spectroscopy

IR: Infrared

LDH: Layered double hydroxide

M: mol L^{-1}

M-F(II)-S-H: Magnesian ferrous silicate hydrate

M-S-H: Magnesium silicate hydrate

MAS: Magic angle spinning

NMR: Nuclear magnetic resonance

ORP: Oxidation reduction potential

PC: Portland cement

PTFE: Polytetrafluoroethylene

SAED: Selected area electron diffraction

SEM: Scanning electron microscopy

SI: Saturation index

STEM: Scanning transmission electron microscopy

TEM: Transmission electron microscopy

TEOS: Tetraethoxysilane

TG: Thermogravimetry

TO: Tetrahedral–octahedral

TOT: Tetrahedral–octahedral–tetrahedral

TRU: Transuranic

w/s: water/solid (a ratio defined on a mass basis)

XAS: X-ray absorption spectroscopy

XRD: X-ray diffraction

Chapter 1: General introduction

1.1 Poorly crystalline Mg silicate formation at low temperatures in geosciences

Mg silicate minerals are ubiquitous components of the lithosphere. Serpentinization is generally considered as a reaction of peridotite and water at high temperatures around mantle wedges or the lithosphere (O'Hanley, 1996). Serpentine is formed by the dissolution of olivine and pyroxene in serpentinization. Talc is also an Mg silicate mineral in ultramafic rocks. However, mineral precipitation at low temperatures (<100°C) is not commonly understood well. Recently, interactions between ultramafic rocks and water at low temperatures are recognized as "low-temperature serpentinization" (Templeton and Ellison, 2020), which have received special attention in natural emplacements such as the Oman ophiolite (Chavagnac et al., 2013) and the Lost City Hydrothermal Field (Allen and Seyfried, 2004). Although serpentine and/or talc (i.e., Mg clay minerals) may even form at low temperatures (Fig. 1.1; Evans, 2004), the formation of Mg silicates is a complex process involving the formation of poorly crystalline precursor phases that may influence the development of final crystalline products (Tosca et al., 2011).

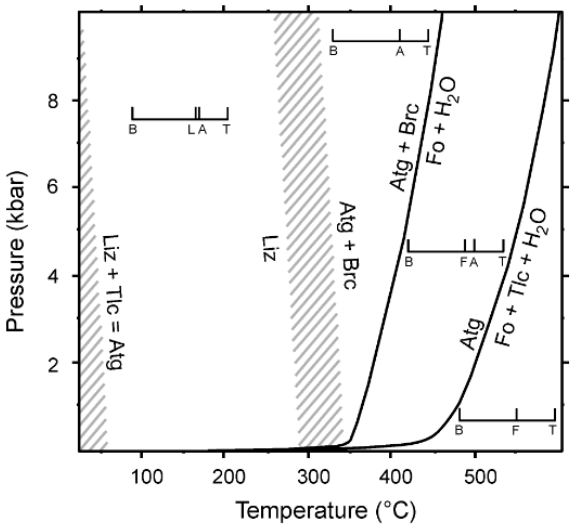

Fig. 1.1. Stable phase diagram in the system Mg–Si–H_2O proposed by Evans (2004). The shades show uncertain areas. Atg: antigorite; Brc: brucite; Fo: forsterite; Liz: lizardite; Tlc: talc.

Poorly crystalline Mg silicate is found from sediments in alluvial fans (Fig. 1.2; de Santiago Buey et al., 2000) and lakes (Milesi et al., 2019) and from crusts and moonmilks in caves (Léveillé et al., 2000; Polyak and Güven, 2000) in alkaline environments. Pozo and Casas (1999) observed Mg-rich clay sediments (kerolite and stevensite) in palustrine-lacustrine environments and proposed that the clay sediments were initially "Si-Mg gel" in early diagenesis.

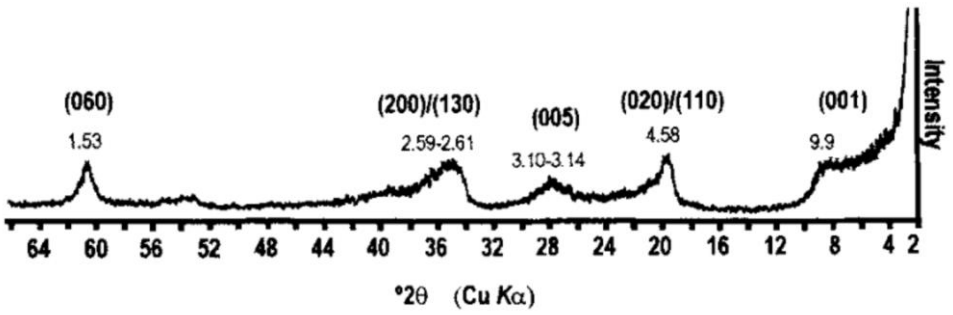

Fig. 1.2. X-ray diffraction (XRD) pattern for the Mg clay sample obtained from the Tagus basin, Spain (de Santiago Buey et al., 2000).

Poorly crystalline Mg silicate is also investigated on the Mars surface, where Mg silicate clay minerals (serpentine and smectite) are distributed (Ehlmann et al., 2011, 2013). Some samples at Yellowknife Bay, Gale Crater, show low crystallinity with broad 00*l* peaks in their XRD profiles (Vaniman et al., 2014; Bristow et al., 2015), indicating stacking faults of the poorly crystalline phyllosilicates. Moreover, various meteorites contain poorly crystalized Mg (or Mg–Fe) phyllosilicates (Tomeoka and Buseck, 1988; Howard et al., 2009; Blinova et al., 2014; King et al., 2015), which is likely formed during aqueous alteration process of meteorites (Igami et al., 2021).

1.2 M-S-H for engineering

Previous studies related to cement engineering identified poorly crystalline Mg silicate as Mg silicate hydrate (M-S-H), which has a structure related to clay minerals (Roosz et al., 2015; Nied et al.,

2016; Tonelli et al., 2016; Zhang et al., 2018; Bernard et al., 2019). Walling and Provis (2016) reviewed applications of Mg-cements including M-S-H. In cement engineering, Ca silicate hydrate (C-S-H) is well known as the major hydration product and the main binding phase of Portland cement (PC). However, in most situations, PC is produced though the calcination of $CaCO_3$ in limestone (i.e., $CaCO_3 \rightarrow CaO + CO_2$) at ~900°C, which requires high energy. The energy can be reduced when cement is made from the calcinated magnesite ($MgCO_3$) because decarbonation of $MgCO_3$ (i.e., $MgCO_3 \rightarrow MgO + CO_2$) occurs at <700°C. M-S-H is a hydration product of MgO-based cement instead of C-S-H. Moreover, M-S-H has been postulated to act as an extra binding phase in cements blended with blast-furnace slag or coal fly ashes, which tend to be richer in Mg than in PC. M-S-H is also a key product when PC is altered by seawater and C-S-H is decalcified (Fig. 1.3; de Weerdt and Justnes, 2015; Jakobsen et al., 2016).

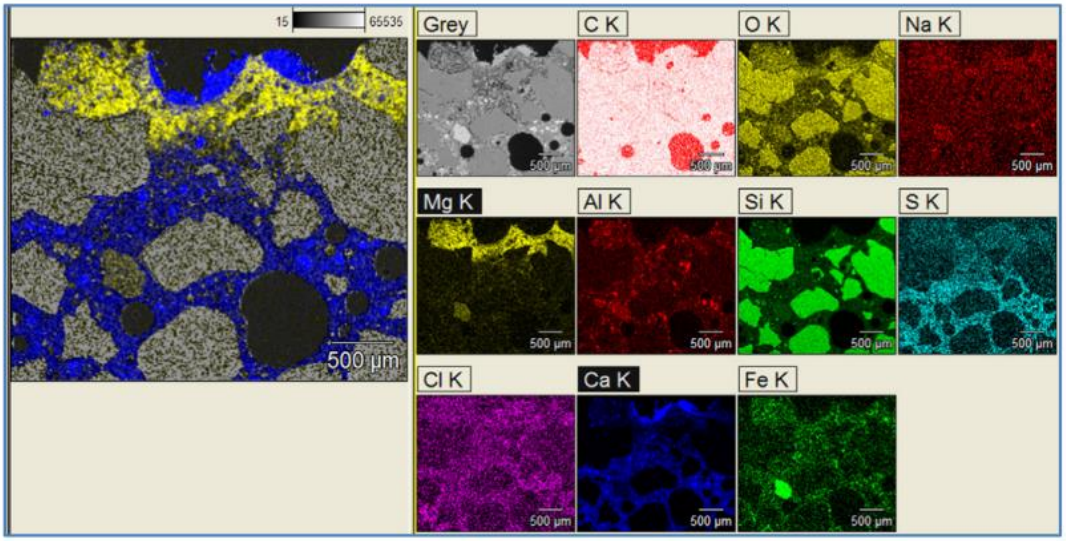

Fig. 1.3. Elemental mapping of the surface of cement concrete subjected to seawater for two years (Jakobsen et al., 2016). The elemental distribution of Mg (yellow, M-S-H) and Ca (blue; C-S-H) is representatively illustrated on the left.

Besides cement engineering, the main target of this study is M-S-H in engineering geology applications. In this study, we identify four scenarios in which M-S-H may strongly influence

geochemical evolution: (1) radioactive waste disposal, (2) geothermal power generation, (3) CO_2 mineralization, and (4) immobilization of hazardous elements in contaminated soil.

Radioactive waste disposal is one of the fields investigating the precipitation of M-S-H. Radioactive waste requires semipermanent isolation in underground repositories (depth > 300 m) to avoid any risk of radiation exposure to the biosphere. Transuranic (TRU) radioactive waste may be enclosed in engineered barriers of clay (bentonite) and concrete in tentative Japanese plans (Fig. 1.4; JAEA, 2018). In this case, when groundwater flows into the cement barriers and alkaline pore fluids are produced, the fluids may alter the bentonite. In situ concrete–clay interaction experiments in underground test sites (Jenni et al., 2014; Dauzeres et al., 2016; Fernández et al., 2017; Mäder et al., 2017; Gaboreau et al., 2020) have shown an Mg-rich zone in the clayey rock around the concrete–clay interface (Fig. 1.5). Some experimental studies have investigated Mg perturbation in bentonite (Fernández et al., 2018; González-Santamaría et al., 2021), in which M-S-H phases were considered secondary phases. Because the geochemical and geophysical characteristics of the secondary phases formed within the engineered barrier influence the long-term performance of engineered barriers, understanding those characteristics will benefit accurate assessments.

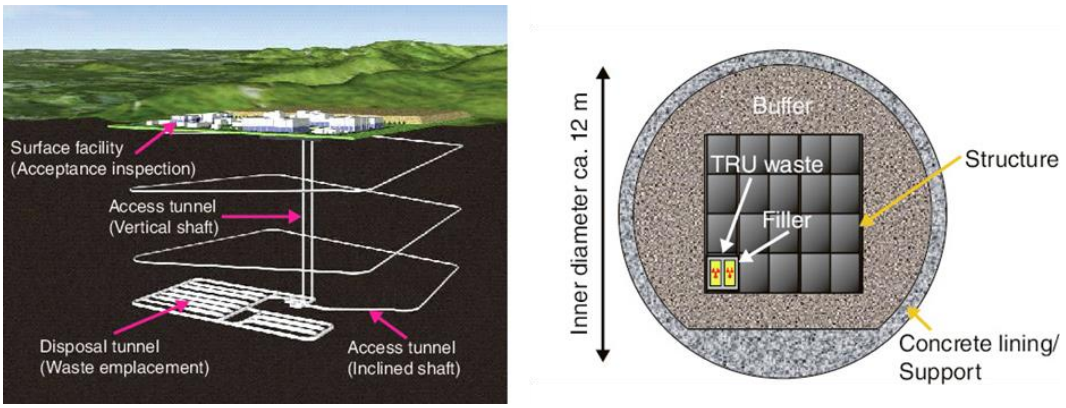

Fig. 1.4. Concept of the TRU waste repository (JAEA, 2018). The left figure shows a conceptual view of TRU waste repository, and the right figure shows a cross-section of the TRU waste disposal tunnel with buffer material.

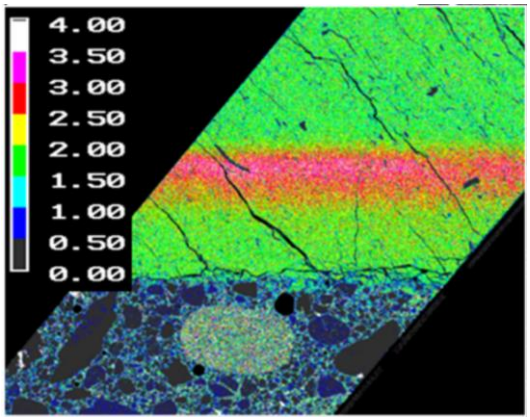

Fig. 1.5. Elemental mapping of Mg at the concrete–clay interface in the 4.9-year aged sample obtained from the Mont Terri rock laboratory, Switzerland (Mäder et al., 2017).

Morita et al. (2017, 2021) identified poorly crystallized Mg silicate scale formed on the inner surface of pipes at the geothermal power plant in Obama-cho, Unzen-shi, Nagasaki, Japan (Fig. 1.6). Scale precipitation reduces the production rate of geothermal energy, which is a significant obstacle in the development of geothermal energy systems. Besides geothermal scales of silica, metal sulfides, and Ca carbonate (Finster et al., 2015), metal silicates cannot be ignored in geothermal systems. Although Al silicates and Fe silicates have been studied extensively (Gallup and Reiff, 1991; Manceau et al., 1995; Gallup, 1997, 1998), fewer studies have examined Mg silicate scales. For example, in Japan, stevensite (Mg silicate clay mineral) scales are observed at Mori geothermal power plant (Kasai et al., 2000) and Sumikawa geothermal power plant (Pascua et al., 2005). An initial phase of Mg silicate precipitates in geothermal systems would be M-S-H (Morita et al., 2021), so that understanding the formation condition of M-S-H is essential for the development of inhibition technology for Mg silicate scales. Moreover, the Mg silicate scale in pipes is also a critical issue for chemical enhanced oil recovery (Umar and Saaid, 2013; Olajire, 2014; Sazali et al., 2015).

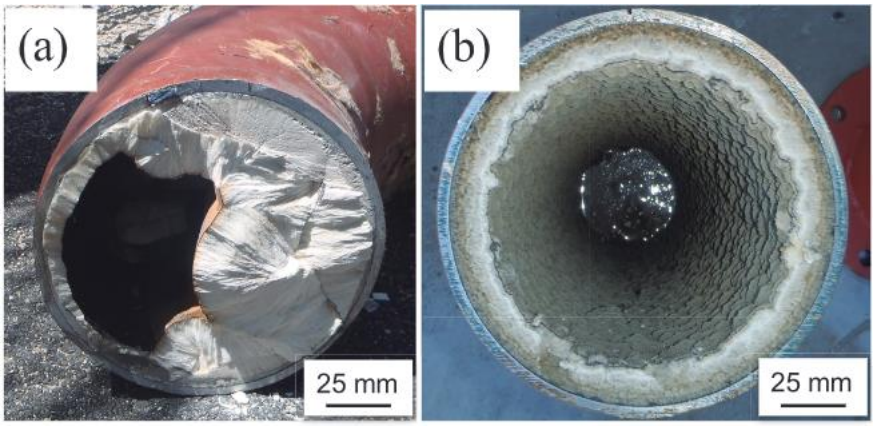

Fig. 1.6. Scale samples in the pipe (a) before the aeration tank and (b) after the aeration tank (Morita et al., 2017). Both samples contain poorly crystalline Mg silicate.

Technologies such as CO_2 geological storage (CGS) and enhanced rock weathering (ERW) have been improving to reduce atmospheric CO_2 (e.g., Sandalow et al., 2021), which leads to global warming and ocean acidification. CO_2 becomes immobile as mineralized in CGS and ERW fields. Having high contents of divalent cations such as Mg^{2+} and Ca^{2+}, some mafic/ultramafic rock (peridotite, basalt, and serpentinite, etc.) with highly alkaline groundwater can be expected to offer the potential for mineral trapping with Mg- and/or Ca-carbonate minerals (Gislason et al., 2010; Schaef et al., 2010; Kelemen et al., 2018, 2019; Raza et al., 2022). For Mg carbonate minerals, precipitation of Mg carbonate hydrate phases such as hydromagnesite ($Mg_5(CO_3)_4(OH)_2{\cdot}4H_2O$), dypingite ($Mg_5(CO_3)_4(OH)_2{\cdot}5H_2O$) and nesquehonite ($MgCO_3{\cdot}3H_2O$) are expected rather than magnesite ($MgCO_3$) and dolomite ($CaMg(CO_3)_2$) because the formation of magnesite and dolomite is kinetically inhibited at temperature below 65°C (Snæbjörnsdóttir et al., 2020). However, precipitation of poorly crystallized Mg silicate (or Mg–Fe silicate) was observed in CO_2-fixation laboratory experiments (Andreani et al., 2009; Hellevang et al., 2017; Rigopoulos et al., 2018; Wolff-Boenisch and Galeczka, 2018). A CO_2-injection field test into serpentinite in Japan showed secondary formation of poorly crystalline Mg silicate (Mg/Si = 1) similar to serpentine (Okamoto et al., 2006; Ninomiya et al., 2007). Fluid analysis in a field test into basalt also

suggest secondary formation of Mg silicate (Oelkers et al., 2019). Therefore, M-S-H precipitation should be taken into account in consideration of CO_2 mineralization.

In boron (B) immobilization in contaminated soils, Mg oxide is often used as a stabilizing agent (García et al., 2004; Wada and Morishita, 2013). Experimental studies have shown that Mg hydroxide (brucite) can adsorb and immobilize aqueous borate species (de la Fuente García-Soto and Muñoz Camacho, 2009; Sasaki et al., 2013), indicating that an Mg oxide treatment is effective for B-contaminated soils. However, the presence of silica in the soils cannot be ignored also in this issue. Nozawa et al. (2018) found that B is incorporated into tetrahedral Si sites in the M-S-H structure during its formation; the B sorption capacity of M-S-H was higher than that of brucite in their experiments. Rather than brucite, M-S-H may thus act as a sorbent for B in soil, with B being released into pore water if secondary M-S-H dissolves.

1.3 Previous study of C-S-H and M-S-H

As described in Section 1.2, C-S-H is the hydration product in PC. PC has been used for over 150 years and C-S-H has been studied extensively for almost a century. Lothenbach and Nonat (2015) reviewed the chemical compositions of C-S-H phases. In many studies, C-S-H phases are synthesized by mixing lime and silica in water at ambient temperature. The chemical compositions of the products (solids) are mirrored in those of the solution. The solid is only C-S-H at $10 < pH < 12.5$, whereas the one is a mixture of C-S-H and amorphous silica at $pH \leq 10$ and C-S-H and portlandite ($Ca(OH)_2$) at $pH \geq 12.5$ (Fig. 1.7). The C-S-H phases show a variety of Ca/Si ratios in the range of ca. 0.75–1.45. When solutions are supersaturated with respect to portlandite, the C-S-H phase with higher Ca/Si (≤ 2) can be formed (Nonat, 2004).

C-S-H is poorly crystalline or nanocrystalline material (Fig. 1.8). Its structure is closed to tobermorite and/or jennite (Taylor, 1993; Richardson, 2008). C-S-H with low Ca/Si has a structure similar to tobermorite (7-fold coordination) and that with high Ca/Si has a structure similar to jennite

(6-fold coordination). Grangeon et al. (2016) proposed evolution of C-S-H structure as a function of Ca/Si ratio (Fig. 1.9). The higher the Ca/Si, the shorter the silicate chains (Fig. 1.9 and 1.Fig. 1.10a), which is due to the lowering of the Si concentrations in solution (Fig. 1.10b) as the Ca concentrations increase.. Whereas the Si bridging tetrahedra are partially eliminated, the linear parallel chains of dimer of Si tetrahedra are preserved.

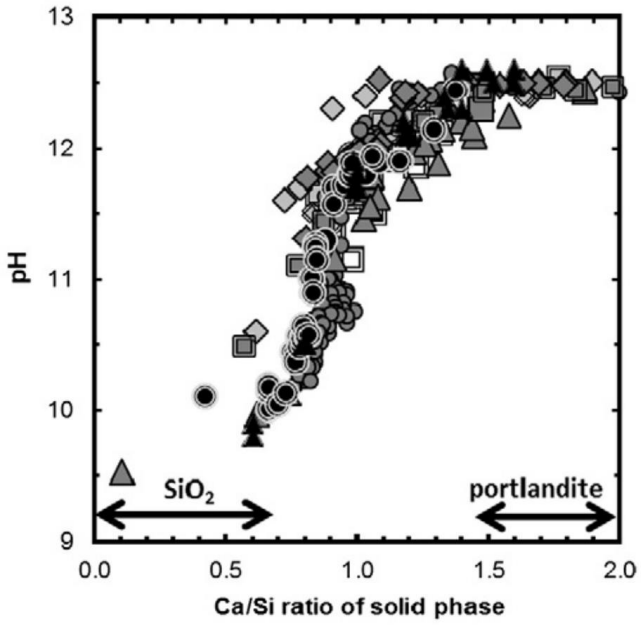

Fig. 1.7. Relation between solid Ca/Si ratio and pH in the C-S-H syntheses (Lothenbach and Nonat, 2015).

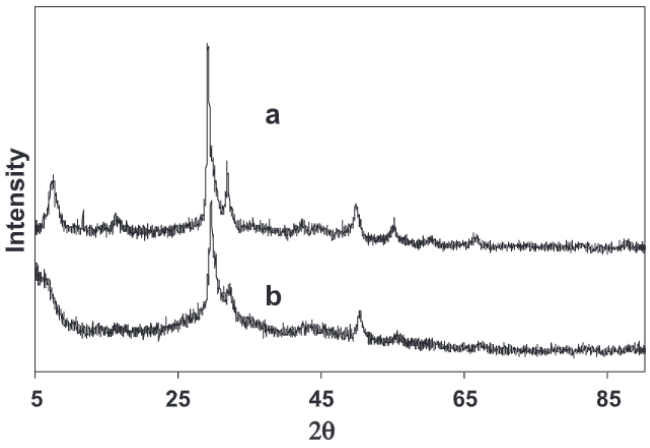

Fig. 1.8. XRD patterns (Cu Kα) of C-S-H obtained (a) in diluted suspension from a mix of CaO and SiO_2 and (b) by hydration of a mix of fine tricalcium silicate (C_3S) and SiO_2 in paste (Nonat, 2004).

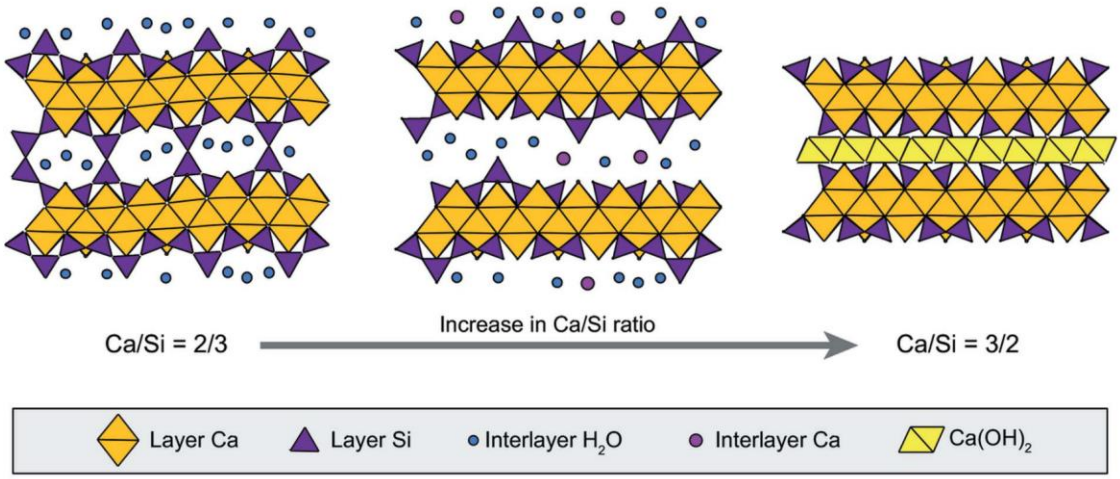

Fig. 1.9. Structural evolution of C-S-H as a function of Ca/Si ratio (Grangeon et al., 2016).

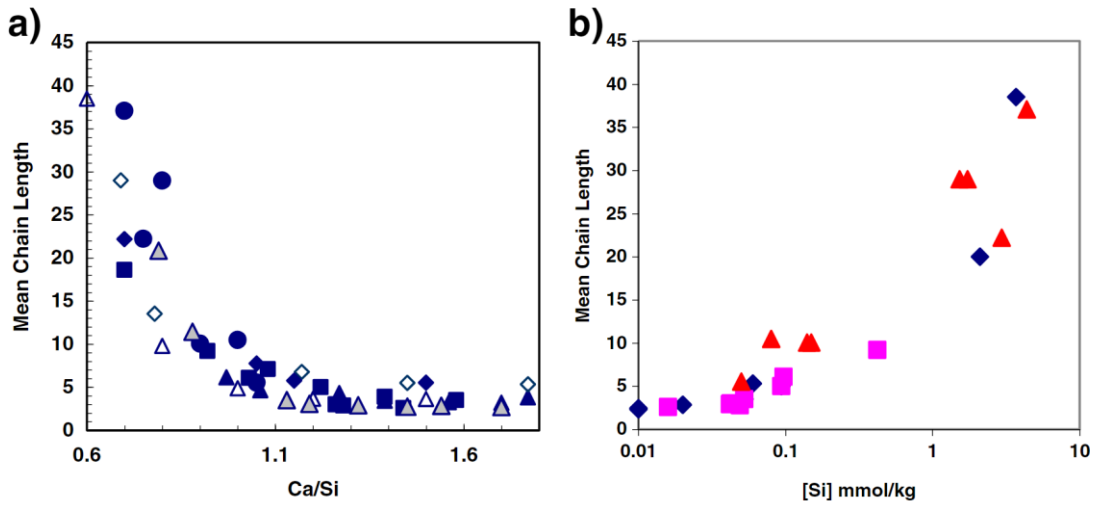

Fig. 1.10. Evolution of the mean chain length of silica in C-S-H as a function of (a) Ca/Si ratio and (b) the aqueous Si concentration in solution (Lothenbach and Nonat, 2015).

The number of previous studies of M-S-H is much smaller than that of C-S-H (Li et al., 2014; Roosz et al., 2015; Nied et al., 2016; Tonelli et al., 2016; Zhang et al., 2018; Bernard et al., 2019a). M-S-H is also poorly crystalline or nanocrystalline (Fig. 1.11) and shows variable chemical compositions. Its crystal structure is somewhat similar to Mg clay minerals (e.g., serpentine: Fig. 1.12; talc: Fig. 1.13;

sepiolite: Fig. 1.14), a conclusion which is, however, still not commonly accepted and has not been clearly confirmed. Chapter 2 reviews previous studies of M-S-H in detail.

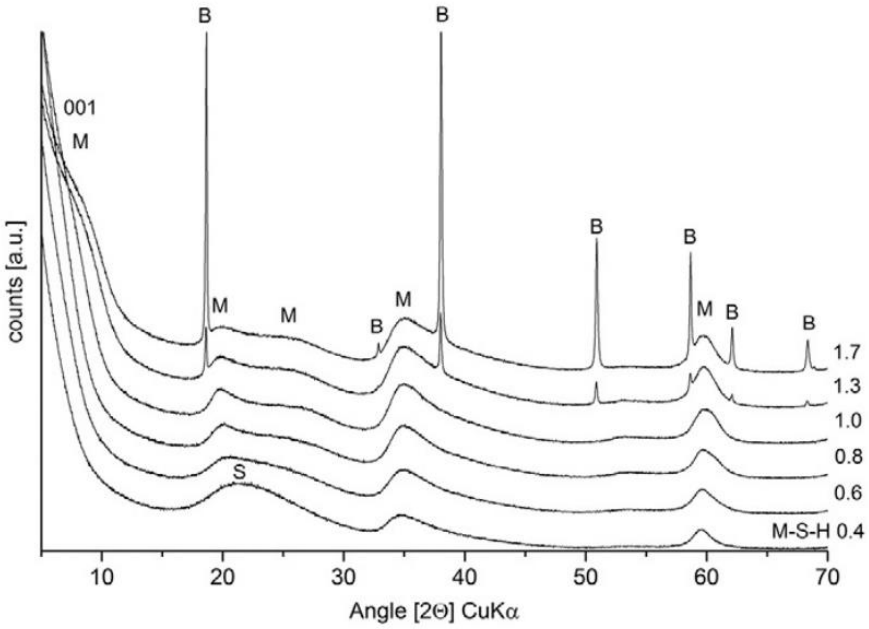

Fig. 1.11. XRD patterns of M-S-H synthesized by Nied et al. (2016). M: M-S-H; B: brucite; S: amorphous silica.

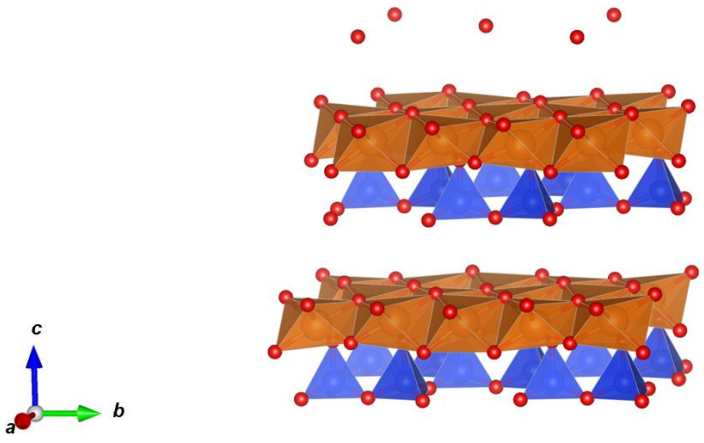

Fig. 1.12. Crystal structure of serpentine (Tetrahedral-octahedral [TO] layers)

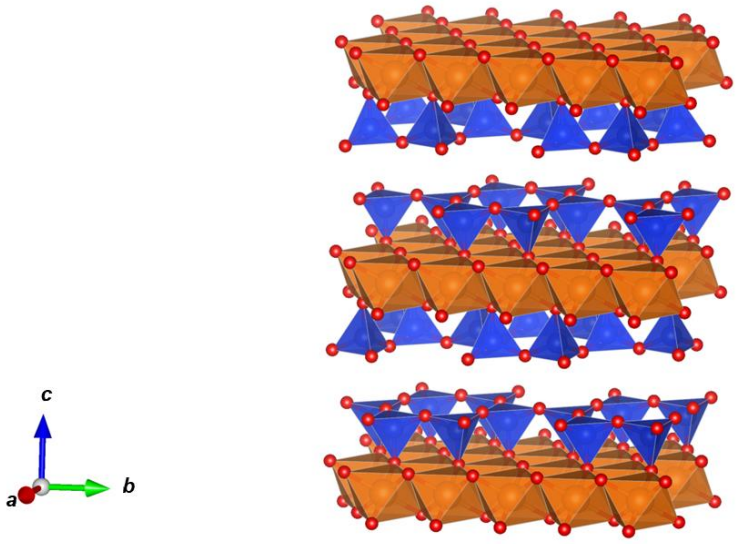

Fig. 1.13. Crystal structure of talc (Tetrahedral-octahedral-tetrahedral [TOT] layers)

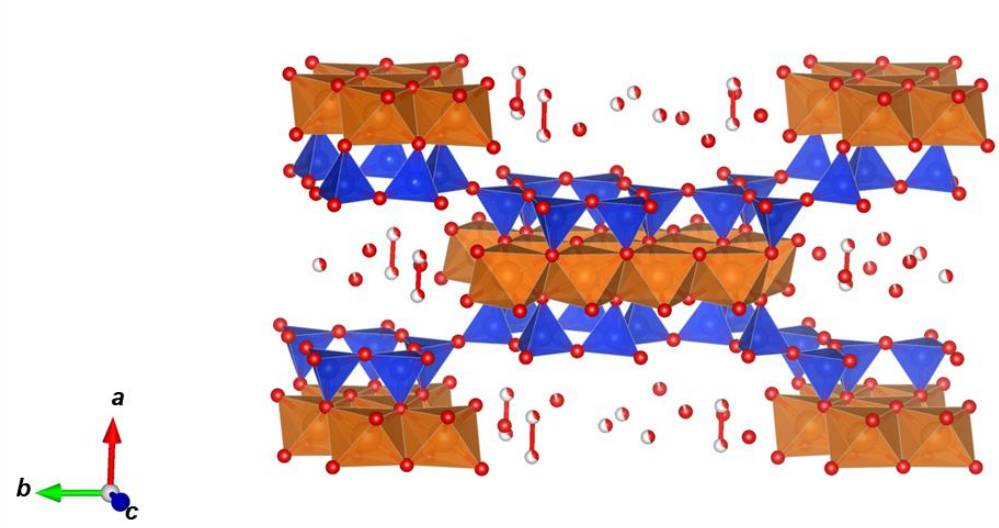

Fig. 1.14. Crystal structure of sepiolite (TOT ribbons)

The structural characteristics of M-S-H are completely different from that of C-S-H, due to the difference in the ionic radii of Mg^{2+} and Ca^{2+} (Mg^{2+} = 0.66 Å and Ca^{2+} = 0.99 Å; Ahrens, 1952). Mg^{2+} is 6-fold coordinated by oxygen ions, whereas Ca^{2+} can also be coordinated by more than six oxygen ions (e.g., 7-fold coordinated Ca^{2+} in tobermorite). M-S-H and C-S-H are separately present in the aqueous reactions of MgO, CaO, and silica fume (Lothenbach et al., 2015; Bernard et al., 2018).

Formation of a solid solution (like “M-C-S-H”) is impossible, although minor amounts of Ca (2 at.%) in M-S-H and Mg (4 at.%) in C-S-H were observed in the experiments conducted by (Fig. 1.15; Lothenbach et al., 2015).

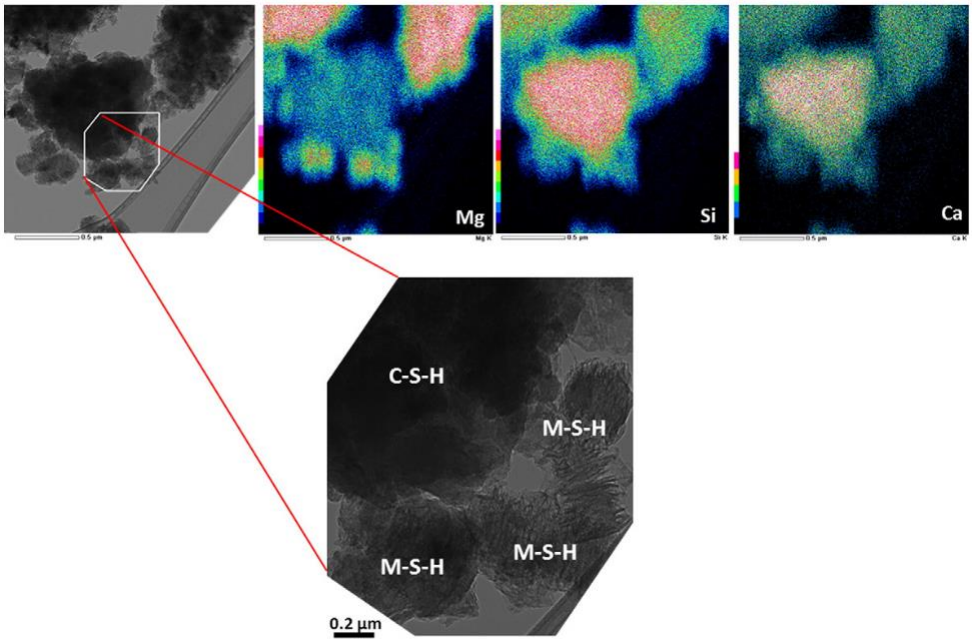

Fig. 1.15. Elemental mappings of the products in the MgO–CaO–SiO_2–H_2O system (Lothenbach et al., 2015).

1.4 Objectives of this study

Objectives of this study are as follows:

[i] To characterize the mineralogical structures of M-S-H,

[ii] To clarify the formation conditions of M-S-H,

[iii] To clarify the geochemical behaviors of M-S-H,

[iv] To predict the formation of M-S-H in engineering geology applications.

This study aims to understand M-S-H formation on the Earth’s surface, examining M-S-H from various approaches such as several laboratory experiments (both in closed systems and open-flow systems), geological surveys, and geochemical modeling.

Chapter 2: Review of M-S-H

2.1 Syntheses of M-S-H in laboratory

Synthetic M-S-H phases have been investigated, especially for the last decade. In most cases, M-S-H samples are synthesized from MgO (or $Mg(OH)_2$) reagent, silica fume, and water (Roosz et al., 2015; Walling et al., 2015; Nied et al., 2016; Tonelli et al., 2016; Bernard et al., 2017, 2019a, b; Vespa et al., 2018).

Roosz et al. (2015) demonstrated that M-S-H phases are poorly crystalline with short range stacking order and identified M-S-H from Mg/Si 0.6 as TOT phyllosilicate and the one from Mg/Si 1.2 as TOT phyllosilicate having tetrahedral defects and a layer charge. Their XRD pattern modeling indicated that the M-S-H crystallites 1.2 have a mean size of 1.5 nm in the *ab* plane and 2.4 nm along c^* axis. Vespa et al. (2018) also suggested that M-S-H shows small coherent regions and TOT layers with defective Si sheets from the results of Mg K-edge X-ray absorption spectroscopy (XAS) and ab-initio calculations.

Nied et al. (2016) synthesized M-S-H from Mg/Si 0.4, 0.6, 0.8, 1.0, 1.3 and 1.7 at 20°C for 1 year and 50°C for 3 months. M-S-H phases showed a variety of Mg/Si (0.75–1.5) and formed at alkaline pH (8.5–10.5) at 20°C (Fig. 2.1). Amorphous silica also formed at pH $\lesssim$ 8.5 and brucite ($Mg(OH)_2$) formed at pH $\gtrsim$ 10.5. As described in Section 1.3, C-S-H phases also show similar trends: (1) various Ca/Si compositions, (2) formation at alkaline pH (10–12.5, which is higher than pH for M-S-H), and (3) simultaneous precipitation with amorphous silica and Ca hydroxide (portlandite) at lower pH and higher pH, respectively. They proposed that M-S-H phases can be divided into two endmembers: Mg/Si 0.75 (a phase similar to talc) and Mg/Si 1.5 (a phase similar to serpentine).

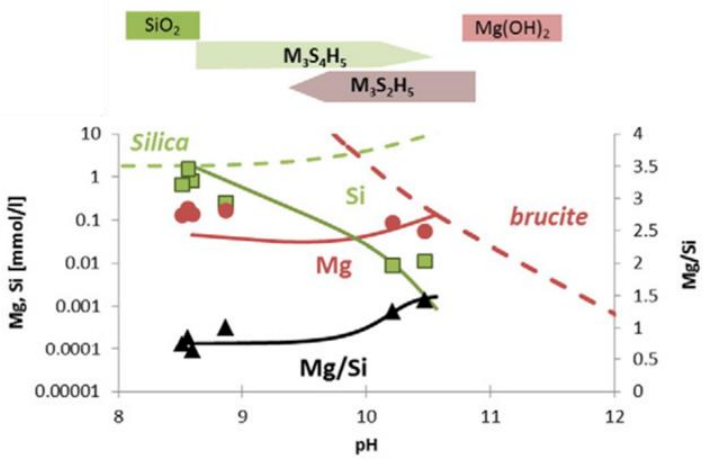

Fig. 2.1. Mg/Si ratio of M-S-H (triangles) and dissolved concentrations of Si (squares) and Mg (circles) as a function of the pH values obtained by Nied et al. (2016).

Bernard et al. (2017) also investigated synthesized M-S-H in the range $0.7 \leq Mg/Si \leq 1.6$ at 0.1 intervals. Their experiments were conducted at 20°C for 2 years and at 50°C and 70°C for 1 year. One of the differences between Bernard et al. (2017) and Nied et al. (2016) is the Mg/Si ratios of M-S-H. Bernard et al. (2017) selected Mg/Si 0.78 and 1.3 as two endmembers of M-S-H. They also suggested a kinetic hindrance of $Mg(OH)_2$ dissolution in the dissolved silica solution.

Bernard et al. (2019a) focused on solid analyses of M-S-H samples synthesized in the previous study (Bernard et al., 2017). Characteristics of TOT phyllosilicate were observed in their XRD analyses for the M-S-H samples (Mg/Si 0.8 and 1.2). However, X-ray pair distribution functions of the M-S-H samples best fit with that of antigorite, when compared with talc, sepiolite, and serpentine minerals (lizardite, chrysotile, and antigorite). Walling et al. (2015) describe that structure of lizardite was similar to the one of the M-S-H sample (Mg/Si = 1) in their ^{29}Si and ^{25}Mg magic angle spinning nuclear magnetic resonance (MAS NMR) analyses.

Pedone et al. (2017) investigated the M-S-H sample (Mg/Si = 1) synthesized by Tonelli et al. (2016) by using density functional theory. The simulated NMR spectra (Pedone et al., 2017) showed a good

agreement with the experimental NMR spectra (Tonelli et al., 2016) as assuming a mixture of amorphized talc and lizardite in a supercell.

Tosca and Masterson (2014) conducted synthetic experiments with aqueous Mg solution ($MgCl_2$) and Si solution (tetraethoxysilane; TEOS) with several Mg/Si molar ratios (0.67, 1, and 6) at different pH: 8.7, 9.0, and 9.4. They observed poorly crystalline Mg silicate precipitates, which were similar to M-S-H. The Mg silicate phases were identified to be sepiolite, kerolite, or stevensite by XRD, Fourier transform infrared (FTIR) spectroscopy, and thermogravimetry with differential thermal analysis (TG/DTA). Brew and Glasser (2005a) also investigated M-S-H synthesized from aqueous Mg solution and Si solution.

As discussed above, studies of M-S-H are still in their infancy. The formation condition of M-S-H phases and their crystal structure have not been clearly confirmed. Since M-S-H is poorly crystalline material, it will be a metastable phase for a long time and transformed into crystalline Mg phyllosilicates (Tosca et al., 2011; Roosz et al., 2015). The crystallization process for Mg phyllosilicates is likely complicated and varies with experimental (or geological) settings. Tutolo et al. (2018) described silica condensation upon Mg octahedral sheets (brucite) is the rate-limiting step for serpentine formation. Besselink et al. (2020) demonstrated that aqueous Mg is slowly incorporated in an amorphous Mg-bearing silicate precursor for Mg smectite (saponite) formation (Fig. 2.2).

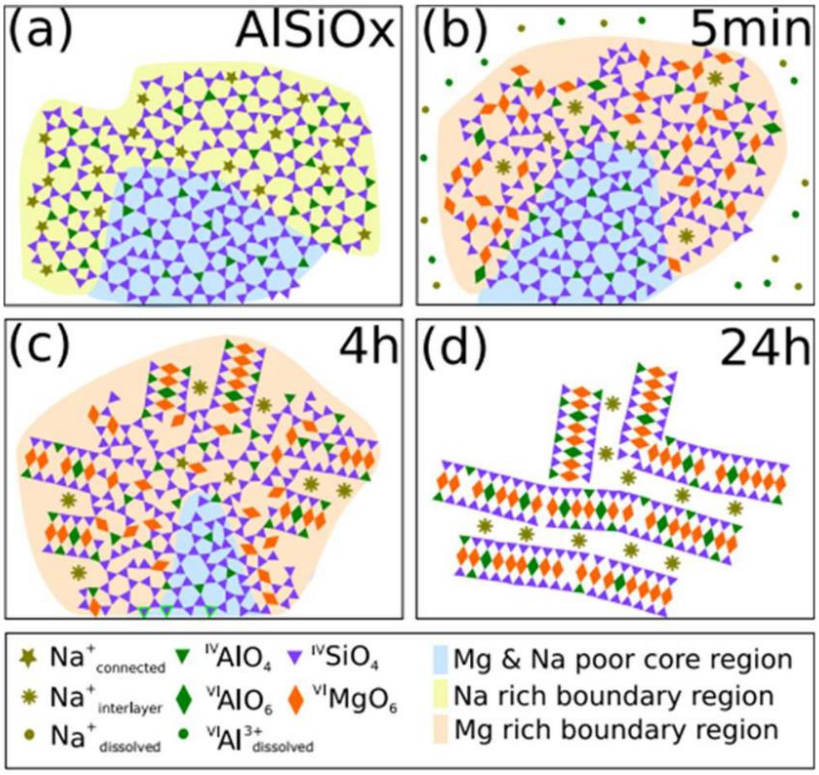

Fig. 2.2. Schematics of Mg smectite (saponite) crystallization (Besselink et al., 2020).

2.2 Thermodynamics of M-S-H

Chemical formulas (Table 2.1) and thermodynamic parameters (Table 2.2) for the M-S-H phases have been suggested in some previous studies. As far as the author knows, the newest paper regarding the thermodynamics of M-S-H was published by Lothenbach et al. (2019). Since the thermodynamic parameters (Table 2.2) were obtained in the batch experiments, further study needs to confirm the applicability to the prediction of M-S-H under the Earth's surface conditions.

Table 2.1.

Chemical equations for the M-S-H samples in the previous studies.

Reference	M-S-H name	Reaction
Nied et al. (2016)	$M_3S_4H_5$	$3MgO{\cdot}4SiO_2{\cdot}5H_2O \Leftrightarrow 3Mg^{2+} + 4SiO_2 + 6OH^- + 2H_2O$
	$M_3S_2H_5$	$3MgO{\cdot}2SiO_2{\cdot}5H_2O \Leftrightarrow 3Mg^{2+} + 2SiO_2 + 6OH^- + 2H_2O$
Bernard et al. (2017)	$M_{0.78}SH_{1.48}$	$(MgO)_{0.78}{\cdot}SiO_2{\cdot}(H_2O)_{1.48} \Leftrightarrow 0.78Mg^{2+} + SiO_2 + 1.56OH^- + 0.7H_2O$
	$M_{1.30}SH_{1.80}$	$(MgO)_{0.78}{\cdot}SiO_2{\cdot}(H_2O)_{1.48} \Leftrightarrow 1.3Mg^{2+} + SiO_2 + 2.6OH^- + 0.5H_2O$
Roosz et al. (2018)	MSH06	$Mg_{0.82}SiO_{2.385}(OH)_{0.87} + 0.745H_2O + 1.64H^+ \Leftrightarrow 0.82\ Mg^{2+} + H_4SiO_4$
	MSH12	$Mg_{1.07}SiO_{2.075}(OH)_{1.99} + 2.14H^+ \Leftrightarrow 1.07\ Mg^{2+} + 0.065H_2O + H_4SiO_4$
Lothenbach et al. (2019)	$M_{1.5}S_2H_{2.5}$	$(MgO)_{1.5}{\cdot}(SiO_2)_2{\cdot}(H_2O)_{2.5} \Leftrightarrow 1.5Mg^{2+} + 2SiO_2 + 3OH^- + H_2O$
	$M_{1.5}SH_{2.5}$	$(MgO)_{1.5}{\cdot}(SiO_2){\cdot}(H_2O)_{2.5} \Leftrightarrow 1.5Mg^{2+} + SiO_2 + 3OH^- + H_2O$

Table 2.2.

Thermodynamic properties of the M-S-H samples in Table 2.1. K: solubility product; $\Delta_fG°$: Gibbs free energy of formation (kJ mol^{-1}); $\Delta_fH°$: enthalpy of formation (kJ mol^{-1}); S°: entropy (J K^{-1} mol^{-1}).

Reference	M-S-H name	Mg/Si	log K	$\Delta_fG°$	$\Delta_fH°$	S°	Temperature
Nied et al. (2016)	$M_3S_4H_5$	0.75	−57.6	−6436.9	no data	no data	20°C
	$M_3S_2H_5$	1.5	−47.1	−4709.5	no data	no data	
Bernard et al. (2017)	$M_{0.78}SH_{1.48}$	0.78	−14.59	−1682.2	−1847	123	20°C
	$M_{1.30}SH_{1.80}$	1.3	−21.44	−2073.2	−2270	119	
Roosz et al. (2018)	MSH06	0.82	9.12	−1454	−1560	80.13	25°C
	MSH12	1.07	12.73	−1739	−1896	75.35	
Lothenbach et al. (2019)	$M_{1.5}S_2H_{2.5}$	0.75	−28.80	−3218	−3508	270	25°C
	$M_{1.5}SH_{2.5}$	1.5	−23.57	−2356	−2594	216	

2.3 Chemical properties of M-S-H

Cation exchange capacity (CEC) for M-S-H is ca. 35–40 meq per 100 g (Bernard et al., 2019a). The higher Mg/Si ratio, the higher pH, the more hydroxyl surface groups, and the higher CEC. This is slightly lower than the CEC of stevensite (Mg smectite) or kerolite–stevensite mixed layered samples (ca. 36–75 meq per 100 g; Shimoda, 1971; Eberl et al., 1982; de Vidales et al., 1991; Benhammou et al., 2009). The positive CEC of M-S-H is reasonable because the zeta potential is negative (in the range from −19 to −28 mV; Bernard et al., 2019a). M-S-H particles uptake alkali ions such as Na^+ (Bernard et al., 2019b), K^+ (Brew and Glasser, 2005b), and Cs^+ (Brew and Glasser, 2005b; Zhang et al., 2020). Heavy metal ions such as Fe^{3+}, Pb^{2+}, and Ni^{2+} are also uptaken by M-S-H (Marsiske et al., 2021). The growth period (Marsiske et al., 2021) and crystallinity (Gainey et al., 2017) of M-S-H are changed when M-S-H precipitates by incorporating Fe^{3+}.

Al^{3+} is also uptaken by M-S-H, forming magnesium alumino silicate hydrate (M-A-S-H; Bernard et al., 2020). Al can substitute both Mg and Si in octahedral and tetrahedral sheets, respectively. Al incorporation is also observed in studies of C-S-H (i.e., C-A-S-H; Lothenbach and Nonat, 2015).

2.4 Formation of M-S-H on the Earth's surface

The formation of M-S-H in nature is reported in a few papers. De Ruiter and Austrheim (2018) observed the formation of M-S-H cement in the ultramafic complex in the presence of quartz-rich felsic glacial deposits (the Feragen Ultramafic Body, Norway; Fig. 2.3). As high pH fluids containing aqueous Mg^{2+} dissolved quartz, M-S-H was formed via an amorphous silica precursor (de Ruiter et al., 2021). The M-S-H formation enhanced the dissolution rate of quartz, which was 3 orders of magnitude higher than the one obtained in experimental studies. In their studies, however, there were no details of observations and analysis of the fluid that leads to the M-S-H formation.

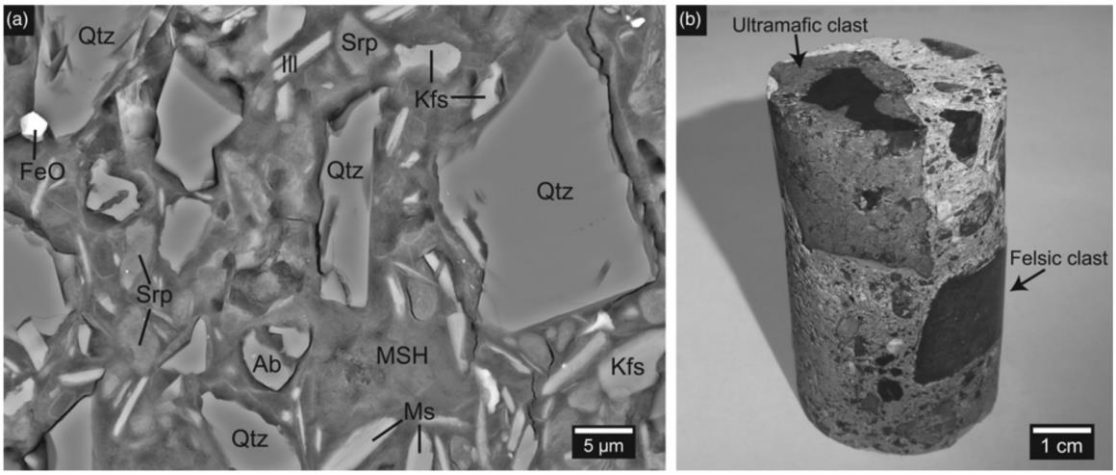

Fig. 2.3. Backscattered electron image of M-S-H cements (a) and photograph of drill core sample with centimeter-scale felsic and ultramafic clasts (b) obtained from the Feragen field area (de Ruiter and Austrheim, 2018). Qtz: quartz; Kfs: K-feldspar; Ab: albite; Srp: serpentine; Ms: muscovite; Ill: illite.

Shimbashi et al. (2018) observed poorly crystalline Fe-and Mg-rich silicate precipitates in pores of Palawan ophiolite with hyperalkaline groundwater. The electron diffraction pattern for the precipitates was similar to the diffraction patterns of M-S-H (Nied et al., 2016). The groundwater was saturated to M-S-H, suggesting that precipitation of M-S-H controlled the groundwater chemistry. Besides the Fe–Mg silicate precipitates, precipitation of C-S-H and tobermorite was also observed (Fig. 2.4; Shimbashi et al., 2020). This phenomenon is similar to the fact that M-S-H and C-S-H separately form when both Mg and Ca are dissolved in alkaline water (Lothenbach et al., 2015). Shimbashi et al. (2022) identified the Fe–Mg silicate precipitates as hydrated TOT phyllosilicate. This was similar to a smectite structure although it had both interlayer cations and interlayer hydroxide sheets.

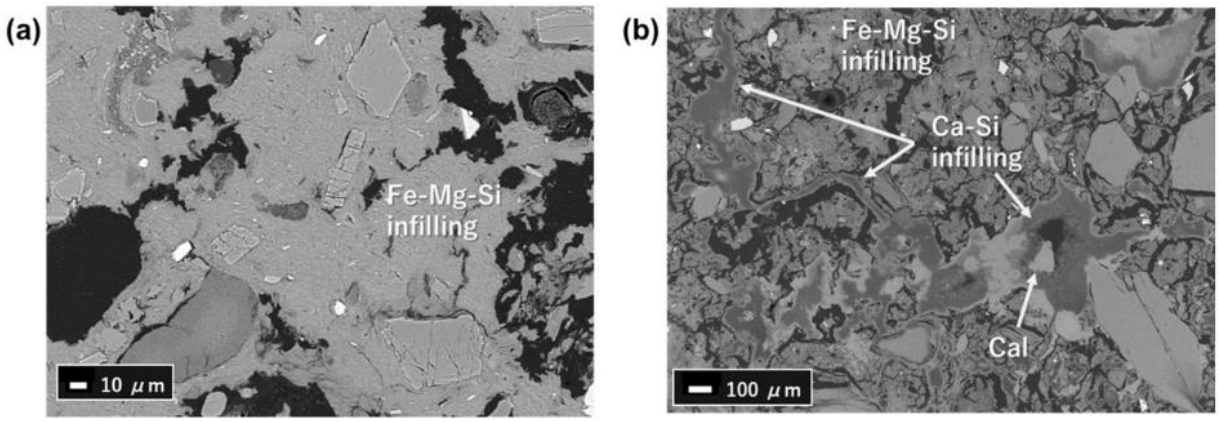

Fig. 2.4. Backscattered electron images of poorly crystalline silicate infillings in Palawan ophiolite (Shimbashi et al., 2020). Cal: calcite.

Mineralogical studies of kerolite and deweylite also help to understand M-S-H in nature. Kerolite is hydrous talc-like mineral (Brindley et al., 1977) and deweylite is a mixture of kerolite and serpentine (Bish and Brindley, 1978). However, kerolite and deweylite have not been accepted as “minerals” by International Mineralogical Association. This may be because they are poorly crystalline phases and nobody has suggested their crystal structural models. In some situations, Mg silicate identified as M-S-H in the engineering fields and Mg silicate identified as kerolite or deweylite may essentially be similar.

Chapter 3: M-S-H syntheses in closed systems

3.1 Introduction

M-S-H samples have been synthesized from MgO, silica fume, and water in most studies (Roosz et al., 2015; Walling et al., 2015; Nied et al., 2016; Tonelli et al., 2016; Bernard et al., 2017, 2019a, b; Vespa et al., 2018). However, structures of M-S-H have not commonly been accepted. The objective of this chapter is to characterize the mineralogical structures of M-S-H (i.e., [i] in Section 1.4). This chapter suggested crystal structures of M-S-H, characterizing M-S-H by a variety of analytical methods: XRD, Raman spectroscopy, NMR spectroscopy, thermal analyses, and transmission electron microscopy (TEM) with energy dispersive X-ray spectroscopy (EDS). Especially, Raman spectroscopy and TEM/EDS have been used in only a few studies (Brew and Glasser, 2005a; Lothenbach et al., 2015; Nied et al., 2016). The structure of TOT layers and TO layers can be distinguished by Raman spectroscopy (Wang et al., 2015) rather than FTIR spectroscopy, and chemical compositions of M-S-H nanoparticles can be analyzed by TEM/EDS. Moreover, this chapter also investigated the phase transformation process of M-S-H phases in 12 years, comparing the 1-month aged, 3-month aged, 6-month aged, and 12-month aged samples. Since M-S-H phases are likely metastable phases, it is essential especially for geoscientists to elucidate their phase transformation behaviors.

3.2 Materials and methods

3.2.1 Experimental procedures

The M-S-H samples were synthesized by mixing MgO (>98.0%, Kanto Chemical, Japan), silica fume (SiO_2, >99.8%, Aerosil® 200, Evonik, Germany), and ultrapure water. Given that endmembers of M-S-H phases show Mg/Si ratios of ca. 0.8 and 1.3 (Bernard et al., 2017), MgO/SiO_2 molar ratios were 0.8 and 1.3 in this chapter. A water/solid (w/s) ratio was 45, which is the same as Nied et al. (2016) and Bernard et al. (2017). The experiments were run at 25°C, 50°C, and 90°C for 1, 2, 3, 6, 9, and 12 months. The samples at 25°C and 50°C were placed on a horizontal shaker (100 rpm), and the ones at 90°C were

manually shaken once a week. After each reaction time, the M-S-H precipitate was obtained by centrifugation (35 min at 3000 rpm) and freeze dried. Solution was passed through a 0.20 μm polytetrafluoroethylene (PTFE) syringe filter.

3.2.2 Analytical methods

For all solution samples, pH was measured with a pH meter and a pH electrode (LAQUA D-72 and 9630-10D, HORIBA Advanced Techno, Co., Ltd.) calibrated with pH 7 and 9 solutions. Concentrations of aqueous Mg in the solution samples were analyzed by inductively coupled plasma atomic emission spectrometry (ICP–AES; ICPE-9000, Shimadzu Corporation).

The M-S-H precipitates synthesized for 1, 3, 6, and 12 months were investigated by following analytical techniques. XRD analyses were obtained with a RINT-2100 diffractometer (Rigaku Corporation) at 30 kV and 20 mA using Cu Kα radiation. Powder XRD patterns of randomly-oriented samples were recorded from 5 to 70° 2θ at a scanning speed of 1° min^{-1}.

Raman spectroscopy was carried out on a Horiba XploRA. The solid samples were pressed into tablets to obtain flat surfaces of the samples. Raman spectra were collected using a 532 nm laser, at a 1800 grooves per millimeter grating, 300 μm confocal hole diameter, and 100 μm slit size. The spectral acquisition time was 60 s and 3 spectra were accumulated and averaged for each sample. The system was calibrated with a silicon standard. In addition to the M-S-H samples, Raman spectroscopy was also conducted with chrysotile (natural sample; Hokkaido, Japan), talc (synthetic material; Matsumura Sangyo Co., Ltd., Japan), sepiolite (natural sample; Tochigi, Japan; Imai et al., 1966), $Mg(OH)_2$ (reagent; Kanto Chemical Co., Inc., Japan), and amorphous silica (Aerosil® 200; Evonik, Germany).

The samples were also analyzed by ^{29}Si MAS NMR spectroscopy with a BRUKER Avance Neo 500 at 99.38 MHz. The powder samples were packed into 3.2 mm zirconia rotors and rotated at MAS rates of 5 kHz. ^{29}Si MAS NMR spectra were recorded using a 30° pulse with a duration of 1.4 μs and a relaxation delay of 20 s, accumulating 2800 scans. The ^{29}Si NMR chemical shifts of the spectra were

referenced to the most intense resonance at −9.7 ppm of an external sample of an hexamethylcyclotrisiloxane ($C_6H_{18}O_3Si_3$). The chemical shift is affected by Q^n silicon species (Q is a silica tetrahedron and n is the number of bridging oxygens for each silicate tetrahedron). The NMR spectra were deconvoluted using Fityk software (Wojdyr, 2010). Lorentzian functions were used for Q^1 and Q^2 species and Gaussian functions were used for Q^3 species (Bernard et al., 2019a).

Thermal behavior of the samples was investigated by TG/DTA with a Shimadzu DTG-60H thermal analyzer. ~8 mg of samples was preheated at 30°C for 180 min and the TG/DTA results were recorded from 30 to 1000°C at a heating rate of 10 °C min^{-1} in nitrogen flux (50 mL min^{-1}). α-alumina powder was used as reference material in the analysis.

The M-S-H samples synthesized at 25°C and 90°C for 1 month and 12 months were further investigated by TEM. The powder sample was dispersed in ethanol under ultrasonic irradiation and one drop of the supernatant was deposited on a copper grid with carbon film (Microgrid type A, Okenshoji Co., Ltd.). The grids were coated with carbon (~2 nm) by precision etching coating system (PECS; Model 682, Gatan, Inc.). TEM images were obtained with JEM-2010 (JEOL Ltd.). EDS was performed with JEM-2100F (JEOL Ltd.), which is equipped with a field emission (FE) electron gun and a scanning transmission electron microscopy (STEM) instrument. The samples were cleaned with an ion cleaner (JIC-410, JEOL Ltd.) to remove any hydrocarbon contamination before the EDS analyses. EDS spectra were acquired for 50 s and the Cliff-Lorimer quantification method was used in JEOL Analysis Station software. Both microscopes were operated at 200 kV during the analyses.

3.3 Results

3.3.1 Solution chemistry

pH at room temperature was in the range of 7.2–8.6 and 9.0–9.9 in the experiments with MgO/SiO_2 0.8 and 1.3, respectively (Fig. 3.1a). The dissolved Mg concentration in the experiments with MgO/SiO_2 0.8 and 1.3 and the dissolved Si concentration in those with MgO/SiO_2 0.8 did not show significant

changes from 1 month to 12 months (Fig. 3.1b–d). The dissolved Si concentration in the experiments with MgO/SiO_2 1.3 was nearly constant (0.012–0.025 mmol L^{-1}, mM) after 6, 9, and 12 months, while it showed the higher values after 1, 2, and 3 months (Fig. 3.1e).

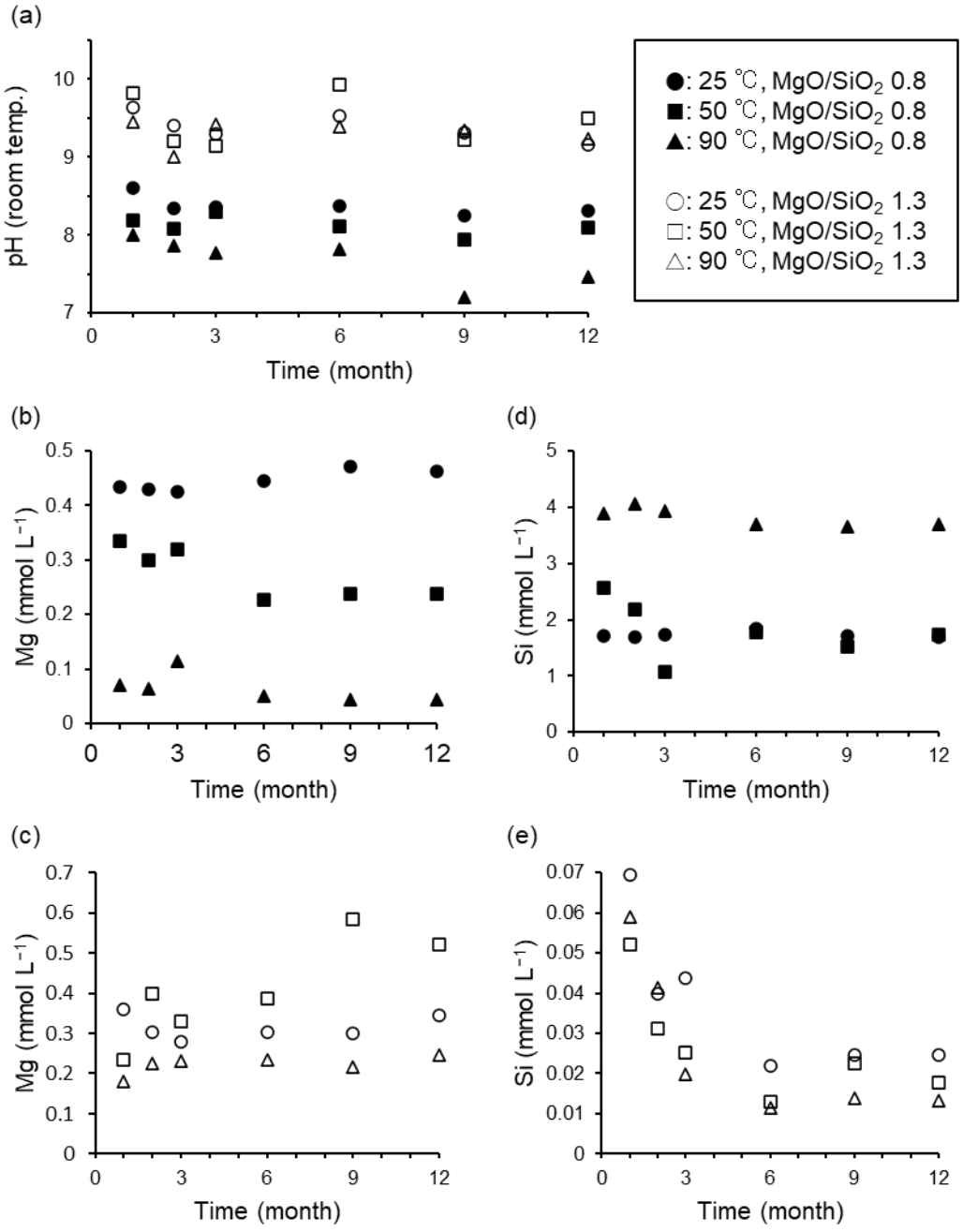

Fig. 3.1. Solution chemistry: (a) pH measured at room temperature (22°C ± 3°C); (b, c) Mg concentration at MgO/SiO_2 0.8 and 1.3; (d, e) Si concentration at MgO/SiO_2 0.8 and 1.3.

3.3.2 XRD analyses

The powder XRD patterns in the range 5–70° 2θ (Fig. 3.2) displayed four broad peaks that are typical characteristics of M-S-H (Nied et al., 2016). Peaks for MgO (periclase), $Mg(OH)_2$ (brucite) and amorphous silica were not clearly detected in this study. The sample at 25°C from MgO/SiO_2 0.8 exhibited the broad peaks at 4.5, 3.3, 2.6, and 1.54 Å (Fig. 3.2a). The samples at 50°C and 90°C from MgO/SiO_2 0.8 exhibited slightly shaper peaks at 4.5, 3.3, 2.6, and 1.53 Å (Fig. 3.2b,c). The samples at 25°C and 50°C from MgO/SiO_2 1.3 showed a broad shoulder in the low-angle region (<15° 2θ) in addition to the peaks at 4.5, 3.3, 2.6, and 1.54 Å (Fig. 3.2d,e).

Significant changes were observed in the XRD profiles for the samples at 90°C from MgO/SiO_2 1.3 (Fig. 3.2f). Under the condition, the 1-month aged sample exhibited four peaks at 4.5, 3.3, 2.6, and 1.54 Å, the same as the samples at 25°C and 50°C from MgO/SiO_2 1.3. As time progressed, the peak at 3.3 Å shifted to 3.6 Å and its intensity became stronger. Moreover, the intensity of the low-angle peak became stronger, and its maximum position was 8.2 Å in the 12-month aged sample.

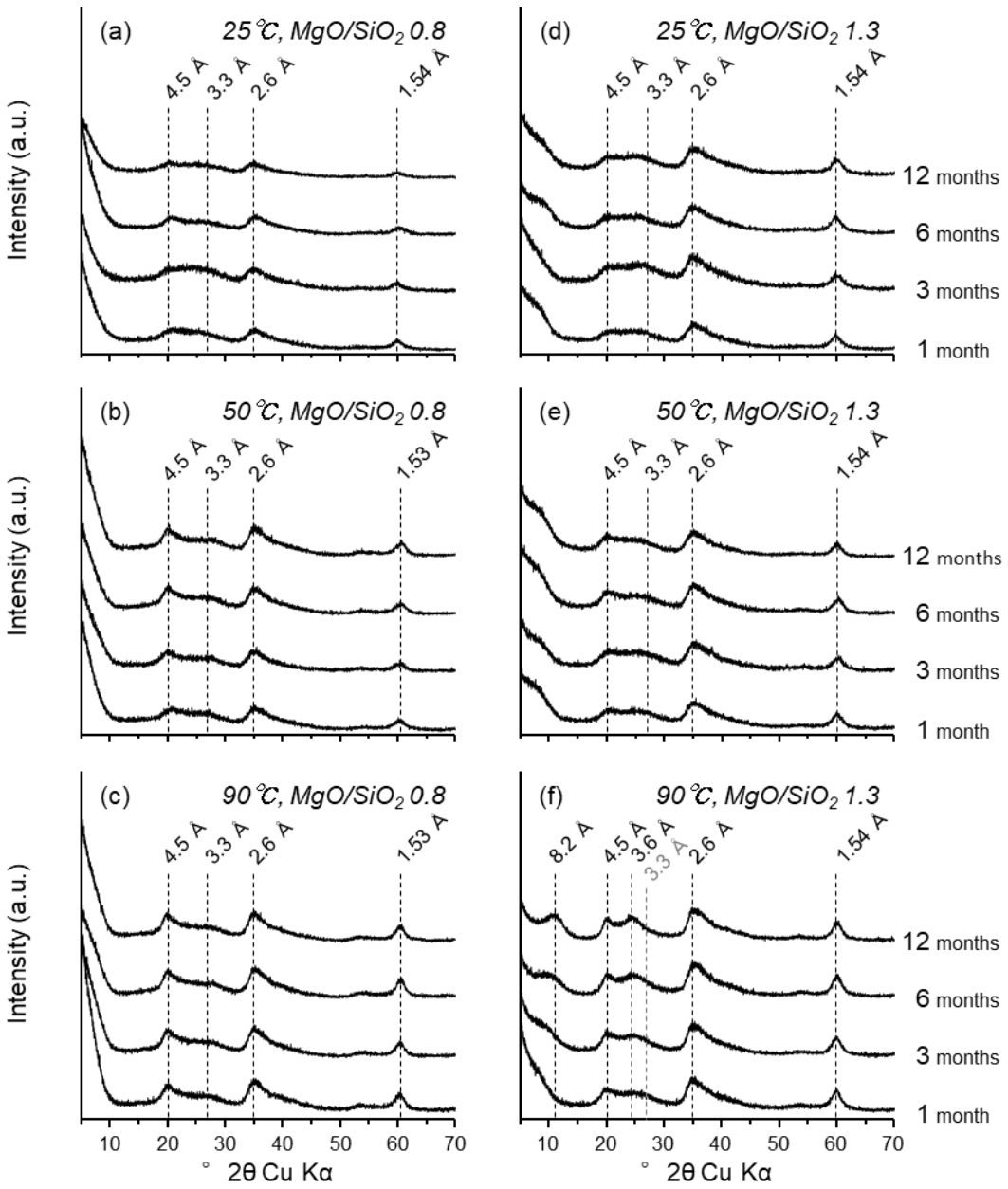

Fig. 3.2. Powder XRD patterns of the M-S-H samples synthesized at (a–c) 25°C, 50°C, and 90°C from MgO/SiO_2 0.8; (d–f) 25°C, 50°C and 90°C from MgO/SiO_2 1.3.

3.3.3 TOT and TO phyllosilicate structures

The Raman spectra for the samples from MgO/SiO_2 0.8 showed the vibration modes related to TOT phyllosilicate (talc) structure, rather than TO phyllosilicate (Fig. 3.3a–c). The spectra were not significantly changed from 1 month to 12 months. In the range 100–1000 cm^{-1}, the strongest peak (675

cm^{-1}) was consistent with Si–O–Si modes of talc (Loh, 1973; Wang et al., 2015). A peak was observed at 185 cm^{-1}, which is similar to $\nu_1(A_{1g})$ modes of MgO_6 octahedra in talc (Loh, 1973). The samples at 25°C exhibited a broad peak in the region 360–375 cm^{-1}, while those at 50 and 90°C exhibited a peak at 360 cm^{-1}. The peak at 360 cm^{-1} corresponds to $\nu_5(E)$ modes of SiO_4 tetrahedra in talc (Loh, 1973).

The samples from MgO/SiO_2 1.3 at 25°C and 50°C showed both characteristics of TOT phyllosilicate (talc) and TO phyllosilicate (chrysotile) structures (Fig. 3.3d,e). The broad peak was observed in the range from 675 cm^{-1} (Si–O–Si modes of talc; Loh, 1973; Wang et al., 2015) to 690 cm^{-1} (Si–O–Si modes of chrysotile; Rinaudo et al., 2003; Wang et al., 2015). The peaks at 185 cm^{-1} and 225 cm^{-1} were close to the ones for $\nu_1(A_{1g})$ mode of MgO_6 octahedra in talc (Loh, 1973) and O–H–O modes in chrysotile (Rinaudo et al., 2003), respectively. A peak at 375 cm^{-1} was observed between $\nu_5(E)$ modes of SiO_4 tetrahedra in talc (~360 cm^{-1}; Loh, 1973) and chrysotile (~390 cm^{-1}; Rinaudo et al., 2003).

While the two peaks centered at 675 cm^{-1} (Si–O–Si modes of talc; Loh, 1973) and 690 cm^{-1} (Si–O–Si modes of chrysotile; Rinaudo et al., 2003) overlapped with similar intensities in the spectrum for 1-month aged sample from MgO/SiO_2 1.3 at 90°C, the intensity of the peak at 675 cm^{-1} was decreasing (i.e., the one at 690 cm^{-1} was relatively increasing) as time progressed (Fig. 3.3f). The similar trend was shown in the region 180–225 cm^{-1}. While two peaks at 180 cm^{-1} ($\nu_1(A_{1g})$ mode of MgO_6 in talc; Loh, 1973) and 225 cm^{-1} (O–H–O modes in chrysotile; Rinaudo et al., 2003) were observed with similar intensities in the spectrum for the 1-month aged sample, the peak at 180 cm^{-1} was fading and the one at 225 cm^{-1} was growing with aging. The peak at ~375 cm^{-1} in the 1-month experiment faintly shifted to 380 cm^{-1} (close to the $\nu_5(E)$ modes of SiO_4 in chrysotile; Rinaudo et al., 2003) in the longer-term experiments. The 6- and 12-month aged samples gradually exhibited new peaks at 130 and 340 cm^{-1}, showing similar characteristics of chrysotile (Rinaudo et al., 2003; Wang et al., 2015). In addition, all the samples from MgO/SiO_2 1.3 exhibited a peak at ~450 cm^{-1}, which was also observed in M-S-H samples synthesized by Lothenbach et al. (2015) and Nied et al. (2016) although it was not identified as specific modes in their studies.

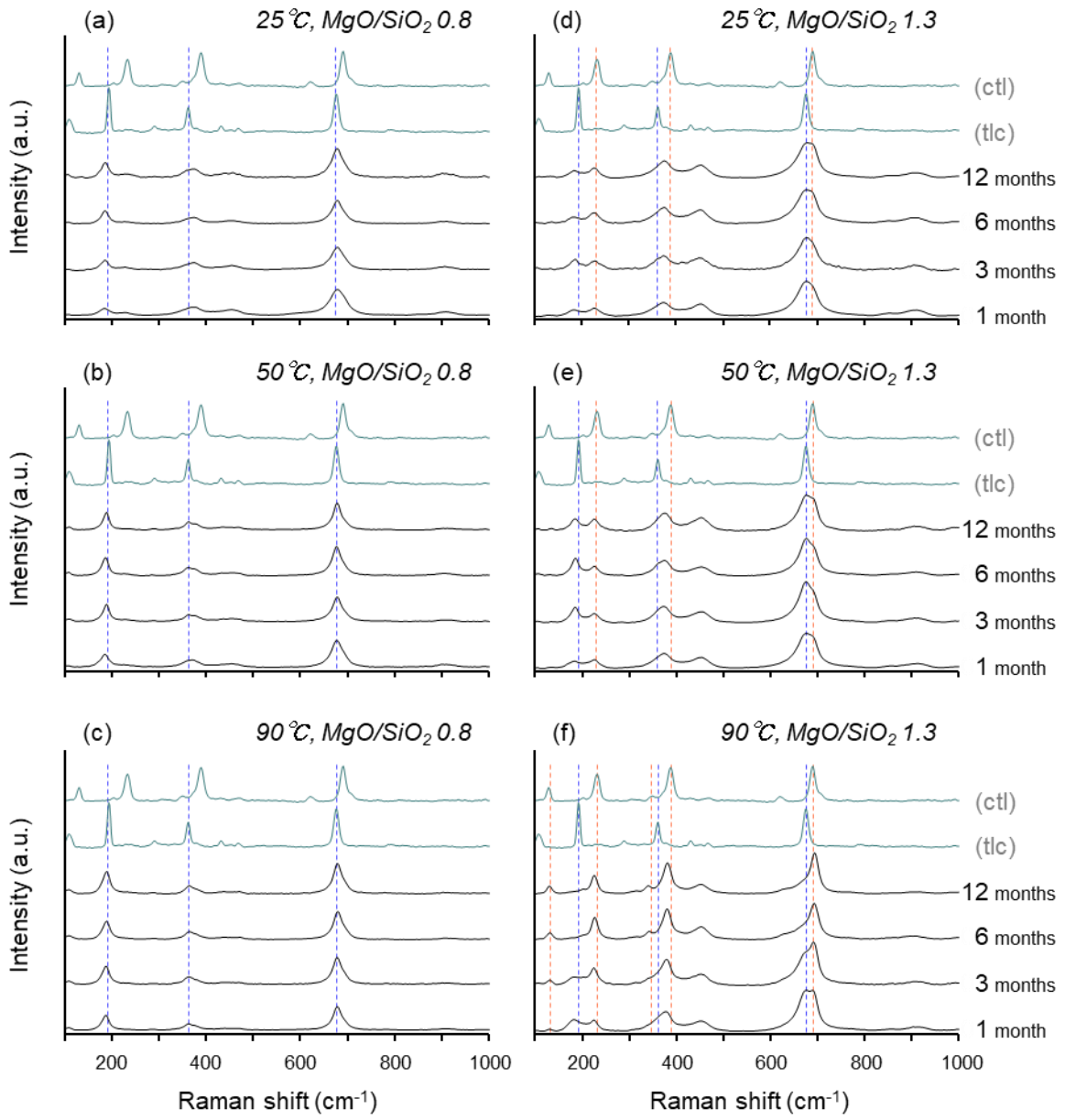

Fig. 3.3. Raman spectra of the M-S-H samples synthesized at (a–c) 25°C, 50°C, and 90°C from MgO/SiO2 0.8; (d–f) 25°C, 50°C, and 90°C from MgO/SiO_2 1.3. Raman spectra for talc (tlc: synthetic material from Matsumura Sangyo Co., Ltd., Japan) and chrysotile (ctl: natural sample from Hokkaido, Japan) are also displayed.

Besides talc, chrysotile, and the synthesized samples, Raman spectra for sepiolite, $Mg(OH)_2$, (brucite), and amorphous silica were obtained (Fig. 3.4). The Raman spectrum for amorphous silica showed broad peaks at 605 cm^{-1} and in the range from ~300 cm^{-1} to ~500 cm^{-1} (Fig. 3.4e), which was not clearly observed in those for the samples in this study

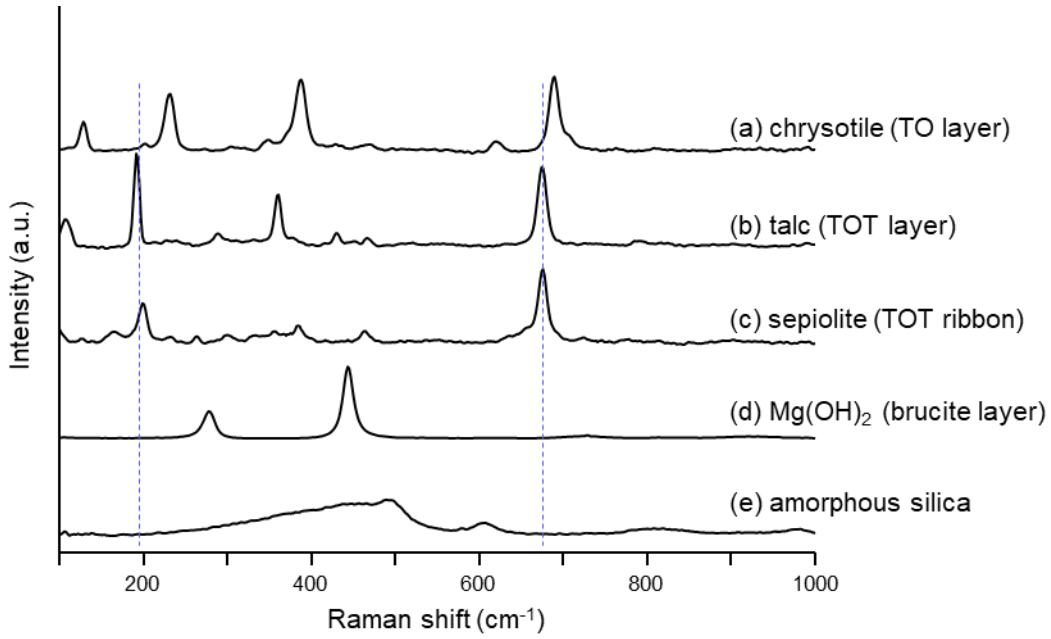

Fig. 3.4. Raman spectra of (a) chrysotile (natural sample; Hokkaido, Japan), (b) talc (synthetic material; Matsumura Sangyo Co., Ltd., Japan), (c) sepiolite (natural sample; Tochigi, Japan; Imai et al., 1966), (d) $Mg(OH)_2$ (reagent; Kanto Chemical Co., Inc., Japan), and (e) amorphous silica ("Aerosil 200"; Evonik, Germany). Analytical conditions for the above samples were the same as those for the M-S-H samples synthesized in this study. The intensity of (d) was shown in 1/4.

3.3.4 Silica polymerization

The ^{29}Si MAS NMR spectra of the samples showed resonances in the range from −70 ppm to −100 ppm (Fig. 3.5). A resonance at −85.3 ppm in each spectrum is assigned to a Q^2 species in M-S-H, and a broad resonance in the range from ca. −90 ppm to −100 ppm is assigned to a Q^3 species in M-S-H (Lothenbach et al., 2015; Nied et al., 2016; Zhang et al., 2018; Bernard et al., 2019a). Resonances originating from amorphous silica structure (a Q^4 peak observed at −110 ppm and a Q^3 peak observed at −101 ppm; Zhang et al., 2018) were not detected in this study.

The area of each Q^n peak in a ^{29}Si MAS NMR spectrum is generally proportional to the amount of each Q^n silicon species, which was evaluated by deconvolutions in this study (Fig. 3.6 and Tables Table

3.1 and Table 3.2). A Q^3 peak was deconvolved into three Q^3 species centered at −92.4 ppm, −94.6 ppm, and −96.7 ppm, which is based on the method of Nied et al. (2016). In addition to the Q^2 and Q^3 species, some samples showed a shoulder at −79.0 ppm, which is assigned to a Q^1 species.

The degree of Q^3 polymerization was evaluated as a $Q^3/(Q^1+Q^2+Q^3)$ area ratio (Fig. 3.7). For the samples from MgO/SiO_2 0.8, the $Q^3/(Q^1+Q^2+Q^3)$ ratios did not significantly change from 1 month to 12 months (Fig. 3.7a). The $Q^3/(Q^1+Q^2+Q^3)$ ratios of the samples for 12 months from MgO/SiO_2 0.8 were 0.6 at 25°C and 0.7 at 50°C and 90°C. However, the $Q^3/(Q^1+Q^2+Q^3)$ ratios tended to increase with reaction time under the MgO/SiO_2 1.3 conditions (Fig. 3.7b). The $Q^3/(Q^1+Q^2+Q^3)$ ratios of the samples for 12 months from MgO/SiO_2 1.3 were 0.4, 0.5, and 0.6, at 25°C, 50°C, and 90°C, respectively, which were lower than those from MgO/SiO_2 0.8.

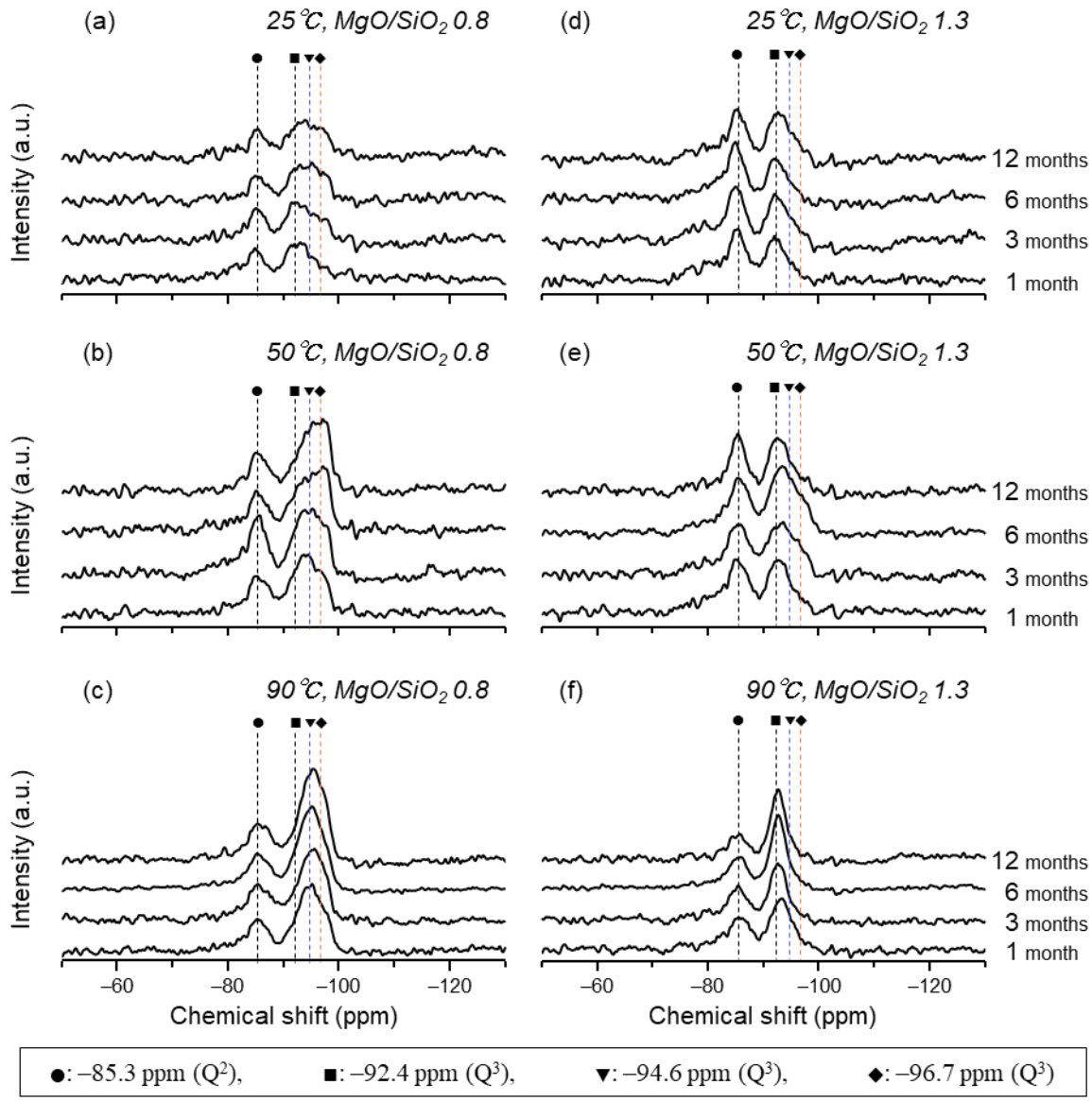

Fig. 3.5. ^{29}Si MAS NMR spectra of the M-S-H samples synthesized at (a–c) 25°C, 50°C, and 90°C from MgO/SiO_2 0.8; (d–f) 25°C, 50°C, and 90°C from MgO/SiO_2 1.3.

	Q^1	Q^2	Q^{3a}	Q^{3b}	Q^{3c}
function :	Lorentzian	Lorentzian	Gaussian	Gaussian	Gaussian
center (ppm) :	–79.0 ± 0.0	–85.3 ± 0.4	–92.4 ± 0.4	–94.6 ± 0.2	–96.7 ± 0.3
HWHM :	2.5 ± 0.1	2.0 ± 0.5	1.8 ± 0.4	1.8 ± 0.2	1.8 ± 0.3

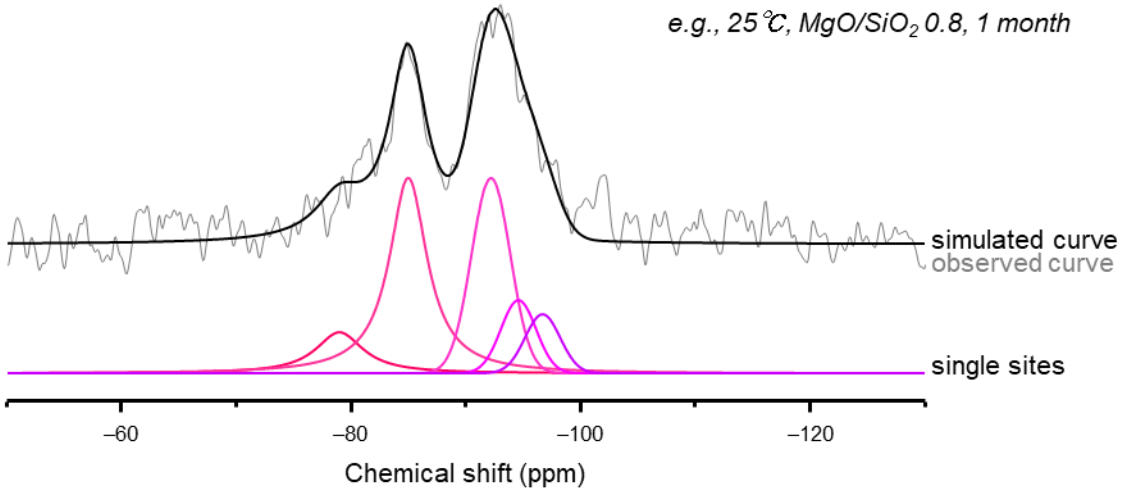

Fig. 3.6. Functions, peak positions, and half width at half maximum (HWHM) in the deconvolution of the ^{29}Si MAS NMR spectra in this study.

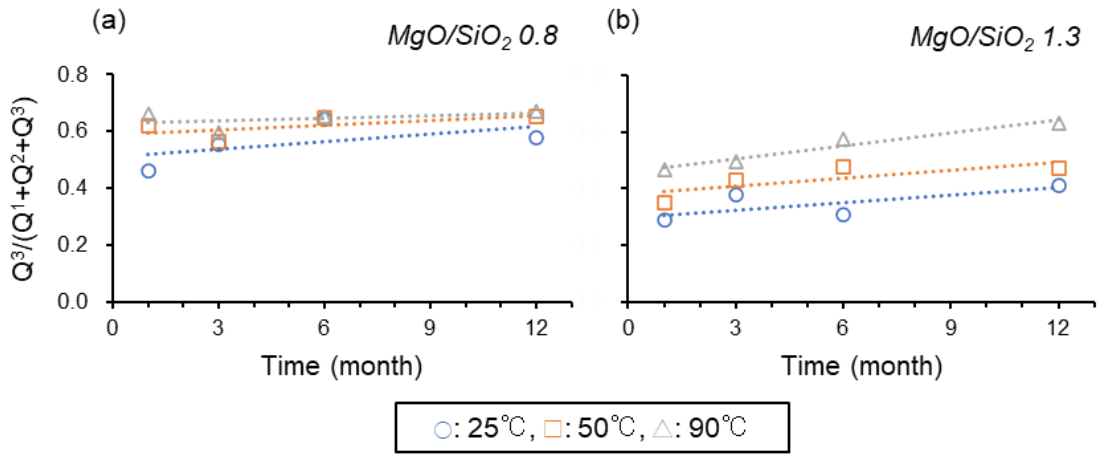

Fig. 3.7. Variation in $Q^3/(Q^1+Q^2+Q^3)$ ratios as a function of time for the M-S-H samples from (a) MgO/SiO_2 0.8 and (b) MgO/SiO_2 1.3. The dotted lines represent least squares regression lines.

Table 3.1.

Deconvolution of the ^{29}Si MAS NMR spectra for the M-S-H samples from MgO/SiO_2 0.8.

			Q^1	Q^2	Q^{3a}	Q^{3b}	Q^{3c}
25°C	1 month	center (ppm)	–79.0	–85.0	–92.2	–94.6	–96.7
		HWHM	2.5	2.0	2.0	1.8	1.8
		height ($\times 10^6$)	320	1511	1510	566	454
		area ($\times 10^6$)	2511	9496	6428	2169	1740
	3 months	center (ppm)	–79.0	–85.1	–92.0	–94.6	–96.7
		HWHM	2.5	1.8	2.0	2.0	1.8
		height ($\times 10^6$)	140	1460	1480	615	732
		area ($\times 10^6$)	1102	8255	6302	2620	2804
	6 months	center (ppm)		–85.2	–92.4	–94.6	–96.7
		HWHM		1.8	1.8	2.0	2.0
		height ($\times 10^6$)		1116	1033	833	912
		area ($\times 10^6$)		6310	3959	3547	3494
	12 months	center (ppm)		–85.2	–92.4	–94.6	–96.7
		HWHM		2.0	2.0	2.0	1.8
		height ($\times 10^6$)		1394	1208	833	953
		area ($\times 10^6$)		8759	5142	3549	3652
50°C	1 month	center (ppm)		–85.4	–92.4	–94.6	–96.7
		HWHM		2.0	2.0	2.0	2.0
		height ($\times 10^6$)		1779	1577	1633	1028
		area ($\times 10^6$)		11178	6716	6953	4376
	3 months	center (ppm)		–85.3	–92.6	–94.6	–96.7
		HWHM		1.7	1.7	1.8	1.7
		height ($\times 10^6$)		2778	1587	1748	1860
		area ($\times 10^6$)		14838	5743	6698	6733
	6 months	center (ppm)		–85.4	–92.4	–94.6	–97.0
		HWHM		1.8	2.2	2.0	1.7
		height ($\times 10^6$)		2021	1186	1531	2420
		area ($\times 10^6$)		11427	5553	6519	8759
	12 months	center (ppm)		–85.4	–92.4	–94.6	–97.0
		HWHM		2.0	2.0	2.0	2.0
		height ($\times 10^6$)		1880	984	1337	2852
		area ($\times 10^6$)		11814	4188	5693	12145
90°C	1 month	center (ppm)		–85.4	–92.4	–94.6	–96.7
		HWHM		2.0	1.6	1.8	2.0
		height ($\times 10^6$)		1969	1733	2662	1922
		area ($\times 10^6$)		12375	5903	10201	8183
	3 months	center (ppm)		–85.7	–92.4	–94.6	–96.7
		HWHM		2.4	1.8	1.8	1.6
		height ($\times 10^6$)		2214	1134	3117	2518
		area ($\times 10^6$)		16690	4346	11944	8577
	6 months	center (ppm)		–85.6	–92.4	–94.6	–96.7
		HWHM		2.2	1.8	1.8	1.8
		height ($\times 10^6$)		4540	3041	7025	5401
		area ($\times 10^6$)		31376	11653	26922	20699
	12 months	center (ppm)		–85.7	–92.4	–94.6	–96.7
		HWHM		2.2	1.8	2.0	1.8
		height ($\times 10^6$)		2263	1101	3762	2990
		area ($\times 10^6$)		15640	4219	16020	11458

Table 3.2.

Deconvolution of the ^{29}Si MAS NMR spectra for the M-S-H samples from MgO/SiO_2 1.3.

			Q^1	Q^2	Q^{3a}	Q^{3b}	Q^{3c}
25°C	1 month	center (ppm)	–79.0	–85.3	–92.4		
		HWHM	2.5	1.8	2.0		
		height ($\times 10^6$)	740	2447	1879		
		area ($\times 10^6$)	5811	13838	8001		
	3 months	center (ppm)	–79.0	–85.1	–92.1	–94.6	–96.7
		HWHM	2.4	1.6	1.6	1.8	1.6
		height ($\times 10^6$)	803	2810	2133	899	425
		area ($\times 10^6$)	6053	14127	7265	3444	1449
	6 months	center (ppm)	–79.0	–84.9	–92.2	–94.6	
		HWHM	2.5	1.6	1.7	1.6	
		height ($\times 10^6$)	411	2741	1678	453	
		area ($\times 10^6$)	3231	13779	6075	1542	
	12 months	center (ppm)	–79.0	–85.2	–92.4	–94.6	
		HWHM	2.5	1.6	1.8	1.8	
		height ($\times 10^6$)	366	2335	1731	952	
		area ($\times 10^6$)	2873	11736	6633	3647	
50°C	1 month	center (ppm)	–79.0	–85.2	–92.4	–94.6	
		HWHM	2.5	2.2	1.8	2.0	
		height ($\times 10^6$)	306	2606	2057	724	
		area ($\times 10^6$)	2403	18011	7884	3083	
	3 months	center (ppm)	–79.0	–85.4	–92.4	–94.4	–96.5
		HWHM	2.5	2.2	2.0	2.0	1.6
		height ($\times 10^6$)	224	2263	1432	1143	617
		area ($\times 10^6$)	1758	15640	6098	4868	2100
	6 months	center (ppm)	–79.0	–85.4	–92.4	–94.6	–96.7
		HWHM	2.5	2.2	1.8	1.8	1.8
		height ($\times 10^6$)	228	3283	2546	2069	1219
		area ($\times 10^6$)	1791	22689	9758	7928	4673
	12 months	center (ppm)		–85.4	–92.2	–94.4	–97.0
		HWHM		1.5	1.5	1.6	1.5
		height ($\times 10^6$)		2821	2222	1025	383
		area ($\times 10^6$)		13296	7097	3491	1222
90°C	1 month	center (ppm)	–79.0	–85.7	–92.4	–94.6	
		HWHM	2.5	2.2	1.8	1.8	
		height ($\times 10^6$)	365	2160	2346	1735	
		area ($\times 10^6$)	2866	14926	8991	6650	
	3 months	center (ppm)		–85.4	–92.4	–94.6	
		HWHM		2.0	1.6	1.6	
		height ($\times 10^6$)		2166	3200	753	
		area ($\times 10^6$)		13606	10899	2565	
	6 months	center (ppm)		–85.4	–92.6	–94.6	
		HWHM		2.0	1.6	2.0	
		height ($\times 10^6$)		3350	7181	1007	
		area ($\times 10^6$)		21046	24461	4287	
	12 months	center (ppm)		–85.3	–92.6	–94.6	
		HWHM		2.0	1.6	2.0	
		height ($\times 10^6$)		1431	4079	367	
		area ($\times 10^6$)		8993	13896	1561	

3.3.5 Thermal behavior

M-S-H samples generally show weight loss in increasing temperature, which is derived from the dehydration of M-S-H (Lothenbach et al., 2015; Nied et al., 2016; Zhang et al., 2018; Bernard et al., 2019a). The differential TG (DTG) curves for the samples synthesized at 25°C and MgO/SiO_2 0.8 illustrated the weight loss mainly in two stages at ~100°C and ~520°C (Fig. 3.8a). The significant weight loss for the samples synthesized at 50°C and MgO/SiO_2 0.8 was observed at ~90°C and the gradual weight loss was observed in the range from ~300°C to ~850°C (Fig. 3.8b). The thermal behavior of the samples synthesized at 90°C and MgO/SiO_2 0.8 was similar to that of the samples synthesized at 50°C although the first weight loss for the sample synthesized at 90°C was observed at ~80°C (Fig. 3.8c). The DTG curves for the samples synthesized at 25°C and 50°C with MgO/SiO_2 1.3 were similar. The first weight loss was observed both at ~100°C and the second was at ~440°C and ~450°C, respectively (Fig. 3.8d,e). The samples synthesized at 90°C with MgO/SiO_2 1.3 for 6 months and 12 months showed weight losses at ~100°C and ~550°C, while those for 1 month and 3 months showed the weight loss at ~360°C in addition to ~100°C and ~550°C (Fig. 3.8f).

The DTA curves for the samples showed endothermic and exothermic peaks (Fig. 3.9). Since dehydration is basically an endothermic reaction, the temperatures for the endothermic peaks (Fig. 3.9) were similar to those for the weight loss (Fig. 3.8). An exothermic peak was observed at ~855°C, ~845°C, and ~845°C in the DTA curve of each sample synthesized with MgO/SiO_2 0.8 at 25°C, 50°C, and 90°C, respectively (Fig. 3.9a–c). As the reaction time progressed under the MgO/SiO_2 1.3 conditions, the positions of the exothermic peaks were shifted to lower temperatures: from ~865°C to ~855°C in the DTA curves of the samples synthesized at 25°C (Fig. 3.9d), from ~865°C to ~840°C in the ones at 50°C (Fig. 3.9d), and from ~850°C to ~835°C in the ones at 90°C (Fig. 3.9f).

The XRD patterns were also obtained for the 1-month and 12-month aged samples that were heated at 1100°C in a muffle furnace (Fig. 3.10). All the M-S-H samples from MgO/SiO_2 0.8 were transformed

into enstatite after the heating. The samples synthesized at 25°C and 50°C with MgO/SiO_2 1.3 were thermally transformed into the mixture of enstatite and forsterite. The 1-month aged sample synthesized at 90°C with MgO/SiO_2 1.3 was transformed into the mixture of enstatite, forsterite, and periclase, while the 12-month aged sample was transformed into the mixture of enstatite and forsterite. In the XRD profile for the heated samples from MgO/SiO_2 1.3 (Fig. 3.10b), the intensity of peaks for enstatite (e.g., at 28.3° and 31.1° 2θ) relatively decreased from 1 month to 12 months at each temperature.

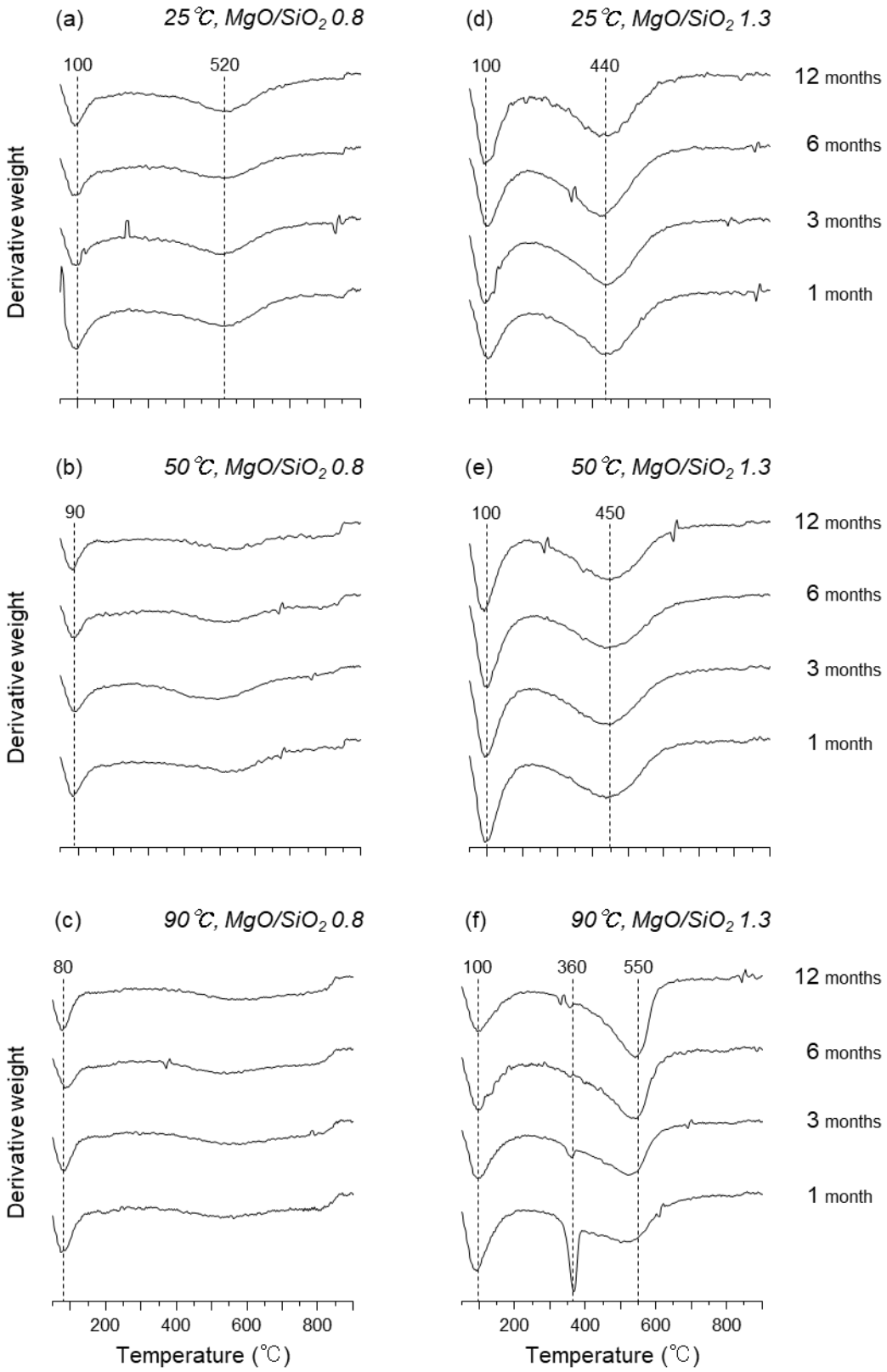

Fig. 3.8. Derivative of TG (wt%/min) curves of the M-S-H samples synthesized at (a–c) 25°C, 50°C, and 90°C from MgO/SiO_2 0.8; (d–f) 25°C, 50°C, and 90°C from MgO/SiO_2 1.3.

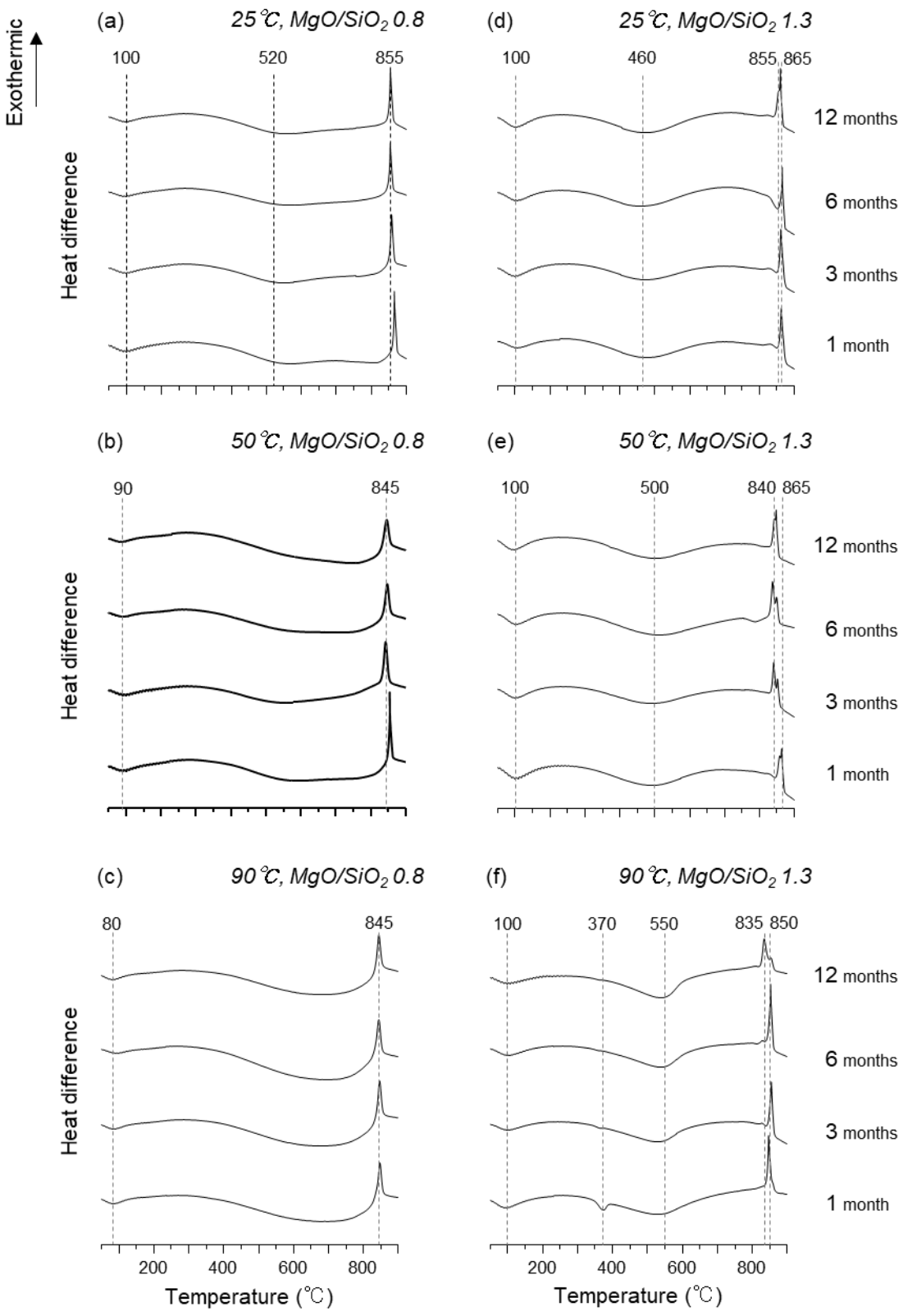

Fig. 3.9. DTA curves of the M-S-H samples synthesized at (a–c) 25°C, 50°C, and 90°C from MgO/SiO_2 0.8; (d–f) 25°C, 50°C, and 90°C from MgO/SiO_2 1.3. The positive peaks exhibit exotherms, and the negative peaks exhibit endotherms.

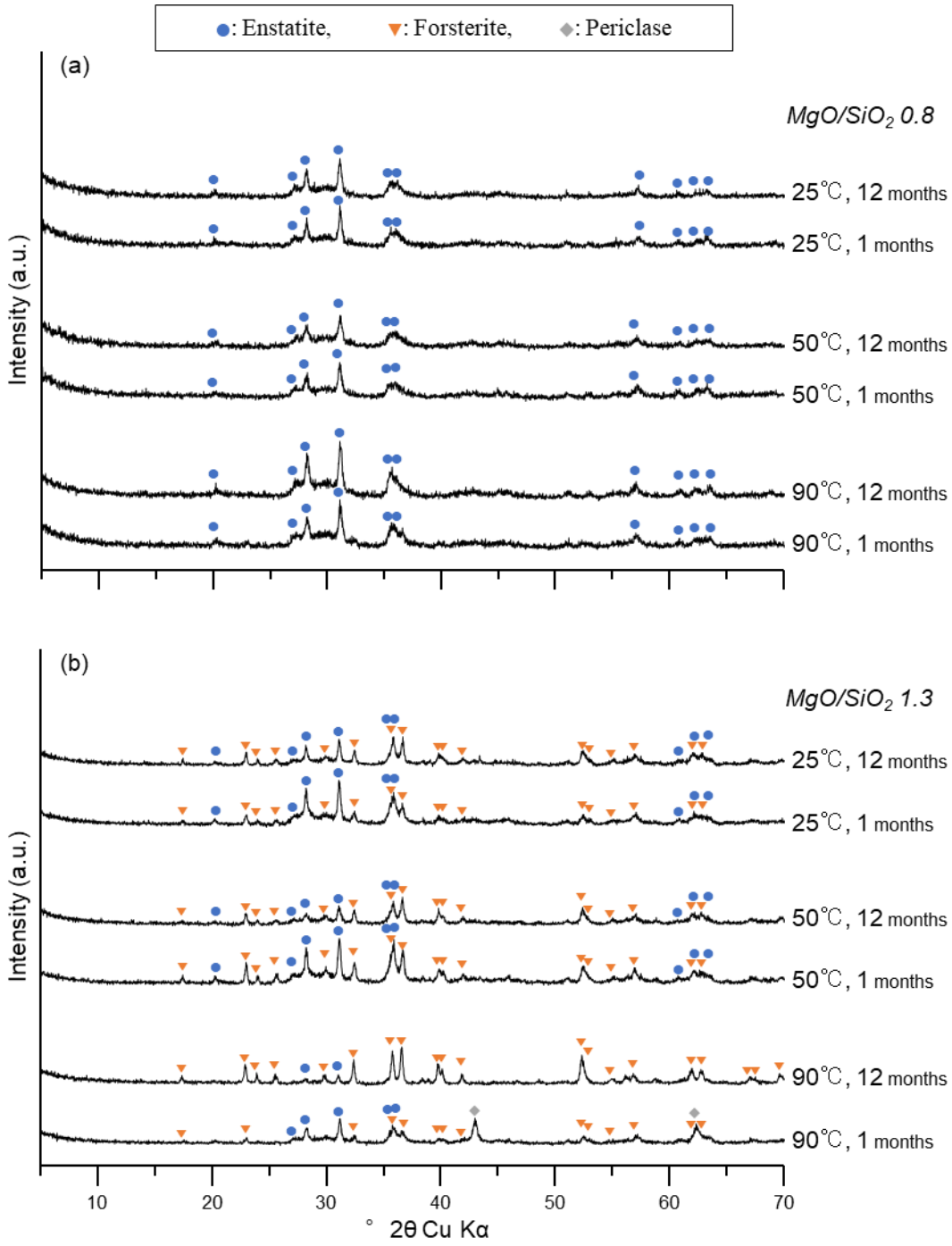

Fig. 3.10. Powder XRD patterns of the M-S-H samples after heating to 1100°C. The M-S-H samples in the figure were synthesized at 25°C, 50°C, and 90°C for 1 month and 12 months from (a) MgO/SiO_2 0.8 and (b) MgO/SiO_2 1.3.

3.3.6 Microscopy and chemistry of the particles

Aggregates of nanoparticles were observed by TEM. The sample at 90°C for 12 months from MgO/SiO_2 0.8 displayed veil-like morphology (Fig. 3.11a). The similar characteristic was also shown in the samples at 90°C for 1 month and the ones at 25°C for 1 month and 12 months from both MgO/SiO_2 conditions (Fig. 3.12). The sample at 90°C for 12 months from MgO/SiO_2 1.3 partially had morphology similar to chrysotile tubes (Fig. 3.11b).

The Mg/Si molar ratios for the particles were evaluated by FE–TEM/EDS (Mg/Si_{EDS}; Fig. 3.13). The Mg/Si_{EDS} of the particles at 25°C for 1 month and 12 months were 0.61–0.69, which did not show significant correlation with reactant MgO/SiO_2 ratios. At 90°C from MgO/SiO_2 1.3, the Mg/Si_{EDS} was 1.01 for the 1-month aged sample and 1.26 for the 12-month aged sample, increasing the standard deviation from 0.06 to 0.12. The Mg/Si_{EDS} at 90°C from MgO/SiO_2 0.8 were 0.74 for both 1-month and 12-month aged samples.

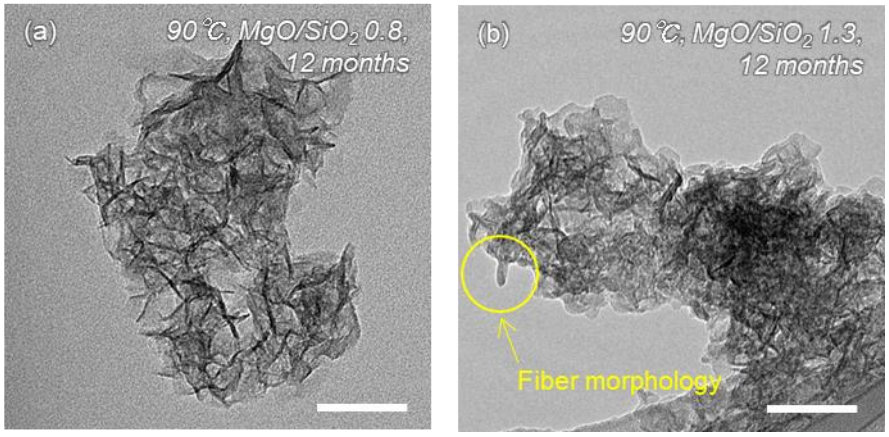

Fig. 3.11. TEM images of M-S-H particles formed at 90°C for 12 months from (a) MgO/SiO_2 0.8 and (b) MgO/SiO_2 1.3. Scale bars are 100 nm.

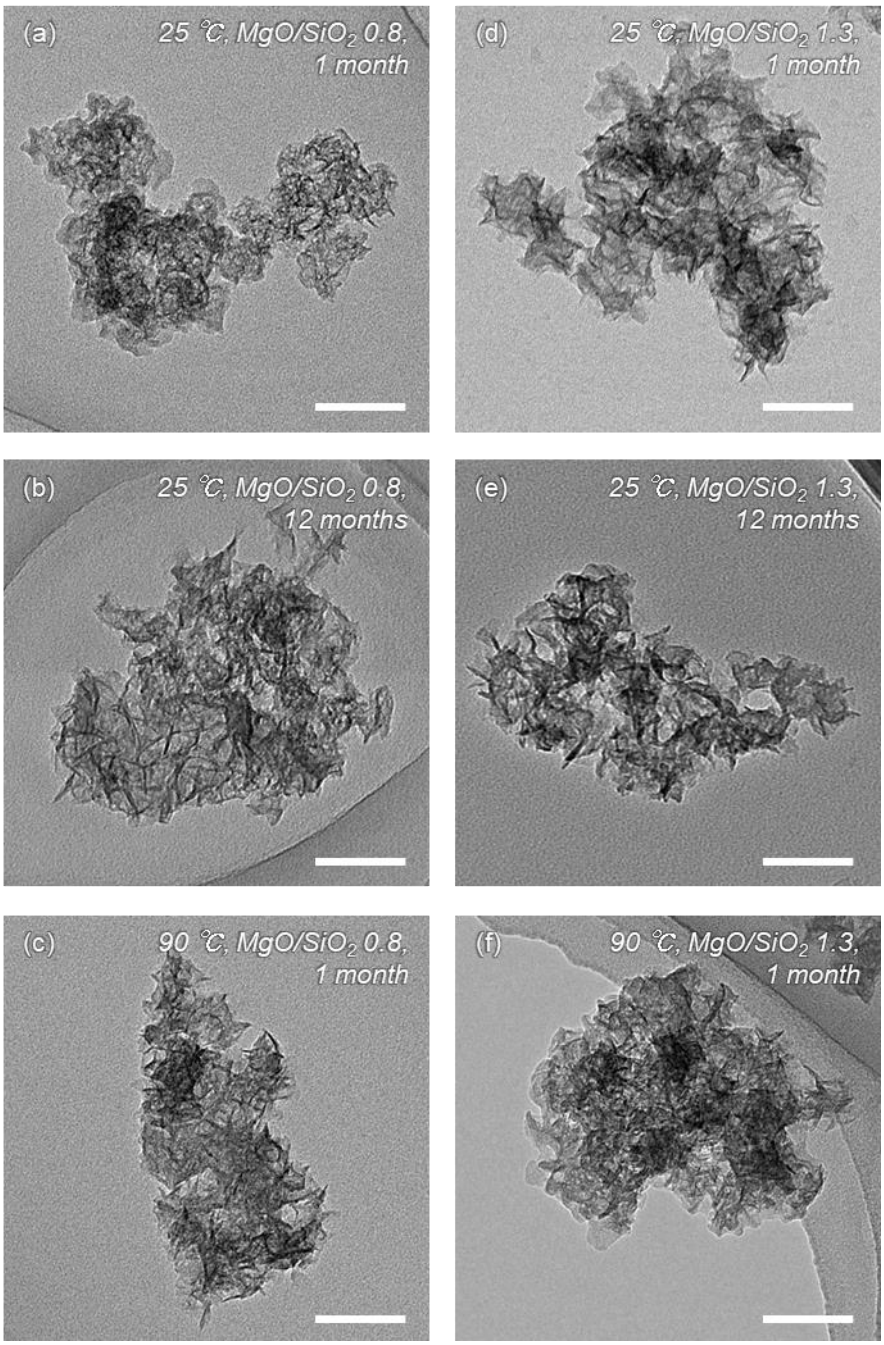

Fig. 3.12. TEM images of M-S-H particles formed (a, b) at 25°C from MgO/SiO_2 0.8 for 1 month and 12 months, (c) at 90°C from MgO/SiO_2 0.8 for 1 month, (d, e) at 25°C from MgO/SiO_2 1.3 for 1 month and 12 months, and (f) at 90°C from MgO/SiO_2 1.3 for 1 month. Scale bars are 100 nm.

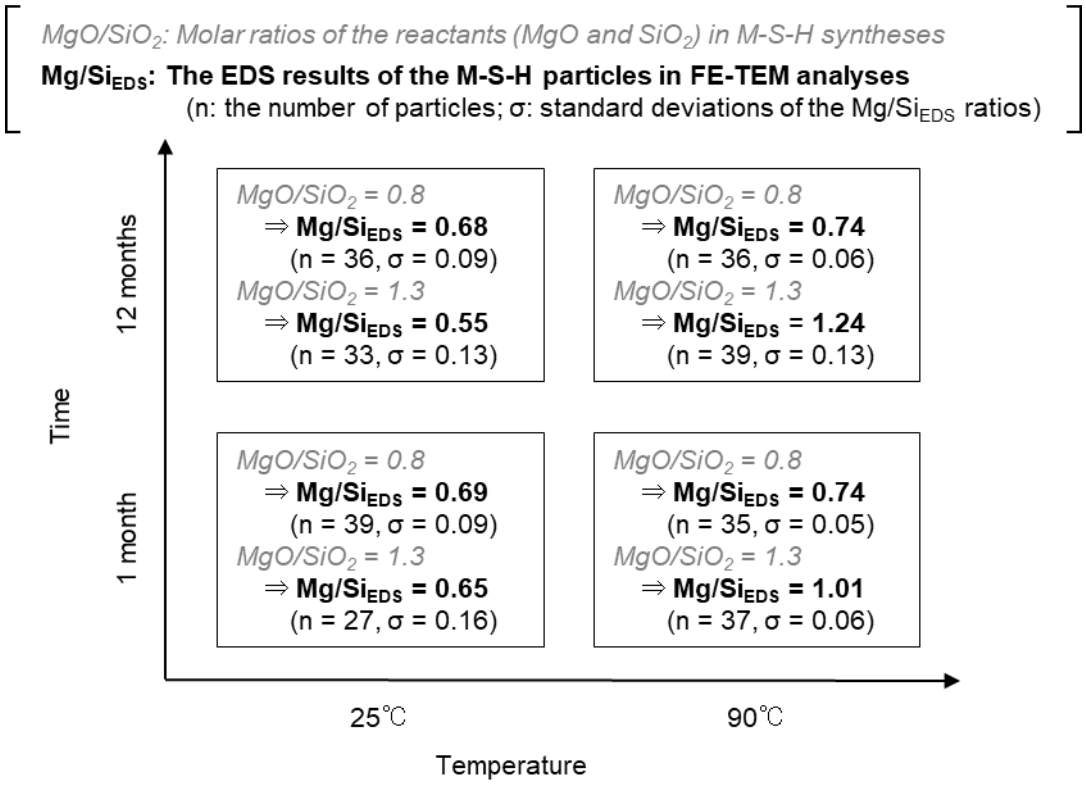

Fig. 3.13. Average Mg/Si molar ratios of M-S-H particles formed at 25°C and 90°C for 1 month and 12 months.

3.4 Discussion

3.4.1 M-S-H precipitates from MgO/SiO_2 0.8

The four XRD peaks (d = 4.5, 3.3, 2.6, and 1.54 Å at 25°C; 4.5, 3.3, 2.6, and 1.53 Å at 50°C and 90°C) indicate the precipitates are poorly crystalline materials and identified as M-S-H (Fig. 3.2a–c). No reflection was observed for the stacking of layers although phyllosilicates generally show the reflection at $d \geq 9.3$ Å (for TOT) or $d \approx 7.3$ Å (for TO) (Brindley and Brown, 1980). The XRD results suggested that the number of stacked layers is small in the M-S-H samples as evaluated in the previous study (Roosz et al., 2015). In Raman spectroscopy, however, the M-S-H samples from MgO/SiO_2 0.8 were identified to be TOT phyllosilicate when compared with vibration modes for TOT and TO phyllosilicate minerals (Fig. 3.3a–c). Structures of sepiolite (modulated phyllosilicate with TOT

ribbons) and talc were not clearly distinguished in the Raman spectra because their high-intensity peaks (~670 cm^{-1} and ~190 cm^{-1}) are observed at similar positions (Fig. 3.4b,c).

The M-S-H samples from MgO/SiO_2 0.8 also showed similar characteristics to TOT phyllosilicate in the thermal analyses. As heated, the samples were transformed into enstatite (Fig. 3.10a), which is consistent with the thermal behavior of TOT phyllosilicate minerals such as talc (MacKenzie and Meinhold, 1994a), stevensite (Shimoda, 1971; Benhammou et al., 2009), and sepiolite (Nagata et al., 1974). The transformation from the M-S-H samples to enstatite likely occurred at ~850°C with the exothermic reaction (Fig. 3.9a–c) as shown in thermal analysis for amorphized talc (at 822–830°C; Liao and Senna, 1992; Aglietti, 1994), stevensite (at 801°C; Benhammou et al., 2009), and sepiolite (at 836°C; Földvári, 2011). Significant weight loss at ~100°C (Fig. 3.8a–c) is possibly due to dehydration of interlayer water from hydrous TOT structure (Shimoda, 1971; Benhammou et al., 2009) or absorbed water or zeolitic water from sepiolite structure (Nagata et al., 1974; Földvári, 2011).

It is difficult to distinguish the structures of TOT phyllosilicates (i.e., talc, stevensite, and sepiolite) in the analyses for the M-S-H samples from MgO/SiO_2 0.8. The M-S-H samples may be mixtures of several phyllosilicates or mixed-layer silicates (Eberl et al., 1982; Khoury et al., 1982; de Vidales et al., 1991). However, the M-S-H samples at 25°C are likely identified to be a sepiolite-like phase because (i) significant weight loss was observed at ~520°C in addition to ~100°C (Fig. 3.8a), (ii) its average Mg/Si ratio was 0.68–0.69 in FE–TEM/EDS (Fig. 3.13), and (iii) the Q^3 peak was broad and the signal intensities were similar at −92.4, −94.6, and −96.7 ppm in the ^{29}Si MAS NMR spectra of the samples for 6 and 12 months (Fig. 3.5a). These three characteristics are similar to sepiolite, rather than the other Mg phyllosilicates. The bound water is removed from sepiolite structure in the range of 250–650°C (Nagata et al., 1974; Földvári, 2011). The Mg/Si is 0.67 for sepiolite ($Mg_4Si_6O_{15}(OH)_2 \cdot 6H_2O$). In ^{29}Si MAS NMR spectroscopy, sepiolite exhibits three Q^3 peaks at −92, −94.3, and −97.8 ppm with similar intensities (d'Espinose de la Caillerie and Fripiat, 1994). In contrast, the M-S-H samples at 50°C and 90°C are likely identified to be a hydrous TOT phase such as stevensite or kerolite (talc with water

molecules; Brindley et al., 1977) because dehydration of absorbed water was mainly observed around 80–90°C (Fig. 3.8b, c). Moreover, the Mg/Si ratio for the samples synthesized at 90°C was 0.74 in FE–TEM/EDS (Fig. 3.13), which is similar to that for stevensite (Mg/Si = 0.725 when its layer charge is 0.2 per formula unit) and kerolite (Mg/Si = 0.75).

The thermal relationship between TOT ribbons and hydrous TOT layers was reported in previous studies. In hydrothermal experiments, natural sepiolite samples are transformed into stevensite (at ca. 200°C–300°C; Guven and Carney, 1979) or hydrated talc (above ca. 300°C; Otsuka et al., 1974). The phase transformation from palygorskite to smectite at 80°C–160°C was also reported by Golden and Dixon (1990). Therefore, the hydrous TOT phyllosilicates are stable especially at high temperatures, rather than the modulated phyllosilicates with TOT ribbons. This is consistent with the characteristics of the M-S-H samples: a sepiolite-like phase at 25°C and a hydrous TOT phase at 50°C and 90°C.

3.4.2 M-S-H precipitates from MgO/SiO_2 1.3

The precipitates from MgO/SiO_2 1.3 at 25°C and 50°C showed the four XRD peaks (d = 4.5, 3.3, 2.6, and 1.54 Å), indicating the precipitates are poorly crystalline materials and identified as M-S-H (Fig. 3.2d,e). A broad shoulder was exhibited in the low-angle region (<15° 2θ) although the center of this reflection was not clear. In the XRD patterns for the precipitates at 90°C, however, the intensity of the low-angle peak became significantly stronger with the reaction time (Fig. 3.2f). The low-angle peak is a typical characteristic of phyllosilicate minerals, showing their layer stacking. The d-spacing for this peak was 8.2 Å for the 12-month aged sample, which was not identified as basal spacings for TOT phyllosilicate ($d \geq 9.3$ Å) or TO phyllosilicate ($d \approx 7$ Å) (Brindley and Brown, 1980).

In Raman spectroscopy, characteristics of both TOT and TO phyllosilicates were exhibited in the samples at 25°C and 50°C from 1 month to 12 months (Fig. 3.3d,e). Although similar characteristics were observed in the samples at 90°C for 1 month, the characteristics of TO phyllosilicate were evident

as time progressed (Fig. 3.3f). Therefore, the M-S-H samples at 25°C and 50°C have both TOT and TO structures and the one at 90°C has a TO structure.

The structure of the M-S-H samples at 25°C and 50°C with both TOT and TO structures cannot be determined specifically in this study. Considering the results of some previous studies, the M-S-H samples from MgO/SiO_2 1.3 at 25°C and 50°C are likely identified to be three possible phases: (i) TOT phyllosilicate with defective Si tetrahedral sheets (Roosz et al., 2015), which indicates TOT-based layers partially having TO units, (ii) a mixture of amorphized talc and amorphized serpentine with water molecules (Pedone et al., 2017), or (iii) deweylite, which is a mixture of TOT and TO phyllosilicate (Bish and Brindley, 1978).

The M-S-H samples for 12 months at 90°C is TO phyllosilicate that is possibly identified to be chrysotile or proto-serpentine (a precursor of chrysotile; Lafay et al., 2016) because the particles partially show morphology similar to chrysotile tubes (Fig. 3.11b). In geology, chrysotile is commonly known as a serpentine mineral that can form even at low temperatures (Craw et al., 1987; Evans, 2004; Okland et al., 2012). Since this sample has absorbed water removed at 100°C (Fig. 3.8f), the XRD peak at d = 8.2 Å might be a basal spacing of a chrysotile structure (~7.3 Å) with water molecules. The M-S-H samples in the initial stage (≤6 months) of synthesis at 90°C are mixtures of TOT and TO phyllosilicates, as discussed for the M-S-H samples synthesized at 25°C and 50°C in the previous paragraph. The significant transformation to chrysotile was also evident in FE–TEM/EDS, showing an increase in Mg/Si ratio for the M-S-H phase (Fig. 3.13).

Thermal analyses also support to understand the mineralogical characteristics of the M-S-H samples from MgO/SiO_2 1.3. The weight losses and endothermic reactions at 100°C were derived from the dehydration of adsorbed water (Figs Fig. 3.8d–f and Fig. 3.9d–f). For the samples synthesized at 25°C and 50°C, the weight losses at 440°C and 450°C and the endothermic reactions at 460°C and 500°C, respectively, would be derived from dehydroxylation from edge sites on the phyllosilicate layers, which was reported in the TOT structure with defective Si tetrahedral sheets (Roosz et al., 2015). The sample

synthesized at 90°C showed weight loss and the endothermic reaction at 550°C, higher than those synthesized at 25°C and 50°C. This is likely due to dehydroxylation from chrysotile structure (Földvári, 2011; Lafay et al., 2016). Considering the dehydroxylation of brucite occurs at 350°C–450°C (Földvári, 2011), the samples for 1 month and 3 months contained brucite (11.5 wt% and 3.10 wt%, respectively; Fig. 3.8f). This is likely because the samples were just manually shaken once a week in the synthesis experiments at 90°C and dissolution of hydrated MgO (i.e., brucite) was not completed.

The DTA peaks for the exothermic reactions (Fig. 3.9d–f) are likely derived from transformation into anhydrous Mg silicate phases. The heated samples were identified as mixtures of enstatite and forsterite (Fig. 3.10b). Periclase was also contained in the sample synthesized at 90°C for 1 month because of the presence of brucite in the experiment. The transformation into enstatite and forsterite was consistent with the thermal characteristics of deweylite (Lapham, 1961) and chrysotile (MacKenzie and Meinhold, 1994b). In the XRD patterns for the heated samples, peak intensities for enstatite decreased from 1 month to 12 months (Fig. 3.10b), resulting in changes in the amount of enstatite and forsterite. This may shift the DTA peak to lower temperatures from 1 month to 12 months (Fig. 3.9d–f). A similar trend was also reported in previous study for the heated M-S-H samples (Walling et al., 2015).

3.4.3 Difference of M-S-H structures from MgO/SiO_2 0.8 and 1.3

Table 3.**3** summarizes the mineralogical characteristics of the M-S-H samples for 12 months in this study. The M-S-H samples from MgO/SiO_2 0.8 is identified to be phyllosilicate with TOT ribbons (a sepiolite-like phase) at 25°C and the one with hydrous TOT layers (a stevensite- or kerolite-like phase) at 50°C and 90°C although the M-S-H samples may also be mixtures (or intermediate phases) of several phyllosilicates or mixed-layer silicates. The M-S-H samples from MgO/SiO_2 1.3 at 25°C and 50°C are identified to be deweylite or phyllosilicate having both TOT and TO units as suggested by Roosz et al. (2015) or Pedone et al. (2017). The M-S-H sample from MgO/SiO_2 1.3 at 90°C is identified as TO

phyllosilicate (chrysotile) with water molecules. The type of phyllosilicate is controlled by the initial MgO/SiO_2 ratio.

Table 3.3.

Summary of mineralogical characteristics of the M-S-H precipitates in the experiments for 12 months.

		MgO/SiO_2	
		0.8	1.3
Temperature	25°C	TOT ribbons (sepiolite-like)	TOT and TO
	50°C	TOT layers (stevensite- or kerolite-like)	TOT and TO
	90°C	TOT layers (stevensite- or kerolite-like)	TO layers (chrysotile-like)

The initial MgO/SiO_2 ratio is also important for silica polymerization. In the experiments with MgO/SiO_2 0.8 at 50°C and 90°C, the $Q^3/(Q^1+Q^2+Q^3)$ ratios were nearly constant from 1 month to 12 months (Fig. 3.7a), indicating that silica was polymerized in the initial stage (≤1 month) and further polymerization did not significantly proceed until 12 months. In the experiments with MgO/SiO_2 0.8 at 25°C, the silica polymerization was still proceeding in 12 months. In contrast, silica was polymerizing in 12 months at all temperatures under the MgO/SiO_2 1.3 conditions (Fig. 3.7b). At each temperature, the $Q^3/(Q^1+Q^2+Q^3)$ ratio in the experiment with MgO/SiO_2 1.3 was lower than those with MgO/SiO_2 0.8. The above differences are likely due to the difference in the amount of silica in the system. Silica was rich and polymerizing fast at MgO/SiO_2 0.8, whereas the smaller amount of silica reacted and polymerized slowly at MgO/SiO_2 1.3. The slow polymerization with MgO/SiO_2 1.3 may account for the trend of the decrease in the dissolved silica concentration with time (Fig. 3.1e). The fact that silica

polymerization of M-S-H was enhanced at higher MgO/SiO_2 is similar to the behavior of C-S-H. As discussed in Section 1.3, silica polymerization of C-S-H proceeds at higher CaO/SiO_2 (Grangeon et al., 2016). Moreover, the samples from both MgO/SiO_2 0.8 and 1.3 showed higher $Q^3/(Q^1+Q^2+Q^3)$ ratios at higher temperatures, indicating that polymerization was enhanced at higher temperatures.

Although the experiments lasted up to 12 months in this work, M-S-H will act as a metastable phase in geological time scales. Assuming that the same phase transformation occurs at 25°C–90°C and the transformation at higher temperatures is faster than that at 25°C, the results suggest that over more extended periods at 25°C (i) the M-S-H phase from MgO/SiO_2 0.8 would be transformed into the hydrous TOT phyllosilicate and (ii) the M-S-H phase from MgO/SiO_2 1.3 would be transformed into TO phyllosilicate. This reaction is possible because the silica was still polymerizing during 12 months at 25°C in this study (Fig. 3.7). From natural sediments at ambient temperature, Krekeler et al. (2005) observed the formation of Mg smectite via palygorskite.

3.5 Summary and conclusions

The M-S-H samples synthesized from MgO, silica fume, and water partially have structures of ordinary phyllosilicate minerals although the M-S-H phases are poorly crystalline materials. The M-S-H samples from MgO/SiO_2 0.8 is identified to be phyllosilicate with TOT ribbons (a sepiolite-like phase) at 25°C and the one with hydrous TOT layers (a stevensite- or kerolite-like phase) at 50°C and 90°C. The M-S-H samples from MgO/SiO_2 1.3 at 25°C and 50°C are identified to be deweylite or phyllosilicate having both TOT and TO units as suggested by Roosz et al. (2015) or Pedone et al. (2017). The M-S-H sample from MgO/SiO_2 1.3 at 90°C is identified as TO phyllosilicate (chrysotile) with water molecules.

Chapter 4: M-S-H syntheses at constant pH

4.1 Introduction

In Chapter 3, the M-S-H samples were synthesized from MgO, silica fume, and water. The MgO/SiO_2 ratios (= 0.8 and 1.3 in Chapter 3) determined the types of phyllosilicate structures. Moreover, pH might also be an important factor in determining the characteristics of precipitates in Mg–Si–H_2O systems. In Chapter 3, pH values were ~8.5 and ~9.5 at MgO/SiO_2 0.8 and 1.3, respectively (Fig. 3.1). To understand the pH effect, the solution pH should be constant even when the initial Mg/Si conditions are different. Therefore, the objectives of this chapter are to characterize precipitates in Mg–Si–H_2O systems at constant pHs and understand the formation conditions of M-S-H, which are related to 12[i] and [ii] in Section 1.4. When M-S-H samples are synthesized from solids (like MgO powder and silica fume), pH is controlled by the dissolution of the solids during the M-S-H synthesis. In Chapter 4, aqueous Mg solution and aqueous Si solution were used in the synthesis experiments and pH was adjusted by adding alkaline solution (NaOH). Given the pH of groundwater in ultramafic rocks (ca. 8–12; Barnes and O'Neil, 1969; Barnes et al., 1978) and pore waters in cement barriers for radioactive waste encapsulation (ca. 10–12.5; Atkinson et al., 1989), M-S-H syntheses were conducted at high pH (10 and 12) and neutral pH (for comparison).

4.2 Materials and methods

4.2.1 Experimental procedures

Synthesis experiments were conducted in an anaerobic chamber filled with N_2 gas at room temperature (20°C–27°C) to avoid the effect of CO_2 contamination on pH in the solutions. O_2 concentration in the chamber was maintained at <1 ppm, as removed by catalytic reaction in the equipment. Ultrapure water was first purged by bubbling N_2 gas through the solution for 24 hours in the chamber. The concentration of dissolved oxygen (DO) in the deoxygenated ultrapure water was 0.00 mg L^{-1}, which was checked with a DO electrode. 50 mM Si solutions were prepared by adding TEOS

($C_8H_{20}SiO_4$; Alfa Aesar, Thermo Fisher Scientific Inc., 98%) to the ultrapure water. 50 mM Mg^{2+}(aq) stock solutions were prepared using magnesium chloride hexahydrate ($MgCl_2 \cdot 6H_2O$; Kanto Chemical Co., Inc., >99 %).

In the synthesis, Mg/Si ratios were 0.4, 0.7, 1.0, 1.3, and 1.5, mixing 100 mL of the Si solutions and 40, 70, 100, 130, and 150 mL of the Mg solutions, respectively. The pH of the mixed solutions was adjusted to 7, 10 and 12 by titrating 1 M NaOH (and 1 M HCl), which were also prepared in the anaerobic chamber using the deoxygenated ultrapure water. The experiments lasted for 24 hours, which was the same as synthetic experiments conducted by Brew and Glasser (2005a) . The pH values had been maintained by additional titration during the experiments. After 24 hours, the samples were filtered through 0.20 μm PTFE filters and rinsed with the ultrapure water. The precipitates were freeze dried and ground with an agate mortar and pestle for solid analyses.

4.2.2 Analytical methods

Concentrations of dissolved Si, Mg, and Na in the filtered solutions were analyzed by ICP–AES (ICPE-9000, Shimadzu Corporation) after dilution with the ultrapure water and acidification with HNO_3. Concentrations of Cl^- in non-acidified solutions were measured by ion chromatography (IC; Dionex Integrion HPIC; Thermo Fisher Scientific Inc.).

Powder XRD patterns from 3 to 80° 2θ were obtained with a Miniflex600-C diffractometer (Rigaku Corporation) equipped with a Co target and a highly sensitive 1D silicon strip detector (D/teX Ultra2). The powdered samples were recorded at scanning speed of 1° 2θ min^{-1} and a scan step of 0.01° 2θ. The operation voltage and current were 40 kV and 15 mA. Each sample was also mounted on an Al-alloy stage.

In situ high temperature XRD (HT–XRD) patterns from 3 to 20° 2θ were collected with the same diffractometer under the same conditions (40kV, 15 mA, 1° 2θ min^{-1}, and 0.01° 2θ step). The HT–XRD patterns for samples at pH 12 from Mg/Si 0.7 and 1.5 were representatively collected. The samples were

mounted on a BTS 500 Benchtop Heating Stage (Anton Paar GmbH), which 500 was equipped with a knife edge and surrounded by a Kapton foil. The height of a knife edge was adjusted to 1.0 mm from the sample surface to minimize background effect in the low-angle region. An XRD patten was recorded at room temperature at first. The sample was heated to 70°C, 150°C, and 300°C. A heating rate from room temperature to 70 °C was 5°C min^{-1} and the ones from 70°C to 150 °C and from 150°C to 300°C were 10°C min^{-1}. The measurement started after maintaining the temperatures for 60 min. N_2 gas (99.999 %) was being supplied into the BTS 500 with a tube during the HT–XRD experiments.

Attenuated total reflection (ATR) FTIR spectroscopy was carried out by using a Nicolet 6700 FTIR spectrometer (Thermo Fisher Scientific Inc.) with a KBr beam splitter and a liquid N_2 cooled mercury cadmium telluride (MCT) detector. The signals of mid-IR spectra recorded by ATR method at lower wavenumbers (<1300 cm^{-1}) are relatively greater than at higher wavenumbers when compared with those recorded by transmission method, which is beneficial in distinguishing several Si–O stretching vibrations at ~1000 cm^{-1} for silicate samples. The powdered samples were deposited on a single bounce diamond ATR crystal with a diameter of 1.5 mm. The effective lower spectral limit is ~650 cm^{-1} in this analysis. Spectra were collected from 650 to 4000 cm^{-1} on a 4 cm^{-1} resolution. A total of 256 scans were recorded, each with a dwell time of 2 seconds. ATR corrections were not applied due to uncertainties in optical properties (e.g., refractive index) for the samples.

Raman spectroscopy was carried out on a Horiba XploRA. The solid samples were pressed into tablets to obtain flat surfaces of the samples. Raman spectra were collected using a 532 nm laser, at a 1800 grooves per millimeter grating, 300 μm confocal hole diameter, and 100 μm slit size. The spectral acquisition time was 60 s and 3 spectra were accumulated and averaged for each sample. The system was calibrated with a silicon standard.

4.3 Results

4.3.1 Solution chemistry

Concentrations of dissolved elements after 24-hour reactions were measured and compositions of precipitates were calculated by mass balance (Table 4.1). Some of dissolved Mg and Si species were consumed as precipitation in the experiments. The experiments at pH 7 showed high residual Mg concentrations in solutions, resulting in low Mg/Si ratios in solids. The Mg/Si ratios in solids were similar to those in initial solutions at pH 10 and 12.

Table 4.1.

Chemical analyses for solutions after 24-hour reactions in Mg–Si–H_2O systems.

System	Synthetic condition		Solution chemistry after 24 hours					Composition (solid)
			pH	Mg (mM)	Si (mM)	Na (mM)	Cl (mM)	
Mg-Si-H_2O	pH 7	Mg/Si 1.5	7.09	29.63	2.90	1.1	64.2	Mg/Si = 0.02
		Mg/Si 1.3	7.13	27.57	2.71	0.6	60.5	Mg/Si = 0.04
		Mg/Si 1.0	7.09	24.44	8.40	0.7	52.7	Mg/Si = 0.03
		Mg/Si 0.7	7.09	20.33	2.71	0.6	44.3	Mg/Si = 0.01
		Mg/Si 0.4	6.98	13.91	2.41	3.4	35.0	Mg/Si = 0.01
	pH 10	Mg/Si 1.5	10.00	2.45	0.06	37.7	48.6	Mg/Si = 1.4
		Mg/Si 1.3	10.02	1.87	0.10	34.4	60.1	Mg/Si = 1.2
		Mg/Si 1.0	9.99	0.54	0.35	34.3	50.7	Mg/Si = 1.0
		Mg/Si 0.7	10.08	0.20	1.42	31.6	45.5	Mg/Si = 0.7
		Mg/Si 0.4	10.06	0.75	5.42	24.9	35.3	Mg/Si = 0.4
	pH 12	Mg/Si 1.5	12.10	0.25	3.53	56.7	56.4	Mg/Si = 1.8
		Mg/Si 1.3	12.03	0.14	3.64	54.5	55.3	Mg/Si = 1.6
		Mg/Si 1.0	12.08	0.59	3.93	54.3	52.9	Mg/Si = 1.2
		Mg/Si 0.7	12.09	1.05	9.47	53.7	39.1	Mg/Si = 1.0
		Mg/Si 0.4	12.00	11.85	29.96	49.0	27.9	Mg/Si = 0.4

4.3.2 XRD analyses

The powder XRD study suggested that precipitates in the Mg–Si–H_2O systems consisted of amorphous silica, Mg hydroxide (brucite), and/or M-S-H. Except for the peaks arising from the sample

holder, the XRD results at pH 7 only revealed a broad peak at ~3.9 Å, which is consistent with amorphous silica (Fig. 4.1a). The XRD patterns for the five samples at pH 10 exhibited four broad peaks at ~4.5, ~3.3, ~2.56, and ~1.55 Å (Fig. 4.1b), which is a typical feature of M-S-H (4.5, 3.3, 2.56, 1.54 Å; Nied et al., 2016). The intensity was relatively high at ~3.9 Å in the XRD pattern for the sample from Mg/Si 0.4 at pH 10. At pH 12, the peaks for M-S-H were observed in all the experiments, and those for brucite were additionally recognized in the experiment from Mg/Si 1.5 (Fig. 4.1c). A broad peak was also shown at $d \geq 10$ Å in each XRD pattern for the sample from all the Mg/Si ratios at pH 12 and from Mg/Si 0.7, 1.0, 1.3, and 1.5 at pH 10.

The reflections at $d \geq 10$ Å in samples from pH 12 were further investigated in HT–XRD experiments. The peak at ~13 Å in the sample from Mg/Si 0.7 gradually shifted to ~10 Å as the sample was heated to 300°C (Fig. 4.2a), while the peak at ~12 Å in the sample from Mg/Si 1.5 shifted from ~12 Å to ~9.3 Å (Fig. 4.2b).

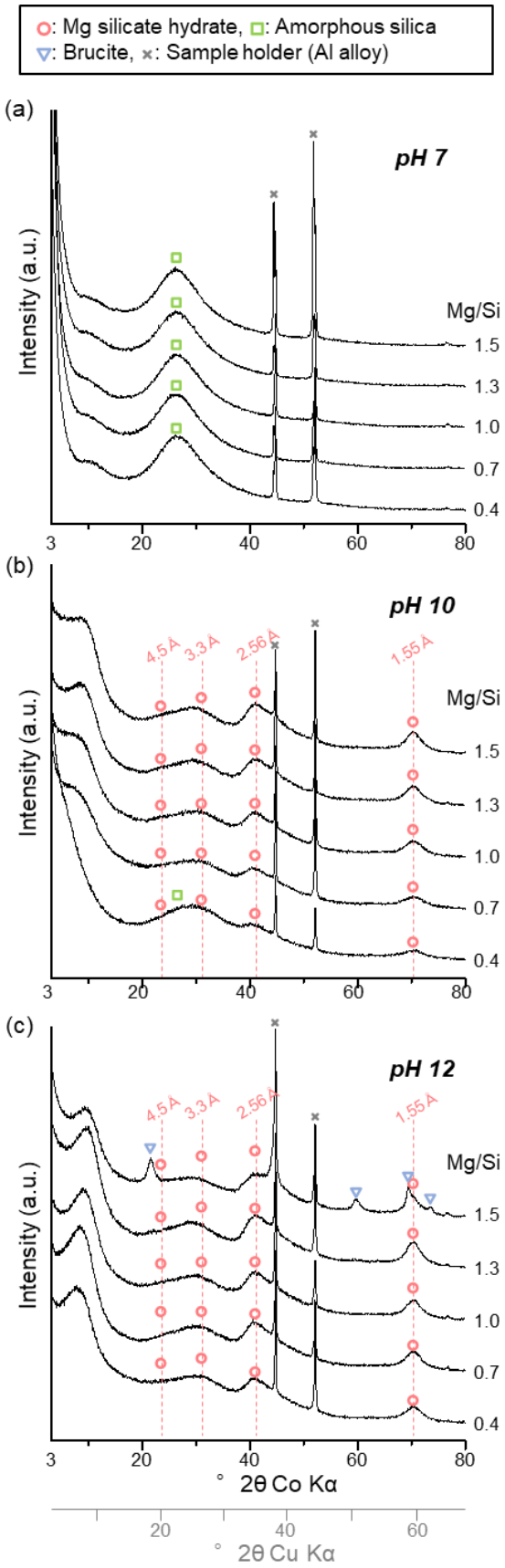

Fig. 4.1. XRD patterns of precipitates in Mg–Si–H_2O systems at (a) pH 7, (b) pH 10, and (c) pH 12.

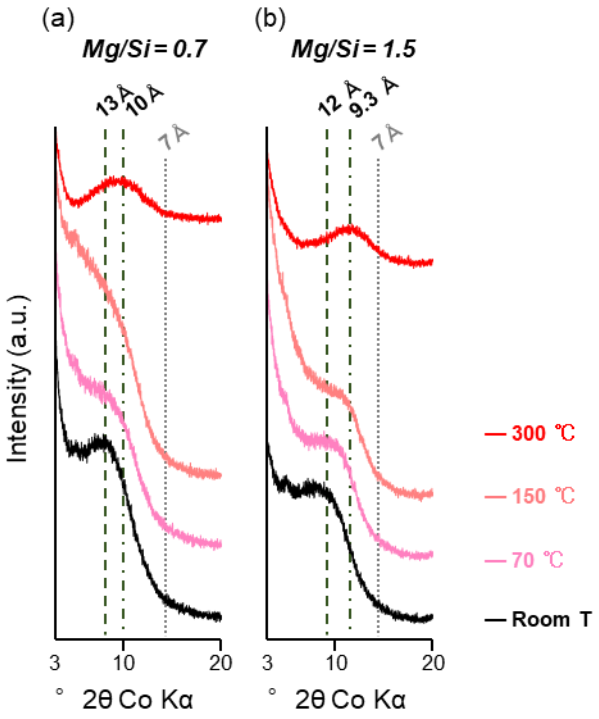

Fig. 4.2. In situ HT−XRD patterns for precipitates at pH 12 from (a) Mg/Si 0.7 and (b) Mg/Si 1.5.

4.3.3 Spectroscopic characterization

The ATR–FTIR spectra for the precipitates in Mg–Si–H_2O systems revealed vibrational bands arising from silicate structures between 1200 and 700 cm^{-1} (Farmer, 1974). All the precipitates at pH 7 exhibited bands at ~800, ~960, and ~1068 cm^{-1} and a shoulder at ~1200 cm^{-1} (Fig. 4.3a). The sample from Mg/Si 0.4 at pH 10 showed bands at ~800, ~896, and ~1012 cm^{-1} and a shoulder at ~1200 cm^{-1} (Fig. 4.3b). For the other samples, additional bands at ~896 and ~996 cm^{-1} were detected (Fig. 4.3b,c).

The Raman spectra for precipitates at pH 7 (Fig. 4.4) and alkaline pHs (10 and 12; Fig. 4.5) were different. The precipitates at pH 7 exhibited a broad peak from ~300 cm^{-1} to ~500 cm^{-1} and at 970 cm^{-1}. For the precipitates at pH 10 and 12, the peaks were exhibited at ~360, ~450, and ~675 cm^{-1}. Raman intensity was observed at ~225 cm^{-1} higher at Mg/Si 1.3 and 1.5. For the precipitates from Mg/Si 1.5 at pH 12, the Raman intensity at ~440 cm^{-1} was high and a peak was additionally exhibited at ~275 cm^{-1}.

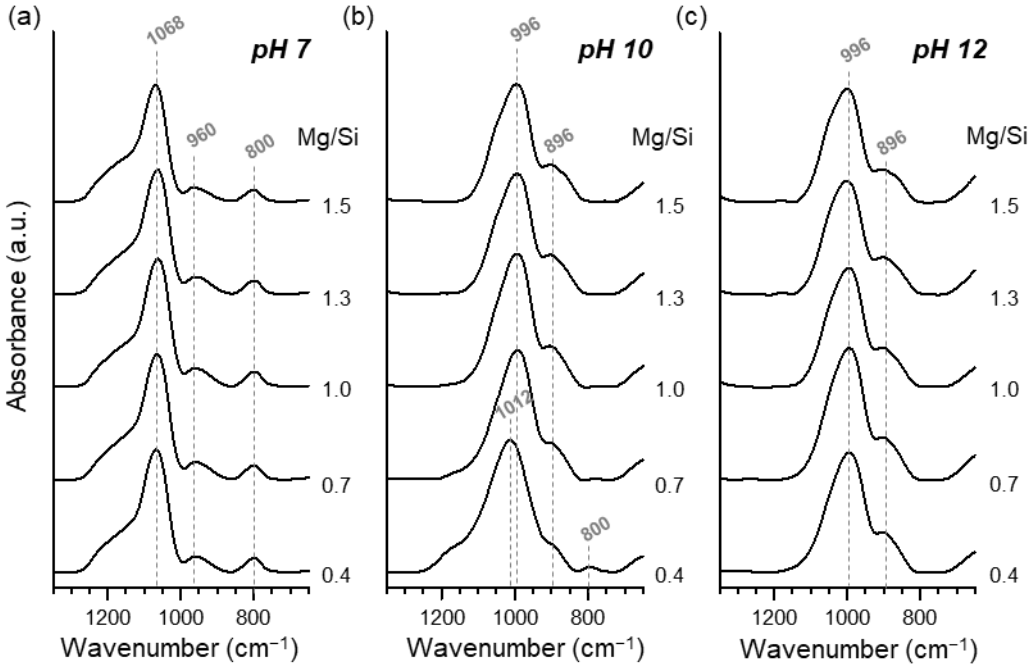

Fig. 4.3. FTIR spectra of precipitates in Mg–Si–H_2O systems at pH (a) 7, (b) 10, and (c) 12.

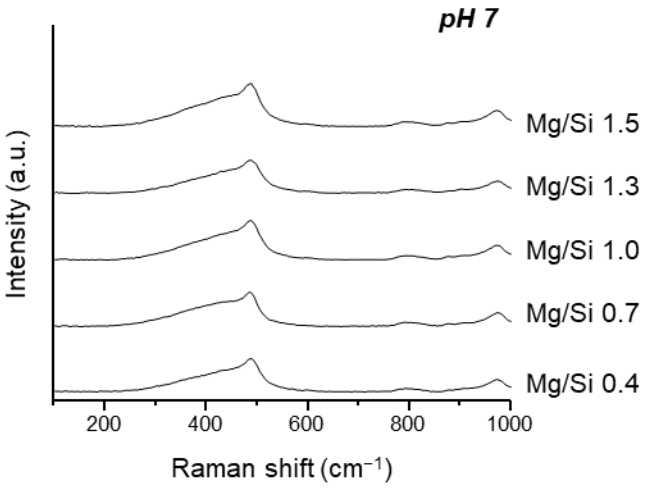

Fig. 4.4. Raman spectra of precipitates in Mg–Si–H_2O systems at pH 7.

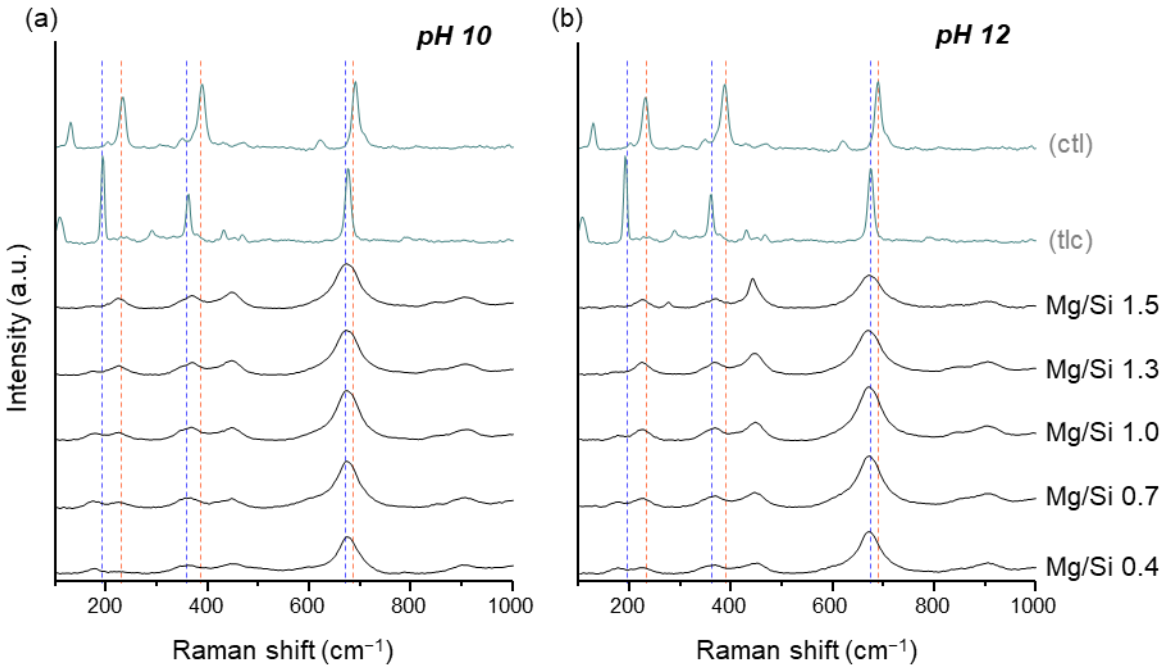

Fig. 4.5. Raman spectra of precipitates in Mg–Si–H_2O systems at pH (a) 10 and (b) 12. Raman spectra for talc (tlc: synthetic material from Matsumura Sangyo Co., Ltd., Japan) and chrysotile (ctl: natural sample from Hokkaido, Japan) are also displayed.

4.4 Discussion

4.4.1 Characterization of the precipitates in Mg–Si–H_2O systems at pH 7, 10, and 12

The XRD revealed the predominant phase in Mg–Si–H_2O systems was amorphous silica at pH 7 and M-S-H at pH 10 and 12 (Fig. 4.1a–c). Mg hydroxide (brucite) was also a component in the sample from Mg/Si 1.5 at pH 12, which is an OH^--rich and Mg^{2+}-rich condition. The samples without amorphous silica also showed low-angle peaks ($d \geq 10$ Å), which are consistent with a basal reflection of TOT phyllosilicates.

The characteristics of precipitates in this study are also discussed from the results of ATR–FTIR spectroscopy in the range 1350–650 cm^{-1}. All bands from the samples at pH 7 (Fig. 4.3a) are interpreted to be vibrations in an amorphous silica structure. Bands at ~800, and ~1068 cm^{-1} are assigned to Si–O stretching vibrations in Q^4 silica structure (Farmer, 1974). Si–O stretching of surface Si–OH groups are

observed at ~960 cm^{-1} (Hino and Sato, 1971), and asymmetric stretch vibrations of Si–O–Si linkages show a broad shoulder around 1200 cm^{-1} in the spectra (Kamitsos et al., 1993). Two bands at ~996 and ~896 cm^{-1} from the samples at the alkaline pHs (Fig. 4.3b, c) are assigned to Si–O stretching vibrations of Q^3 silica and Q^2 silica in M-S-H structure, respectively (Nied et al., 2016; Bernard et al., 2017). The Q^2 will be silica at edge sites, as crystallite size in the *ab* plane of M-S-H is small (~1.5 nm; Roosz et al., 2015). The spectrum for the sample from Mg/Si 0.4 at pH 10 shows characteristics of both M-S-H and amorphous silica (Fig. 4.3b), which is consistent with the fact that the diffraction intensity at ~3.9 Å was relatively high in the XRD pattern (Fig. 4.1b).

The Raman spectra for the alkaline pHs (Fig. 4.5) indicated the structure of the M-S-H precipitates in detail. The peaks at ~675 and ~360 cm^{-1} were characteristics of TOT phyllosilicate (Si–O–Si modes and ν_5(E) modes of SiO_4 tetrahedra, respectively; Loh, 1973). The peak was also observed at ~450 cm^{-1}, the same as M-S-H samples synthesized by Lothenbach et al. (2015) and Nied et al. (2016) and in Chapter 3 (Fig. 3.3). Raman spectra at ~225 cm^{-1} at Mg/Si 1.3 and 1.5 were consistent with O–H–O modes of chrysotile (Rinaudo et al., 2003), suggesting that the M-S-H precipitates at high Mg/Si partially have a TO phyllosilicate structure.

The Raman spectra also demonstrate the formation of Mg hydroxide and amorphous silica. Mg hydroxide (Fig. 3.4d and Lutz et al., 1994) was confirmed by the two peaks at ~275 and ~440 cm^{-1} at pH 12 and Mg/Si 1.5 (Fig. 4.5b). Raman spectra of the pH 7 samples with a broad peak in the range from ~300 cm^{-1} to ~500 cm^{-1} and at 970 cm^{-1} (Fig. 4.4) were consistent with that of amorphous silica (Chemtob et al., 2012).

In the HT–XRD experiments, the samples at pH 12 from Mg/Si 0.7 and 1.5 were identified as hydrous TOT phyllosilicates. The sample from Mg/Si 0.7 at pH 12 showed a *d*-value shift from ~13 Å to ~10 Å with heating (Fig. 4.2a), corresponding to the behavior of smectite- or vermiculite-group minerals (Brindley and Brown, 1980). Smectite and vermiculite have expandable TOT layers containing water molecules, so that dehydration occurs as temperature increases. In this study, however, this sample

cannot be identified to be vermiculite because trivalent cations (e.g., Al^{3+}) are needed for isomorphous substitution in the tetrahedral and/or octahedral sheets to form trioctahedral vermiculite (i.e., layer charge > 0.6 electrons per formula unit). Therefore, the M-S-H sample from the Mg/Si 0.7 likely forms the structure of stevensite, which is an Mg-silicate smectite with a layer charge (< 0.6 electrons per formula unit) derived from octahedral deficiencies (Brindley and Brown, 1980) and balanced by interlayer cations (likely Na^{+}).

The HT–XRD patterns for the sample from Mg/Si 1.5 at pH 12 showed a *d*-value shift from ~12 Å to ~9.3 Å (Fig. 4.2b). Unlike the sample from Mg/Si 0.7, a *d*-value of ~9.3 Å suggests a talc-like structure (TOT without interlayer cations), possibly kerolite, which is a hydrous mineral characterized by disordered layers and weak swelling properties in water (Brindley et al., 1977; Brindley and Brown, 1980).

In a previous study conducted by Roosz et al. (2015), an M-S-H sample synthesized at Mg/Si 0.6 showed TOT phyllosilicate structure, while the one synthesized at Mg/Si 1.2 showed TOT phyllosilicate with defects in the Si tetrahedral sheets. The sample from Mg/Si 1.5 in this study may also have significant defects in their Si tetrahedral sheets of TOT layers, showing partially TO units. This is consistent with the fact that the samples from Mg/Si 1.3 and 1.5 in the alkaline solutions exhibited O–H–O modes of chrysotile in Raman spectroscopy (Fig. 4.5). There may be fewer vacancies in its Mg octahedral sheets as the system contains sufficient Mg ions.

To summarize this subsection, compositions of solid phases in Mg–Si–H_2O systems are illustrated in Fig. 4.**6**. Amorphous silica is a dominant phase at pH 7. M-S-Hs that are poorly-crystalline hydrous TOT phyllosilicates, are formed at pH 10 and 12. In addition, amorphous silica is precipitated under the Si-rich condition at pH 10 and Mg hydroxide (brucite) is formed under the Mg-rich condition at pH 12.

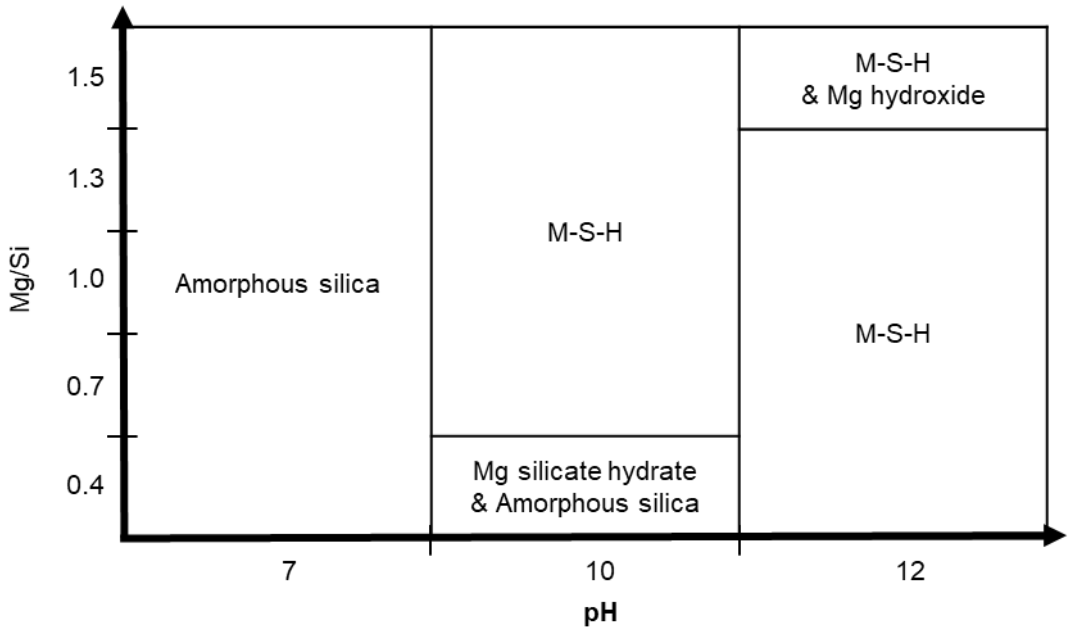

Fig. 4.6. Precipitates in Mg–Si–H_2O systems at pH 7, 10, and 12.

4.4.2 Effect of pH in M-S-H synthesis

M-S-H synthesized at higher pH may have a larger size of coherent scattering domain and/or better periodicity in the *c** direction because the XRD peaks at low-angle regions (d ≥ 10 Å) in the pH 12 samples were slightly sharper than those in the pH 10 samples (Fig. 4.1b,c). A similar trend was also observed in Chapter 3. A broad peak (or a broad shoulder) was evident in the XRD patterns of the M-S-H samples from MgO/SiO_2 1.3 (Fig. 3.2d–f), whereas it was not clearly recognized from MgO/SiO_2 0.8 (Fig. 3.2a–c). The solution pH in the experiments with MgO/SiO_2 1.3 was higher than the one with MgO/SiO_2 0.8 (Fig. 3.1a). Therefore, higher pH may enhance the layer stacking in this study.

pH did not affect the phyllosilicate types (TOT or TO) of M-S-H. Factors affecting the phyllosilicate types are likely complicated. Although Mg/Si ratio is an important parameter in Chapter 3, all the M-S-H samples (0.4 ≤ Mg/Si ≤ 1.5) in Chapter 4 were identified as TOT phyllosilicate. Other parameters such as w/s ratio and the presence of alkali ions (e.g., Na^+) also be non-negligible for determining the phyllosilicate types.

4.5 Summary and conclusions

This chapter describes the characteristics of the products formed by mixing aqueous Mg solution and aqueous Si solution (Mg/Si = 0.4, 0.7, 1.0, 1.3, and 1.5) at pH 7, 10, and 12. M-S-H formed in the alkaline solutions. Amorphous silica also precipitated at pH 10 with a high amount of Si (i.e., Mg/Si 0.4) and Mg hydroxide also precipitated at pH 12 with a high amount of Mg (i.e., Mg/Si 1.5). In the experiments, all the M-S-H samples were identified as TOT phyllosilicate, indicating that pH and Mg/Si ratio did not affect phyllosilicate types.

Chapter 5: M-S-H formation in open-flow systems

5.1 Introduction

Batch experiments (i.e., under zero-flow conditions) have been undertaken in most previous studies and Chapters 3 and 4. However, M-S-H formation in flow-through experiments (i.e., under open-flow conditions) has not been studied. Such experiments would better represent natural surface/subsurface environments where ground and/or surface waters dissolve primary minerals. This chapter aims to elucidate the precipitation of M-S-H under open-flow conditions in flow-through experiments at pH 10 and 50°C and assess their formation condition (related to [i] and [iii] in Section 1.4). This pH is within the range of that measured in pore waters of engineered barriers used in long-term encapsulation of radioactive waste (Atkinson et al., 1989) and groundwater involved in geological CO_2 storage in ultramafic rocks (Okamoto et al., 2006; Ninomiya et al., 2007). The temperature is consistent with that of the clay buffer material used in radioactive waste (NUMO, 2021) and CO_2 storage (Snæbjörnsdóttir et al., 2020) sites.

5.2 Materials and methods

5.2.1 Materials

MgO powder (DENMAG® SSP#3, purity 99.8%; Tateho Chemical Industries, Japan) was used as the starting material, sieved to a particle size of 75–150 μm. Scanning electron microscopy (SEM) images of unreacted MgO particles indicated an angular shape (Fig. 5.1). The Brunauer–Emmett–Teller (BET) specific surface area was 0.1542 ± 0.0150 m^2 g^{-1}.

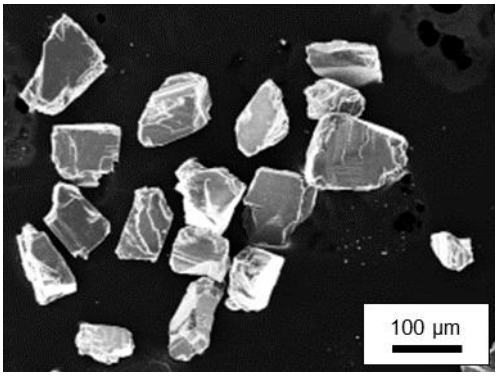

Fig. 5.1. Secondary-electron image of unreacted MgO powder.

5.2.2 Experimental Setup

Three flow-through experiments were undertaken using non-stirred 40 mL reaction cells (Fig. 5.2), with 1.00 g of MgO powder in each. PTFE filters (0.22 µm) were placed at cell inlets and outlets to prevent particle loss. The cells were fully immersed in a thermostatic water bath held at a temperature of 50°C. The powder reacted with the input solution injected into the bottom chamber of the cells using a Gilson® peristaltic pump.

Three input solutions were prepared using Millipore MQ water with an initial pH of 10. In one (blank) experiment, the input solution contained no Si; in the other two experiments, Si was added as Na_2SiO_3 (pure reagent, Merck KGaA) to obtain input Si concentrations ($[Si]_{in}$) of 0.15 or 1.5 mM. Both Si-rich solutions were undersaturated with respect to amorphous silica. The Si concentrations in the experiments are similar to those in groundwater (Mg^{2+}–HCO_3^- type) in ultramafic rock masses (0.08–0.4 mM; Barnes and O'Neil, 1969; Okland et al., 2012; Giampouras et al., 2020). The pH of input solutions was adjusted by addition of HCl and NaOH.

The experiments ran for 23 days. Output solution was collected periodically and weighed to monitor the fluid flow rate. The flow rate was held constant at 0.076 mL min^{-1} for the $[Si]_{in}$ 1.5 mM experiment, 0.065 mL min^{-1} for the $[Si]_{in}$ 0.15 mM experiment, and 0.054 mL min^{-1} for the blank experiment to yield

residence times within cells of 9, 10, and 12 h, respectively. On completion of the experiments, reacted solid samples were retrieved by centrifugation and air-dried for analysis.

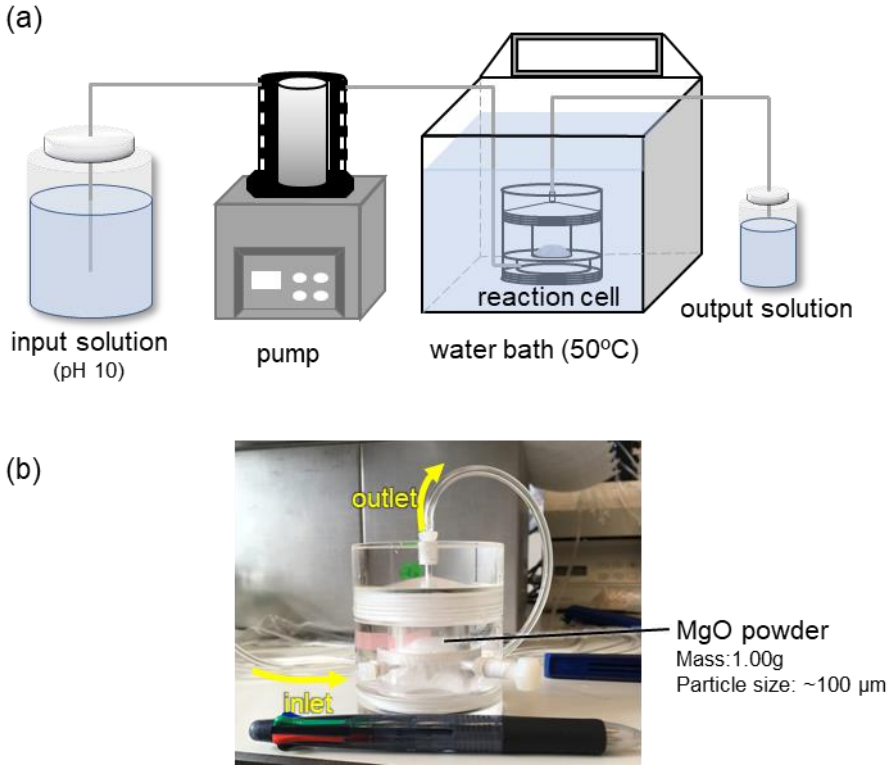

Fig. 5.2. Experimental setup: (a) schematic diagram of the flow-through system and (b) photograph of a flow-through reaction cell.

5.2.3 Solution analyses

The pH of input and output solutions was measured at room temperature (22°C ± 3°C) using an Orion Dual Star (Thermo Fisher Scientific, USA) pH electrode, standardized against pH 2, 4, 7, and 9.2 buffer solutions, with a reported accuracy of ±0.02 pH units. The pH at 50°C (experimental temperature) was then calculated. The Mg and Si concentrations of the solutions were determined by ICP–AES (Perkin Elmer Optima 8300, USA) with detection limits of 2.1×10^{-7} M and 7.1×10^{-7} M, respectively, and uncertainties of ±3%.

5.2.4 Solid analyses

The BET specific surface areas of unreacted MgO powder and solid samples retrieved at the conclusion of the experiments were determined with a surface-area analyzer (Micromeritics ASAP 2000; USA) using five-point N_2 adsorption isotherms with sample N_2 degassing for 2 h at 137 °C. Under these conditions, loosely bound interlayer water in M-S-H particles was likely removed (Nied et al., 2016).

Powder XRD analyses of MgO powder and retrieved solid samples involved a RINT-2100 diffractometer (Rigaku Corporation, Japan) operating at 30 kV and 20 mA, equipped with a Cu target. Diffraction profiles were collected over 5°–80° 2θ at a scanning speed of 0.1° min^{-1}.

FTIR spectra were recorded in the mid-IR region using an FTIR-4100 spectrometer (JASCO Corporation, Japan) over a wavelength range of 400–4000 cm^{-1} with a spectral resolution of 1.0 cm^{-1}. Pellets were prepared by mixing 1.6 wt.% sample powder with 98.4 wt.% KBr. The KBr was dried before use by heating at 110°C for 3 h.

Solid-state ^{29}Si NMR spectra were acquired using an Avance Neo 500 spectrometer (Bruker, USA) at 99.38 MHz. Powder samples were packed into 3.2 mm zirconia rotors and rotated at MAS rates of 5 kHz. The ^{29}Si NMR spectral chemical shifts were referenced to the most intense resonance at −9.7 ppm of an external sample of hexamethylcyclotrisiloxane ($C_6H_{18}O_3Si_3$). ^{29}Si dipolar decoupling (DD) MAS NMR spectra were recorded with a 30° pulse (1.4 μs) and a relaxation delay of 20 s, following the ^{29}Si NMR procedure of Bernard et al. (2019a), and 2800 scans were accumulated. Moreover, ^{1}H–^{29}Si cross-polarization (CP) MAS NMR spectra were recorded with a contact time of 2 ms, which is within the range where Q^1 and Q^2 silicon sites have the highest intensities (2–4 ms; Bernard et al., 2019a). The relaxation delay was 10 s, and 6000 scans were accumulated. The H decoupling involved a SPINAL64 pulse sequence.

SEM cross-section analyses of reacted MgO particles involved a JSM-IT200 instrument (JEOL, Japan) equipped for EDS. Secondary-electron images were obtained at 15 kV accelerating voltage.

Polished sections of solid samples embedded in resin were prepared following the method of Owada et al. (2014), which does not use water. The polished sections were carbon-coated before observation.

Reacted powder retrieved from the experiments was analyzed by TEM using a JEM-2010 instrument (JEOL, Japan). The powder was dispersed in ethanol ultrasonically and one drop of the supernate deposited on a copper grid with a carbon film (Microgrid type A, Okenshoji, Japan). Using this procedure, product particles of much smaller size than that of the primary MgO powder were extracted from the reacted powder. TEM images and electron diffraction patterns were obtained at an operating voltage of 200 kV. EDS mapping with STEM involved a Titan3 G2 60-300 STEM system (FEI, Thermo Fisher Scientific, USA) operated at 60 kV. The STEM system was equipped with a FE electron gun and an FEI Super-X EDS detector system comprising four separate silicon drift detectors. An EDS spectrum for an aggregate of nanoparticles from both Si-solution experiments was obtained using a STEM/EDS mapping analysis. An Mg/Si atomic ratio of the nanoparticle aggregate was calculated by the Cliff–Lorimer method using peak intensity of Mg (K line) and Si (K line) in the EDS spectrum.

5.3 Results

5.3.1 Aqueous chemistry

Temporal trends in outflow Mg and Si aqueous concentrations during the three experiments are shown in Fig. 5.3. The Mg concentrations increased sharply in the first 50 h before decreasing gradually to a steady state at 150 h (Fig. 5.3a). Achievement of steady state was verified by a series of constant (differing by <6%) Mg output concentrations. Steady-state Mg concentrations were 0.17, 0.12, and 0.04 mM in the blank, $[Si]_{in}$ 0.15 mM, and $[Si]_{in}$ 1.5 mM experiments, respectively. In the Si-solution experiments, the output Si concentration also attained steady states (Fig. 5.3b) of 1.11 and 0.10 mM in the $[Si]_{in}$ 1.5 and 0.15 mM experiments, respectively. The steady-state pH in the three experiments was 10 ± 0.2 (Fig. 5.4).

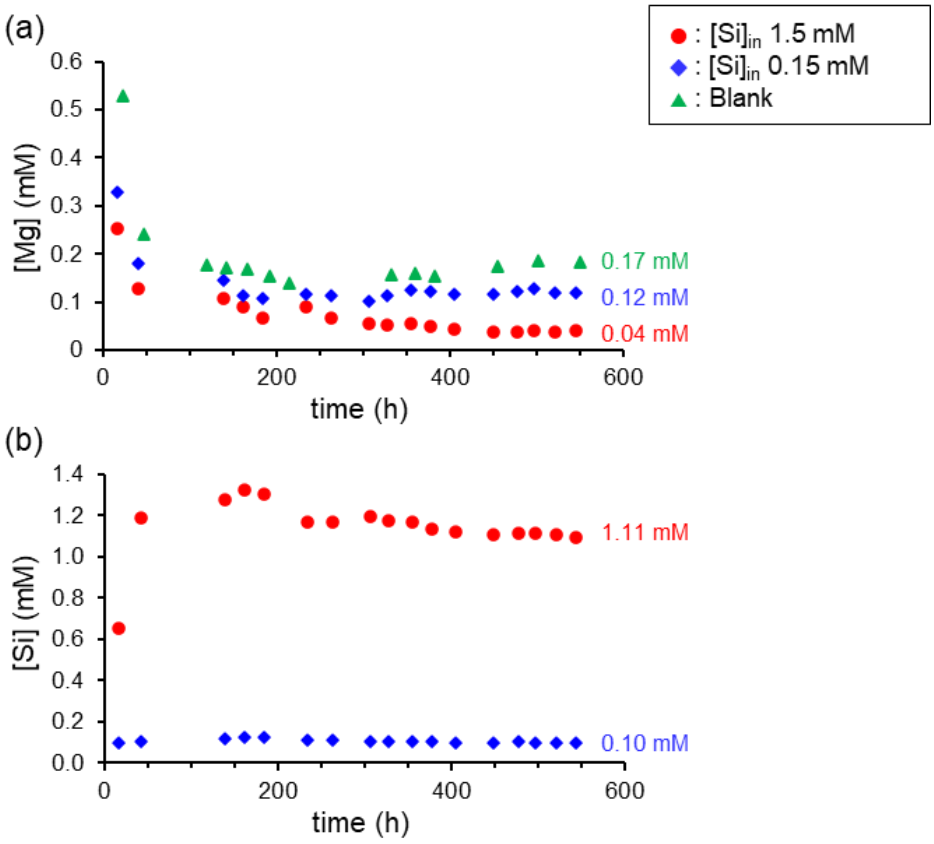

Fig. 5.3. Trends in Mg (a) and Si (b) concentration in output solutions as a function of time.

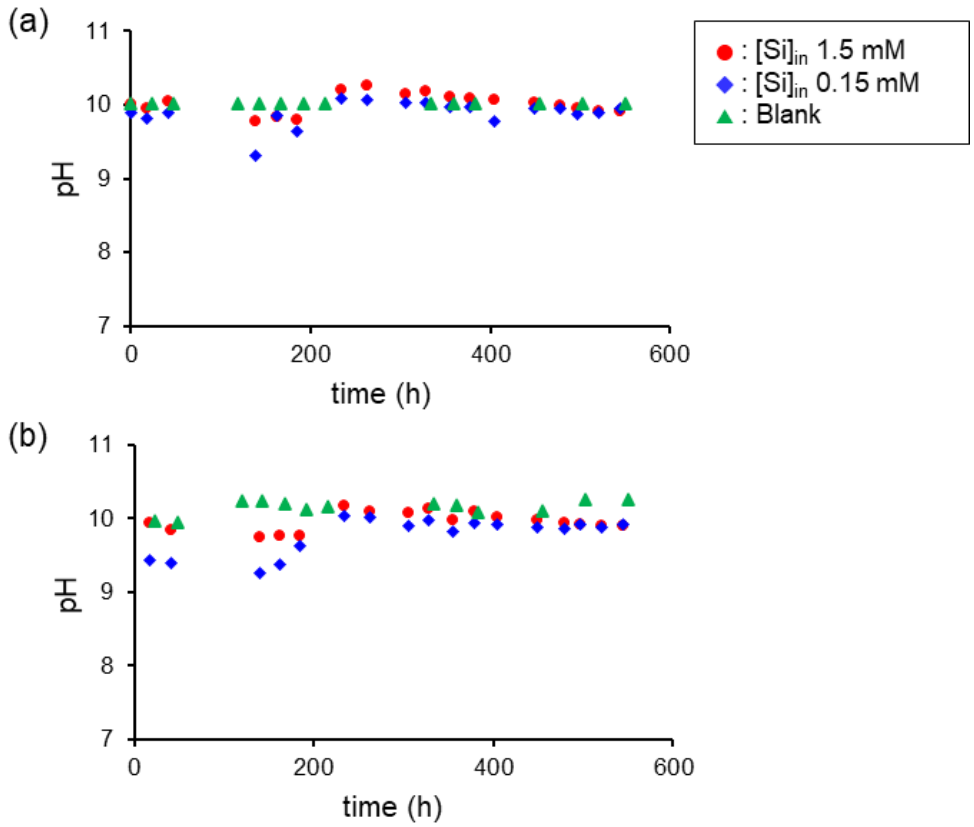

Fig. 5.4. Variation in pH as a function of time for (a) input solutions and (b) output solutions.

5.3.2 Solid characterization

BET specific surface areas of reacted samples increased by factors of 2.6 and 3.5 in the $[Si]_{in}$ 1.5 mM and $[Si]_{in}$ 0.15 mM experiments, respectively, with respect to the unreacted sample (Table 5.1).

Table 5.1.

BET specific surface areas of reacted samples and unreacted MgO powder.

Sample	$[Si]_{in}$ 1.5 mM	$[Si]_{in}$ 0.15 mM	Unreacted MgO
Surface area (m^2/g)	0.4044 ± 0.0410	0.5361 ± 0.0540	0.1542 ± 0.0150

In the XRD patterns of powder samples reacted with the Si solutions, peaks for MgO (periclase) were predominant, and low-intensity peaks for $Mg(OH)_2$ (brucite) were also detected (Fig. 5.5). In addition, low-intensity peaks were detected at 38.6° and 55.7° 2θ (Fig. 5.5b) in the reacted and unreacted samples, respectively, indicating possible impurities in the starting material. A broad hump at ~24° 2θ was due to the background of the sample holder. M-S-H peaks at 19.7°, 26.7°, 35.0°, and 59.9° 2θ (Nied et al., 2016)are not clearly evident in the profiles.

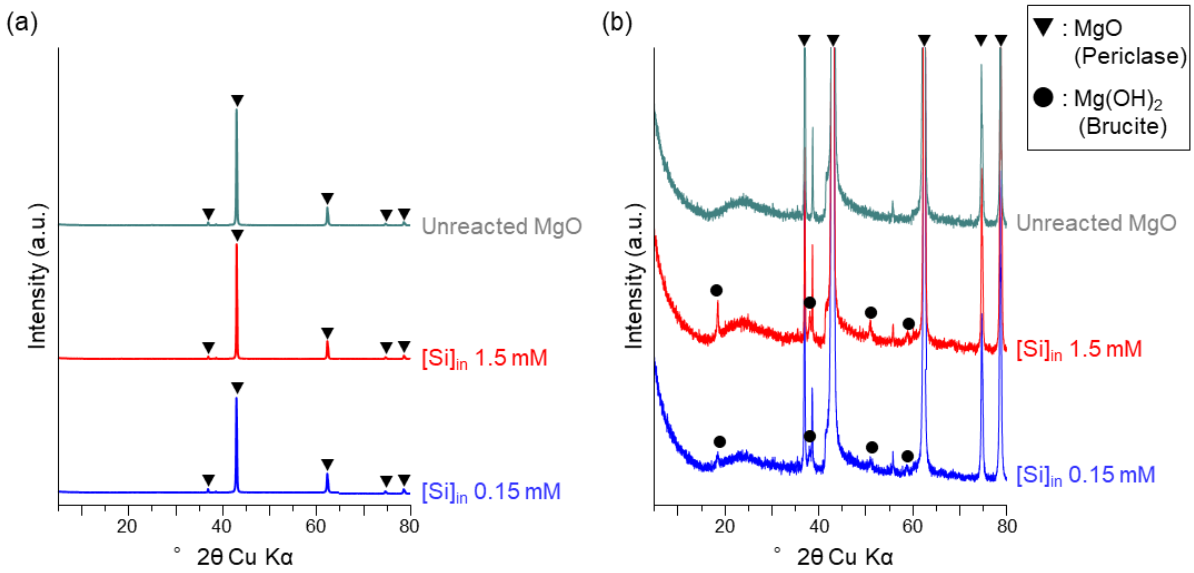

Fig. 5.5. XRD patterns of solid samples (a) and a magnified view showing low intensity peaks (b).

Spectroscopic analyses revealed the presence of silicate phases in the reacted samples. IR bands at ~440 cm^{-1} (Mg–O stretching vibration; Selvam et al., 2011; Raveesha et al., 2019) and at 3698 cm^{-1} (O–H stretching vibration of brucite; Farmer, 1974) were evident in the FTIR spectra of reacted samples (Fig. 5.6). The FTIR spectrum of the sample from the $[Si]_{in}$ 1.5 mM experiment also displayed a broad band at ~1000 cm^{-1}, consistent with the Si–O stretching vibration of silicate phases (Farmer, 1974). This IR band was not clearly evident in the spectrum of the sample from the $[Si]_{in}$ 0.15 mM experiment.

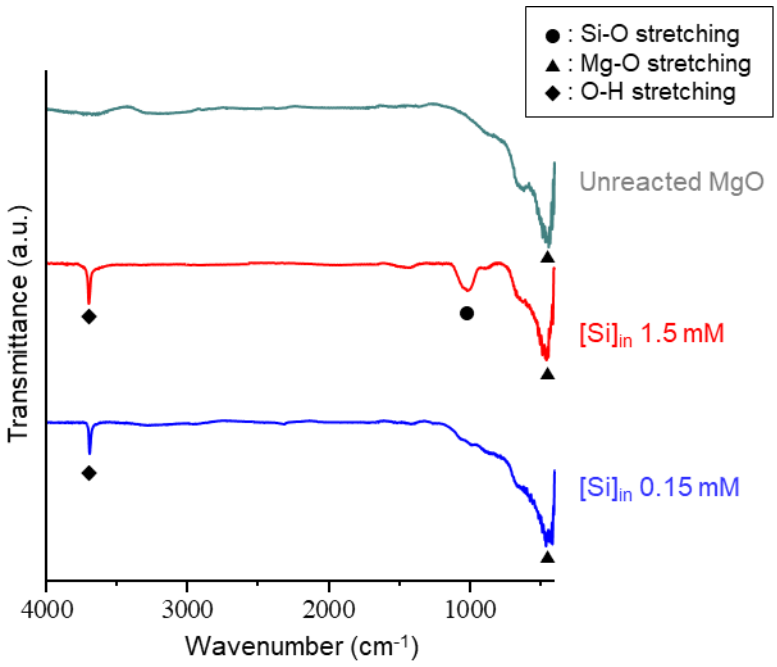

Fig. 5.6. FTIR spectra of solid samples.

The ^{29}Si NMR spectra also revealed the presence of silicate phases. The ^{1}H–^{29}Si CP MAS NMR spectra of reacted powder samples in both Si-solution experiments displayed resonances at chemical shifts of −79.0, −85.4, and −92.1 ppm (Fig. 5.7), corresponding to Q^1, Q^2, and Q^3 silicon sites, respectively, consistent with the results for synthetic M-S-H samples in previous studies (Nied et al., 2016; Tonelli et al., 2016; Zhang et al., 2018; Bernard et al., 2019a). Weak signals for Q^1, Q^2 and Q^3 sites were recognized in the ^{29}Si DD MAS NMR spectrum for the solid sample in the $[Si]_{in}$ 1.5 mM experiment, but no such signal was detected in the $[Si]_{in}$ 0.15 mM experiment (Fig. 5.7).

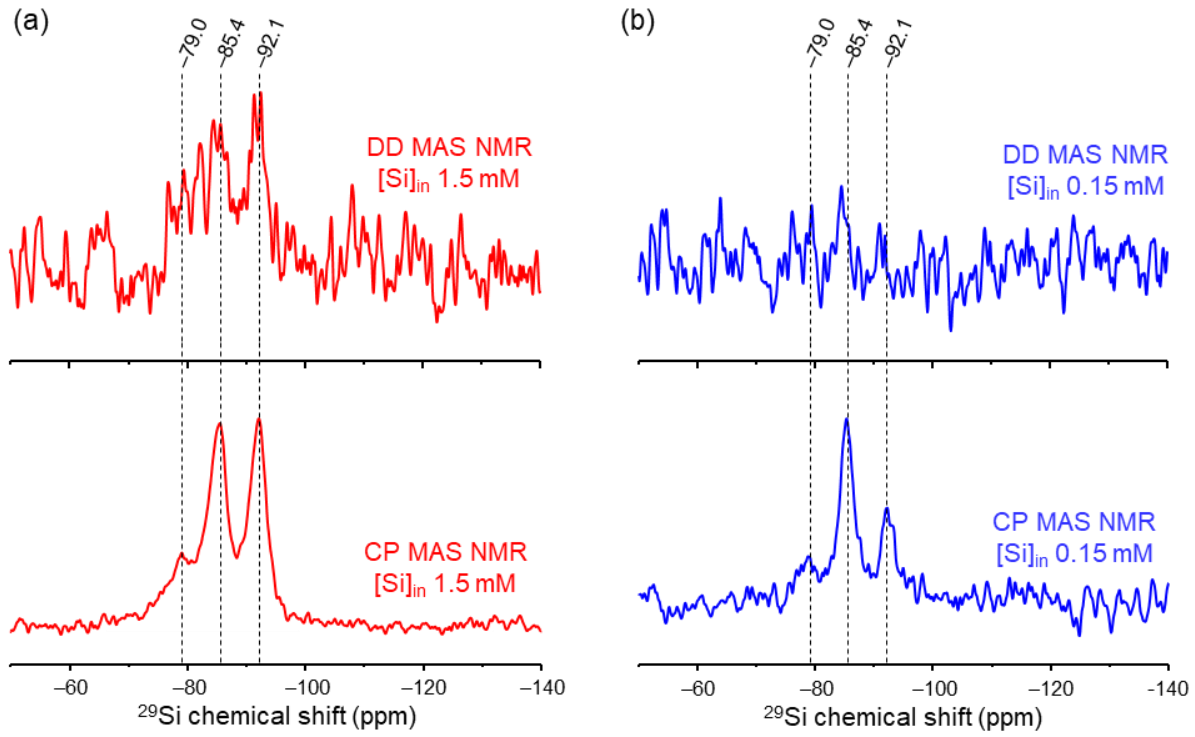

Fig. 5.7. ^{29}Si DD MAS NMR and ^{1}H–^{29}Si CP MAS NMR spectra of solids retrieved from the $[Si]_{in}$ 1.5 mM (a) and $[Si]_{in}$ 0.15 mM (b) experiments.

Cross-section SEM images of particles embedded in resin after the experiments indicate angular shapes and sizes of ~100 µm, similar to those of unreacted particles (Figs Fig. 5.1 and Fig. 5.8). Elemental mapping indicates the presence of Si and Mg in the reacted particles in both Si-solution experiments (Fig. 5.8c–j). Si was uniformly distributed on the surface edges of MgO particles in the $[Si]_{in}$ 1.5 mM experiment (Fig. 5.8d) and intermittently distributed in the $[Si]_{in}$ 0.15 mM experiment (Fig. 5.8h).

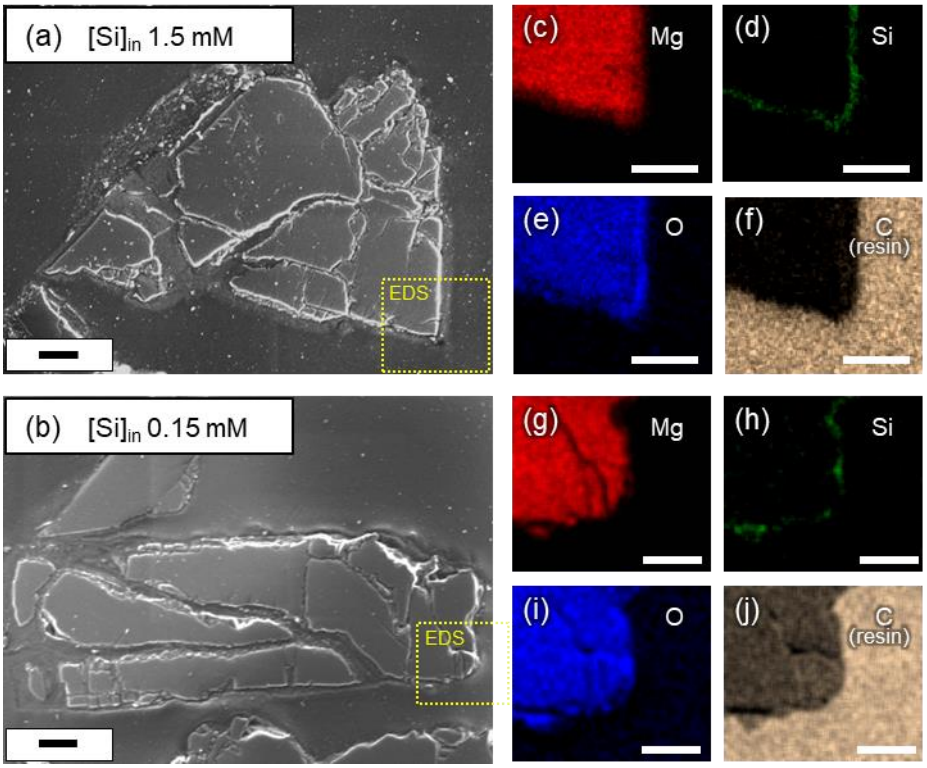

Fig. 5.8. SEM/EDS analysis of particle cross-sections. (a, b) Secondary-electron images of representative particles from the $[Si]_{in}$ 1.5 mM and 0.15 mM experiments, respectively; (c–f) Mg, Si, O, and C distributions in a selected region of (a); (g–j) Mg, Si, O, and C distributions in a selected region of (b), respectively. Scale bars are 10 µm.

TEM analysis of the sample from the $[Si]_{in}$ 1.5 mM experiment displayed an aggregate of nanoparticles (Fig. 5.9a,b), with the electron diffraction pattern of the aggregate exhibiting four diffuse rings (Fig. 5.9c). This indicates that the particles comprise poly- and poorly crystalline materials. The *d* values were 4.5, 3.4, 2.7, and 1.5 Å, consistent with those of synthetic M-S-H samples (Nied et al., 2016). STEM/EDS elemental analysis indicated that the observed aggregates contained Mg, Si and O distributed homogeneously over the mapped surfaces (Fig. 5.9d–f). An Mg/Si atomic ratio of 1.00 was obtained by applying the Cliff–Lorimer quantification to the EDS spectrum of the scanned area in the $[Si]_{in}$ 1.5 mM experiment (Fig. 5.9g). Based on the analytical uncertainty (standard deviation × 3), the Mg/Si ratio was 1.00 ± 0.09.

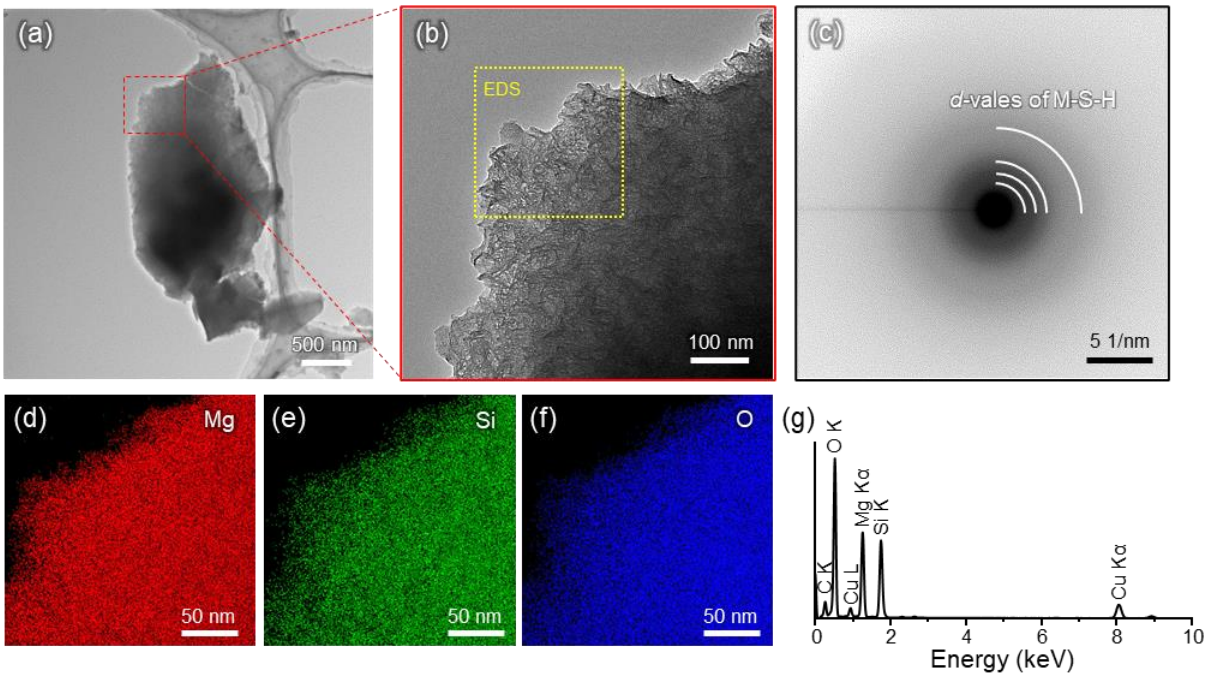

Fig. 5.9. TEM analysis of a solid sample from the $[Si]_{in}$ 1.5 mM experiment. (a) TEM image of representative particles; (b) high-magnification image of the area selected in (a); (c) electron diffraction pattern; (d–f) Mg, Si, and O distributions in the area selected in (b); (g) EDS spectrum of the area selected in (b).

An aggregate of M-S-H nanoparticles was also observed in the sample from the $[Si]_{in}$ 0.15 mM experiment (Fig. 5.10). These particles displayed a veil-like morphology with curled edges (Fig. 5.10a, b). The four diffused rings (d = 4.5, 3.4, 2.7, and 1.5 Å) were also evident in the electron diffraction pattern (Fig. 5.10c). Mg, Si, and O were distributed homogeneously over the aggregate (Fig. 5.10d–f), and elemental quantification of the EDS spectrum (Fig. 5.10g) yielded an Mg/Si ratio of 1.59 ± 0.15.

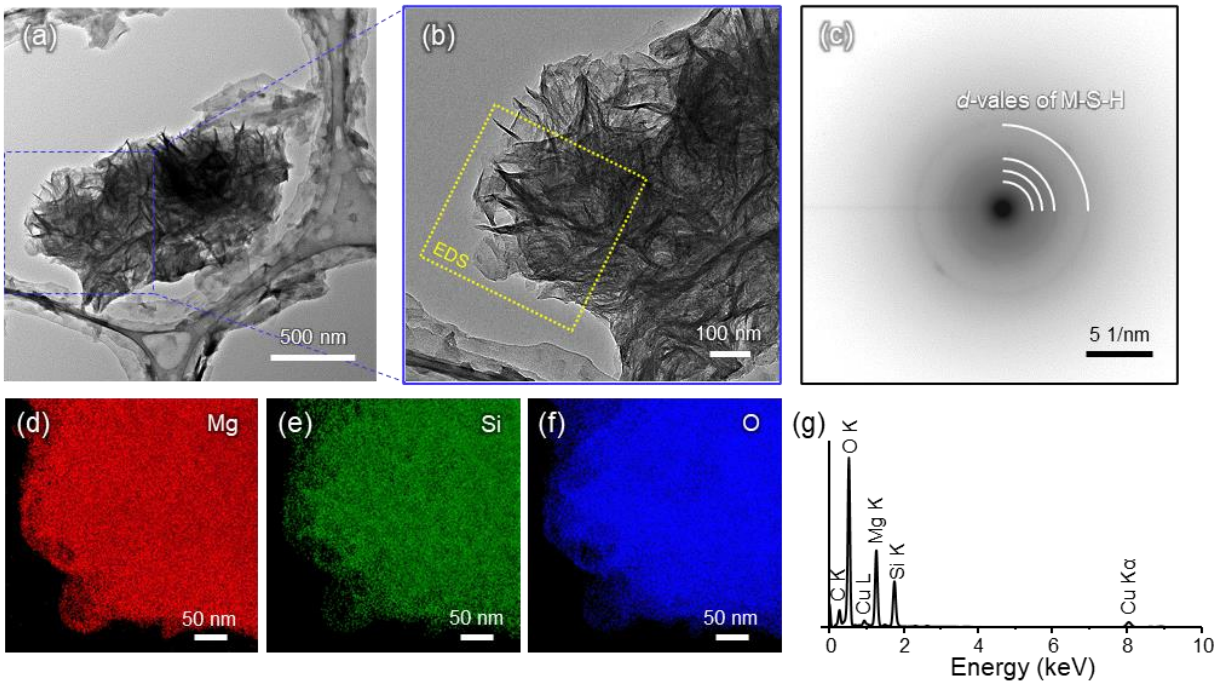

Fig. 5.10. TEM analysis of solid sample from the $[Si]_{in}$ 0.15 mM experiment. (a) TEM image of representative particles; (b) high-magnification image of the area selected in (a); (c) electron diffraction pattern; (d–f) Mg, Si, and O distributions in the area selected in (b); (g) EDS spectrum of the area selected in (b).

5.4 Discussion

5.4.1 M-S-H precipitation

The lack of XRD peaks associated with M-S-H in retrieved samples (Fig. 5.5) is likely due to the small amounts precipitated and their nano-crystallinity. However, electron diffraction patterns did indicate the presence of M-S-H (Figs Fig. 5.9c and Fig. 5.10c), yielding *d* values consistent with those of synthetic M-S-H (Nied et al., 2016).

The different Mg/Si ratios obtained in STEM/EDS analyses (1.00 ± 0.09 in the $[Si]_{in}$ 1.5 mM experiment and 1.59 ± 0.15 in the $[Si]_{in}$ 0.15 mM experiment; Figs Fig. 5.9g and Fig. 5.10g) suggest that the chemical composition of M-S-H products varies with the Si concentration of the injected solution. Nied et al. (2016) reported that synthesized M-S-H phases have Mg/Si ratios between the values of two endmembers with Mg/Si ratios of 0.75 and 1.5. These endmembers are defined as $M_{1.5}S_2H_{2.5}$

($(MgO)_{1.5}(SiO_2)_2(H_2O)_{2.5}$) and $M_{1.5}SH_{2.5}$ ($(MgO)_{1.5}(SiO_2)(H_2O)_{2.5}$) in the Cemdata18 thermodynamic database (Lothenbach et al., 2019). Mg/Si ratios of M-S-H precipitates from the flow-through experiments were within the range of 0.75–1.5, within uncertainty. Furthermore, elemental SEM/EDS mapping indicates precipitation of M-S-H on MgO particles (Fig. 5.8), with the M-S-H being distributed uniformly in the $[Si]_{in}$ 1.5 mM experiment (Fig. 5.8d) and distributed intermittently in the $[Si]_{in}$ 0.15 mM experiment (Fig. 5.8h), indicating that the amount of M-S-H formed in the $[Si]_{in}$ 1.5 mM experiment is greater.

The results of the spectroscopic analyses also support the formation of M-S-H. The sample retrieved from the $[Si]_{in}$ 1.5 mM experiment displayed Si–O bond peaks in the FTIR spectrum (Fig. 5.6), which is a characteristic of synthetic M-S-H samples (Tosca and Masterson, 2014; Nied et al., 2016; Tonelli et al., 2016; Bernard et al., 2017; Zhang et al., 2018). The ^{29}Si NMR analyses identified Q^1, Q^2, and Q^3 signals of silica species in both CP MAS NMR and DD MAS NMR spectra (Fig. 5.7a). For the crystal structure of M-S-H, Roosz et al. (2015) interpreted Q^3 species as representing silicate sheet structures, and Q^1 and Q^2 species as edge sites of silicate sheets or vacant sites in the sheets. The sample from the $[Si]_{in}$ 0.15 mM experiment also displayed Q^1, Q^2, and Q^3 species in CP MAS NMR spectra (Fig. 5.7b) but showed no Si resonances in DD MAS NMR spectra or Si–O bands in FTIR spectra (Fig. 5.6). This is likely due to the amount of M-S-H in the $[Si]_{in}$ 0.15 mM experiment being lower than in the 1.5 mM experiment. However, CP MAS NMR spectra, which enhance signal intensity when protons are in the vicinity of silica species, exhibited Si resonances for solids retrieved from the $[Si]_{in}$ 0.15 mM experiment.

In the CP MAS NMR spectra of both Si-solution experiments, the chemical shift of Q^3 species was −92.1 ppm, whereas M-S-H samples synthesized in batch experiments (Nied et al., 2016; Tonelli et al., 2016; Zhang et al., 2018; Bernard et al., 2019a) exhibited a Q^3 signal that could be deconvolved into several Q^3 peaks at about −95 and/or −97 ppm, and at –92 ppm (Table 5.2). Nied et al. (2016) and Bernard et al. (2019a) interpreted the chemical shifts at −95 and −97 ppm as being related to those of serpentine (Mägi et al., 1984; MacKenzie and Meinhold, 1994b) and talc (Mägi et al., 1984; MacKenzie

and Meinhold, 1994a; Dumas et al., 2013), respectively. Zhang et al. (2018) recognized a Q^3 species at about −92 ppm in a seven-day aged sample (i.e., in the initial stage of M-S-H synthesis) and two Q^3 species at −92 and −97 ppm in a 28-day aged M-S-H sample. The author therefore suggests that the M-S-H here, with Q^3 at about −92 ppm, is an immature phase in the process of crystal growth, in which serpentine (Q^3 = −95 ppm) and/or talc (−97 ppm) may form during a longer experiment. In batch experiments (Nied et al., 2016; Tonelli et al., 2016; Zhang et al., 2018; Bernard et al., 2019a), crystal growth was observed because a large amount of silica reacted from the beginning, whereas in the flow-through experiments silica was supplied gradually.

Table 5.2.

^{29}Si NMR chemical shifts for M-S-H samples formed in this study and synthesized in previous studies, and for Mg phyllosilicate minerals (serpentine and talc).

Sample	Reference	Chemical shift (ppm)		
		Q^3	Q^2	Q^1
Samples formed in the flow-through experiments	This study	–92.1	–85.4	–79.0
M-S-H samples synthesized in batch experiments	Nied et al. (2016)	–92.4, –94.6, –96.7	–85.4	–78.3
	Tonelli et al. (2016)	–92.9, –95.2	–86.3	–79.6, –82.1
	Zhang et al. (2018)	–92.6, –97.2	–85.7	–80.5
	Bernard et al. (2019)	–92.7, –94.7, –96.7	–85.5	–78.3
Serpentine (natural)	Mägi et al. (1984)	–94.0	—	—
	MacKenzie and Meinhold (1994b)	–93	—	—
Talc (natural)	Mägi et al. (1984)	–98.1	—	—
	MacKenzie and Meinhold (1994a)	–97.7	—	—
Talc (synthetic)	Dumas et al. (2013)	–97, –95	—	—

5.4.2 M-S-H precipitation and Mg hydroxide dissolution

The chemical compositions of the steady-state solutions were plotted in phase diagrams (Fig. 5.11) using the Geochemist's Workbench software (GWB v. 12) with the thermo.tdat database (Lawrence Livermore National Laboratory, LLNL). Thermodynamic data for the M-S-H endmembers ($M_{1.5}S_2H_{2.5}$ and $M_{1.5}SH_{2.5}$; Lothenbach et al., 2019) were added to the database.

Precipitation of M-S-H is expected from thermochemical calculations (Fig. 5.11a). In the Mg–Si–H_2O system, the output-solution data point of the $[Si]_{in}$ 0.15 mM experiment plots in the stability field for $M_{1.5}SH_{2.5}$ (Mg/Si ratio = 1.5), corresponding to the M-S-H phase with Mg/Si = 1.59 ± 0.15 (STEM/EDS result; Fig. 5.10g). The output-solution data point for the $[Si]_{in}$ 1.5 mM experiment plots on the boundary between the stability fields of $M_{1.5}S_2H_{2.5}$ and $M_{1.5}SH_{2.5}$. Considering an Mg/Si ratio of 1.00 ± 0.09 (STEM/EDS result; Fig. 5.9g), this suggests the possible formation of an intermediate phase between $M_{1.5}S_2H_{2.5}$ and $M_{1.5}SH_{2.5}$; i.e., $M_{1.5}S_{1.5}H_{2.5}$. Saturation indices (SI = log $IAP/K_{eq\text{-}50°C}$, where IAP = ion activity product and K_{eq} = equilibrium constant) for the M-S-H phases in the $[Si]_{in}$ 1.5 mM experiment ($SI_{M1.5SH2.5}$ = 1.7 and $SI_{M1.5S2H2.5}$ = 3.3) are higher than those in the $[Si]_{in}$ 0.15 mM experiment ($SI_{M1.5SH2.5}$ = 0.87 and $SI_{M1.5S2H2.5}$ = 1.5). This SI difference could increase the rate of M-S-H precipitation in the $[Si]_{in}$ 1.5 mM experiment relative to that in the $[Si]_{in}$ 0.15 mM experiment.

The steady-state solutions of the $[Si]_{in}$ 1.5 mM and 0.15 mM experiments plot in the stability fields for Mg silicate clay minerals (sepiolite, talc, and serpentine (chrysotile)). Although these minerals were not identified as reaction products in the flow-through experiments, transformation of M-S-H to Mg phyllosilicate phases is possible over long periods, with M-S-H acting as a precursor metastable phase.

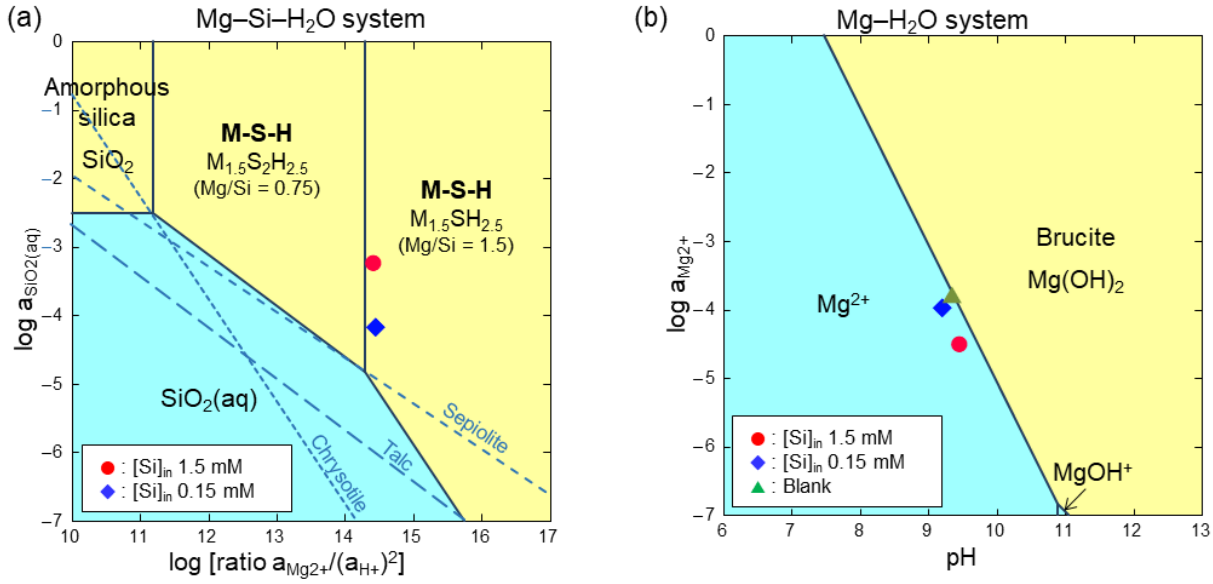

Fig. 5.11. Output solution data at steady state in phase diagrams for (a) silicate phases including M-S-H and (b) Mg hydroxide phases at 50°C. Thermodynamic data for M-S-H (Lothenbach et al., 2019) were added to the LLNL database.

Dissolution of the primary material is represented by the phase diagram for the Mg–H_2O system (Fig. 5.11). The overall dissolution reaction of MgO at pH > 7 is controlled by the formation of an $Mg(OH)_2$ layer (Figs Fig. 5.5 and Fig. 5.6) on the MgO surface (Vermilyea, 1969; Fruhwirth et al., 1985), and the rate is controlled by dissolution of $Mg(OH)_2$, releasing Mg into solution:

$$MgO_{(solid)} + H_2O \rightarrow MgOH_{(surface)}^{+} + OH^{-} \rightarrow MgOH^{+}{\cdot}OH_{(surface)}^{-} \rightarrow Mg^{2+} + 2OH^{-} \quad (1)$$

Steady-state data points for the Si-solution experiments plot in the stability fields of aqueous species and are undersaturated with respect to $Mg(OH)_2$ (brucite), whereas a data point for the blank experiment plots near the boundary between the stability fields of $Mg(OH)_2$ and aqueous Mg^{2+}. The saturation indices for $Mg(OH)_2$, $SI_{Mg(OH)2}$, are −0.08 for the blank experiment and −0.50 and −0.54 for the $[Si]_{in}$ 0.15 mM and 1.5 mM experiments, respectively. Addition of Si to the input solutions thus results in low *SI* values with respect to $Mg(OH)_2$, which could lead to dissolution of $Mg(OH)_2$. Although the *SI* values are negative, $Mg(OH)_2$ forms (Figs Fig. 5.5 and Fig. 5.6) due to MgO hydroxylation and dissolves during

the experiments. Hydroxylation of the MgO surface does not require $SI > 0$ and may occur even under acidic conditions (Wogelius et al., 1995).

To summarize, experiments with higher initial Si concentrations have higher *SI* values with respect to M-S-H, and lower *SI* values with respect to $Mg(OH)_2$. This suggests that the more Si in the system, the greater the dissolution of $Mg(OH)_2$ and precipitation of M-S-H. It follows that, in Mg–Si–H_2O systems, when aqueous Si reacts with dissolved Mg to form M-S-H, $Mg(OH)_2$ dissolution is promoted.

5.4.3 Rates of Mg hydroxide dissolution and M-S-H precipitation

The steady-state Mg concentration in the blank experiment was used to calculate the dissolution rate of $Mg(OH)_2$ using the expression:

$$R_{diss,Mg(OH)2} = q \times [Mg]_{st\text{-}st} \quad (2)$$

where q (L s^{-1}) is the fluid flow rate and $[Mg]_{st\text{-}st}$ (mol L^{-1}, M) is the steady-state Mg concentration in the output solution (0.17 mM; Fig. 5.3a). The resulting steady-state dissolution rate was $(1.53 \pm 0.09) \cdot 10^{-10}$ mol s^{-1}, which can be normalized to the total surface area of the reacted powder as $R_{diss,Mg(OH)2}/A_{final}$, where A_{final} = BET specific surface area (Table S1) × $mass_{final}$, which is the calculated final mass of the reacted MgO:

$$mass_{final} = 1.00 - \Sigma\,(q \times [Mg]_{out} \times \Delta t \times 40.3) \quad (3)$$

where $[Mg]_{out}$ is the output Mg concentration, Δt is the time interval between two consecutive output solutions, and 40.3 is the molecular weight of MgO. Hence, $mass_{final}$ = 0.922 g (i.e., dissolved mass = 7.8% of initial mass) and the normalized $Mg(OH)_2$ dissolution rate was $(1.08 \pm 0.12) \cdot 10^{-9}$ mol m^{-2} s^{-1}, similar to that obtained by Pokrovsky and Schott (2004) at pH 10, close-to-equilibrium conditions ($SI_{Mg(OH)2} \approx -0.1$) and 25°C.

In the Si-solution experiments, $[Mg]_{st\text{-}st}$ was lower than that in the blank experiment (Fig. 5.3a), with Mg being consumed by M-S-H precipitation. Using the Si concentrations in the Si-solution experiments (Fig. 5.3b), the precipitation rate, $R_{ppt.M\text{-}S\text{-}H}$, of the M-S-H phase was calculated as

$$\nu_{Si} \times R_{ppt,M\text{-}S\text{-}H} = q \times ([Si]_{in} - [Si]_{st\text{-}st}) \quad (4)$$

where ν_{Si} is the stoichiometric coefficient of Si in the precipitated M-S-H and $[Si]_{st\text{-}st}$ is the steady-state Si concentration. Therefore, $R_{ppt,M1.5S1.5H2.5} = 4.94 \cdot 10^{-10}$ mol s^{-1} for $M_{1.5}S_{1.5}H_{2.5}$ ($[Si]_{in}$ = 1.5 mM and $[Si]_{st\text{-}st}$ = 1.11 mM) and $R_{ppt,M1.5SH2.5} = 3.61 \cdot 10^{-11}$ mol s^{-1} for $M_{1.5}SH_{2.5}$ ($[Si]_{in}$ = 0.15 mM and $[Si]_{st\text{-}st}$ = 0.10 mM). These rates indicate that the precipitation of M-S-H is more rapid in the experiment with the higher Si concentration.

Using the steady-state aqueous concentrations, a stoichiometric ratio for the solid was calculated as

$$(Mg/Si)_{aq,M\text{-}S\text{-}H} = (R_{diss,Mg(OH)2}/q - [Mg]_{st\text{-}st})/([Si]_{in} - [Si]_{st\text{-}st}) \quad (5)$$

and compared with the solid $(Mg/Si)_{solid,M\text{-}S\text{-}H}$ ratio obtained from the STEM–EDS analysis. In the $[Si]_{in}$ 1.5 mM experiment, $(Mg/Si)_{aq,M\text{-}S\text{-}H}$ = 0.21 and $(Mg/Si)_{solid,M\text{-}S\text{-}H}$ = 1.00 ± 0.09; and in the $[Si]_{in}$ 0.15 mM experiment, $(Mg/Si)_{aq,M\text{-}S\text{-}H}$ = 0.43 and $(Mg/Si)_{solid,\ M\text{-}S\text{-}H}$ = 1.59 ± 0.15. The $(Mg/Si)_{aq,M\text{-}S\text{-}H}$ values are thus a factor of 4.8 (for the higher-Si solution) and 3.7 (lower-Si solution) lower than those from the STEM–EDS analysis.

A possible explanation for this discrepancy is that the dissolution rates of $Mg(OH)_2$ in the Si-solution experiments were higher than that in the blank experiment with a consequently higher release of Mg to solution. Pokrovsky and Schott (2004) showed that the brucite dissolution rate is independent of $SI_{Mg(OH)2}$ (i.e., dissolution rate constant) when $SI_{Mg(OH)2} < -1$. At higher $SI_{Mg(OH)2}$ values the rate is affected by the solution saturation state (i.e., close-to-equilibrium conditions) to decrease towards zero at equilibrium. Therefore, since the $SI_{Mg(OH)2}$ values calculated for the high and low Si-solution experiments are lower (−0.54 and −0.50, respectively) than that of the blank experiment ($SI_{Mg(OH)2}$ = −0.08), the dissolution rate of $Mg(OH)_2$ could be faster in the Si-solution experiments than in the blank experiment to obtain stoichiometric values ($(Mg/Si)_{aq,M\text{-}S\text{-}H} = (Mg/Si)_{solid,M\text{-}S\text{-}H}$). Using Eq. (5), these rates would be $5.45 \cdot 10^{-10}$

mol s^{-1} and $2.16 \cdot 10^{-10}$ mol s^{-1}, i.e., a factor of 3.6 and 1.4 higher than that of the blank experiment ($1.53 \cdot 10^{-10}$ mol s^{-1}). Bernard et al. (2017) proposed a kinetic hindrance of brucite dissolution at high Si concentrations (>1 mM) during M-S-H formation that may account for a lower $Mg(OH)_2$ dissolution rate. A Si effect on the $Mg(OH)_2$ dissolution is therefore probable. Nevertheless, as the current data set cannot be used to differentiate between these two possible reaction mechanisms, a simpler dissolution kinetic effect (Pokrovsky and Schott, 2004) is here invoked.

Differences between open-flow systems (flow-through experiments) and closed systems (batch experiments) can also affect the kinetics of MgO dissolution and M-S-H formation. In batch experiments, Li et al. (2014) and Zhang et al. (2018) suggested that formation of $Mg(OH)_2$ on the MgO surface limited M-S-H formation as pH varied. Initial hydration of MgO increased pH to values of > 10.5, and subsequent dissolution of silica and formation of M-S-H lowered the pH to ~9.5. However, in the flow-through experiments here, the pH was maintained at ~10 (pH of the input solution), and the input Si concentration was kept constant. Under these conditions, $Mg(OH)_2$ (brucite) dissolved at pH < 10.5, and M-S-H was precipitated owing to the release of Si and Mg. Therefore, $Mg(OH)_2$ did not retard M-S-H formation.

5.5 Summary and conclusions

This chapter showed that M-S-H forms at pH 10 and 50°C in open-flow (flow-through) systems. The chemical composition of the M-S-H formed depends on the Si concentration in the input solution, with the Mg/Si ratio decreasing with increasing Si concentration (Mg/Si ratio = 1.59 ± 0.15 with [Si] = 0.15 mM, and 1.00 ± 0.09 at 1.5 mM). Aqueous Si plays a crucial role in the dissolution kinetics of primary Mg-bearing minerals such as $Mg(OH)_2$. Dissolved Mg and Si are consumed during M-S-H precipitation, promoting the dissolution of Mg-bearing minerals. With increasing Si concentration, the solution becomes more supersaturated with respect to M-S-H and more undersaturated with respect to

$Mg(OH)_2$, so the higher the amount of Si in the system, the greater the dissolution of $Mg(OH)_2$ and precipitation of M-S-H.

Chapter 6: M-S-H formation on the Earth surface

6.1 Introduction

While the experimental study of M-S-H has been performed, there are few studies related to the observation of natural M-S-H samples even when M-S-H is essentially thought to form in natural surface/subsurface environments. Although de Ruiter and Austrheim (2018) and de Ruiter et al. (2021) reported the formation of M-S-H cement in an ultramafic complex in the presence of quartz-rich felsic glacial deposits, they had no information on observations and analysis of the fluid that leads to the M-S-H formation. There are still insufficient mineralogical and geochemical studies on the M-S-H formation in natural settings. Therefore, this chapter investigated present-day natural precipitation of M-S-H to confirm and characterize the M-S-H precipitated in natural alkaline surface environments and assess the formation conditions and processes of M-S-H (related to [i] and [iii] in Section 1.4).

6.2 Geologic setting

In order to observe present-day precipitation of M-S-H under natural alkaline conditions, the author focused on a geological setting with ultramafic rock and water.

Ultramafic rock is found in various regions around the Kamuikotan tectonic belt in Hokkaido, which is one of the Japanese islands (Fig. 6.1a). The Kamuikotan tectonic belt is characterized by zones of ultramafic rock running north-south intermittently and identified as a typical high-pressure/low-temperature metamorphic belt from the late Mesozoic age (Asahina and Komatsu, 1979). Ueda (2005) described subduction zone tectonics to demonstrate the formation of the Kamuikotan tectonic belt. Due to tectonic interaction between the Eurasian plate and an oceanic plate in the Cretaceous period (before formation of the current Japanese islands including Hokkaido), ophiolite (lower Sorachi ophiolite) was being uplifted, while metamorphosing with Cretaceous accretionary complexes. The ophiolite is largely composed of mafic rock (MORB-like tholeiite) and ultramafic rock (serpentinized peridotite), so that ultramafic rock is observed in the Kamuikotan tectonic belt with crystalline schists and Cretaceous

sedimentary rock. In the ultramafic rock, there are few fresh peridotites unaffected by serpentinization (Asahina and Komatsu, 1979). Serpentinite mélange and turbidite are commonly observed in the Kamuikotan tectonic belt as a result of the subduction zone tectonics (Katoh and Nakagwa, 1986; Ueda, 2005).

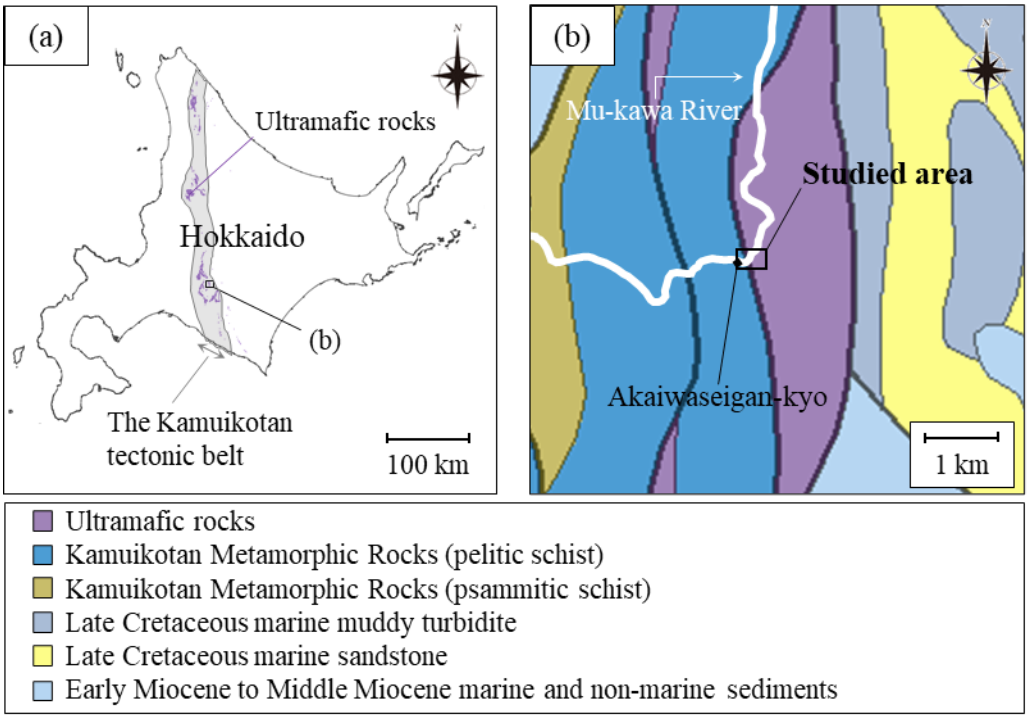

Fig. 6.1. Geological setting around the Kamuikotan tectonic belt in Hokkaido, Japan (after Geological survey of Japan, 2022). (a) Distribution of ultramafic rocks in the Kamuikotan tectonic belt; (b) Geological map around studied area.

The samples analyzed in this study were collected from one of the ultramafic regions within the Kamuikotan tectonic belt (Fig. 6.1b). The studied area is located near Akaiwaseigan-kyo, a gorge consisting of red chert and metamorphosed tuff. Ultramafic rock here is mainly serpentinite that was originally harzburgite and dunite with a small amount of lherzolite (Katoh and Nakagawa, 1986). The fresh serpentinite rock and its crushed sediments are observed on the surface in the studied area due to landslides (Fig. 6.2). Samples were collected from two specific sites, S1 and S2, where seepage was flowing from the surface of the ultramafic rock mass. Grayish and whitish sediments were observed on

the surface around the seepages in S1 and S2, respectively (Fig. 6.3). We collected surface waters around the sediments, seepage waters, and the surface sediments, which were aggregates of grains bound to each other due to cementation. In addition, a fragment of bedrock was collected to compare the characteristics of the sediments with those of the bedrock in and around this area. Typical serpentine veins were observed in some rocks (Fig. 6.4), and only the minerals composing the serpentine veins were removed and collected for the analyses.

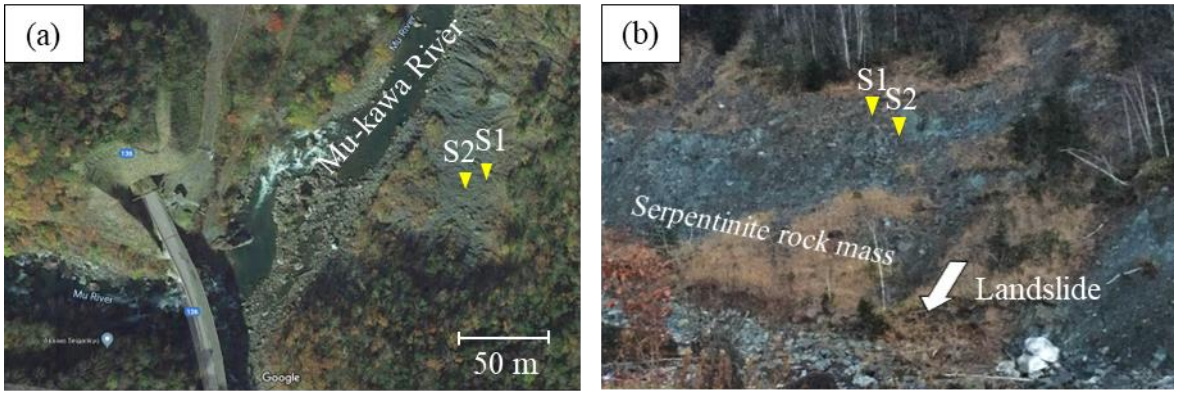

Fig. 6.2. Photographs showing location of sampling sites (S1 and S2). (a) Overhead view of the studied area (after Google); (b) Photograph of an ultramafic rock mass and the sampling sites.

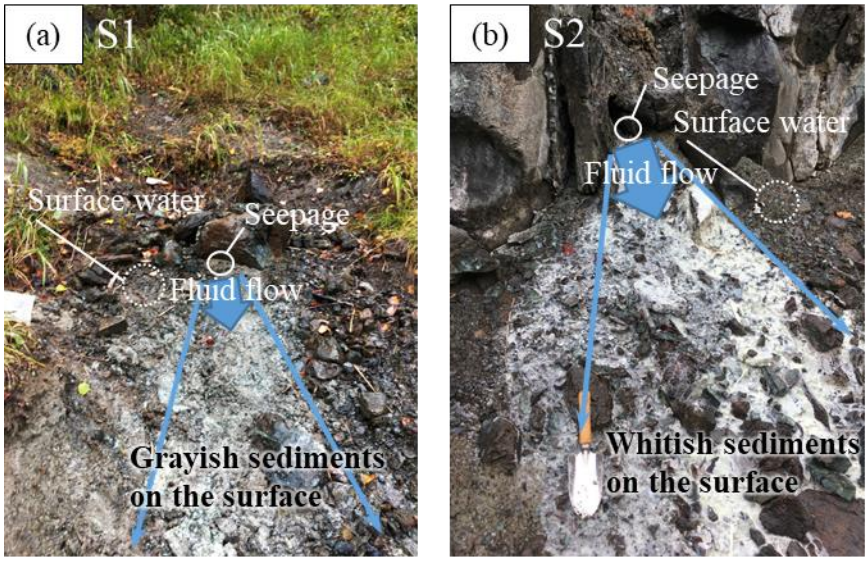

Fig. 6.3. Photographs of the sampling sites: (a) S1and (b) S2.

Fig. 6.4. Photograph of serpentine veins.

6.3 Analytical methods

6.3.1 Solution analyses

The pH and oxidation reduction potential (ORP) of the liquid samples were measured on site by electrodes (pH: 9625-10D; Eh: 9300-10D, Horiba, Ltd.) and meters (pH: LAQUAact D-74; ORP: LAQUAact D-75, Horiba, Ltd.). The ORP values were measured by an Ag/AgCl electrode with 3.33 mM KCl and corrected using the following equation (Matsushita et al., 1974):

$$Eh = ORP_{Ag/AgCl} + 206 - 0.7 \times (T - 25),$$

where Eh is an ORP value measured by a standard hydrogen electrode (mV), $ORP_{Ag/AgCl}$ is an ORP value measured by the Ag/AgCl electrode (mV), and T is the temperature (°C). Alkalinities were measured by titrating HNO_3 (Kanto Chemical Co., Inc.) into 50 mL of liquid samples that had been filtered through 0.45 μm PTFE membrane filters. The Inflection Point Titration method (Rounds, 2012) was applied to obtain the alkalinities and the concentrations of HCO_3^- and CO_3^{2-}.

To analyze major cations and anions other than H^+/OH^- and HCO_3^-/CO_3^{2-}, the collected liquid samples were filtered through 0.2 μm and 0.45 μm PTFE membrane filters, respectively. In addition, and only for analysis of major cations, the filtered solutions were acidified by 1 vol% HNO_3 (Kanto Chemical Co., Inc.). After the liquid samples were brought back to the laboratory, concentrations of the

metal cations and Si were determined by ICP–AES (ICPE-9000, Shimadzu Corp.), and those of the anions were determined by IC (861 Advanced Compact IC, Metrohm AG).

6.3.2 Solid analyses

The sediments and rock samples were air-dried for the solid analyses. Both samples were crushed with an agate mortar for powder XRD analysis to determine bulk mineralogy of the samples. An X-ray diffractometer (RINT-2100, Rigaku Corp.) was operated at 30 kV and 20 mA and equipped with a Cu target. Randomly oriented powder samples were scanned from 2 to 70° 2θ at a scanning speed of 1° min^{-1}.

Polished sections of sediment samples were made by a method patented by Owada et al. (2014) to observe the microstructure of sediments. Conventional methods for making petrographic sections are not suitable for unstable specimens such as clay because petrographic structures of clayey samples are ordinarily broken during polishing of the samples by water or oil, where these liquids protect the samples from the heat generated during the cutting and grinding processes. However, the method developed by Owada et al. (2014) does not require liquid addition and frictional heat is minimized, so that samples are not influenced by the liquids or heating. The collected sediment samples in this study are clayey cemented aggregates, and the Owada et al. (2014) method retains the sedimented form of the sample during the polishing.

The occurrence of precipitates was observed by optical microscopy (BX60, Olympus Corp.) with reflected light. To mineralogically identify particles composing the sediments, micro-Raman spectroscopy (XploRA, Horiba, Ltd.) was applied. Micro-Raman spectroscopy is a powerful tool to identify mineral particles of the micrometer scale, distinguishing polymorphs. The author referred to previous studies by Rinaudo et al. (2003) for identifying the serpentine minerals (chrysotile, lizardite, and antigorite), and Kontoyannis and Vagenas (2000) for identifying Ca carbonate polymorphs (calcite, aragonite, and vaterite). During the analysis, Raman spectra were obtained using a 532-nm laser, at a

2400 grooves per millimeter grating, 100 μm confocal hole diameter, and 100 μm slit size. The spectral acquisition time was 20 s and data for 3 spectra were recorded for each sample. The system was calibrated with a silicon standard.

Some of solid phases in the polished sections were observed in further detail by TEM to discuss the morphology at the nanometer scale, the crystallinity, and chemical composition of the phases. These specimens were picked out by a micromanipulator (Quick Pro, Micro Support Co., Ltd) and a hard tool probe (TP-005, Micro Support Co., Ltd), and placed on copper grids with carbon films (Microgrid type A, Okenshoji Co., Ltd.). They were analyzed transmission electron microscopically (JEM-2010, JEOL Ltd.) at an operating voltage of 200 kV. An EDS detector attached to the TEM was also used to determine the chemical compositions of the minerals. Particles composing the serpentine veins in the rock (Fig. 6.4) were also observed by TEM for comparison with the picked out phases from the sediment sections. Before the TEM observations, powdered samples from serpentine veins were dispersed in ethanol and one drop of the sample suspension was deposited on the grids.

6.4 Results

6.4.1 Water chemistry

Table 6.1 shows the water chemistry of the liquid samples: surface waters from S1 (S1-sf) and S2 (S2-sf), and seepage waters from S1 (S1-sp) and S2 (S2-sp). The pH values of all the water samples were alkaline, and the pH values of seepage water samples (~10.5) were higher than those of the surface water samples (~9.5). The Eh values of all samples were somewhat high (~400 mV), indicating oxidized aquatic environments. The ICP–AES analysis showed that the liquid samples contained detectable concentrations of Na, K, Mg, Ca, and Si. In terms of anions, the IC analysis showed concentrations of Cl^-, SO_4^{2-}, and NO_3^-/NO_2^-, and the alkalinity measurements indicated concentrations of HCO_3^-/CO_3^{2-}. Combining the results of the concentrations of cations and anions, the calculated charge imbalances were within ±14% for all the liquid samples. Stiff diagrams of the water chemistry show that major

chemical compositions of S1-sf, S2-sf, S1-sp and S2-sp were similar, dominated by Mg^{2+} and HCO_3^- /CO_3^{2-} (Fig. 6.5). Particularly the S2-sp contained slightly higher Ca concentration than the other samples.

Table 6.1.

On-site measurements of the surface waters from S1 and S2 (S1-sf and S2-sf) and the seepage waters from S1 and S2 (S1-sp and S2-sp), and their concentrations of major cations and anions.

Sample		S1-sf	S2-sf	S1-sp	S2-sp
pH	-	9.69	9.58	10.34	10.67
Eh	mV	410	397	377	361
Na	mg/L	1.62	1.72	1.88	1.96
K	mg/L	0.244	0.269	0.219	0.279
Mg	mg/L	18.4	15.3	24.4	13.7
Ca	mg/L	1.31	3.44	1.38	10.4
Si	mg/L	0.083	0.008	0.112	0.009
Cl^-	mg/L	5.91	19.3	5.54	17.5
SO_4^{2-}	mg/L	1.48	0.60	4.27	<0.03
NO_3^-	mg/L	1.18	1.08	2.82	2.91
NO_2^-	mg/L	1.10	<0.02	<0.02	<0.02
Alkalinity	mg/L as $CaCO_3$	100.1	69.7	108.1	70.5
HCO_3^-	mg/L	79.2	60.7	54.9	18.0
CO_3^{2-}	mg/L	19.7	10.9	33.9	24.8

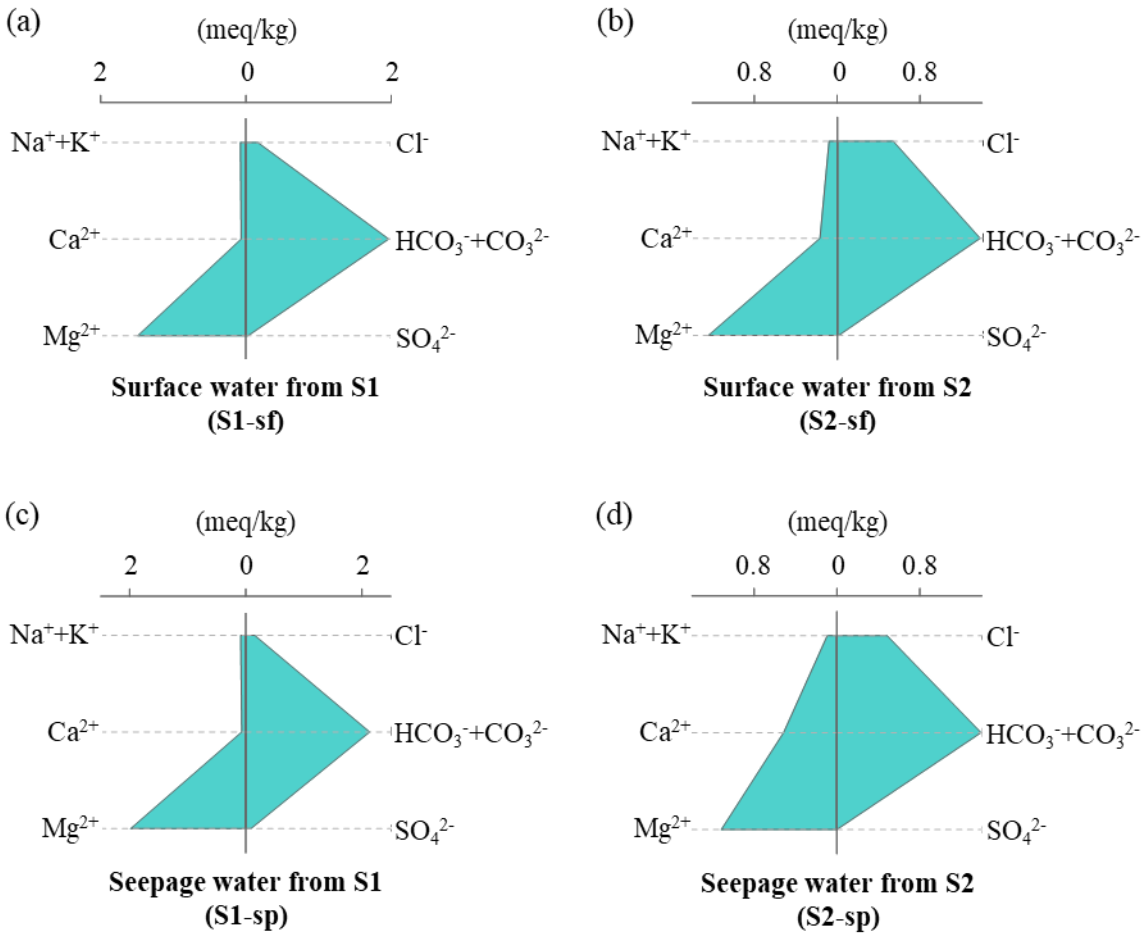

Fig. 6.5. Stiff diagrams showing the water chemistry of (a) surface water from S1, (b) surface water from S2, (c) seepage water from S1, and (d) seepage water from S2, which are obtained from Table 6.1.

6.4.2 Bulk mineralogy

The XRD profiles of all the bedrock samples (whole bedrock and veins in the bedrock; Fig. 6.4) and sediments from S1 and S2 showed that they were dominated by peaks for serpentine (Fig. 6.6). Whereas some peaks for serpentine ($d \approx 7.27$, 4.56, 3.64, and 1.53 Å) were observed in all the samples, other peaks for serpentine were observed at a variety of positions among the samples originating in different species of serpentine (chrysotile, lizardite, and antigorite). The XRD profile of the whole bedrock samples indicated lizardite, and that of the vein samples indicated chrysotile. No peaks for antigorite were identified in either sample. Serpentine species in the sediment samples are impossible to

distinguish only in XRD profiles because the intensities of peaks other than $d \approx 7.27$, 4.56, 3.64, and 1.53 Å are too low to be identified.

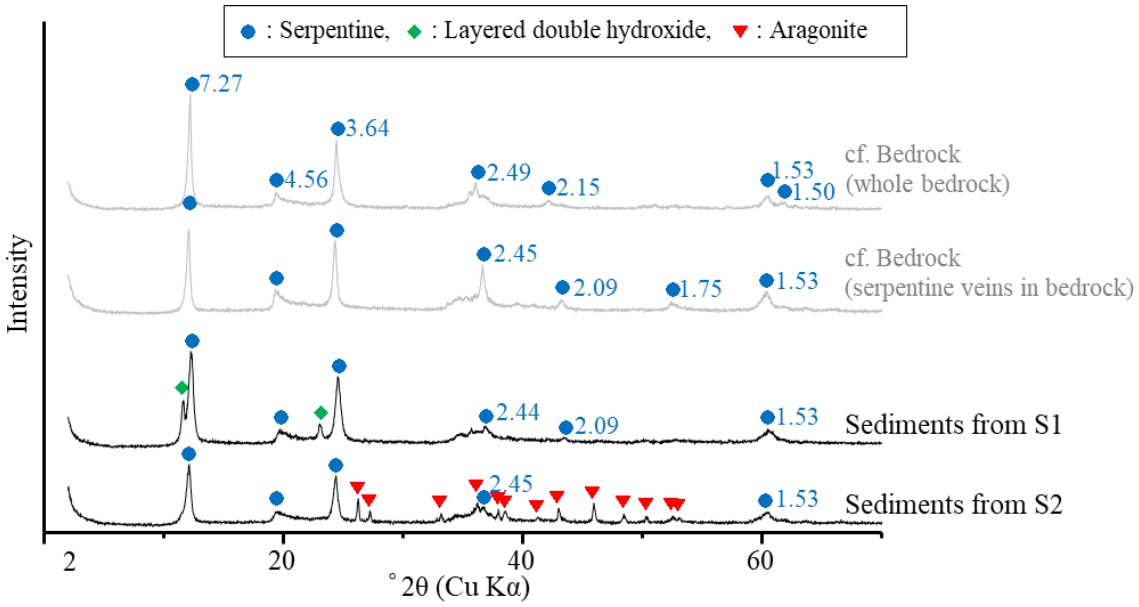

Fig. 6.6. XRD patterns of the sediments and bedrock. Peak positions of serpentine are displayed as *d*-values (Å).

Other than serpentine, there were no peaks for minerals generally composing ultramafic rock (olivine, pyroxene, etc.) or for byproducts arising from the serpentinization process (brucite, magnetite, etc.) in any of the samples, suggesting that the collected bedrock samples are serpentinite mainly composed of just serpentines (chrysotile and lizardite).

Sediment samples from S1 and S2 also showed peaks for hydrotalcite-like layered double hydroxide (LDH) and aragonite, respectively. The presence of M-S-H was not clearly shown in the samples although M-S-H synthesized in previous studies has broad humps around 4.51, 3.34, 2.56, and 1.54 Å in the XRD profiles (Nied et al., 2016).

6.4.3 Microscopic observation and micro-Raman spectroscopy

A polished section of sediment from S1 was observed by optical microscope, and the results showed rounded grains (P1 and P2) and a scale-like grain (P3) (Fig. 6.7a). In addition, a solid phase with ambiguous morphology (P4) was observed around the grains (i.e., P1, P2, and P3). Microscopic observation of the sediment from S2 showed an aggregate (P5) of fine needle-like grains and a rod-like grain (P6) (Fig. 6.7b), also here there was a solid phase of ambiguous morphology (P7) around the grains (i.e., P5 and P6). Here it is noteworthy that P4 and P7 bind the grains in S1 and S2, respectively, and other than in Fig. 7a and Fig. 7b, this kind of solid phase was also commonly observed around grains in the polished sections.

Micro-Raman spectroscopy was used to determine the mineralogy of the particles in the sediments, identifying P1, P2, P4, P6, and P7 as chrysotile, P3 as lizardite, and P5 as aragonite (Fig. 6.7c–e). The chrysotile identified in P1, P2, P4, P6, and P7 showed Raman spectra with similar peaks, excluding the effect of resin. However, given the morphology and texture of the phases, P4 and P7 must be considered to be different from P1, P2, and P6 as they do not have well defined shapes.

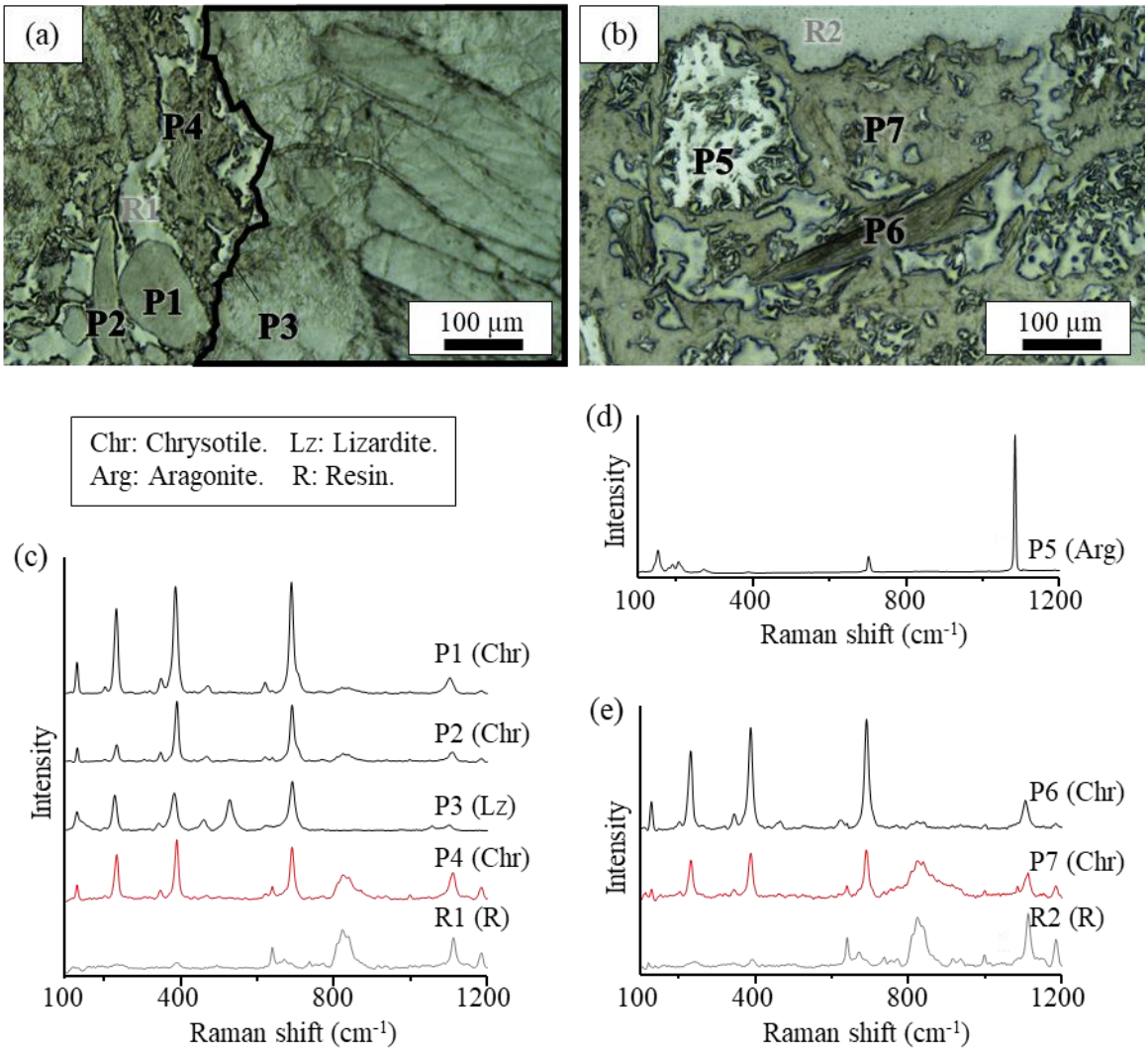

Fig. 6.7. Microanalyses of collected sediments. (a) Optical microscopic image of a section showing a lump of sediments from S1; (b) Optical microscopic image of a section showing a lump of sediments from S2; (c) Raman spectra of P1–P4 and R1 in (a); (d) Raman spectrum of P5 in (b); (e) Raman spectra of P6, P7, and R2 in (b).

6.4.4 Nano-scale observation

The TEM observations of chrysotile crystals from the bedrock samples showed that they are of tubular shape (length > 1 µm, Fig. 6.8a; width ~ 43 nm, Fig. 6.8b,c). The selected area electron diffraction (SAED) pattern of one of the tubular crystals showed typical diffraction spots of chrysotile (Fig. 6.8d). Strictly, the identified chrysotile was determined as clino-chrysotile because 20*l* spots are not diffracted

at even intervals, following TEM studies on serpentine minerals by Zussman et al. (1957) and Yada (1979).

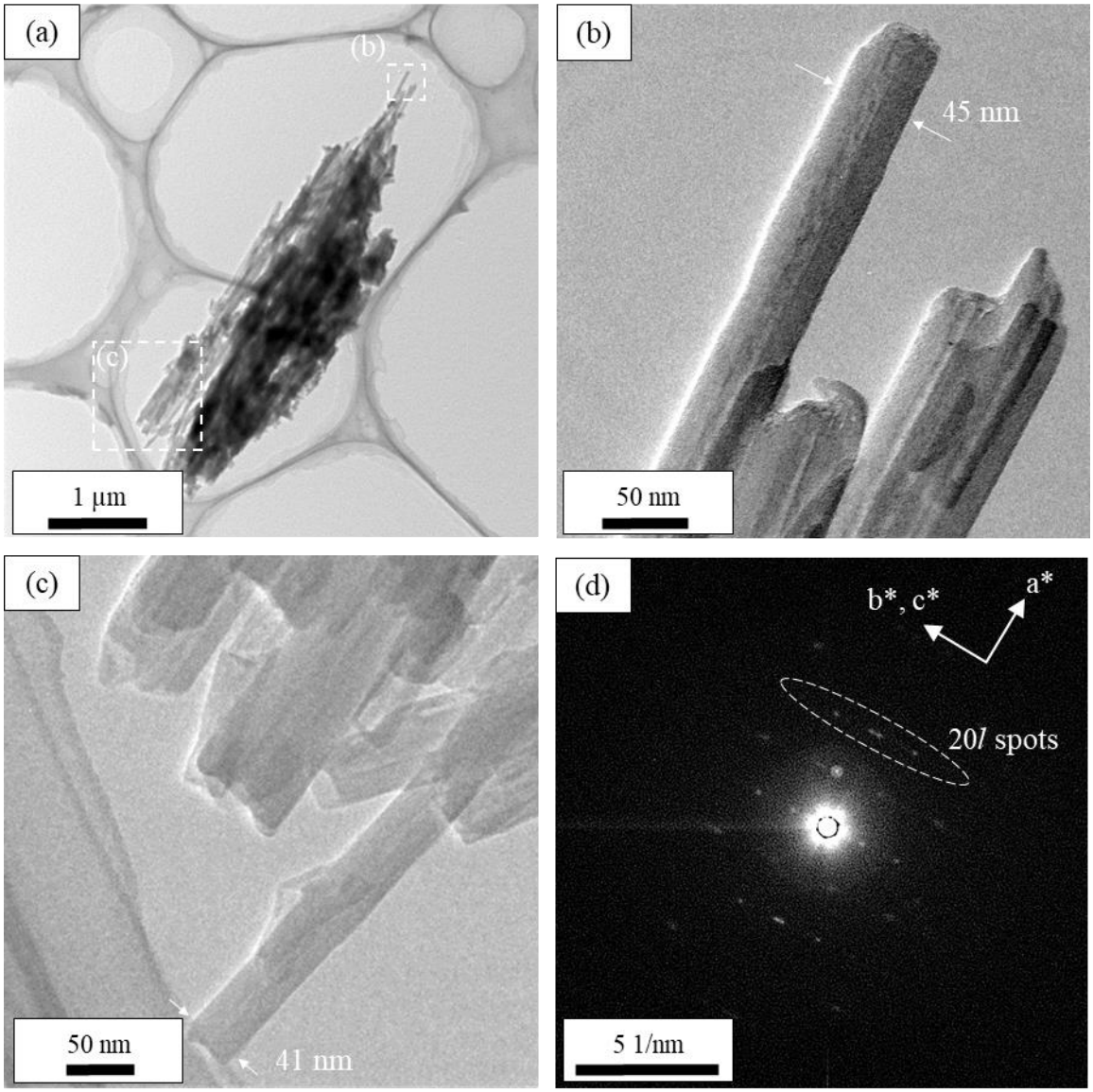

Fig. 6.8. TEM results of particles composing the bedrock. (a) TEM image of representative particles; (b), (c) High magnification images of the areas displayed by dotted lines in (a); (d) SAED pattern of the area in (b).

The P4 and P7 in the polished section (Fig. 6.7a,b) were picked out by a micromanipulator for the TEM observations. The P4 was an aggregate of nano-tubes (length $\lesssim$ 500 nm; width ~ 30–50 nm) with some indeterminate components (Fig. 6.9a). A SAED pattern of the aggregate of particles showed six diffuse rings (Fig. 6.9b), indicating that the particles consisted of poly- and poorly crystalline minerals.

The *d*-values of these were 7.3, 4.5, 3.7, 2.5, 1.5, and 1.3 Å, which is consistent with those of chrysotile. The P7 were also an aggregate of nano-tubular particles and indeterminate components (Fig. 6.10a). Observation with higher magnification showed that the tubular particles have various widths (~30 – ~70 nm; Fig. 6.10b,c). The tube length of particles composing P7 was much shorter than that of the chrysotile from the bedrock. The SAED pattern of the aggregate of P7 was also similar to that of P4 (Fig. 6.10d). The above results indicate that P4 and P7 are poorly crystalline chrysotile and that they have similar characteristics, completely different from the chrysotile composing bedrock.

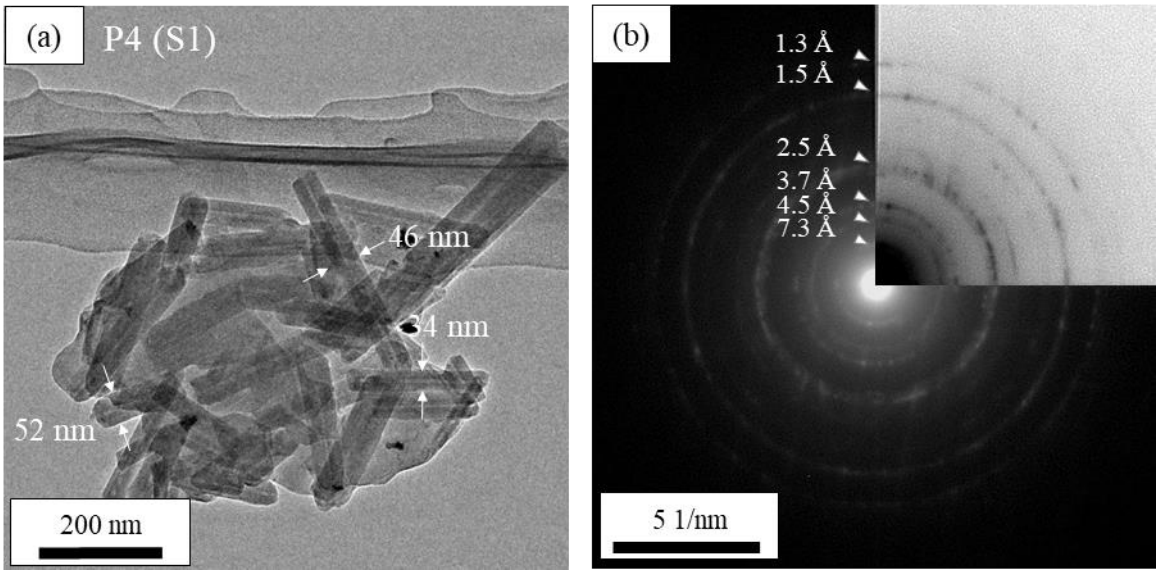

Fig. 6.9. TEM results of P4 in Fig. 6.7a. (a) TEM image of observed particles; (b) SAED pattern of the area in (a).

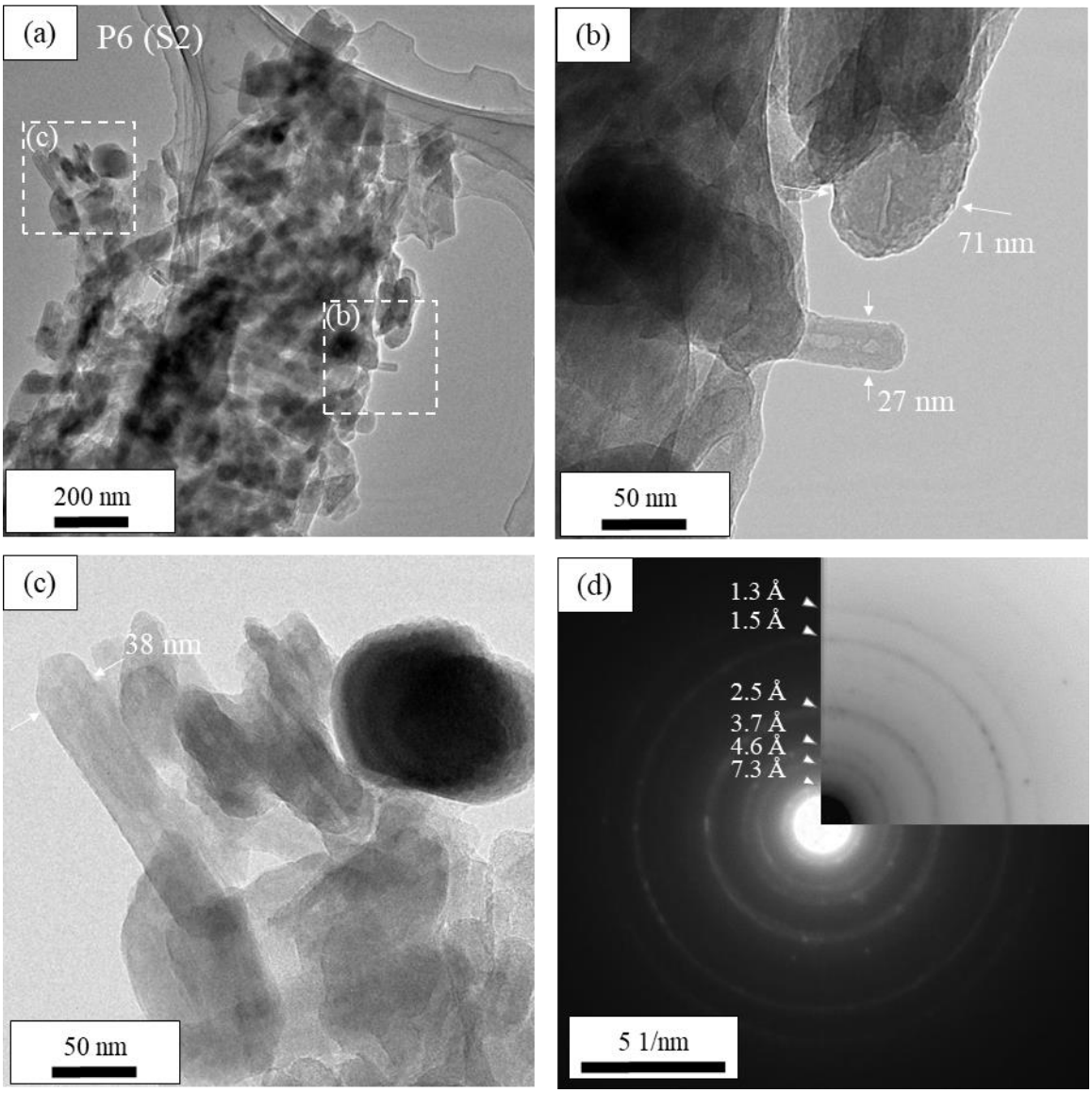

Fig. 6.10. TEM results of P7 in Fig. 6.7b. (a) TEM image of representative particles; (b), (c) High magnification images of the areas displayed by dotted lines in (a); (d) SAED pattern of the area in (a).

During the TEM observations, EDS spectra were obtained on the above particles. All the EDS spectra had peaks related to C, O, Mg, Si, Fe, and Cu (Fig. 6.10Fig. 6.11). Because the samples were placed on copper grids coated with carbon films, the EDS spectra demonstrate that the chrysotile from the bedrock, P4, and P7 were mainly composed of Mg, Si, and O with a small amount of Fe. There were no significant differences in the chemical compositions among the three above samples.

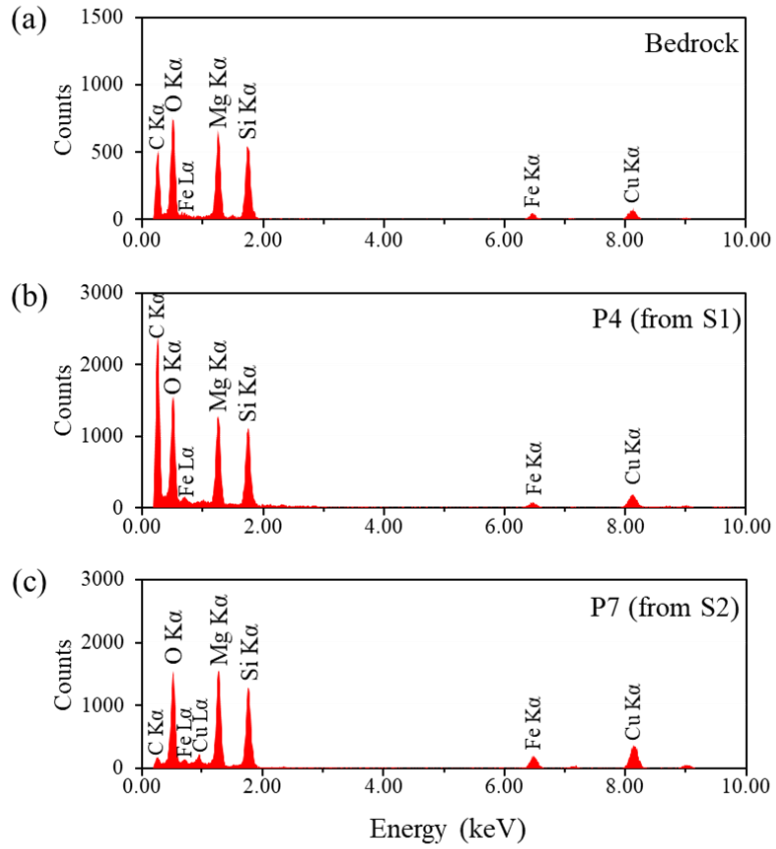

Fig. 6.11. EDS results obtained during TEM observations. (a) EDS spectrum of particles composing the bedrock in Fig. 6.8a; (b) EDS spectrum of P4 in Fig. 6.9a; (c) EDS spectrum of P7 in Fig. 6.10a.

6.5 Discussion

6.5.1 Characteristics of minerals in the bedrock

Minerals composing the bedrock in the studied area are mainly chrysotile and lizardite, which was demonstrated by the XRD analysis (Fig. 6.6). Katoh and Nakagawa (1986) reported that the major serpentines in the ultramafic rock around the Kamuikotan tectonic belt are chrysotile and lizardite, not antigorite, based on a geologic survey throughout the belt, and this is consistent with the findings of this study.

The chrysotile in the bedrock was characterized in detail by TEM. In general, chrysotile crystals have a cylindrical and tubular structure of 22–65 nm width (Wicks and O'Hanley, 1988). Chrysotile is

commonly composed of Mg, Si and O/OH with some substitutions by other elements such as Al, Fe, and Ni (Wicks and O'Hanley, 1988). Given polytypes of chrysotile, chrysotile formed in harzburgite or dunite is generally clino-chrysotile rather than ortho-chrysotile (O'Hanley, 1996). The above characteristics of chrysotile are consistent with those determined in this study (Figs Fig. 6.8 and Fig. 6.11a), which demonstrates that the chrysotile observed in this study is a quite common chrysotile.

6.5.2 Formation of magnesium silicate hydrates

Discussing the several analytical results of sediment samples, this section establishes that the sediment samples here contain solid phases precipitated on the surface of serpentine, and that some of the phases are M-S-H.

Bulk XRD analysis indicates that the sediment samples from S1 and S2 contain serpentine with LDH and aragonite, respectively (Fig. 6.6). Considering that the XRD profiles of the bedrock samples do not have peaks for LDH and aragonite, the LDH and aragonite would be precipitated at the sites. Precipitation of M-S-H is not clearly identified in the XRD profiles of the sediment samples. However, the intensities of the peaks for serpentine (esp. peaks other than at $d \approx 7.27$, 4.56, 3.64, and 1.53 Å) are lower than those of the bedrock samples. This invites the suggestion that sediment samples may also contain poorly crystalline precipitates, and that the broad peaks of the poorly crystalline precipitate may be overlapping peaks of crystalline serpentine.

The precipitates were observed in the sediment samples by microscopy and mineralogically identified by micro-Raman spectroscopy. Some solid phases with ambiguous morphologies (P4 and P7; Fig. 6.7a,b) are observed around grains with more clearly defined shapes (P1, P2, P3, P5 and P6; Fig. 6.7a,b), and theses phases bind the grains together. Therefore, the sediment samples may be assigned as cemented aggregate of grains formed on site. The micro-Raman spectroscopy identified P1, P2, P3, P4, P6, and P7 as chrysotile or lizardite (Fig. 6.7c,e). Considering the above characteristics of the sediment samples, the mineralogy of the bedrock samples (detailed in the Subsection 6.5.1), and the geological

setting of the sites, the author wishes to assign P1, P2, P3, and P6 to be detrital grains from the bedrock, and P4 and P7 as precipitated phases although all of P1, P2, P3, P4, P6, and P7 show similar Raman spectra. Taken together, the various results make it appear that P4 and P7 are precipitated interstitially around the detrital serpentine particles.

Further characterization of the precipitated phases (P4 and P7) was performed by TEM. The P4 and P7 are aggregates of indeterminate components with the nano-tubular crystals. The tube lengths are much shorter than that of usual chrysotile (Figs Fig. 6.8a, Fig. 6.9a, and Fig. 6.10a), and the width varies around ~30 – ~70 nm (Figs Fig. 6.9a and Fig. 6.10b,c). The SAED patterns show diffuse rings, and the *d*-values are consistent with chrysotile (Figs Fig. 6.9b and Fig. 6.10d). Taken together, the above characteristics suggest that P4 and P7 are chrysotile, but poorly crystalline and not highly ordered phases. Additionally, the EDS results indicate that P4 and P7 are mainly composed of Mg, Si, and O, which is similar to commonly occurring chrysotile (Fig. 6.11), suggesting the conclusion of P4 and P7 as M-S-H having the structure of poorly crystalline chrysotile. The characteristics (morphology, particle size, and SAED) of the M-S-H were similar to those of "proto-serpentine" which is a poorly crystalline phase acting as a precursor to chrysotile in hydrothermal experiments by Lafay et al. (2016).

In summary, the above analyses may be seen to confirm present-day precipitation of M-S-H on the surface of the ultramafic rock mass. However, it is probably difficult for the precipitates to remain in this form on the surface of the ultramafic rock mass due to weathering and/or landslides. Therefore, precipitation of M-S-H likely occurs extremely rapidly compared with geological time scale.

6.5.3 Formation conditions and processes of magnesium silicate hydrates

The water chemistry in the studied sites is consistent with the water chemistry in ultramafic bodies in general, as reported by previous studies. Surface waters and seepage waters were essentially identified as Mg^{2+}–HCO_3^- type water (Fig. 6.5), which Barnes and O'Neil (1969) and Barnes et al. (1978) characterized as a typical water chemistry of ultramafic bodies including serpentinite. Barnes and O'Neil

(1969) mentioned that this water chemistry may be attributed to weathering phenomena with meteoric water. In the studied sites, meteoric water reacts with minerals (mainly serpentine) in ultramafic rock, generating alkaline water. Residence time of the groundwater is likely longer than surface water, which is suggested by the pH of the seepage water being slightly higher than that of the surface water (Table 6.1). Barnes and O'Neil (1969) also reported that Ca in solution is supplied from orthopyroxene. The author collected the seepage sample from S2 with somewhat high Ca concentration (Table 6.1 and Fig. 6.5). This sample indicates that the groundwater generating the seepage possibly had some interaction with orthopyroxene within the ultramafic body although orthopyroxene was not detectable in the XRD profiles of the collected bedrock samples from the surface of the outcrop (Fig. 6.6).

To confirm the precipitation and discuss its conditions from the water chemistry, the chemical compositions of the liquid samples (surface waters and seepage waters from S1 and S2) were plotted in thermodynamic stability diagrams in the Mg–Si–H_2O, Ca–Si–H_2O, Mg–CO_2–H_2O, and Ca–CO_2–H_2O systems (Fig. 6.12) obtained using the Geochemist's Workbench software (GWB v. 12) with the Thermoddem database (Blanc et al., 2012). The composition of M-S-H can be derived from two end-members (Mg/Si = 0.75 and 1.5; Nied et al., 2016), thermodynamic data for these two types of M-S-H obtained from Lothenbach et al. (2019) were added to Thermoddem to consider them in the Mg–Si–H_2O system.

First, precipitation of M-S-H can also be expected from the thermodynamic calculations. The surface waters (S1-sf and S2-sf) are undersaturated with M-S-H at both S1 and S2, while the seepage waters (S1-sp and S2-sp) are oversaturated with M-S-H ($M_{1.5}SH_{2.5}$; Fig. 6.12a). If S1-sf/S2-sf is mixed with S1-sp/S2-sp around S1/S2, the mixed solution (S1-mix/S2-mix) may be saturated with the M-S-H. Both sites show the surface water having higher activity of Si than the seepage water, and it may be assumed that mixing seepage with surface water would cause precipitation of M-S-H. This is consistent with the observation that precipitation occurred on the surface of the ultramafic rock mass at both S1 and S2 (Fig. 6.3). Additionally, this thermodynamic discussion of $M_{1.5}SH_{2.5}$ is also consistent with the

analyses of the solids, demonstrating that the M-S-H formed in the studied sites has a chrysotile-like crystal structure (Figs Fig. 6.7, Fig. 6.9, and Fig. 6.10) as $M_{1.5}SH_{2.5}$ (Mg/Si = 1.5) has been proposed to have a serpentine-like crystal structure, while $M_{1.5}S_2H_{2.5}$ (Mg/Si = 0.75) has been proposed to have a talc-like crystal structure (Nied et al., 2016). No C-S-H phases would be expected to precipitate since all the water samples are undersaturated for C-S-H formations (Fig. 6.12b).

Second, precipitation of carbonate minerals could also be expected by thermodynamic calculations. No Mg-carbonate mineral such as nesquehonite, which is a magnesium carbonate hydrate precipitated at ambient temperatures (Cheng et al., 2009), can be expected to precipitate because of the undersaturation (Fig. 6.12c). For aragonite, a Ca carbonate mineral, the mixed solutions are oversaturated, and the saturation index of the mixed solution at S2 is much higher than that at S1 (Fig. 6.12d). Further, the mixed solution at S2 is saturated with monohydrocalcite (Fig. 6.12d). As aragonite easily forms under high saturation index conditions (Romanek et al., 2011) or it may form via monohydrocalcite as a metastable precursor (Munemoto and Fukushi, 2008), the water chemistry of S2 may satisfy conditions for aragonite precipitation better than that of S1. This is consistent with the observation that aragonite is observed only with S2 (Figs Fig. 6.6 and Fig. 6.7d). Calcite is not considered in this calculation because dissolved Mg generally inhibits calcite formation (Kitano, 1962), something which is also supported by the absence of calcite as determined in this study.

In summary, mixing of the solutions of surface waters and seepage waters induced the formation of M-S-H in both S1 and S2 and that of aragonite in S2. The M-S-H is likely formed because dissolved Mg preferentially binds to dissolved silica, and not to carbonate and hydroxide ions under the geochemical conditions of the studied sites. Tutolo and Tosca (2018) observed mineral paragenesis of M-S-H and aragonite in experiments around pH 10, which is consistent with the results of the solid analyses and thermodynamic calculations of the liquid samples in this study.

As discussed above, fluid mixing is an important factor to understand the geochemical processes of M-S-H formation at the sites studied. For the present study, the author collected sediments on the surface

of an ultramafic rock mass where landslides occur. The surface layer of the ultramafic rock mass contains much surface water derived from meteoric water, which is a factor contributing to the landslides. In this situation, precipitation is likely affected by both surface water and seepage water. When seepage water merges with surface water displaying high activity of the dissolved Si, the mixed solution would induce the M-S-H formation, and consequently generate M-S-H on the surface of an ultramafic rock mass. This kind of fluid mixing for secondary mineral precipitation was also observed around alkaline springs on the Oman ophiolite by Anraku et al. (2017), and it does not appear to be in any way an extraordinary phenomenon around ultramafic regions.

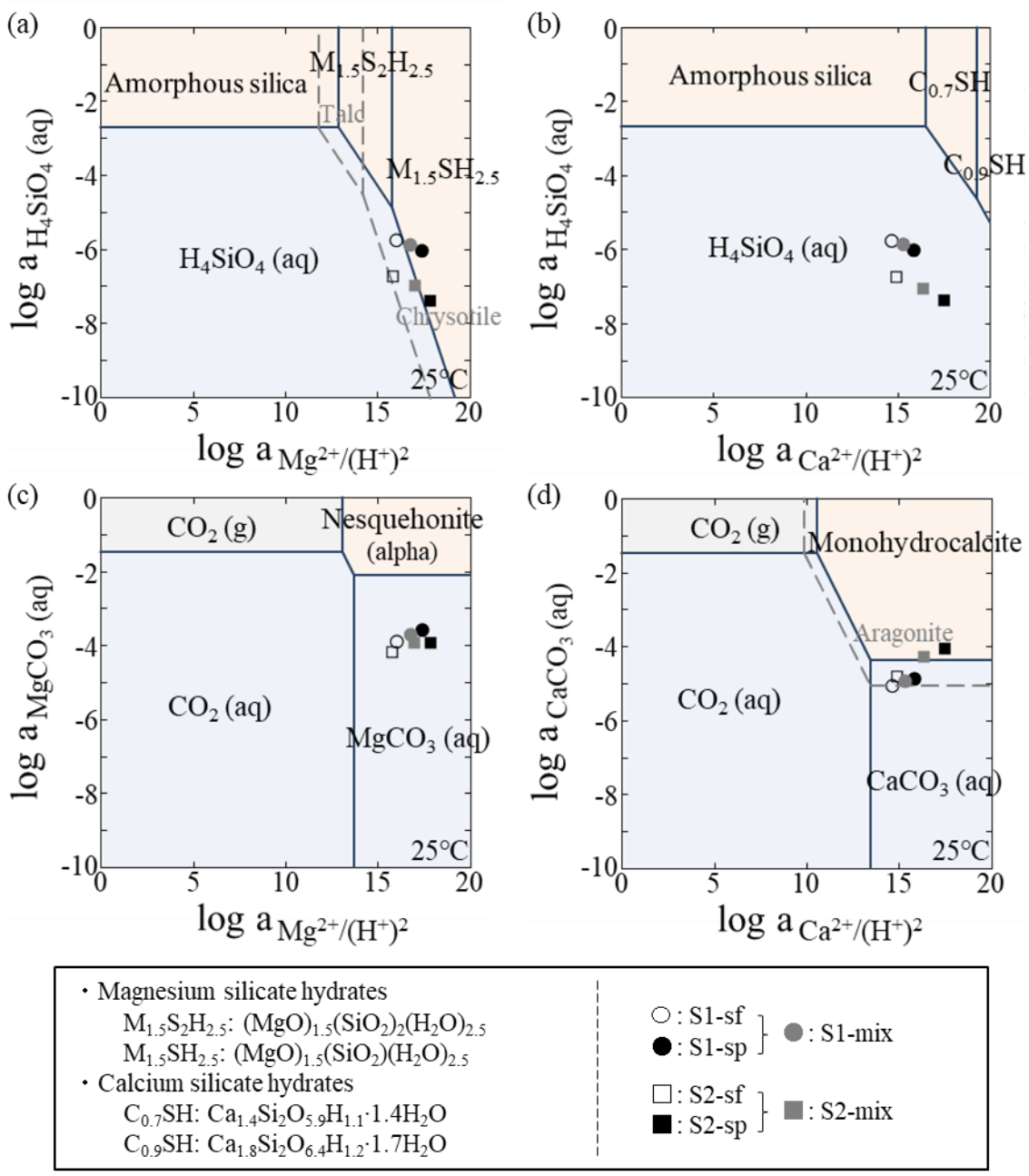

Fig. 6.12. Stability diagrams and thermodynamics of liquid samples in the (a) Mg–Si–H_2O system, (b) Ca–Si–H_2O system, (c) Mg–CO_2–H_2O system, and (d) Ca–CO_2–H_2O system at ambient temperature. Grayish solid symbols display 1:1 mixed solution of surface water and seepage water. Dashed lines show stability boundaries of talc and chrysotile in (a) and aragonite in (d).

6.5.4 Mineralogical and hydrogeochemical trends of Mg phyllosillciate formation in nature

The author investigated the water samples and the M-S-H samples identified as poorly crystalline chrysotile. The water chemistry possibly affects the mineralogical characteristics of Mg phyllosilicates formed in nature. Fig. 6.13 displays the data on water samples at six sites including S2 in this study.

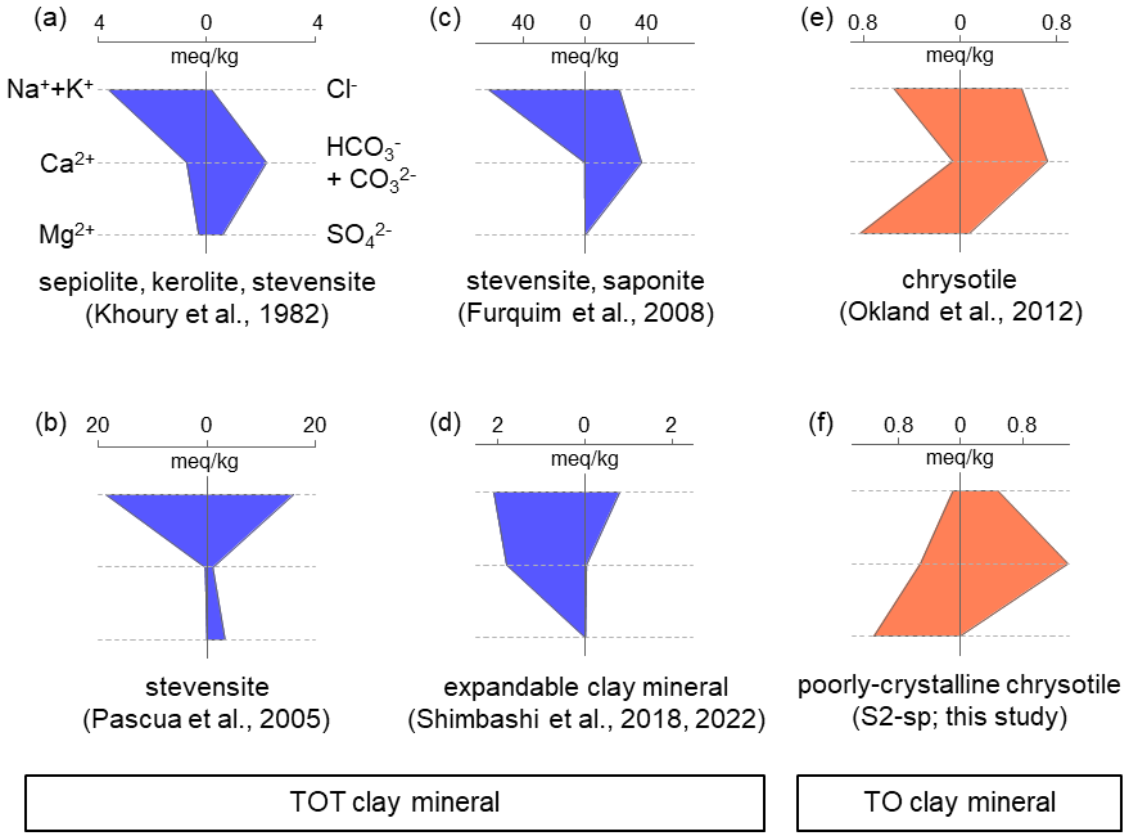

Fig. 6.13. Chemistry of water involved in the formation of Mg phyllosilicate minerals: (a) groundwater in the Amargosa Desert (Nevada; Khoury et al., 1982); (b) geothermal water in the Sumikawa geothermal power plant (Japan; Pascua et al., 2005); (c) surface/subsurface water in the Pantanal wetland (Brazil; Furquim et al., 2008); (d) groundwater in the Palawan Ophiolite Complex (the Philippines; Shimbashi et al., 2018, 2022); (e) groundwater in the Leka Ophiolite Complex (Norway; Okland et al., 2012); (f) seepage water (S2-sp) from ultramafic rock mass in Kamuikotan metamorphic belt (Japan; this study).

The alkali ions (Na^+ and K^+) are predominant cation species in the solutions when Mg-rich TOT phyllosilicate forms (Fig. 6.13a–d), while Mg^{2+} is predominant when Mg-rich TO phyllosilicate forms

(Fig. 6.13e,f). The presence of the alkali ions in the system may be an essential factor in determining phyllosilicate types of M-S-H. This trend may account for the results in Chapter 4, which showed that the M-S-H with TOT layers formed even when the initial Mg/Si ratio was higher than 1. However, more case studies of Mg silicate (especially TO clay minerals) formation in nature at low temperatures are needed to confirm this assumption.

6.5.5 Differences between magnesium silicate hydrates in laboratory experiments and in nature

Since previous studies on M-S-H have mostly been experimental studies, this subsection will now discuss differences between the M-S-H reported in previous experimental studies and the M-S-H observed in this field survey. In most studies, the M-S-H samples have been synthesized by using reagents of MgO and SiO_2 with w/s ratios ≤ 50 at around room temperature, and the XRD results showed four broad humps rather than distinct peaks (Chapters 3 and 4 in this dissertation; Roosz et al., 2015; Nied et al., 2016; Bernard et al., 2017). Furthermore, the *d*-values analyzed by XRD (4.5, 3.3, 2.6, and 1.5 Å) in the synthetic M-S-H from these studies are similar to some of those obtained from the SAED in TEM analysis of the natural M-S-H from this study (7.3, 4.5, 3.7, 2.5, 1.5, and 1.3 Å; Figs Fig. 6.9b and Fig. 6.10d). Results of the XRD and other analyses such as spectroscopy suggest that the experimental products have remarkably disordered and defective structures, which would indicate that the synthetic M-S-H samples are only poorly crystalline when compared with the M-S-H in this study, and that the synthetic M-S-H samples are somewhat different materials from the natural M-S-H samples. This is likely because the saturation states of the dissolved Mg and Si in the experiments were much higher than those in nature.

It should also be noted that transformation of M-S-H possibly occurs after the primary precipitation of M-S-H. Although synthetic M-S-H samples are made under limited condition with respect to reaction time, some natural M-S-H samples may be transformed into more stable phases on geological time scales. The M-S-H in this study may evolve into crystalline chrysotile even at ambient temperatures. In

the stability diagram of an Mg–Si–H_2O system, the S1-mix and S2-mix are located in a stability field of M-S-H ($M_{1.5}SH_{2.5}$), which is essentially a location within a stability field of chrysotile (Fig. 6.12a). Since the M-S-H in this study are poorly crystalline chrysotile with nano-tubular particles, the M-S-H is possibly a metastable phase and the phase transformation from this M-S-H into chrysotile will proceed over long time scales.

6.6 Summary and conclusions

In this chapter, the author identified and verified the present-day precipitation of M-S-H on the surface of an ultramafic rock mass in the Kamuikotan tectonic belt, Hokkaido, Japan. Sediments around seepage contained M-S-H that was likely precipitated at ambient temperatures on site and was mineralogically identified as poorly crystalline chrysotile, in addition to detrital serpentine from the bedrock. The M-S-H was different from commonly occurring chrysotile composing the bedrock with respect to morphology, particle size, and crystallinity, while the chemical compositions were similar.

Precipitation of the M-S-H is influenced by seepage and surface water around the studied sites. Seepage water merges with surface water having high activity levels of Si, making the mixed solution induce the M-S-H formation. Precipitation of M-S-H is presumably not an extraordinary phenomenon in natural Mg–Si–H_2O systems where geochemical settings are subjects to alkaline fluid that shows high Si activity and meets thermodynamic conditions for M-S-H formation. Furthermore, even in Mg–Ca–Si–CO_2–H_2O systems, M-S-H precipitates simultaneously with aragonite.

Chapter 7: F(II)-S-H and M-F(II)-S-H formation

7.1 Introduction

Formation of M-S-H is observed in natural emplacements (especially, ultramafic rocks; Chapter 6 and de Ruiter and Austrheim, 2018). For geochemical reactions in nature, it is important to note that Mg^{2+} is often dissolved with Fe^{2+} in water. Since Mg^{2+} and Fe^{2+} show similar ionic radii (Mg^{2+} = 0.66 Å and Fe^{2+} = 0.74 Å; Ahrens, 1952) and 6-fold coordination with oxygen, aqueous Fe^{2+} in solution is possibly consumed by precipitation of Fe(II) silicate or Mg–Fe(II) silicate. Therefore, the study in this chapter aims to understand the effect of Fe(II) during M-S-H formation (related to [iii] in Section 1.4). First, this chapter demonstrated and characterized "Fe(II) silicate hydrate" (F-(II)-S-H) in Fe(II)–Si–H_2O systems and compared it with the M-S-H in Chapter 4. Second, this chapter investigated the formation of "Mg–Fe(II) silicate hydrates" (M-F(II)-S-H; solid solutions of M-S-H and F(II)-S-H). The concept of F(II)-S-H and M-F(II)-S-H has not been discussed in previous study and only a few studies reported interactions between Fe(II) and silica at ambient temperature (Tosca et al., 2016; Francisco et al., 2020).

7.2 Materials and methods

7.2.1 Experimental procedures

Experimental procedures in this chapter were similar to those in Chapter 4. The experiments were conducted in an anaerobic chamber filled with N_2 gas (O_2 concentration < 1 ppm) at room temperature (20°C–27°C). O_2 concentration in the chamber was maintained at <1 ppm. Ultrapure water was first purged by bubbling N_2 gas through the solution for 24 hours in the chamber (DO = 0.00 mg L^{-1}). 50 mM Si solutions were prepared by adding TEOS ($C_8H_{20}SiO_4$; Alfa Aesar, Thermo Fisher Scientific Inc., 98%) to the ultrapure water. 50 mM Fe^{2+}(aq) stock solutions were prepared with iron(II) chloride tetrahydrate ($FeCl_2 \cdot 4H_2O$; FUJIFILM Wako Pure Chemical Corporation, > 99 %).

For the synthesis in Fe(II)–Si–H_2O systems, Fe(II)/Si ratios were 0.4, 0.7, 1.0, 1.3, and 1.5, mixing 100 mL of the Si solutions and 40, 70, 100, 130, and 150 mL of the Fe(II) solutions, respectively. The pH of the mixed solutions was adjusted to 7, 10 and 12 by titrating 1 M NaOH (and 1 M HCl). The experiments lasted for 24 hours. The pH values had been maintained by additional titration during the experiments. After 24 hours, the greenish precipitates were collected after filtered through 0.20 μm PTFE filters and rinsed with the ultrapure water. The precipitates were dried under the low humidity conditions of the anaerobic chamber at ambient temperature and ground with an agate mortar and pestle for solid analyses.

An experiment in an Mg–Fe(II)–Si–H_2O system was also carried out in the anaerobic chamber for 24 hours. The 50 mM Mg solution ($MgCl_2 \cdot 6H_2O$, Kanto Chemical Co., Inc.) and the 50 mM Fe(II) solution were added into the Si solution under the condition of (Mg + Fe)/Si = 1, Mg/Fe = 1, and pH = 12. Procedures for solution preparation and solid-liquid separation in this experiment was the same as the ones in the Fe(II)–Si–H_2O experiments. Greenish white precipitate was collected from this experiment.

7.2.2 Analytical methods

Concentrations of dissolved Si, Mg, Fe(II), and Na in the filtered solutions were analyzed by ICP–AES (ICPE-9000 and ICPS-7500, Shimadzu Corporation) after dilution with the ultrapure water and acidification with HNO_3. Concentrations of Cl^- in non-acidified solutions were measured by IC (Dionex Integrion HPIC; Thermo Fisher Scientific Inc.).

Powder XRD patterns from 3 to 80° 2θ were obtained with a Miniflex600-C diffractometer (Rigaku Corporation) equipped with a Co target and a D/teX Ultra2 detector. The powdered samples were recorded at scanning speed of 1° 2θ min^{-1} and a scan step of 0.01° 2θ. The operation voltage and current were 40 kV and 15 mA. An air-sensitive sample holder with a knife edge (A00012148; Rigaku Corporation) was used to prevent sample oxidation during the measurement. Each sample was mounted

on an Al-alloy stage and covered with an X-ray transparent film in the anaerobic chamber. After recording XRD patterns for the Fe-contained samples, the X-ray transparent film was removed in the air, and measurements for the samples exposed in the air for 5 min were subsequently started without the X-ray transparent cover.

In situ HT–XRD patterns from 3 to 20° 2θ were collected with the same diffractometer under the same conditions (40kV, 15 mA, 1° 2θ min^{-1}, and 0.01° 2θ step). The HT–XRD patterns for samples at pH 12 from Fe/Si 0.7 and 1.5 were representatively collected. The samples were mounted on a BTS 500 Benchtop Heating Stage (Anton Paar GmbH) in the anaerobic chamber. An XRD patten was recorded at room temperature, 70°C, 150°C, and 300 °C. N_2 gas (99.999 %) was being supplied into the BTS 500 with a tube during the HT–XRD experiments.

ATR–FTIR spectroscopy was carried out by using a Nicolet 6700 FTIR spectrometer (Thermo Fisher Scientific Inc.) with a KBr beam splitter and a liquid N_2 cooled mercury cadmium telluride (MCT) detector. The powdered samples were deposited on a single bounce diamond ATR crystal with a diameter of 1.5 mm. Spectra were collected from 650 to 4000 cm^{-1} on a 4 cm^{-1} resolution. A total of 256 scans were recorded, each with a dwell time of 2 seconds. The samples were analyzed in the air, so that the samples were exposed for ~10 min.

The precipitate in the Mg–Fe(II)–Si–H_2O system were analyzed in further detail by TEM. The sample was dispersed in ethanol under ultrasonic irradiation and one drop of the supernatant was deposited on a copper grid with carbon film (Microgrid type A, Okenshoji Co., Ltd.). This preparation was conducted in the N_2 atmosphere. TEM images and electron diffraction patterns were obtained with a JEM-2010 instrument (JEOL Ltd.) at an operating voltage of 200 kV. STEM/EDS mapping were obtained with a Titan3 G2 60-300 instrument (FEI, Thermo Fisher Scientific Inc.) operating at 60 kV. The Titan3 G2 is equipped with a FE electron gun and a FEI Super-X EDS detector system, which consists of four separate silicon drift detectors.

7.3 Results

7.3.1 Solution chemistry

The concentrations of dissolved elements after 24 hours were measured and the compositions of precipitates were calculated by mass balance (Table 7.1). Although Fe/Si ratios of solids were low ($0.2 \leq Fe/Si \leq 0.6$) in the experiments at pH 7 in the Fe(II)–Si–H_2O systems, they were higher than Mg/Si ratios of solids in the Mg–Si–H_2O systems ($0.01 \leq Mg/Si \leq 0.04$; Table 4.1). For experiments at pH 10 and 12 in the Fe(II)–Si–H_2O systems, Fe/Si ratios of precipitates were similar to the initial conditions and dissolved Fe concentrations were extremely low (~0.001 mM).

In the Mg–Fe(II)–Si–H_2O system at pH 12, the similar amount of aqueous Mg and Fe were removed from solution by precipitation. Aqueous Mg concentration at (Mg + Fe)/Si = 1 (initial) in the Mg–Fe(II)–Si–H_2O system was the same as the one at Mg/Si = 1 in the Mg–Si–H_2O system (Table 4.1), whereas aqueous Fe concentration in the Mg–Fe(II)–Si–H_2O system was 100 times higher than the one at Fe/Si 1 in the Fe(II)–Si–H_2O system.

Table 7.1

Chemical analyses for solutions after 24-hour reactions in Fe(II)–Si–H_2O systems and the Mg–Fe(II)–Si–H_2O system.

System	Synthetic condition		Solution chemistry after 24 hours						Composition (solid)
			pH	Mg (mM)	Fe (mM)	Si (mM)	Na (mM)	Cl (mM)	
Fe(II)-Si-H_2O	pH 7	Fe/Si 1.5	6.95	*no data*	26.0	8.21	6.6	63.4	Fe/Si = 0.3
		Fe/Si 1.3	6.89	*no data*	21.9	6.50	8.7	57.3	Fe/Si = 0.4
		Fe/Si 1.0	6.88	*no data*	14.7	7.53	16.5	49.1	Fe/Si = 0.6
		Fe/Si 0.7	6.98	*no data*	15.8	7.19	4.5	42.0	Fe/Si = 0.2
		Fe/Si 0.4	6.90	*no data*	9.3	6.84	7.4	27.8	Fe/Si = 0.2
	pH 10	Fe/Si 1.5	10.05	*no data*	0.0008	0.01	58.7	67.6	Fe/Si = 1.5
		Fe/Si 1.3	9.94	*no data*	0.0012	0.01	47.7	54.8	Fe/Si = 1.3
		Fe/Si 1.0	9.94	*no data*	0.0012	0.01	43.2	48.6	Fe/Si = 1.0
		Fe/Si 0.7	10.09	*no data*	0.0076	0.20	37.7	41.2	Fe/Si = 0.7
		Fe/Si 0.4	10.05	*no data*	0.0006	7.60	29.6	28.7	Fe/Si = 0.5
	pH 12	Fe/Si 1.5	11.95	*no data*	0.0016	0.05	64.7	61.1	Fe/Si = 1.5
		Fe/Si 1.3	11.83	*no data*	0.0015	0.06	59.5	54.7	Fe/Si = 1.3
		Fe/Si 1.0	11.87	*no data*	0.0012	0.06	47.0	48.8	Fe/Si = 1.0
		Fe/Si 0.7	11.95	*no data*	0.0013	1.80	50.0	31.6	Fe/Si = 0.7
		Fe/Si 0.4	12.01	*no data*	0.0014	11.63	53.0	34.5	Fe/Si = 0.6
Mg-Fe(II)-Si-H_2O	pH 12	(Mg+Fe)/Si 1.0 Mg/Fe 1.0	12.05	0.59	0.57	6.33	52.0	44.5	(Mg+Fe)/Si = 1.3 Mg/Fe = 1.0

7.3.2 Solid analyses for the samples in the Fe(II)-Si-H_2O systems

The XRD patterns for all samples in the Fe(II)–Si–H_2O systems were obtained in N_2 atmosphere and showed two broad peaks at ~2.68 and ~1.60 Å (Fig. 7.1a–c). These *d*-values were assigned to F(II)-S-H in this study and similar to the ones of synthetic Fe(II) silicate samples in previous studies: 2.68 and 1.59 Å (Francisco et al., 2020) and 2.57 and 1.56 Å (Tosca et al., 2016). A broad peak for amorphous silica at ~ 3.9 Å was also recognized in each XRD pattern at pH 7. The XRD patterns from Fe/Si 1.5 (pH 10 and 12), Fe/Si 1.3 (pH 10 and 12), and Fe/Si 1.0 (pH 12) exhibited peaks for $Fe(OH)_2$ (4.6, 2.8, 2.4, 1.78, 1.63, and 1.54 Å; Bernal et al., 1959). The peak at $d \geq 10$ Å was also recognized and two broad humps at ~4.6 and ~3.3 Å were faintly shown in the XRD patterns for precipitates at pH 10 and 12.

XRD patterns for the samples synthesized in the Fe(II)–Si–H_2O systems were also obtained in air (Fig. 7.1d–f). The two XRD peaks for the F-S-H phase were observed at ~2.68 and ~1.60 Å in air, which were similar to those obtained in N_2 atmosphere. The XRD patterns obtained in air for precipitates at pH 10 and 12 also exhibited peak at large *d* values (≥10 Å), ~4.6 Å and ~3.3 Å. Differences between the XRD patterns in air and those in N_2 atmosphere were peaks for Fe hydroxide. Its XRD peaks in air were identified as Fe(III) hydroxide (6-line ferrihydrite; Eggleton and Fitzpatrick, 1988; Drits et al., 1993), instead of Fe(II) hydroxide.

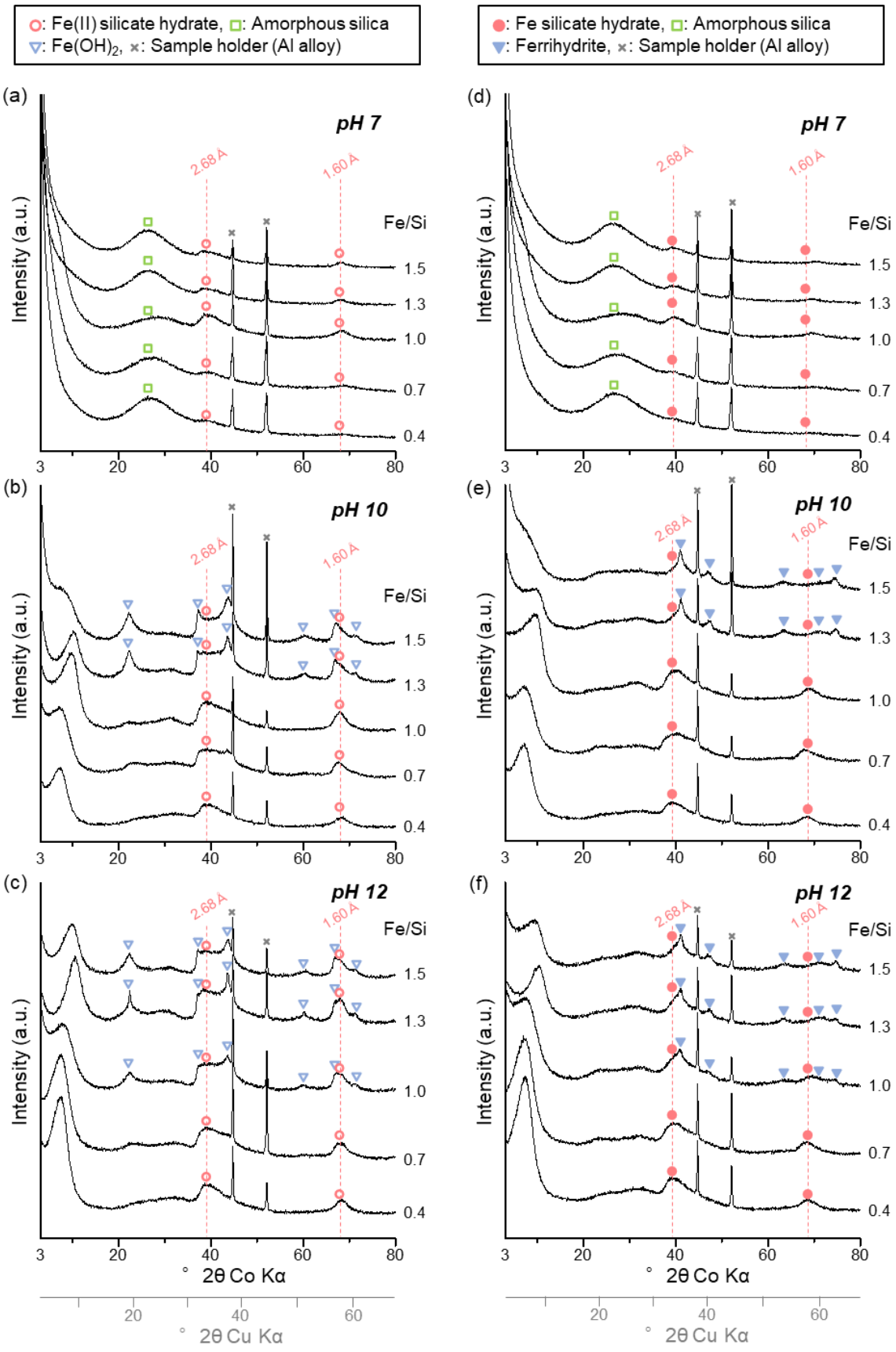

Fig. 7.1. XRD patterns of precipitates in Fe(II)–Si–H_2O systems at (a) pH 7, (b) pH 10, and (c) pH 12 in the N_2 atmosphere and (d) pH 7, (e) pH 10, and (f) pH 12 in the air.

In HT–XRD experiments, thermal behavior of F(II)-S-H samples (Fig. 7.2) was similar to that of M-S-H samples (Fig. 4.2). For the sample from Fe/Si 0.7, the peak at ~14 Å shifted to ~10 Å during heating to 300°C, while that from Fe/Si 1.5 shifted from ~10 Å to ~9.5 Å as the sample was heated to 150°C, before disappearing at 300°C.

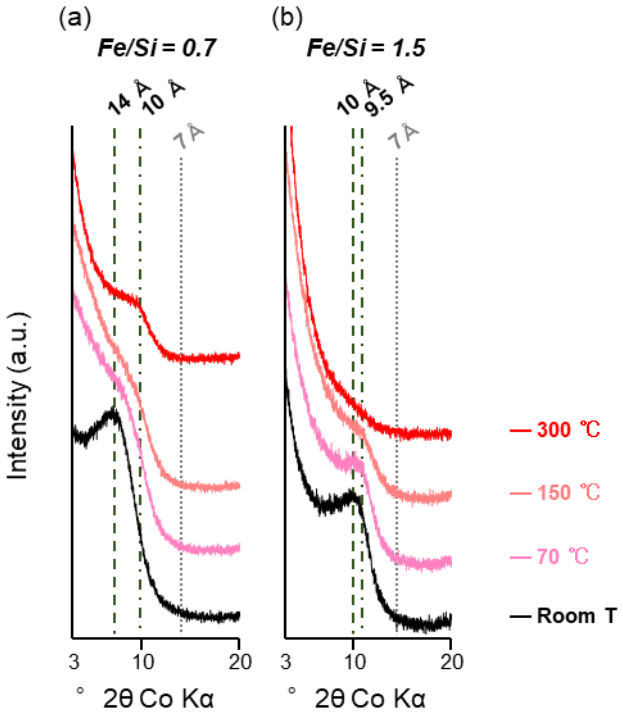

Fig. 7.2. In situ HT–XRD patterns for precipitates at pH 12 from (a) Fe/Si 0.7 and (b) Fe/Si 1.5.

Precipitates in Fe(II)–Si–H_2O systems showed IR bands related to silicate between 1200 and 700 cm^{-1}. The precipitates at pH 7 exhibited bands at ~800, ~968, ~1064, and ~1200 cm^{-1} (Fig. 7.3a), which were similar to observations in the Mg–Si–H_2O system (Fig. 4.3a). However, the band at ~968 cm^{-1} in the Fe(II)–Si–H_2O experiments showed relatively high absorbance compared to the band at ~960 cm^{-1} in the Mg–Si–H_2O experiments (Fig. 4.3). The precipitate from Fe/Si 0.4 at pH 10 showed a strong band at ~1020 cm^{-1} and a weak band at ~800 cm^{-1}, while the ones from Fe/Si 0.7, 1.0, 1.3, and 1.5 at pH 10 only showed a band at ~980 cm^{-1} (Fig. 7.3b). At pH 12, a band was observed in each IR spectrum within

the range 1200–700 cm^{-1} (Fig. 7.3c). The band centered at ~980 cm^{-1} in the samples from Fe/Si 0.4 and 0.7 shifted to lower wavenumbers with increasing the Fe/Si ratios (~952 cm^{-1} in the sample from Fe/Si 1.5).

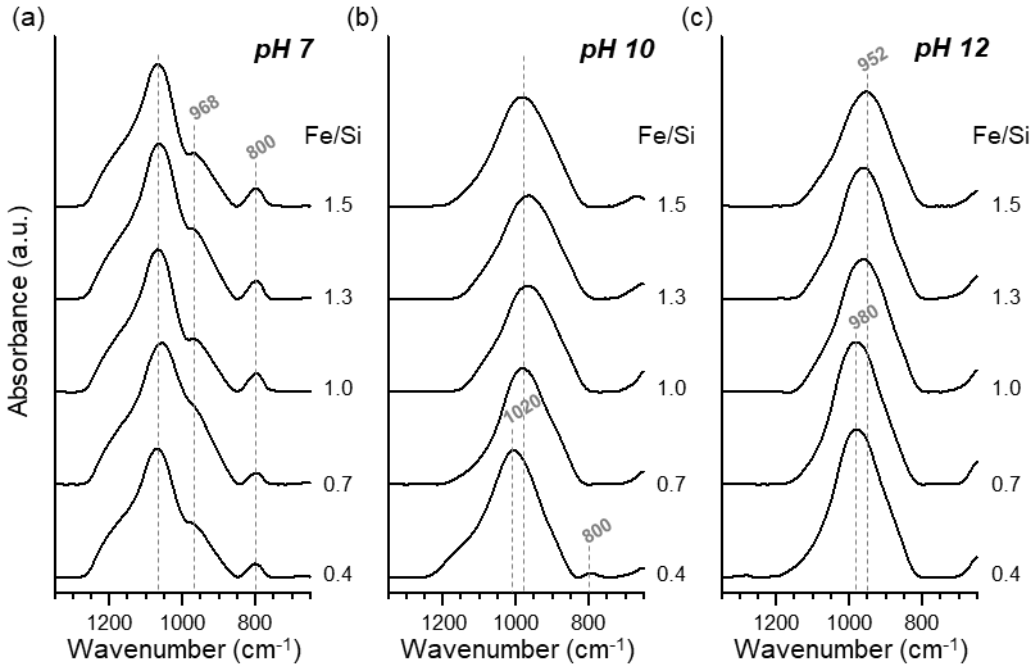

Fig. 7.3. FTIR spectra of precipitates in Fe(II)–Si–H_2O systems at pH (a) 7, (b) 10, and (c) 12.

7.3.3 Solid analyses for the samples in the Mg–Fe(II)–Si–H_2O system

The precipitate in the Mg–Fe(II)–Si–H_2O system was characterized by XRD analysis (Fig. 7.4) and ATR–FTIR spectroscopy (Fig. 7.5). The precipitates clearly exhibited two diffraction peaks at 2.62 and 1.57 Å, which were intermediate between those in M-S-H (2.56 and 1.55 Å) and F(II)-S-H (2.68 and 1.60 Å). An IR absorption band in the solid sample was observed at 988 cm^{-1}, while that in the M-S-H sample was at 996 cm^{-1} and that in the F(II)-S-H sample was at 960 cm^{-1}.

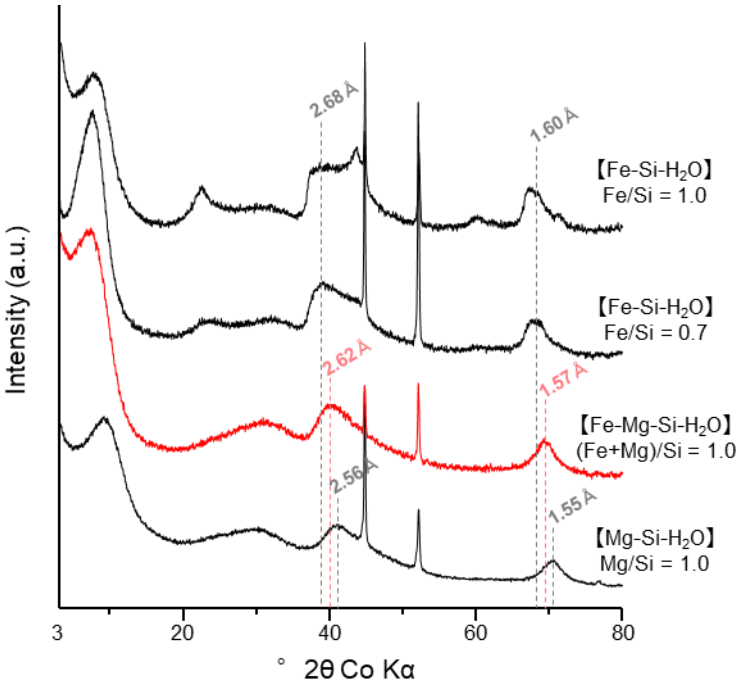

Fig. 7.4. XRD pattern of precipitate in the Mg–Fe(II)–Si–H_2O system at pH 12. Data on precipitates in Mg–Si–H_2O (Fig. 4.1) and Fe(II)–Si–H_2O systems (Fig. 7.1) at pH 12 are displayed for comparison.

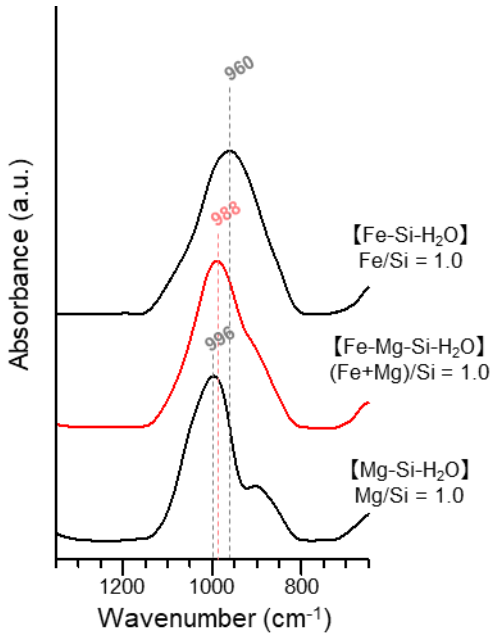

Fig. 7.5. FTIR spectrum of precipitate in the Mg–Fe(II)–Si–H_2O system at pH 12. Data on precipitates in Mg–Si–H_2O (Fig. 4.3) and Fe(II)–Si–H_2O systems (Fig. 7.3) at pH 12 are displayed for comparison.

Further characterization using TEM showed aggregates of nanoparticles with ambiguous morphologies (Fig. 7.6a). The nanoparticles were composed of Mg, Fe, Si, and O (Fig. 7.6b). The non-crystalline particles exhibited diffuse diffraction rings (Fig. 7.6c), with *d*-values consistent with those found with XRD (Fig. 7.4). Nano-scale elemental mapping with a field emission electron gun showed homogeneous distribution with respect to Mg, Fe, and Si (Fig. 7.6d–f). The Cliff-Lorimer method was applied to quantify elemental compositions, resulting in Mg/Fe = 1.0 and (Mg + Fe)/Si = 0.9.

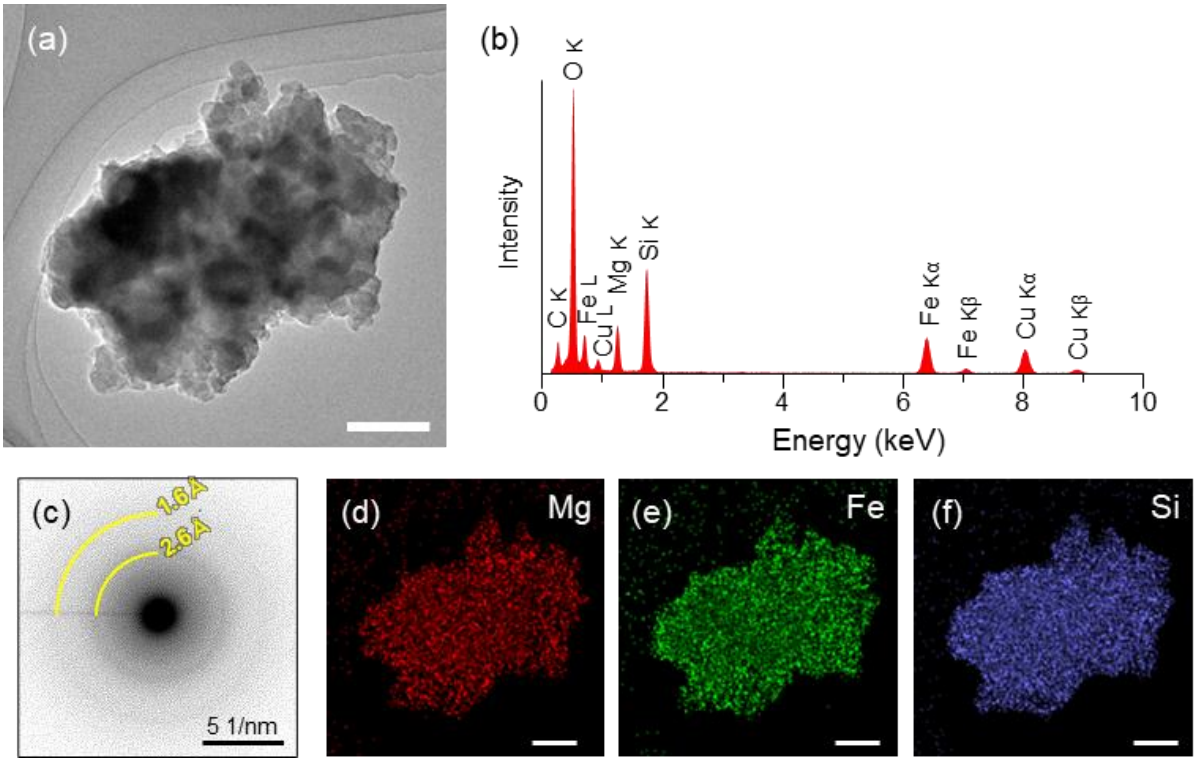

Fig. 7.6. TEM analysis for a precipitate in the Mg–Fe(II)–Si–H_2O system at pH 12. (a) TEM image; (b) EDS spectrum; (c) Electron diffraction pattern; (d–f) STEM/EDS mapping for Mg, Fe, and Si, respectively. Scall bars in (a), (d), (e), and (f) are 200 nm.

7.4 Discussion

7.4.1 Precipitation in the Fe(II)-Si-H_2O systems

Peaks for $Fe(OH)_2$ were observed in the XRD patterns for the samples from Fe/Si 1.5 (pH 10 and 12), Fe/Si 1.3 (pH 10 and 12), and Fe/Si 1.0 (pH 12), indicating that the air-sensitive sample holder used in this work can maintain anoxic conditions during the XRD analyses (Fig. 7.1b,c). These XRD patterns were changed by exposing the samples to the air (Fig. 7.1e,f). Peaks for 6-line ferrihydrite were observed instead of $Fe(OH)_2$, which indicates that Fe(II) hydroxide was oxidized to Fe(III) hydroxide. In the range 3–80° 2θ Co Kα (3.4–1.39 Å), Eggleton and Fitzpatrick (1988) identified 6 reflections for 6-line ferrihydrite (2.52, 2.23, 1.98, 1.72, 1.51, and 1.46 Å). The reflection at 1.98 Å (= 53.7° 2θ Co Kα) was not clearly observed in Fig. 7.1e,f because this reflection shows relatively weak intensity (Eggleton and Fitzpatrick, 1988; Drits et al., 1993) and this was possibly overlapped with the strong peak from the sample holder.

XRD peaks for F(II)-S-H were identified at all pH conditions (Fig. 7.1a–c). Peaks at 2.68 and 1.60 Å were not shifted between in the N_2 atmosphere (Fig. 7.1a–c) and in the air (Fig. 7.1d–f). F(II)-S-H structures will not be reconstructed when the samples were exposed to air in a short time. A synthetic Fe-saponite sample oxidized in air-saturated water (Chemtob et al., 2017) and a ferrian saponite sample in nature (Kodama et al., 1988) showed d_{060} similar to unoxidized Fe(II)-saponite. Noda et al. (2021) observed that d_{060} and d_{02l} for Fe(II)-saponite synthesized in an anoxic condition were not shifted after air exposure for ~10 hours. XAS in the Noda et al. (2021) study indicated only ~10 % of Fe(II) was oxidized. Therefore, only a small degree of oxidation likely occurred during 5 minutes of air exposure for the F(II)-S-H in this study. Even when Fe(II) in the Fe silicate hydrate is oxidized to Fe(III), its structure is unlikely to be modified. F(II)-S-H is thus relatively stable in oxic environments compared with Fe(II) hydroxide.

At pH 10 and 12, two weak reflections at ~4.6 and ~3.3 Å may also be assigned to F(II)-S-H (Fig. 7.1b,c,e,f), similar to M-S-H (Fig. 4.1b,c). The XRD analyses in Tosca et al. (2016) study exhibited

some reflections around the same positions, which may also be identified as Fe(II) silicate in addition to reflections at 2.57 and 1.56 Å. The four *d*-values for F(II)-S-H (4.6, 3.3, 2.68, and 1.60 Å) are slightly larger than those for M-S-H (4.5, 3.3, 2.56, and 1.55 Å) because Fe^{2+} ionic radius is larger than Mg^{2+} ionic radius (Fe^{2+} = 0.74 Å, Mg^{2+} = 0.66 Å; Ahrens, 1952). At pH 7, amorphous silica peaks were also exhibited in the XRD patterns of the precipitates (Fig. 7.1a,d).

The XRD patterns of the precipitates at alkaline pH in the Fe(II)–Si–H_2O systems also exhibited a broad peak at $d \geq 10$ Å (Fig. 7.1b,c), which is similar to the ones in precipitates from the Mg–Si–H_2O systems (Fig. 4.1b,c). The peak was also assigned to F(II)-S-H and further investigated by HT–XRD experiments. For the sample from Fe/Si 0.7 at pH 12, the position of the broad peak at d ≥ 10 Å shifted to larger *d* positions upon heating to 300°C (Fig. 7.2a), analogous to the behavior of the M-S-H sample from Mg/Si 0.7 at pH 12 (Fig. 4.2a). The peak for the sample from Fe/Si 1.5 at pH 12 was also shifted at 150°C (Fig. 7.2b). The reflection at 9.5 Å is consistent with a basal spacing of minnesotaite, which is a Fe(II) silicate mineral based on a talc structure (Guggenheim and Eggleton, 1986). In this context, the HT–XRD results for the F(II)-S-H samples suggest the same conclusion as those for the Mg-silicate samples. The F(II)-S-H sample from Fe/Si 0.7 has "Fe-stevensite" structure, and the F(II)-S-H sample from Mg/Si 1.5 has structure similar to "Fe-kerolite". Here, "Fe-stevensite" and "Fe-kerolite" are defined as Fe(II) silicate having stevensite and kerolite structures in which Fe^{2+} ions substitute for Mg^{2+} ions.

The XRD study in this work demonstrates layer stacking periodicity related to TOT phyllosilicate ($d \geq 10$ Å), whereas the one in Francisco et al. (2020) study did not exhibit clear basal reflections for phyllosilicate structures. The XRD patterns in this work were recorded by using Co Kα radiation, while those in Francisco et al. (2020) were recorded by using Cu Kα radiation. The Co target generally shows higher XRD intensity for Fe-bearing material than the Cu target. The XAS study in Francisco et al. (2020) indicates that Fe(II) silicate precipitates locally have a TO phyllosilicate (greenalite) structure. Given this discussion, F(II)-S-H (especially from high Fe/Si conditions) would locally have (i) TO units

in TOT layers that was observed in Fe-altered bentonite (Wilson et al., 2006) or (ii) the tetrahedral defects in TOT layers (Roosz et al., 2015; The partial Si defects in TOT layers may be identified to be partial TO structure in TOT layers).

The results of ATR–FTIR spectroscopy support to understand the XRD results. The ATR–FTIR spectra also indicated that the redox state of Fe was mainly Fe(II) because H–O–Fe^{3+} bending vibrations for Fe(III) phyllosilicate (in the range 900–800 cm^{-1}; Stubičan and Roy, 1961) was not observed in this study. The samples from Fe/Si 0.7, 1.0, 1.3, and 1.5 at pH 10 exhibited an absorption band at ~980 cm^{-1} (Fig. 7.3a), which can be assigned to Si–O stretching vibrations for F(II)-S-H. At pH 12, the samples from Fe/Si 0.4 and 0.7 also showed the band at ~980 cm^{-1}, while the ones from Fe/Si 1.0, 1.3, and 1.5 showed the band at lower frequencies (Fig. 7.3b). In general, the absorption maxima for Si–O stretching vibrations shift to higher frequencies with increasing degree of silica polymerization (Kieffer, 1979). For the F(II)-S-H samples synthesized under the low aqueous silica conditions, silica polymerization did not proceed, which may account for thermally weak structures in HT–XRD experiments (Fig. 7.2b) and the Si defects in TOT layers. The sample from Fe/Si 0.4 at pH 10 is composed of silica and F(II)-S-H phases because a large band centered at 1020 cm^{-1} is likely a combination of Si–O stretching vibrations of those phases and a band at ~800 cm^{-1} is assigned to Si–O stretching vibrations for the silica phase (Fig. 7.3b).

The ATR–FTIR spectra of the precipitates at pH 7 exhibited absorption bands for amorphous silica: Si–O stretching vibrations at ~800 and ~1064 cm^{-1} (Farmer, 1974) and asymmetric stretching vibrations of Si–O–Si linkages for silica at ~1200 cm^{-1} (Kamitsos et al., 1993) (Fig. 7.3a). Although these characteristics are similar to the one in the Mg–Si–H_2O systems at pH 7 (Fig. 4.3a), bands at ~968 cm^{-1} in the Fe(II)–Si–H_2O systems show higher relative intensities than bands at ~960 cm^{-1} in the Mg–Si–H_2O systems. This is likely due to overlap of Si–O stretching of the F(II)-S-H and that of the amorphous silica surface groups (Si–OH, ~960 cm^{-1}; Hino and Sato, 1971). Hence, the precipitates at pH 7 in the Fe(II)–Si–H_2O systems consisted of amorphous silica and F(II)-S-H.

Fig. 7.7 summarizes the results of the solid analyses. F(II)-S-H were observed at all the conditions. Even at pH 7, F(II)-S-H were precipitated although M-S-H were not. The conclusion that F(II)-S-H phases form at pH 7 is also supported by the facts that (i) Fe/Si ratios (~0.3) in the Fe(II)–Si–H_2O systems were higher than Mg/Si ratios (~0.02) in the Mg–Si–H_2O systems (Table 7.1), and (ii) the precipitates showed greenish color in the Fe(II)–Si–H_2O systems. In addition to F(II)-S-H, formation of amorphous silica was recognized in the experiments under the Si-rich condition at pH 10 (Fe/Si 0.4) and under all the conditions at pH 7, and Fe(II) hydroxide was observed under the Fe-rich conditions at pH 10 (Fe/Si 1.3 and 1.5) and pH 12 (Fe/Si 1.0, 1.3, and 1.5).

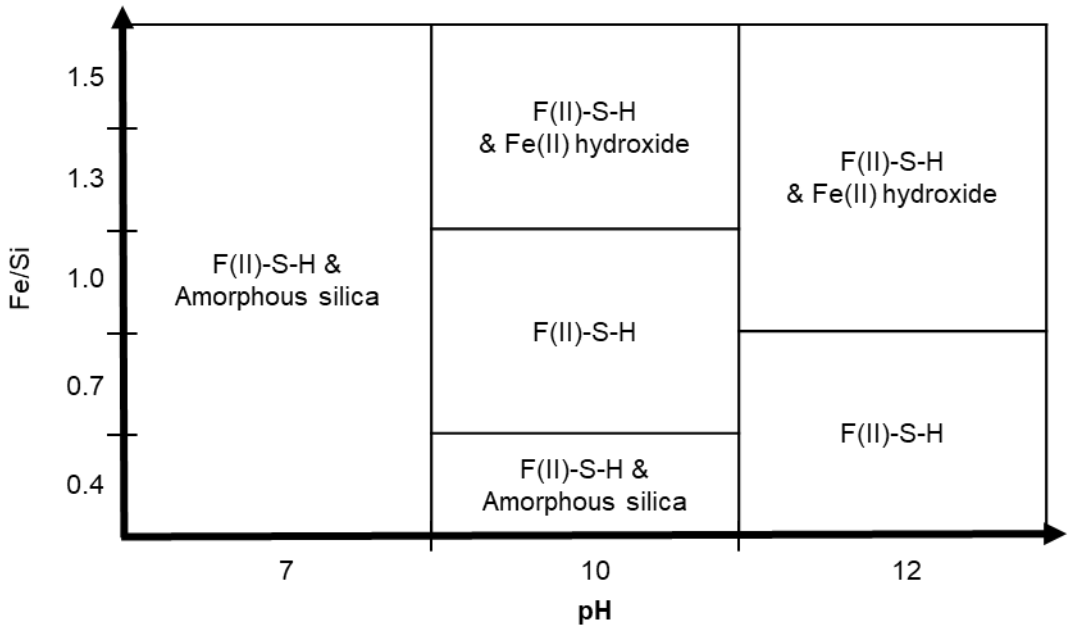

Fig. 7.7. Precipitates in Fe(II)–Si–H_2O systems at pH 7, 10, and 12.

7.4.2 Precipitation in the Mg–Fe(II)–Si–H_2O system

The synthetic experiment in the Mg–Fe(II)–Si–H_2O system revealed formation of M-F(II)-S-H. STEM/EDS mapping illustrated homogeneous distribution of Mg, Fe, and Si (Fig. 7.6), suggesting that a solid solution phase is formed in the system containing both Mg and Fe(II). Considering that crystal structures of both M-S-H and F(II)-S-H are based on hydrous TOT phyllosilicate such as stevensite and

kerolite, M-F(II)-S-H likely also has the hydrous TOT phyllosilicate structure. The *hk* reflections for the silicate hydrates in the range of 2.56–2.68 Å and 1.55–1.60 Å (Fig. 7.4) indicate that the lattice parameters *a* and *b* of the M-F(II)-S-H may be intermediate values between those of the M-S-H and the F(II)-S-H. Moreover, the M-F(II)-S-H showed intermediate spectroscopic characteristics with respect to Si–O vibrations (Fig. 7.5).

As initial solution concentrations of dissolved Mg and Fe are the same, the composition of Mg and Fe in the solid phase are also equal, which was evaluated by solution concentration measurements (Table 7.1) and the Cliff-Lorimer quantification for solid particles in STEM/EDS analysis (Fig. 7.6b). At pH 12, dissolved Mg concentration in the Mg–Fe(II)–Si–H_2O system and that from Mg/Si 1 in the Mg–Si–H_2O system (Table 4.1) were equal, whereas Fe concentration in the Mg–Fe(II)–Si–H_2O system and that from Fe/Si 1 in the Fe(II)–Si–H_2O system were completely different. Therefore, the solution chemistry for silicate precipitation in the Mg–Fe(II)–Si–H_2O system is similar to that in the Mg–Si–H_2O system, not Fe(II)–Si–H_2O system.

Future study needs to further understand solid solution series between M-S-H and F(II)-S-H. M-F(II)-S-H will have various Mg/Fe ratios. With increasing Mg/Fe ratios, the *hk* reflections of the M-F(II)-S-H will be observed at larger *d* positions within the range of 2.56–2.68 Å and 1.55–1.60 Å. The similar trend is observed in XRD patterns of the Mg–Fe(II) saponite samples hydrothermally synthesized by Baldermann et al. (2014) and Chemtob et al. (2015).

7.5 Summary and conclusions

This chapter confirmed the formation of poorly crystalline Fe(II) silicate at low temperature (F(II)-S-H). F(II)-S-H structure is likely similar to M-S-H although F(II)-S-H can form even at neutral pH. Fe(II) hydroxide phases also form with F(II)-S-H in alkaline solution in Fe–Si–H_2O systems, similar to the case in Mg–Si–H_2O systems. Moreover, this chapter demonstrated a solid solution of M-S-H and F(II)-S-H (i.e., M-F(II)-S-H), showing intermediate characteristics of M-S-H and F(II)-S-H.

Chapter 8: Geochemical reaction modeling of M-S-H formation for geoengineering applications

8.1 Introduction

M-S-H has not been commonly considered in geoengineering although it possibly forms in various environments. The objective of this chapter is to estimate the formation of M-S-H in geothermal scaling and ERW using geochemical modeling (i.e., [iv] in Section 1.4). Effects of M-S-H formation on these two fields have not been considered sufficiently in previous studies, whereas those for cement production and radioactive waste management have been discussed especially in recent years. This chapter used the "React" module of the Geochemist's Workbench software (GWB v. 12). The thermodynamic data for M-S-H obtained by Lothenbach et al. (2019) were added to the Thermoddem database (Blanc et al., 2012).

8.2 Formation of M-S-H scale in geothermal powerplants

Mg silicate precipitation is observed at a binary cycle geothermal power plant in Obama-cho, Unzen-shi, Nagasaki, Japan (Morita and Umezawa, 2016; Morita et al., 2017). The Obama geothermal water shows pH 8.2 and Na^+–Cl^- type (Table 8.1). The scale is composed of aragonite and poorly crystalline Mg silicate (= M-S-H), the same as the mineral paragenesis in Chapter 6. Since aragonite and M-S-H tend to form at high pH, adding acid would inhibit their formation.

1 kg of the Obama geothermal water (100°C) was assumed in the modeling. The dissolved species (Table 8.1) were added to the "*Basis*" and pH was set to slide from 8.2 to 4.0 in the "*Reactants*" of the React module. This section shows the thermodynamically stable phases, so that precipitation kinetics is not considered. This calculation suppressed the formation of the following minerals: anthophyllite, antigorite, calcite, chrysotile, cristobalite, cummingtonite, diopside, dolomite, enstatite, forsterite, huntite, lizardite, magnesite, quartz, sepiolite, talc, and tremolite. Rather than $M_{1.5}SH_{2.5}$ (M-S-H with

Mg/Si 1.5), $M_{1.5}S_2H_{2.5}$ (M-S-H with Mg/Si 0.75) is used in this modeling because Mg/Si ratios of the M-S-H samples showed 0.57–0.94 in the field experiments (Morita et al., 2021).

Table 8.1.

The concentration of major dissolved species at 102**°C** in the Obama geothermal water (Morita et al., 2017).

pH	8.2
Na (ppm)	2510
K (ppm)	290
Ca (ppm)	134
Mg (ppm)	128
Cl^- (ppm)	4530
SO_4^{2-} (ppm)	297
Al (ppm)	< 0.01
HCO_3^- (ppm)	166
F^- (ppm)	0.53
B (ppm)	15.2
As (ppm)	0.42
SiO_2 (ppm)	223

The modeling results (Fig. 8.1) showed formation of M-S-H and aragonite with minor brucite at the original pH (i.e., 8.2). The more acid reacts, the lower pH becomes. The amount of aragonite decreases until ~8.5 mmol of acid is added (pH 6.83) and that of M-S-H decreases until ~13.5 mmol of acid is added (pH 6.39). Chalcedony starts to precipitate when ~11.5 mmol of acid is added (pH 6.43) although the amount of chalcedony becomes constant with >14 mmol acid (pH 6.36). To inhibit Mg silicate formation and reduce the amount of scales, 14 mmol of acid (per 1 kg) should be added and pH $\lesssim$ 6.4 will be required. Although this treatment cannot inhibit the silica (chalcedony) scale, the volume of the silica scale is smaller than the volume of the original scale (M-S-H and aragonite precipitates at pH 8.2). It is worth avoiding the M-S-H scale as M-S-H is possibly transformed into smectite (stevensite or saponite), which shows high expandability and low permeability.

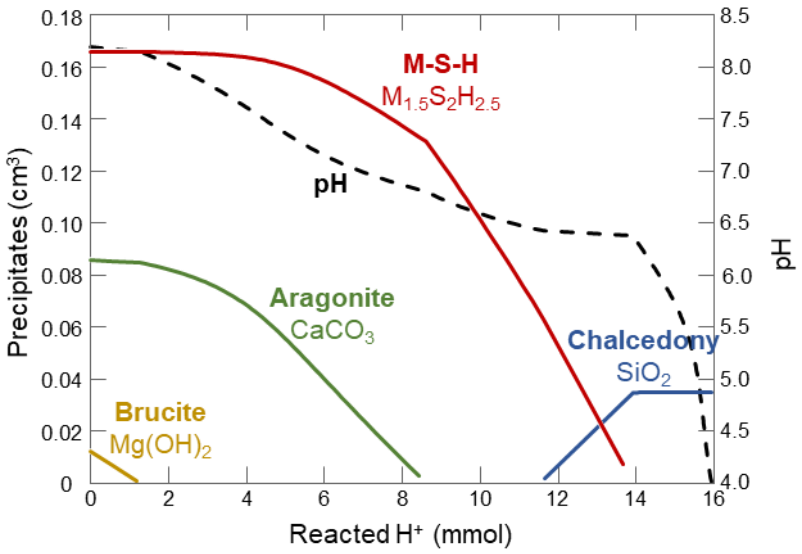

Fig. 8.1. Effect of the acid addition on precipitation in the Obama geothermal water (1 kg).

8.3 Formation of M-S-H in ERW

Forsterite (Mg olivine; Mg_2SiO_4) is one of the key minerals for ERW. Forsterite is a common component of ultramafic rock (peridotite) and mafic rock (basalt). Since divalent ions like Mg^{2+} can be used for CO_2 mineralization, forsterite is effective because of its high dissolution rate and high Mg content. Its Mg^{2+} release rate is fast at a wide pH range (Snæbjörnsdóttir et al., 2020) and its Mg/Si ratio is high (= 2) when compared with other Mg silicate minerals (e.g., Mg/Si = 1.5 for serpentine, = 1 for enstatite, = 0.875 for cummingtonite or anthophyllite, and = 0.75 for talc). The best scenario is that Mg carbonate and silica are precipitated by the dissolution of forsterite (Fig. 8.2).

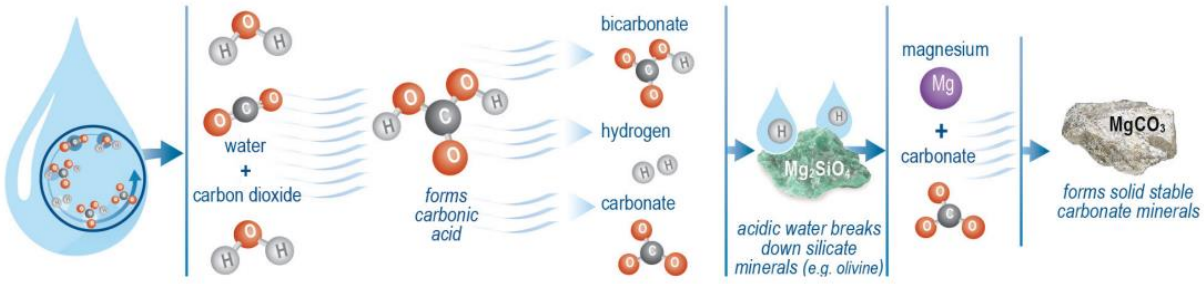

Fig. 8.2. CO_2 mineralization process from forsterite (Sandalow et al., 2021).

Therefore, this section investigated the precipitation of secondary phases in a forsterite–CO_2–H_2O system. In this modeling, forsterite (total mass = 2 kg) was gradually added to water (1 kg at 25°C) equilibrated with CO_2 in the air (Fig. 8.3). CO_2 gas (fugacity = $10^{-3.5}$) was contained in the "*Basis*" and 2 kg of forsterite was added to the "*Reactants*" with the constant fugacity of CO_2 gas. This section shows the final state of the reaction, so that precipitation kinetics was not considered. This calculation suppressed the formation of the following minerals: anthophyllite, antigorite, chalcedony, chrysotile, coesite, cristobalite, cummingtonite, enstatite, lizardite, magnesite, quartz, sepiolite, and talc. Rather than $M_{1.5}S_1H_{2.5}$ (M-S-H with Mg/Si 0.75), $M_{1.5}S_2H_{2.5}$ (M-S-H with Mg/Si 0.75) is used in this modeling because the Mg/Si ratio of forsterite is >1 and precipitation of serpentine-type M-S-H was observed on the ultramafic rock in Chapter 6. Magnesite ($MgCO_3$) formation was suppressed because of kinetic inhibition at low temperatures (Snæbjörnsdóttir et al., 2020).

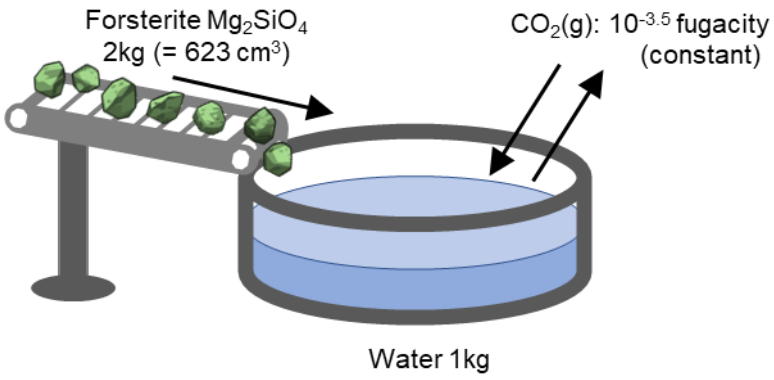

Fig. 8.3. Concept of the geochemical reaction modeling in forsterite–CO_2–H_2O system.

Here, the results of calculations without and with M-S-H are illustrated in Fig. 8.4a and b, respectively. The amount of secondary minerals is increasing by adding forsterite to the system. When M-S-H is not considered in the calculation, ~6 mol of hydromagnesite is precipitated by adding 2 kg forsterite. When M-S-H is considered in the calculation, however, only ~1.5 mol of hydromagnesite is finally precipitated with ~14 mol of M-S-H. Although ~1 kg of CO_2 is thought to be removed from the

atmosphere without considering M-S-H formation, only ~250 g of CO_2 is removed as M-S-H forms (Fig. 8.5). This study suggests that simulation of CO_2 mineralization in ERW must include formation of M-S-H in addition to carbonate minerals.

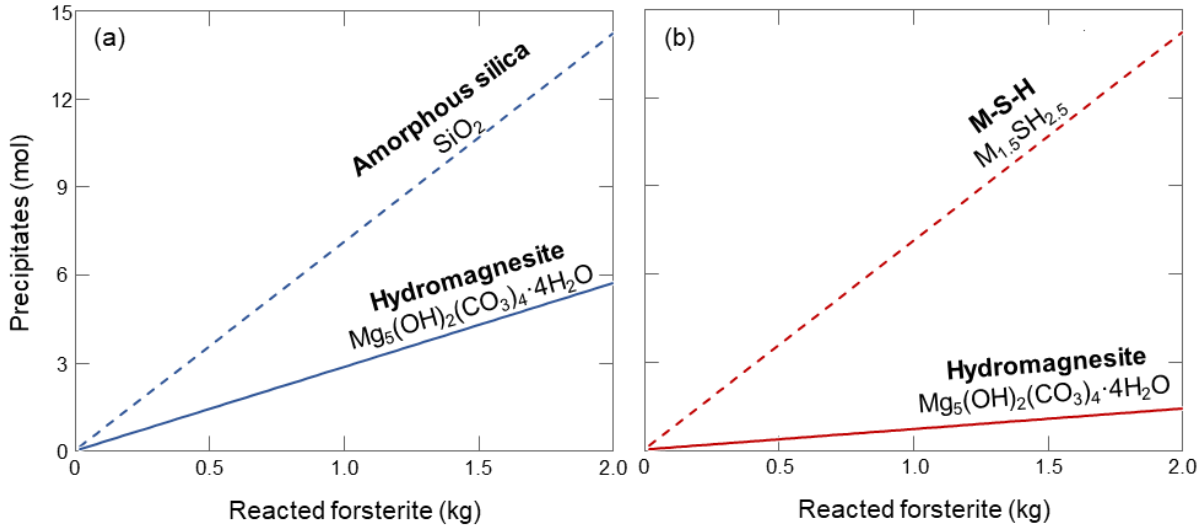

Fig. 8.4. Prediction of secondary phases in the forsterite–CO_2–H_2O system (Fig. 8.3) (a) without and (b) with considering M-S-H formation.

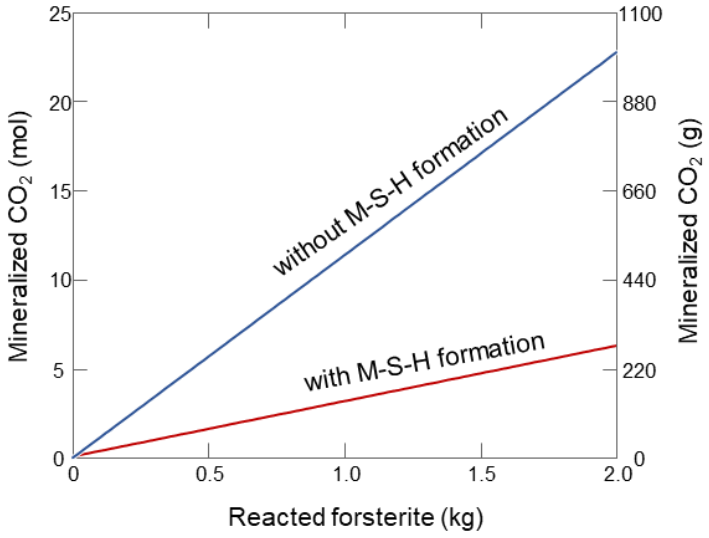

Fig. 8.5. Prediction of the amount of mineralized CO_2 in the forsterite–CO_2–H_2O system (Fig. 8.3) (a) without and (b) with considering M-S-H formation.

Future studies should seek measures to avoid M-S-H formation and enhance CO_2 mineralization. Ca carbonate will precipitate by the dissolution of mafic rocks with a large amount of Ca (e.g., basalt containing wollastonite or anorthite). In this case, C-S-H would not precipitate (as shown in Chapter 6 and Section 8.2). If forsterite dissolves in CO_2-rich environments, Mg carbonate may preferentially precipitate rather than M-S-H. For example, in CGS, a large amount of Mg carbonate may precipitate when fluids with high concentrations of CO_2 (i.e., high-pressure CO_2) are injected into ultramafic or mafic rocks (Felmy et al., 2012).

8.4 Summary and conclusions

The geochemical reaction modeling suggests the formation of M-S-H as a geothermal scale and a weathering product from forsterite. pH treatment will inhibit M-S-H and aragonite scaling in Obama geothermal water. When more than 14 mmol acids (per 1 kg) are added and pH becomes ≤ 6.4, M-S-H and aragonite would not precipitate. This method can minimize the volume of scales in pipes although silica scaling would occur. M-S-H formation is also predicted in ERW fields. During the weathering process of forsterite in air-saturated water, most aqueous Mg^{2+} derived from forsterite dissolution will be consumed by precipitation of M-S-H, rather than Mg carbonate phases. The effect of M-S-H on ERW must not be ignored.

Chapter 9: General conclusions and implications

9.1 Conclusions

The author investigated the formation of M-S-H phases, poorly crystalline phyllosilicates, with batch experiments, flow-through experiments, geologic surveys, and geochemical modeling. Subsections 9.1.1 and 9.1.2 conclude the results of this study.

9.1.1 Mineralogical characteristics and formation conditions of M-S-H phases

The M-S-H phases synthesized from MgO and silica fume (MgO/SiO_2 = 0.8 and 1.3) in solution (w/s ratio = 45) showed phyllosilicate structures based on TOT or TO units (Chapter 3). From MgO/SiO_2 0.8, M-S-H phases were identified to be phyllosilicate with TOT ribbons (a sepiolite-like phase) at 25°C and the one with hydrous TOT layers (a stevensite- or kerolite-like phase) at 50°C and 90°C. From MgO/SiO_2 1.3, M-S-H phases are identified to be phyllosilicate having both TOT and TO units at 25°C and 50°C and TO phyllosilicate (chrysotile) at 90°C. Assuming that the phase transformation behaviors are the same at 25°C–90°C and the transformation at higher temperatures is faster than that at 25°C, the results suggest that over more extended periods even at 25°C (i) the M-S-H phase from MgO/SiO_2 0.8 would be transformed into the hydrous TOT phyllosilicate and (ii) the M-S-H phase from MgO/SiO_2 1.3 would be transformed into TO phyllosilicate. In natural sediments at ambient temperature, Krekeler et al. (2005) observed the formation of Mg smectite via palygorskite, and Chapter 6 in this dissertation showed the formation of poorly-crystalline chrysotile.

In contrast, the M-S-H samples synthesized by mixing aqueous Mg solution and aqueous Si solution at alkaline pH (10 and 12) with Mg/Si 0.4, 0.7, 1.0, 1.3, and 1.7 are identified as TOT phyllosilicate, indicating that Mg/Si ratio does not affect phyllosilicate types in the syntheses (Chapter 4). Factors such as the w/s ratio and the presence of alkali ions (e.g., Na^+) may also determine the phyllosilicate types. It is also important to note that M-S-H phases form at alkaline pHs and do not form at neutral pH.

M-S-H can precipitate in open-flow systems (Chapters 5 and 6), as well as in closed systems. An aqueous Si supply is necessary for the M-S-H formation. This study demonstrates the M-S-H formation at low temperatures, while Tutolo et al. (2018) studied Mg silicate formation from brucite (brucite silicification) in hydrothermal flow-through experiments at 150°C. M-S-H formation is likely a commonly occurring phenomenon under Earth surface conditions.

9.1.2 Geochemical behaviors of M-S-H

The M-S-H formation affects the dissolution kinetics of primary Mg-bearing minerals such as $Mg(OH)_2$ (Chapter 5). Dissolved Mg and Si are consumed during M-S-H precipitation, promoting the dissolution of the Mg-bearing minerals. With increasing Si concentration, the solution becomes more supersaturated with respect to M-S-H and more undersaturated with respect to $Mg(OH)_2$, so the higher the amount of Si in the system, the greater the dissolution of $Mg(OH)_2$ and precipitation of M-S-H.

In Mg–Fe(II)–Si–H_2O systems, M-F(II)-S-H phases can form, showing intermediate characteristics of M-S-H and F(II)-S-H (Chapter 7). In Mg–Ca–Si–H_2O systems, the formation of two separate M-S-H and C-S-H phases is known (Lothenbach et al., 2015; Bernard et al., 2018). This is due to the difference in their ionic radii ($Mg^{2+} \approx Fe^{2+} < Ca^{2+}$). It is observed that M-S-H (without Ca) precipitates simultaneously with aragonite on the surface of the ultramafic rock in Mg–Ca–Si–CO_2–H_2O systems around pH 10 (Chapter 6).

9.2 Implications

9.2.1 Implications for geosciences

Mineral–water interaction in ultramafic rocks around the Earth's surface is recognized as "low-temperature serpentinization" (Templeton and Ellison, 2020). However, this study suggests that the secondary silicate can be M-S-H, which has TOT and/or TO units (Chapter 3). Products in the low-

temperature serpentinization are not always serpentine (TO phyllosilicate). The Mg/Si ratio of pore fluids in the ultramafic rock is likely an important factor determining the phyllosilicate types (Chapter 3) although other parameters (w/s ratio or concentrations of alkali ions) may also affect the structure of M-S-H (Chapter 4). Moreover, M-F(II)-S-H phases possibly form where Mg^{2+} is dissolved with Fe^{2+} in the pore fluids of the ultramafic rocks (Chapter 7).

M-S-H would be metastable phases and transformed into more stable silicate minerals in long time scales (Chapter 3). This suggests that where there are interactions of ultramafic rocks and alkaline fluids on the Earth surface, some serpentinites may consist of M-S-H (and possibly crystalline serpentine generated by phase transformation from the M-S-H) as well as serpentine generated by ordinarily considered "serpentinization" (Chapter 6).

The formation of M-S-H has likely been neglected in earlier geological studies because of their low crystallinity. For instance, the M-S-H sample (synthesized at pH 12 and Mg/Si 1.3 in Chapter 4) and forsterite (collected from the Damaping area of Hebei Province, China) were mixed with an agate mortar and pestle and characterized by XRD (Miniflex600-C with D/teX Ultra2 at 40kV, 15 mA, 1° 2θ min^{-1}, and 0.01° 2θ step; Subsection 4.2.2). The peaks for M-S-H are not clearly shown in the XRD profile of the mixtures of M-S-H (≤50 wt%) and forsterite (≥50 wt%), whereas they can be observed when M-S-H is a predominant phase (≥80 wt%) in the sample (Fig. 9.1).

The results of this study also indicate that the presence of aqueous Si contributes to increasing dissolution of primary Mg-bearing minerals (Chapter 5). This appears inconsistent with earlier studies: Pokrovsky and Schott (2000) found that forsterite dissolution was inhibited by dissolved silica at alkaline pH; Oelkers and Gislason (2001) and Oelkers and Schott (2001) found that dissolution rates of enstatite and basaltic glass are independent of dissolved silica concentration; Cama et al. (2000) found that the smectite dissolution rate decreases with increasing aqueous silica concentration at pH 8.8 because of the deviation from equilibrium and/or Si inhibition; but these studies did not consider the formation of secondary minerals such as M-S-H.

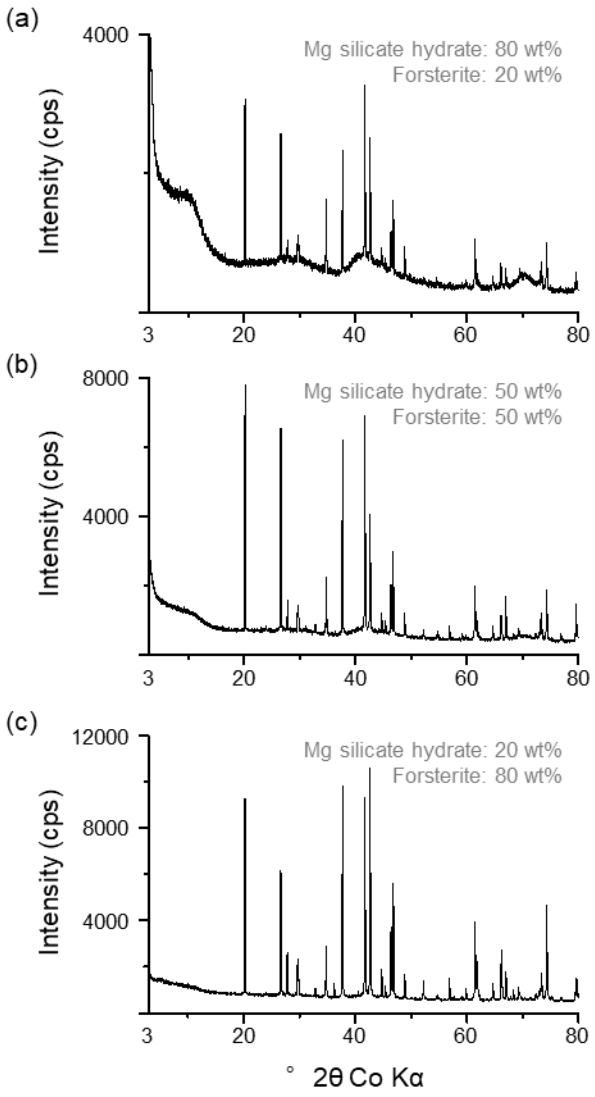

Fig. 9.1. XRD patterns of mixtures of the M-S-H synthesized in Chapter 4 (Mg/Si 1.3 at pH 12) and forsterite.

9.2.2 Implications for geoengineering

This study would also provide significant implications for the engineering geology applications. M-S-H phases are likely precursors for Mg silicate minerals (e.g., stevensite) in geothermal scaling at ~100°C (Chapter 3). There will be few kinetic hindrances for forming M-S-H in open-flow systems (Chapter 5). M-S-H forms at alkaline pH and does not form at neutral pH (or most likely at acid pH) (Chapter 4), so that the pH treatment can avoid the M-S-H precipitation (Chapter 8).

For CGS or ERW, Mg carbonate minerals have been expected as host phases for CO_2 trapping as well as Ca carbonates. However, this study suggests that the M-S-H phase should be considered to assess the amount of fixed CO_2 (Chapter 8). M-S-H will precipitate in some environments in which aqueous Mg has previously been thought to be consumed by precipitation as Mg carbonate or Mg hydroxide phases. With respect to thermodynamics, M-S-H, Mg carbonate, and Mg hydroxide phases can commonly form under similar pH conditions. However, M-S-H may preferentially form when the system includes Si. Mg hydroxide forms in the excess dissolved Mg (Chapter 4). Likewise, Mg carbonates may be predominant products under CO_2, HCO_3^-, or CO_3^{2-}-rich conditions in Mg–Si–CO_2–H_2O systems. In the system containing Ca, dissolved Mg is consumed by precipitation of M-S-H, while dissolved carbonate species are consumed by that of Ca carbonate, rather than Mg carbonate (Chapter 6). For CO_2 mineralization (especially in ERW), therefore, Ca-bearing rocks should be selected as the reactants.

Formation of M-S-H will also be a key issue for radioactive waste disposal in underground repositories. This study demonstrates M-S-H formation by the flow of the Si-rich solution (1.5 mM, near-saturation with respect to amorphous silica) in Chapter 5. Given that the pore fluids of concrete materials show high Si concentration and those of bentonite are saturated with respect to amorphous silica (Suzuki-Muresan et al., 2011), M-S-H is possibly formed with the groundwater flow towards the engineered barriers. Under the Si-rich conditions, the M-S-H phase may show characteristics of hydrous TOT phyllosilicate (Chapters 3 and 5). The advantages of hydrous TOT phyllosilicate formation for the barriers will be great potential for radionuclide (e.g., Cs) retention as decreasing pores (Cuevas et al., 2016; Fernández et al., 2018) or trapping the radionuclides (Brew and Glasser, 2005b; Zhang et al., 2020).

References

1. Aglietti E. F. (1994) The effect of dry grinding on the structure of talc. *Appl Clay Sci* **9**, 139–147.

2. Ahrens L. H. (1952) The use of ionization potentials Part 1. Ionic radii of the elements. *Geochim Cosmochim Acta* **2**, 155–169.

3. Allen D. E. and Seyfried W. E. (2004) Serpentinization and heat generation: Constraints from Lost City and Rainbow hydrothermal systems. *Geochim Cosmochim Acta* **68**, 1347–1354.

4. Andreani M., Luquot L., Gouze P., Godard M., Hoisé E. and Gibert B. (2009) Experimental study of carbon sequestration reactions controlled by the percolation of CO2-rich brine through peridotites. *Environ Sci Technol* **43**, 1226–1231.

5. Anraku S., Matsubara I., Morimoto K. and Sato T. (2017) Geochemical factors for secondary mineral formation at naturally-occurring hyperalkaline spring in Oman ophiolite. *Journal of the Clay Science Society of Japan (in Japanese with English abstract)* **55**, 17–30.

6. Asahina T. and Komatsu M. (1979) The Horokanai ophiolitic complex in the Kamuikotan tectonic belt, Hokkaido, Japan. *Journal of the Geological Society of Japan* **85**, 317–330.

7. Atkinson A., Everitt N. M. and Guppy R. M. (1989) Time Depndence of pH in a Cementitious Repository. *Materials Research Society Symposium Proceedings* **127**, 439–446.

8. Baldermann A., Dohrmann R., Kaufhold S., Nickel C., Letofsky-Papst I. and Dietzel M. (2014) The Fe-Mg-saponite solid solution series – a hydrothermal synthesis study. *Clay Miner* **49**, 391–415.

9. Barnes I. and O'Neil J. R. (1969) The Relationship between Fluids in Some Fresh Alpine-Type Ultramafics and Possible Modern Serpentinization, Western United States. *Geol Soc Am Bull* **80**, 1947–1960.

10. Barnes I., O'Neil J. R. and Trescases J. J. (1978) Present day serpentinization in New Caledonia, Oman and Yugoslavia. *Geochim Cosmochim Acta* **42**, 144–145.

11. Benhammou A., Tanouti B., Nibou L., Yaacoubi A. and Bonnet J. P. (2009) Mineralogical and physicochemical investigation of mg-smectite from jbel ghassoul, Morocco. *Clays Clay Miner* **57**, 264–270.

12. Bernal J. D., Dasgupta D. R. and Mackay A. L. (1959) The Oxides and Hydroxides of Iron and Their Structural Inter-Relationships. *Clay Miner* **4**, 15–30.

13. Bernard E., Lothenbach B., Cau-Dit-Coumes C., Chlique C., Dauzères A. and Pochard I. (2018) Magnesium and calcium silicate hydrates, Part I: Investigation of the possible magnesium incorporation in calcium silicate hydrate (C-S-H) and of the calcium in magnesium silicate hydrate (M-S-H). *Applied Geochemistry* **89**, 229–242.

14. Bernard E., Lothenbach B., Cau-Dit-Coumes C., Pochard I. and Rentsch D. (2020) Aluminum incorporation into magnesium silicate hydrate (M-S-H). *Cem Concr Res* **128**, 105931.

15. Bernard E., Lothenbach B., Chlique C., Wyrzykowski M., Dauzères A., Pochard I. and Cau-Dit-Coumes C. (2019a) Characterization of magnesium silicate hydrate (M-S-H). *Cem Concr Res* **116**, 309–330.

16. Bernard E., Lothenbach B., Pochard I. and Cau-Dit-Coumes C. (2019b) Alkali binding by magnesium silicate hydrates. *Journal of the American Ceramic Society* **102**, 6322–6336.

17. Bernard E., Lothenbach B., Rentsch D., Pochard I. and Dauzères A. (2017) Formation of magnesium silicate hydrates (M-S-H). *Physics and Chemistry of the Earth* **99**, 142–157.

18. Besselink R., Stawski T. M., Freeman H. M., Hövelmann J., Tobler D. J. and Benning L. G. (2020) Mechanism of Saponite Crystallization from a Rapidly Formed Amorphous Intermediate. *Cryst Growth Des* **20**, 3365–3373.

19. Bish D. L. and Brindley G. W. (1978) Deweylites, mixtures of poorly crystalline hydrous serpentine and talc-like minerals. *Mineral Mag* **42**, 75–79.

20. Blanc P., Lassin A., Piantone P., Azaroual M., Jacquemet N., Fabbri A. and Gaucher E. C. (2012) Thermoddem: A geochemical database focused on low temperature water/rock interactions and waste materials. *Applied Geochemistry* **27**, 2107–2116.

21. Blinova A. I., Zega T. J., Herd C. D. K. and Stroud R. M. (2014) Testing variations within the Tagish Lake meteorite-I: Mineralogy and petrology of pristine samples. *Meteorit Planet Sci* **49**, 473–502.

22. Brew D. R. M. and Glasser F. P. (2005a) Synthesis and characterisation of magnesium silicate hydrate gels. *Cem Concr Res* **35**, 85–98.

23. Brew D. R. M. and Glasser F. P. (2005b) The magnesia-silica gel phase in slag cements: Alkali (K, Cs) sorption potential of synthetic gels. *Cem Concr Res* **35**, 77–83.

24. Brindley G. W., Bish D. L. and Wan H.-M. (1977) The nature of kerolite, its relation to talc and stevensite. *Mineral Mag* **41**, 443–452.

25. Brindley G. W. and Brown G. (1980) *Crystal structures of clay minerals and their X-Ray identification*., Mineralogical Society of Great Britain and Ireland.

26. Bristow T. F., Bish D. L., Vaniman D. T., Morris R. v., Blake D. F., Grotzinger J. P., Rampe E. B., Crisp J. A., Achilles C. N., Ming D. W., Ehlmann B. L., King P. L., Bridges J. C., Eigenbrode J. L., Sumner D. Y., Chipera S. J., Moorokian J. M., Treiman A. H., Morrison S. M., Downs R. T., Farmer J. D., des Marais D., Sarrazin P., Floyd M. M., Mischna M. A. and McAdam A. C. (2015) The origin and implications of clay minerals from Yellowknife Bay, Gale crater, Mars. *American Mineralogist* **100**, 824–836.

27. Cama J., Ganor J., Ayora C. and Lasaga C. A. (2000) Smectite dissolution kinetics at 80°C and pH 8.8. *Geochim Cosmochim Acta* **64**, 2701–2717.

28. Chavagnac V., Monnin C., Ceuleneer G., Boulart C. and Hoareau G. (2013) Characterization of hyperalkaline fluids produced by low-temperature serpentinization of mantle peridotites in the Oman and Ligurian ophiolites. *Geochemistry, Geophysics, Geosystems* **14**, 2496–2522.

29. Chemtob S. M., Nickerson R. D., Morris R. v., Agresti D. G. and Catalano J. G. (2017) Oxidative Alteration of Ferrous Smectites and Implications for the Redox Evolution of Early Mars. *J Geophys Res Planets* **122**, 2469–2488.

30. Chemtob S. M., Nickerson R. D., Morris R. v., Agresti D. G. and Catalano J. G. (2015) Synthesis and structural characterization of ferrous trioctahedral smectites: Implications for clay mineral genesis and detectability on Mars. *J Geophys Res Planets* **120**, 1119–1140.

31. Chemtob S. M., Rossman G. R. and Stebbins J. F. (2012) Natural hydrous amorphous silica: Quantitation of network speciation and hydroxyl content by 29Si MAS NMR and vibrational spectroscopy. *American Mineralogist* **97**, 203–211.

32. Cheng W., Li Z. and Demopoulos G. P. (2009) Effects of Temperature on the Preparation of Magnesium Carbonate Hydrates by Reaction of MgCl2 with Na2CO3. *Chin J Chem Eng* **17**, 661–666.

33. Craw D., Landis C. A. and Kelsey P. I. (1987) Authigenic chrysotile formation in the matrix of Quaternary debris flows, northern Southland, New Zealand. *Clays Clay Miner* **35**, 43–52.

34. Cuevas J., Ruiz A. I., Fernández R., Torres E., Escribano A., Regadío M. and Turrero M. J. (2016) Lime mortar-compacted bentonite-magnetite interfaces: An experimental study focused on the understanding of the EBS long-term performance for high-level nuclear waste isolation DGR concept. *Appl Clay Sci* **124–125**, 79–93.

35. Dauzeres A., Achiedo G., Nied D., Bernard E., Alahrache S. and Lothenbach B. (2016) Magnesium perturbation in low-pH concretes placed in clayey environment - Solid characterizations and modeling. *Cem Concr Res* **79**, 137–150.

36. d'Espinose de la Caillerie J.-B. and Fripiat J. J. (1994) A reassessment of the 29Si MAS-NMR spectra of sepiolite and aluminated sepiolite. *Clay Miner* **29**, 313–318.

37. Drits V. A., Sakharov B. A., Salyn A. L. and Manceau A. (1993) Surface structural model for ferrihydrite. *Clay Miner* **28**, 185–207.

38. Dumas A., Martin F., le Roux C., Micoud P., Petit S., Ferrage E., Brendlé J., Grauby O. and Greenhill-Hooper M. (2013) Phyllosilicates synthesis: a way of accessing edges contributions in NMR and FTIR spectroscopies. Example of synthetic talc. *Phys Chem Miner* **40**, 361–373.

39. Eberl D. D., Jones B. F. and Khoury H. N. (1982) Mixed-layer kerolite/stevensite from the Amargosa Desert, Nevada. *Clays Clay Miner* **30**, 321–326.

40. Eggleton R. A. and Fitzpatrick R. W. (1988) New Data and a Revised Structural Model for Ferrihydrite. *Clays Clay Miner* **36**, 111–124.

41. Ehlmann B. L., Berger G., Mangold N., Michalski J. R., Catling D. C., Ruff S. W., Chassefière E., Niles P. B., Chevrier V. and Poulet F. (2013) Geochemical consequences of widespread clay mineral formation in Mars' ancient crust. *Space Sci Rev* **174**, 329–364.

42. Ehlmann B. L., Mustard J. F., Murchie S. L., Bibring J. P., Meunier A., Fraeman A. A. and Langevin Y. (2011) Subsurface water and clay mineral formation during the early history of Mars. *Nature* **479**, 53–60.

43. Evans B. W. (2004) International Geology Review. *Int Geol Rev* **46**, 479–506.

44. Farmer V. C. (1974) *The Infrared Spectra of Minerals*., Mineralogical Society, London.

45. Felmy A. R., Qafoku O., Arey B. W., Hu J. Z., Hu M., Todd Schaef H., Ilton E. S., Hess N. J., Pearce C. I., Feng J. and Rosso K. M. (2012) Reaction of water-saturated supercritical CO2 with forsterite: Evidence for magnesite formation at low temperatures. *Geochim Cosmochim Acta* **91**, 271–282.

46. Fernández R., González-Santamaría D., Angulo M., Torres E., Ruiz A. I., Turrero M. J. and Cuevas J. (2018) Geochemical conditions for the formation of Mg silicates phases in bentonite and implications for radioactive waste disposal. *Applied Geochemistry* **93**, 1–9.

47. Fernández R., Torres E., Ruiz A. I., Cuevas J., Alonso M. C., García Calvo J. L., Rodríguez E. and Turrero M. J. (2017) Interaction processes at the concrete-bentonite interface after 13 years of FEBEX-Plug operation. Part II: Bentonite contact. *Physics and Chemistry of the Earth* **99**, 49–63.

48. Finster M., Clark C., Schroeder J. and Martino L. (2015) Geothermal produced fluids: Characteristics, treatment technologies, and management options. *Renewable and Sustainable Energy Reviews* **50**, 952–966.

49. Földvári M. (2011) *Handbook of thermogravimetric system of minerals and its use in geological practice*., Geological Institute of Hungary.

50. Francisco P. C. M., Mitsui S. and Ishidera T. (2020) Interaction of Fe II and Si under anoxic and reducing conditions: Structural characteristics of ferrous silicate co-precipitates. *Geochim Cosmochim Acta* **270**, 1–20.

51. Fruhwirth O., Herzog G. W., Hollerer I. and Rachetti A. (1985) Dissolution and hydration kinetics of MgO. *Surface Technology* **24**, 301–317.

52. Furquim S. A. C., Graham R. C., Barbiero L., de Queiroz Neto J. P. and Vallès V. (2008) Mineralogy and genesis of smectites in an alkaline-saline environment of Pantanal wetland, Brazil. *Clays Clay Miner* **56**, 579–595.

53. Gaboreau S., Rodríguez-Cañas E., Maeder U., Jenni A., Turrero M. J. and Cuevas J. (2020) Concrete perturbation in a 13-year in situ concrete/bentonite interaction from FEBEX experiments. New insight of 2:1 Mg phyllosilicate precipitation at the interface. *Applied Geochemistry* **118**, 104624.

54. Gainey S. R., Hausrath E. M., Adcock C. T., Tschauner O., Hurowitz J. A., Ehlmann B. L., Xiao Y. and Bartlett C. L. (2017) Clay mineral formation under oxidized conditions and implications for paleoenvironments and organic preservation on Mars. *Nat Commun* **8**, 1–7.

55. Gallup D. L. (1998) Aluminum Silicate Scale Formation and Inhibition (2): Scale SOlubilities and Laboratory and Field Inhibition Tests. *Geothermics* **27**, 485–501.

56. Gallup D. L. (1997) Aluminum silicate scale formation and inhibition: scale characterization and laboratory experiments. *Geothermics* **26**, 483–499.

57. Gallup D. L. and Reiff W. M. (1991) Characterization of geothermal scale deposits by Fe-57 mössbauer spectroscopy and complementary x-ray diffraction and infra-red studies. *Geothermics* **20**, 207–224.

58. García M. A., Chimenos J. M., Fernández A. I., Miralles L., Segarra M. and Espiell F. (2004) Low-grade MgO used to stabilize heavy metals in highly contaminated soils. *Chemosphere* **56**, 481–491.

59. Geological Survey of Japan (2022) Seamless Digital Geological Map of Japan (V2).

60. Giampouras M., Garrido C. J., Bach W., Los C., Fussmann D., Monien P. and García-Ruiz J. M. (2020) On the controls of mineral assemblages and textures in alkaline springs, Samail Ophiolite, Oman. *Chem Geol* **533**, 119435.

61. Gislason S. R., Wolff-Boenisch D., Stefansson A., Oelkers E. H., Gunnlaugsson E., Sigurdardottir H., Sigfusson B., Broecker W. S., Matter J. M., Stute M., Axelsson G. and Fridriksson T. (2010) Mineral sequestration of carbon dioxide in basalt: A pre-injection overview of the CarbFix project. *International Journal of Greenhouse Gas Control* **4**, 537–545.

62. Golden D. C. and Dixon J. B. (1990) Low-temperature alteration of palygorskite to smectite. *Clays Clay Miner* **38**, 401–408.

63. González-Santamaría D. E., Justel A., Fernández R., Ruiz A. I., Stavropoulou A., Rodríguez-Blanco J. D. and Cuevas J. (2021) SEM-EDX study of bentonite alteration under the influence of cement alkaline solutions. *Appl Clay Sci* **212**.

64. Grangeon S., Claret F., Roosz C., Sato T., Gaboreau S. and Linard Y. (2016) Structure of nanocrystalline calcium silicate hydrates: Insights from X-ray diffraction, synchrotron X-ray absorption and nuclear magnetic resonance. *J Appl Crystallogr* **49**, 771–783.

65. Guggenheim S. and Eggleton T. (1986) Structural modulations in iron-rich and magnesium-rich minnesotaite. *The Canadian Mineralogist* **24**, 479–497.

66. Guven N. and Carney L. L. (1979) The hydrothermal transformation of sepiolite to stevensite and the effect of added chlorides and hydroxides. *Clays Clay Miner* **27**, 253–260.

67. Hellevang H., Haile B. G. and Tetteh A. (2017) Experimental study to better understand factors affecting the CO2 mineral trapping potential of basalt. *Greenhouse Gases: Science and Technology* **2**, 143–157.

68. Hino M. and Sato T. (1971) Infrared absorption spectra of silica gel - H216O, D216O and H218O systems. *Bull Chem Soc Jpn* **44**, 33–37.

69. Howard K. T., Benedix G. K., Bland P. A. and Cressey G. (2009) Modal mineralogy of CM2 chondrites by X-ray diffraction (PSD-XRD). Part 1: Total phyllosilicate abundance and the degree of aqueous alteration. *Geochim Cosmochim Acta* **73**, 4576–4589.

70. Igami Y., Tsuchiyama A., Yamazaki T., Matsumoto M. and Kimura Y. (2021) In-situ water-immersion experiments on amorphous silicates in the MgO–SiO2 system: implications for the onset of aqueous alteration in primitive meteorites. *Geochim Cosmochim Acta* **293**, 86–102.

71. Imai N., Otsuka R., Nakamura T. and Inoue H. (1966) A new occurrence of well-crystallized sepiolite from the Kuzu District, Tochigi Prefecture, Central Japan. *Journal of the Clay Science Society of Japan (in Japanese with English abstract)* **6**, 30–40.

72. JAEA (Japan Atomic Energy Agency) (2018) *JAEA R&D Review 2017-18*. ed. H. Mineo, Ibaraki, Japan.

73. Jakobsen U. H., de Weerdt K. and Geiker M. R. (2016) Elemental zonation in marine concrete. *Cem Concr Res* **85**, 12–27.

74. Jenni A., Mäder U., Lerouge C., Gaboreau S. and Schwyn B. (2014) In situ interaction between different concretes and Opalinus Clay. *Physics and Chemistry of the Earth* **70–71**, 71–83.

75. Kamitsos E. I., Patsis A. P. and Kordas G. (1993) Infrared-reflectance spectra of heat-treated sol-gel-derived silica. *Phys Rev B* **48**, 12499–12505.

76. Kasai K., Sato K., Kimura S., Shakunaga N. and Obara K. (2000) Characterization of smectite scale and scale inhibition test by pH control at the Mori geothermal power plant, Japan. In *Proceedings of the World Geothermal Congress 2000* pp. 1331–1336.

77. Katoh T., and Nakagawa M. (1986) Tectogenesis of ultramafic rocks in the Kamuikotan tectonic belt, Hokkaido, Japan. *Monograph of the Association for the Geological Collaboration in Japan (in Japanese with English abstract)* **31**, 119–135.

78. Kelemen, P. B., Aines, R., Bennett, E., Benson, S. M., Carter, E., Coggon, J. A., De Obeso, J. C., Evans, O., Gadikota, G., Dipple, G. M., Godard, M., Harris, M., Higgins, J. A., Johnson, K. T. M., Kourim, F., Lafay, R., Lambart, S., Manning, C. E., Matter, J. M., Michibayashi, K., Morishita, T., Noël, J., Okazaki, K., Renforth, P., Robinson, B., Savage, H., Skarbek, R., Spiegelman, M. W., Takazawa, E., Teagle, D., Urai, J. L. and Wilcox, J. (2018) *In situ* carbon mineralization in ultramafic rocks: Natural processes and possible engineered methods. *Energy Procedia* 146, 92–102.

79. Kelemen, P., Benson, S. M., Pilorgé, H., Psarras, P. and Wilcox, J. (2019) An Overview of the Status and Challenges of CO_2 Storage in Minerals and Geological Formations. *Frontiers in Climate* **1**, 1–20.

80. Khoury H., Eberl D. D. and Jones B. F. (1982) Origin of Magnesium Clays from the Amargosa Desert, Nevada. *Clays Clay Miner* **30**, 327–336.

81. Kieffer S. W. (1979) Thermodynamics and lattice vibrations of minerals: 2. Vibrational characteristics of silicates. *Reviews of Geophysics* **17**, 20–34.

82. King A. J., Schofield P. F., Howard K. T. and Russell S. S. (2015) Modal mineralogy of CI and CI-like chondrites by X-ray diffraction. *Geochim Cosmochim Acta* **165**, 148–160.

83. Kitano Y. (1962) The Behavior of Various Inorganic Ions in the Separation of Calcium Carbonate from a Bicarbonate Solution. *Bull Chem Soc Jpn* **35**, 1973–1980.

84. Kodama H., de Kimpe C. R. and Dejou J. (1988) Ferrian saponite in a gabbro saprolite at Mont Megantic, Quebec. *Clays Clay Miner* **36**, 102–110.

85. Kontoyannis C. G. and Vagenas N. v. (2000) Calcium carbonate phase analysis using XRD and FT-Raman spectroscopy. *Analyst* **125**, 251–255.

86. Krekeler M. P. S., Hammerly E., Rakovan J. and Guggenheim S. (2005) Microscopy studies of the palygorskite-to-smectite transformation. *Clays Clay Miner* **53**, 92–99.

87. de la Fuente García-Soto M. M. and Muñoz Camacho E. (2009) Boron removal by means of adsorption processes with magnesium oxide - Modelization and mechanism. *Desalination* **249**, 626–634.

88. Lafay R., Fernandez-Martinez A., Montes-Hernandez G., Auzende A. L. and Poulain A. (2016) Dissolution-reprecipitation and self-assembly of serpentine nanoparticles preceding chrysotile formation: Insights into the structure of proto-serpentine. *American Mineralogist* **101**, 2666–2676.

89. Lapham D. M. (1961) New data on deweylite. *American Mineralogist* **46**, 168–188.

90. Léveillé R. J., Fyfe W. S. and Longstaffe F. J. (2000) Unusual Secondary Ca-Mg-Carbonate-Kerolite Deposits in Basaltic Caves, Kauai, Hawaii. *J Geol* **108**, 613–621.

91. Li Z., Zhang T., Hu J., Tang Y., Niu Y., Wei J. and Yu Q. (2014) Characterization of reaction products and reaction process of MgO–SiO2–H2O system at room temperature. *Constr Build Mater* **61**, 252–259.

92. Liao J. and Senna M. (1992) Thermal behavior of mechanically amorphized talc. *Thermochim Acta* **197**, 295–306.

93. Loh E. (1973) Optical vibrations in sheet silicates. *Journal of Physics C: Solid State Physics* **6**, 1091–1104.

94. Lothenbach B., Kulik D. A., Matschei T., Balonis M., Baquerizo L., Dilnesa B., Miron G. D. and Myers R. J. (2019) Cemdata18: A chemical thermodynamic database for hydrated Portland cements and alkali-activated materials. *Cem Concr Res* **115**, 472–506.

95. Lothenbach B., Nied D., L'Hôpital E., Achiedo G. and Dauzères A. (2015) Magnesium and calcium silicate hydrates. *Cem Concr Res* **77**, 60–68.

96. Lothenbach B. and Nonat A. (2015) Calcium silicate hydrates: Solid and liquid phase composition. *Cem Concr Res* **78**, 57–70.

97. Lutz H. D., Möller H. and Schmidt M. (1994) Lattice vibration spectra. Part LXXXII. Brucite-type hydroxides M(OH)2 (M = Ca, Mn, Co, Fe, Cd) - IR and Raman spectra, neutron diffraction of Fe(OH)2. *J Mol Struct* **328**, 121–132.

98. MacKenzie K. J. D. and Meinhold R. H. (1994a) The thermal reactions of talc studied by 29Si and 25Mg MAS NMR. *Thermochim Acta* **244**, 195–203.

99. MacKenzie K. J. D. and Meinhold R. H. (1994b) Thermal reactions of chrysotile revisited: a 29Si and 25Mg MAS NMR study. *American Mineralogist* **79**, 43–50.

100. Mäder U., Jenni A., Lerouge C., Gaboreau S., Miyoshi S., Kimura Y., Cloet V., Fukaya M., Claret F., Otake T., Shibata M. and Lothenbach B. (2017) 5-year chemico-physical evolution of concrete–claystone interfaces, Mont Terri rock laboratory (Switzerland). *Swiss J Geosci* **110**, 307–327.

101. Mägi M., Lippmaa E., Samoson A., Engelhardt G. and Grimmer A. R. (1984) Solid-state high-resolution silicon-29 chemical shifts in silicates. *Journal of Physical Chemistry* **88**, 1518–1522.

102. Manceau A., Ildefonse P., Hazemann J. L., Flank A. M. and Gallup D. (1995) Crystal chemistry of hydrous iron silicate scale deposits at the salton sea geothermal field. *Clays Clay Miner* **43**, 304–317.

103. Marsiske M. R., Debus C., di Lorenzo F., Bernard E., Churakov S. v. and Ruiz-Agudo C. (2021) Immobilization of (aqueous) cations in low pH M-S-H cement. *Applied Sciences (Switzerland)* **11**.

104. Matsushita H., Maruyama H., Aomi T., and Ishikawa N. (1974) Silver-silver chloride electrode prepared with the use of molten silver chloride. *Memoirs of Chubu Institute of Technology* **10-A**, 117–122.

105. Milesi V. P., Jézéquel D., Debure M., Cadeau P., Guyot F., Sarazin G., Claret F., Vennin E., Chaduteau C., Virgone A., Gaucher E. C. and Ader M. (2019) Formation of magnesium-smectite during lacustrine carbonates early diagenesis: Study case of the volcanic crater lake Dziani Dzaha (Mayotte – Indian Ocean). *Sedimentology* **66**, 983–1001.

106. Morita M., Goto Y., Motoda S. and Fujino T. (2017) Thermodynamic analysis of silica-based scale precipitation induced by magnesium ion. *Journal of the Geothermal Research Society of Japan* **39**, 191–201.

107. Morita M. and Umezawa O. (2016) A model of scale formation process to inner wall of carbon steel pipe for transporting hot spring water. *Journal of the Japan Institute of Metals and Materials (in Japanese with English abstract)* **80**, 309–316.

108. Morita M., Yamaguchi A., Koyama S. and Motoda S. (2021) Geothermics Method for imitating magnesium silicate scale formed at the geothermal power plant in Obama Hot Spring , Japan. *Geothermics* **96**, 102203.

109. Munemoto T. and Fukushi K. (2008) Transformation kinetics of monohydrocalcite to aragonite in aqueous solutions. *Journal of Mineralogical and Petrological Sciences* **103**, 345–349.

110. Nagata H., Shimoda S. and Sudo T. (1974) On dehydration of bound water of sepiolite. *Clays Clay Miner* **22**, 285–293.

111. Nied D., Enemark-Rasmussen K., L'Hopital E., Skibsted J. and Lothenbach B. (2016) Properties of magnesium silicate hydrates (M-S-H). *Cem Concr Res* **79**, 323–332.

112. Ninomiya J., Mizuochi Y., Katoh T., Okamoto M. and Yajima T. (2007) CO2 Fixation in the Serpentinite-Groundwater System. *Journal of the Clay Science Society of Japan (in Japanese with English abstract)* **46**, 28–32.

113. Noda N., Yamashita S., Takahashi Y., Matsumoto M., Enokido Y., Amano K., Kawai T., Sakuma H., Fukushi K., Sekine Y. and Nakamura T. (2021) Anaerobic microscopic analysis of ferrous saponite and its sensitivity to oxidation by earth's air: Lessons learned for analysis of returned samples from mars and carbonaceous asteroids. *Minerals* **11**, 1244.

114. Nonat A. (2004) The structure and stoichiometry of C-S-H. *Cem Concr Res* **34**, 1521–1528.

115. Nozawa S., Sato T. and Otake T. (2018) Effect of Dissolved Silica on Immobilization of Boron by Magnesium Oxide. *Minerals* **8**, 76.

116. NUMO (Nuclear Waste Management Organization of Japan) (2021) *The NUMO Pre-siting SDM-based Safety Case*, NUMO-TR-21-01.

117. Oelkers, E. H., Butcher, R., von Strandmann, P. A. P., Schuessler, J. A., Von Blanckenburg, F., Snæbjörnsdóttir, S. Ó., Mesfin, K., Aradóttir, E. S., Gunnarsson, I., Sigfússon, B., Gunnlaugsson, E., Matter, J. M., Stute, M. and Gislason, S. R. (2019) Using stable Mg isotope signatures to assess the fate of magnesium during the *in situ* mineralisation of CO_2 and H_2S at the CarbFix site in SW-Iceland. *Geochim Cosmochim Acta* **245**, 542–555.

118. Oelkers E. H. and Gislason S. R. (2001) The mechanism, rates and consequences of basaltic glass dissolution: I. An experimental study of the dissolution rates of basaltic glass as a function of aqueous Al, Si and oxalic acid concentration at 25°C and pH = 3 and 11. *Geochim Cosmochim Acta* **65**, 3671–3681.

119. Oelkers E. H. and Schott J. (2001) An experimental study of enstatite dissolution rates as funcion of pH, temperature, and aqueous Mg and Si concentration, and the mechanism of pyroxene/pyroxenoid dissolution. *Geochim Cosmochim Acta* **65**, 1219–1231.

120. O'Hanley D. S. (1996) *Serpentinites: Records of Tectonic and Petrological History*., Oxford University Press.

121. Okamoto I., Mizuochi Y., Ninomiya A., Kato T., Yajima T. and Ohsumi T. (2006) In-situ test on CO_2 fixation by serpentinite rock mass in Japan. *8-th International Conference of Greenhouse Gas Control Technologies*.

122. Okland I., Huang S., Dahle H., Thorseth I. H. and Pedersen R. B. (2012) Low temperature alteration of serpentinized ultramafic rock and implications for microbial life. *Chem Geol* **318–319**, 75–87.

123. Olajire A. A. (2014) Review of ASP EOR (alkaline surfactant polymer enhanced oil recovery) technology in the petroleum industry: Prospects and challenges. *Energy* **77**, 963–982.

124. Otsuka R., Sakamoto T. and Hara Y. (1974) Phase Transformations of Sepiolite under Hydrothermal Conditions. *Journal of the Clay Science Society of Japan (in Japanese with English abstract)* **14**, 8–19.

125. Owada A., Sato T., Hirabayashi E., Nagayoshi K., and Suzuki M. (2014) Japan Patent Kokai, 5633078.

126. Pascua C., Charnock J., Polya D. A., Sato T., Yokoyama S. and Minato M. (2005) Arsenic-bearing smectite from the geothermal environment. *Mineral Mag* **69**, 897–906.

127. Pedone A., Palazzetti F. and Barone V. (2017) Models of Aged Magnesium-Silicate-Hydrate Cements Based on the Lizardite and Talc Crystals: A Periodic DFT-GIPAW Investigation. *Journal of Physical Chemistry C* **121**, 7319–7330.

128. Pokrovsky O. S. and Schott J. (2004) Experimental study of brucite dissolution and precipitation in aqueous solutions: Surface speciation and chemical affinity control. *Geochim Cosmochim Acta* **68**, 31–45.

129. Pokrovsky O. S. and Schott J. (2000) Kinetics and mechanism of forsterite dissolution at 25°C and pH from 1 to 12. *Geochim Cosmochim Acta* **64**, 3313–3325.

130. Polyak V. J. and Güven N. (2000) Authigenesis of trioctahedral smectite in magnesium-rich carbonate speleothems in Carlsbad Cavern and other caves of the Guadalupe Mountains, New Mexico. *Clays Clay Miner* **48**, 317–321.

131. Pozo M. and Casas J. (1999) Origin of kerolite and associated Mg clays in palustrine-lacustrine environments. The Esquivias deposit (Neogene Madrid Basin, Spain). *Clay Miner* **34**, 395–418.

132. Raveesha H. R., Nayana S., Vasudha D. R., Begum J. P. S., Pratibha S., Ravikumara C. R. and Dhananjaya N. (2019) The electrochemical behavior, antifungal and cytotoxic activities of phytofabricated MgO nanoparticles using Withania somnifera leaf extract. *Journal of Science: Advanced Materials and Devices* **4**, 57–65.

133. Raza, A., Glatz, G., Gholami, R., Mahmoud, M. and Alafnan, S. (2022) Carbon mineralization and geological storage of CO_2 in basalt: Mechanisms and technical challenges. *Earth-Science Reviews* **229**, 104036.

134. Richardson I. G. (2008) The calcium silicate hydrates. *Cem Concr Res* **38**, 137–158.

135. Rigopoulos, I., Harrison, A. L., Delimitis, A., Ioannou, I., Efstathiou, A. M., Kyratsi, T. and Oelkers, E. H. (2018). Carbon sequestration via enhanced weathering of peridotites and basalts in seawater. *Applied Geochemistry* **91**, 197-207.

136. Rinaudo C., Gastaldi D. and Belluso E. (2003) Characterization of chrysotile, antigorite and lizardite by FT-Raman spectroscopy. *The Canadian Mineralogist* **41**, 883–890.

137. Romanek C. S., Morse J. W. and Grossman E. L. (2011) Aragonite Kinetics in Dilute Solutions. *Aquat Geochem* **17**, 339–356.

138. Roosz C., Grangeon S., Blanc P., Montouillout V., Lothenbach B., Henocq P., Giffaut E., Vieillard P. and Gaboreau S. (2015) Crystal structure of magnesium silicate hydrates (M-S-H): The relation with 2:1 Mg-Si phyllosilicates. *Cem Concr Res* **73**, 228–237.

139. Roosz C., Vieillard P., Blanc P., Gaboreau S., Gailhanou H., Braithwaite D., Montouillout V., Denoyel R., Henocq P. and Madé B. (2018) Thermodynamic properties of C-S-H, C-A-S-H and M-S-H phases: Results from direct measurements and predictive modelling. *Applied Geochemistry* **92**, 140–156.

140. Rounds S.A. (2012) Alkalinity and acid neutralizing capacity. In: *Techniques of Water-Resources Investigations*, Book 9, Chap. A6 (F.D. Wilde, editor.). United States Geological Survey, Reston, Virginia.

141. de Ruiter L. and Austrheim H. (2018) Formation of magnesium silicate hydrate cement in nature. *J Geol Soc London*.

142. de Ruiter L., Gunnæs A. E., Dysthe D. K. and Austrheim H. (2021) Quartz dissolution associated with magnesium silicate hydrate cement precipitation. *Solid Earth* **12**, 389–404.

143. Sandalow D., Aines R., Friedmann J., Kelemen P., McCormick C., Power I., Schmidt B. and Wilson S. A. (2021) *Carbon Mineralization Roadmap Draft October 2021*., Lawrence Livermore National Lab.(LLNL), Livermore, CA.

144. de Santiago Buey C., Suárez Barrios M., García Romero E. and Doval Montoya M. (2000) Mg-rich smectite “precursor” phase in the Tagus basin, Spain. *Clays Clay Miner* **48**, 366–373.

145. Sasaki K., Qiu X., Moriyama S., Tokoro C., Ideta K. and Miyawaki J. (2013) Characteristic Sorption of H3BO3/B(OH)4− on Magnesium Oxide. *Material Transactions* **54**, 1809–1817.

146. Sazali R. A., Sorbie K. S. and Boak L. S. (2015) The Effect of pH on Silicate Scaling. *SPE European Formation Damage Conference and Exhibition*.

147. Schaef H. T., McGrail B. P. and Owen A. T. (2010) Carbonate mineralization of volcanic province basalts. *International Journal of Greenhouse Gas Control* **4**, 249–261.

148. Selvam N. C. S., Kumar R. T., Kennedy L. J. and Vijaya J. J. (2011) Comparative study of microwave and conventional methods for the preparation and optical properties of novel MgO-micro and nano-structures. *J Alloys Compd* **509**, 9809–9815.

149. Shimbashi M., Sato T., Yamakawa M., Fujii N. and Otake T. (2018) Formation of Fe- and Mg-rich smectite under hyperalkaline conditions at Narra in Palawan, the Philippines. *Minerals* **8**, 155.

150. Shimbashi M., Yokoyama S., Kikuchi R., Otake T. and Sato T. (2022) Characteristics and formation pathways of iron- and magnesium-silicate-hydrates and Smectites under natural alkaline conditions. *Clays Clay Miner* **70**, 1–22.

151. Shimbashi M., Yokoyama S., Watanabe Y., Sato T., Otake T., Kikuchi R., Yamakawa M. and Fujii N. (2020) Formation of natural silicate hydrates by the interaction of alkaline seepage and sediments derived from serpentinized ultramafic rocks at Narra, Palawan, the Philippines. *Minerals* **10**, 719.

152. Shimoda S. (1971) Mineralogical studies of a species of stevensite from the Obori mine, Yamagata Prefecture, Japan. *Clay Miner* **9**, 185–192.

153. Snæbjörnsdóttir S. Ó., Sigfússon B., Marieni C., Goldberg D., Gislason S. R. and Oelkers E. H. (2020) Carbon dioxide storage through mineral carbonation. *Nat Rev Earth Environ* **1**, 90–102.

154. Stubičan V. and Roy R. (1961) Infrared spectra of layer-structure silicates. *Journal of the American Ceramic Society* **44**, 625–627.

155. Suzuki-Muresan T., Vandenborre J., Abdelouas A. and Grambow B. (2011) Solution controls for dissolved silica at 25, 50 and 90°C for quartz, Callovo-Oxfordian claystone, illite and MX80 bentonite. *Physics and Chemistry of the Earth* **36**, 1648–1660.

156. Taylor H. F. W. (1993) Nanostructure of C-S-H: Current Status. *Advanced cement based materials* **1**, 38–46.

157. Templeton A. S. and Ellison E. T. (2020) Formation and loss of metastable brucite: Does Fe(II)-bearing brucite support microbial activity in serpentinizing ecosystems? *Philosophical Transactions of the Royal Society A: Mathematical, Physical and Engineering Sciences* **378**.

158. Tomeoka K. and Buseck P. R. (1988) Matrix mineralogy of the Orgueil CI carbonaceous chondrite. *Geochim Cosmochim Acta* **52**, 1627–1640.

159. Tonelli M., Martini F., Calucci L., Fratini E., Geppi M., Ridi F., Borsacchi S. and Baglioni P. (2016) Structural characterization of magnesium silicate hydrate: towards the design of eco-sustainable cements. *Dalton Transactions* **45**, 3294–3304.

160. Tosca N. J., Guggenheim S. and Pufahl P. K. (2016) An authigenic origin for Precambrian greenalite: Implications for iron formation and the chemistry of ancient seawater. *Bulletin of the Geological Society of America* **128**, 511–530.

161. Tosca N. J., Macdonald F. A., Strauss J. v., Johnston D. T. and Knoll A. H. (2011) Sedimentary talc in Neoproterozoic carbonate successions. *Earth Planet Sci Lett* **306**, 11–22.

162. Tosca N. J. and Masterson A. L. (2014) Chemical controls on incipient Mg-silicate crystallization at 25ºC: Implications for early and late diagenesis. *Clay Miner* **49**, 165–194.

163. Tutolo B. M., Luhmann A. J., Tosca N. J. and Seyfried W. E. (2018) Serpentinization as a reactive transport process: The brucite silicification reaction. *Earth Planet Sci Lett* **484**, 385–395.

164. Tutolo B. M. and Tosca N. J. (2018) Experimental examination of the Mg-silicate-carbonate system at ambient temperature: Implications for alkaline chemical sedimentation and lacustrine carbonate formation. *Geochim Cosmochim Acta* **225**, 80–101.

165. Ueda H. (2005) Accretion and exhumation structures formed by deeply subducted seamounts in the Kamuikotan high-pressure/temperature zone, Hokkaido, Japan. *Tectonics* **24**, 1–17.

166. Umar A. A. and Saaid I. B. M. (2013) Silicate scales formation during asp flooding: A review. *Research Journal of Applied Sciences, Engineering and Technology* **6**, 1543–1555.

167. Vaniman D. T., Bish D. L., Ming D. W., Bristow T. F., Morris R. v and Blake D. F. (2014) Mineralogy of a Mudstone at Yellowknife Bay, Gale Crater, Mars. *Science (1979)* **343**, 1243480.

168. Vermilyea D. A. (1969) The dissolution of MgO and Mg(OH)2 in aqueous solutions. *J Electrochem Soc* **116**, 1179–1183.

169. Vespa M., Lothenbach B., Dähn R., Huthwelker T. and Wieland E. (2018) Characterisation of magnesium silicate hydrate phases (M-S-H): A combined approach using synchrotron-based absorption-spectroscopy and ab initio calculations. *Cem Concr Res* **109**, 175–183.

170. de Vidales J. L. M., Pozo M., Alia J. M., Garcia-Navarro F. and Rull F. (1991) Kerolite-stevensite mixed-layers from the Madrid Basin, Central Spain. *Clay Miner* **26**, 329–342.

171. Wada S. and Morishita T. (2013) Stabilization of Heavy Metals Contaminated Soils by Magnesium Oxide and Related Chemical and Mineralogical Reactions. *Journal of the Clay Science Society of Japan (in Japanese with English abstract)* **51**, 107–117.

172. Walling S. A., Kinoshita H., Bernal S. A., Collier N. C. and Provis J. L. (2015) Structure and properties of binder gels formed in the system Mg(OH)2-SiO2-H2O for immobilisation of Magnox sludge. *Dalton Transactions* **44**, 8126–8137.

173. Walling S. A. and Provis J. L. (2016) Magnesia-Based Cements: A Journey of 150 Years, and Cements for the Future? *Chem Rev* **116**, 4170–4204.

174. Wang A., Freeman J. J. and Jolliff B. L. (2015) Understanding the Raman spectral features of phyllosilicates. *Journal of Raman Spectroscopy* **46**, 829–845.

175. de Weerdt K. and Justnes H. (2015) The effect of sea water on the phase assemblage of hydrated cement paste. *Cem Concr Compos* **55**, 215–222.

176. Wicks F.J. and O'Hanley D.S. (1988) Serpentine minerals: structure and petrology. Pp. 91-159 in: Hydrous Phyllosilicates (S.W. Bailey, editor). *Reviews in Mineralogy* **19**, Mineralogical Society of America, Washington, D.C.

177. Wilson J., Cressey G., Cressey B., Cuadros J., Ragnarsdottir K. V., Savage D. and Shibata M. (2006) The effect of iron on montmorillonite stability. (II) Experimental investigation. *Geochim Cosmochim Acta* **70**, 323–336.

178. Wogelius R. A., Refson K., Fraser D. G., Grime G. W. and Goff J. P. (1995) Periclase surface hydroxylation during dissolution. *Geochim Cosmochim Acta* **59**, 1875–1881.

179. Wojdyr M. (2010) Fityk: a general-purpose peak fitting program. *J Appl Crystallogr* **43**, 1126–1128.

180. Wolff-Boenisch D. and Galeczka I. M. (2018) Flow-through reactor experiments on basalt-(sea)water-CO2 reactions at 90 °C and neutral pH. What happens to the basalt pore space under post-injection conditions? *International Journal of Greenhouse Gas Control* **68**, 176–190.

181. Yada K. (1979) Microstructure of chrysotile and antigorite by high-resolution electron microscopy. *Can Mineral* **17**, 679–691.

182. Zhang T., Li T., Zou J., Li Y., Zhi S., Jia Y. and Cheeseman C. R. (2020) Immobilization of radionuclide 133Cs by magnesium silicate hydrate cement. *Materials* **13**.

183. Zhang T., Zou J., Wang B., Wu Z., Jia Y. and Cheeseman C. R. (2018) Characterization of magnesium silicate hydrate (MSH) gel formed by reacting MgO and silica fume. *Materials* **11**, 1–15.

184. Zussman J., Brindley G. W. and Comer J. J. (1957) Electron Diffraction Studies of Serpentine Minerals. *American Mineralogist* **42**, 133–153.